NASA/TP-1999-209835

Uncertainty Analysis of Inertial Model Attitude Sensor Calibration and Application With a Recommended New Calibration Method

John S. Tripp and Ping Tcheng
Langley Research Center, Hampton, Virginia

December 1999

The NASA STI Program Office . . . in Profile

Since its founding, NASA has been dedicated to the advancement of aeronautics and space science. The NASA Scientific and Technical Information (STI) Program Office plays a key part in helping NASA maintain this important role.

The NASA STI Program Office is operated by Langley Research Center, the lead center for NASA's scientific and technical information. The NASA STI Program Office provides access to the NASA STI Database, the largest collection of aeronautical and space science STI in the world. The Program Office is also NASA's institutional mechanism for disseminating the results of its research and development activities. These results are published by NASA in the NASA STI Report Series, which includes the following report types:

- TECHNICAL PUBLICATION. Reports of completed research or a major significant phase of research that present the results of NASA programs and include extensive data or theoretical analysis. Includes compilations of significant scientific and technical data and information deemed to be of continuing reference value. NASA counterpart of peer-reviewed formal professional papers, but having less stringent limitations on manuscript length and extent of graphic presentations.

- TECHNICAL MEMORANDUM. Scientific and technical findings that are preliminary or of specialized interest, e.g., quick release reports, working papers, and bibliographies that contain minimal annotation. Does not contain extensive analysis.

- CONTRACTOR REPORT. Scientific and technical findings by NASA-sponsored contractors and grantees.

- CONFERENCE PUBLICATION. Collected papers from scientific and technical conferences, symposia, seminars, or other meetings sponsored or co-sponsored by NASA.

- SPECIAL PUBLICATION. Scientific, technical, or historical information from NASA programs, projects, and missions, often concerned with subjects having substantial public interest.

- TECHNICAL TRANSLATION. English-language translations of foreign scientific and technical material pertinent to NASA's mission.

Specialized services that complement the STI Program Office's diverse offerings include creating custom thesauri, building customized databases, organizing and publishing research results . . . even providing videos.

For more information about the NASA STI Program Office, see the following:

- Access the NASA STI Program Home Page at *http://www.sti.nasa.gov*

- Email your question via the Internet to help@sti.nasa.gov

- Fax your question to the NASA STI Help Desk at (301) 621-0134

- Telephone the NASA STI Help Desk at (301) 621-0390

- Write to:
  NASA STI Help Desk
  NASA Center for AeroSpace Information
  7121 Standard Drive
  Hanover, MD 21076-1320

NASA/TP-1999-209835

Uncertainty Analysis of Inertial Model Attitude Sensor Calibration and Application With a Recommended New Calibration Method

John S. Tripp and Ping Tcheng
Langley Research Center, Hampton, Virginia

National Aeronautics and
Space Administration

Langley Research Center
Hampton, Virginia 23681-2199

December 1999

Available from:

NASA Center for AeroSpace Information (CASI)
7121 Standard Drive
Hanover, MD 21076-1320
(301) 621-0390

National Technical Information Service (NTIS)
5285 Port Royal Road
Springfield, VA 22161-2171
(703) 605-6000

Contents

Tables

Figures

Symbols

AOA	angle of attack
A_x,A_y,A_z	azimuth angle for x-, y-, and z-axis sensors, rad (values in text are given in degrees, but radians are required for equations)
b_x,b_y,b_z,b_α	sensor offset for x-, y-, z-, and single-axis sensors, V
ß$_\alpha$,ß$_R$	N- and M-element calibration pitch and roll angle sets
$\mathbf{C}$	4×2 parameter matrix or 4×3 parameter matrix
C,C'	cardinality of set
C_{MR},C_R,C_{2R},C_α, $C_{2\alpha}$	constant
$\mathbf{c}$	3×1 parameter vector for single-axis sensor without roll or 4×1 parameter vector for x-, y-, and z-axis sensors with roll
$\widehat{\mathbf{c}}$	least-squares estimate of $\mathbf{c}$
$\mathbf{c}_x$, $\mathbf{c}_y$, $\mathbf{c}_z$	4×1 parameter vectors of x-, y-, and z-axis sensors with roll
$\mathbf{c}_\alpha$	3×1 parameter vector for single-axis sensor without roll
D, D$_0$, D$_1$	calibration experimental design
D	determinant of submatrix of $\mathbf{P}$
$\widehat{\mathrm{e}}$	vector of residuals
$\|\|\widehat{\mathrm{e}}\|\|$	norm of $\widehat{\mathbf{e}}$
$\widehat{e}_k$	kth element of residual vector $\widehat{\mathbf{e}}$
$(F_{\mathrm{bias}})_{95}$	F-distributed limit at 95 percent confidence level
$(F_{bS})_{95}$	F-distributed limit for test values of significant offset and sensitivity drift
$\mathbf{F_c}$	gradient matrix of $\mathbf{f}(\mathbf{C},\mathbf{z})$ with respect to $\mathbf{c}$
$\mathbf{F_{cc}}$	$L \times L \times K$ array
$\mathbf{F}_{\mathbf{cc}_k}$	kth $L \times L$ matrix contained in array $\mathbf{F_{cc}}$
$F_{L,K-L}(\alpha)$	α-percentile value of F-distribution with L, $K - L$ degrees of freedom
$\mathbf{F}_{x_\mathbf{c}}$,$\mathbf{F}_{y_\mathbf{c}}$,$\mathbf{F}_{z_\mathbf{c}}$	$K \times 4$ gradient matrices of $\mathbf{f}(\mathbf{c},\mathbf{Z})$ with respect to $\mathbf{c}$ for x-, y-, and z-axis sensors
$\mathbf{F_z}$	2×2 Jacobian matrix or 2×3 Jacobian matrix
$\mathbf{F}_{\alpha\mathbf{c}}$	$K \times 3$ gradient matrix of $\mathbf{f}(\mathbf{c},\boldsymbol{\alpha})$ with respect to $\mathbf{c}$
$\mathbf{f}(\mathbf{C},\mathbf{z})$	1×2 vector or 1×3 vector
$\mathbf{f}(\mathbf{c},\mathbf{Z})$	$K \times 1$ vectors of x-, y-, and z-axis sensor output observations
$\mathbf{f}_b$,$\mathbf{f}_S$,$\mathbf{f}_\Omega$,$\mathbf{f}_A$	column vectors of matrix $\mathbf{F_c}$
f_b,f_S,f_Ω,f_A,f_R,f_α	$\partial f/\partial b, \partial f/\partial S, \partial f/\partial \Omega, \partial f/\partial A, \partial f/\partial R, \partial f/\partial \alpha$ with x, y, z subscript denoting corresponding sensor

$f_{bb}, f_{bS}, f_{b\Omega}, f_{bA}, f_{SS}, f_{S\Omega}, f_{SA}, \ldots, f_{\Omega\Omega}, f_{\Omega A}, f_{AA}$	element of $\mathbf{F_{cc}}$
$f_{bb_k}, \ldots$	element of kth $L \times L$ subarray of $\mathbf{F_{cc}}$
$\mathbf{f_c}$	4×1 gradient vector with respect to $\mathbf{c}$
$\mathbf{f_{cc}}_{ij}$	ijth column vector of length K of $\mathbf{F_{cc}}$
$f_x(\mathbf{c}_x,\mathbf{z}_k), f_y(\mathbf{c}_y,\mathbf{z}_k), f_z(\mathbf{c}_z,\mathbf{z}_k), \ldots, f_\alpha(\mathbf{c}_\alpha,\mathbf{z}_k)$	kth applied input sensor output of x-, y-, z-, and single-axis sensors
f_{xb}, f_{yb}, f_{zb}	$\partial f/\partial b, \ldots$ for x-, y-, and z-sensor
$\mathbf{f}_{x_b}, \mathbf{f}_{x_S}, \mathbf{f}_{x_\Omega}, \mathbf{f}_{x_A}$	column vectors of matrix $\mathbf{F}_{x_c}$
$\mathbf{f}_\alpha$	2×1 gradient vector with respect to α, $\partial\mathbf{f}/\partial\alpha$
$\mathbf{f}_{\alpha_\mathbf{c}}$	3×1 gradient vector with respect to $\mathbf{c}$
$\mathbf{G}_c$	$K \times 4$ matrix
$\mathbf{g}$	3×1 gravitational vector
$\mathbf{g}_b, \mathbf{g}_S, \mathbf{g}_\Omega, \mathbf{g}_A$	$K \times 1$ gradient vector
$\mathbf{g}_c$	4×1 vector
$\mathbf{g}_{c_k}$	kth column of matrix $\mathbf{G}_c$
$\mathbf{g}_\mathrm{M}$	transformed gravitational force vector
$\mathbf{g}_\mathrm{q}$	gravitational force vector transformed into sensor coordinates
$\mathbf{g}_{q_x}, \mathbf{g}_{q_y}, \mathbf{g}_{q_z}$	transformed gravitational force vector of x-, y- and z-axis sensors
$g_{q_x}, g_{q_y}, g_{q_z}$	x-, y-, and z-components of vector $\mathbf{g}_\mathrm{q}$
$\mathbf{g}_{x_b}, \ldots$	$K \times 1$ gradient vector for x-axis sensor
$\mathbf{g}_{x_c}, \mathbf{g}_{y_c}, \mathbf{g}_{z_c}$	4×1 vector $\mathbf{g}_c$ for x-, y-, and z-axis sensors
$\mathbf{g}_{z_b}, \ldots$	$K \times 1$ gradient vector for z-axis sensor
$\mathbf{H}_c$	$K \times 4$ matrix
$\mathbf{H}_E$	$L \times L$ matrix
$\mathbf{h}(\mathbf{v},\mathbf{c})$	$K \times 1$ nonlinear system of equations
$\mathbf{h}_c$	4×1 vector
$\mathbf{h}_{c_k}$	kth row of matrix $\mathbf{H}_c$
$h_{e_{ij}}$	ijth element of $\mathbf{H}_E$
$\mathbf{h}_{x_c}, \mathbf{h}_{y_c}, \mathbf{h}_{z_c}$	4×1 vector $\mathbf{h}_c$ for x-, y-, and z-axis sensors
$\mathbf{I}$	identity matrix
$I_{bb}, I_{bS}, I_{b\Omega}, I_{bA}, I_{SS}, I_{S\Omega}, I_{SA}, \ldots, I_{\Omega\Omega}, I_{\Omega A}, I_{AA}$	evaluated definite integral
$I_{x_{bb}}, \ldots$	definite integral for x-axis sensor
$I_{y_{bb}}, \ldots$	definite integral for y-axis sensor
$I_{z_{bb}}, \ldots$	definite integral for z-axis sensor

$\mathbf{I}_\phi$	matrix of subintegrals
$\mathbf{I}_{\phi_{ij}}$	ijth element of matrix $\mathbf{I}_\phi$
i,j,k,m,n	integer index
$\Im$	test volume
K,L,M,N	integer
K_a,K_R	row and column decimation factors
M_D	number of minimal design copies within a design
q_R	quadratic form
q_{R_x},q_{R_y},q_{R_z}	quadratic form for x-, y-, and z-axis sensors
$\mathbf{R}$	$L \times L$ moment matrix
R	roll angle, rad (values in text are given in degrees, but radians are required for equations)
$\widehat{R}$	inferred roll angle, rad (values in text are given in degrees, but radians are required for equations)
$R_{\min},R_{\max}$	minimum and maximum roll angle, rad (values in text are given in degrees, but radians are required for equations)
$\mathbf{R}_x,\mathbf{R}_y,\mathbf{R}_z$	moment matrix for x-, y-, and z-axis sensors
$r_{\alpha_{bb}}, \ldots$	elements of 4×4 matrices $\mathbf{R}$ and $\mathbf{P}$ for single-axis sensor without roll
$r_{bb},r_{bS},r_{b\Omega},r_{bA},r_{SS},r_{S\Omega},$ $r_{SA}, \ldots ,r_{\Omega\Omega},r_{\Omega A}, r_{AA}$	elements in 4×4 matrices $\mathbf{R}$ and $\mathbf{P}$
$r_{x_{bb}}, \ldots$	elements of 4×4 matrices $\mathbf{R}$ and $\mathbf{P}$ for x-axis sensor
$r_{y_{bb}}, \ldots$	elements of 4×4 matrices $\mathbf{R}$ and $\mathbf{P}$ for y-axis sensor
$r_{z_{bb}}, \ldots$	elements of 4×4 matrices $\mathbf{R}$ and $\mathbf{P}$ for z-axis sensor
S	sensor sensitivity, V/g
$S_A,S_{2\alpha},S_R,S_{2R}$	constant
S_E	standard error
S_x,S_y,S_z,S_α	sensitivity for x-, y-, z-, and single-axis sensors, V/g
T	calibration experimental design
T_b, T_S	test value for significant sensor offset and sensitivity drift
T_{bias}	test value for significant bias error
$\mathbf{T}_\alpha(\alpha),\mathbf{T}_R(R),\mathbf{T}_Y(Y)$	coordinate transformation matrices in pitch, roll, and yaw
$t_k(\alpha)$	α-percentile value of two-tailed t-distribution with k degrees of freedom
$\mathbf{U}_\mathbf{Y}$	$K \times K$ output uncertainty covariance matrix
V	figure of merit
V_N	unnormalized figure of merit

V_R	normalized mean variance over reduced usage range
$\mathbf{v}$	1×2 observed output vector or $K \times 1$ vector of observed outputs
$\mathbf{v}_x,\mathbf{v}_y,\mathbf{v}_z,\mathbf{v}_\alpha$	$K \times 1$ vectors of x-, y-, z-, and single-axis sensor outputs
v_x,v_y,v_z,v_α	observed output for x-, y-, z-, and single-axis sensors, V
w,w_x,w_y,w_z	$= \sin\,\Omega$, $\sin\,\Omega_x$, $\sin\,\Omega_y$, $\sin\,\Omega_z$, respectively
x, y, z	axes
Y	yaw angle, rad (values in text are given in degrees, but radians are required for equations)
$\mathbf{Z}$	$K \times 1$ or $K \times 2$ design matrix without and with roll inputs
$\mathbf{z}$	1×2 input vector of independent variables α and R
$\widehat{\mathbf{z}}$	1×2 vector of inferred inputs
α	pitch angle, rad (values in text are given in degrees, but radians are required for equations)
$\widehat{\alpha}$	inferred pitch angle, rad (values in text are given in degrees, but radians are required for equations)
$\alpha_{\min}$, $\alpha_{\max}$	minimum and maximum pitch angle, rad (values in text are given in degrees, but radians are required for equations)
$\mathbf{\Gamma}_A,\mathbf{\Gamma}_W$	4×4 unitary matrix
$\Delta\,\cos\,\alpha,\Delta\,\cos\,2\alpha$, $\Delta\,\cos\,R,\Delta\,\cos\,2R$, $\Delta\,\sin\,\alpha,\Delta\,\sin 2\,\alpha$, $\Delta\,\sin\,R,\Delta\,\sin\,2R$	constant
ΔR	roll angle difference
$\Delta\alpha$	pitch angle difference
δR	uncertainty of R
$\delta\widehat{R}$	uncertainty of $\widehat{R}$
$\delta\widehat{v}_{P_0}$	uncertainty of predicted output $\widehat{v}$ following new measurement
$\delta v_x,\delta v_y,\delta v_z$	element of $\delta\widehat{\mathbf{v}}$
$\delta\widehat{\mathbf{v}}$	uncertainty of predicted output vector $\widehat{\mathbf{v}}$
$\delta\widehat{\mathbf{z}}$	uncertainty of inferred input vector
$\delta\widehat{\alpha}$	uncertainty of $\widehat{\alpha}$
Ξ	4×4 matrix
$\mathbf{P}$	4×4 matrix
$\mathbf{P}_{ij}^{-1}$	ijth element of matrix $\mathbf{P}^{-1}$
$\mathbf{P}_x,\mathbf{P}_y,\mathbf{P}_z$	modified moment matrix for x-, y-, and z-axis sensors
$\rho_{b_\Omega},\rho_{b_A},\rho_{S_\Omega},\rho_{S_A}$, ρ_{Ω_Ω}, $\rho_{\Omega_A}, \ldots, \rho_{\alpha_A}$	elements in 4×4 matrix $\mathbf{P}$
$\rho_{x_{b\Omega}}, \ldots$	elements of 4×4 matrix $\mathbf{P}$ for x-axis sensor

$\rho_{y_{b\Omega}}, \ldots$	elements of 4×4 matrix $\mathbf{P}$ for y-axis sensor
$\rho_{z_{b\Omega}}, \ldots$	elements of 4×4 matrix $\mathbf{P}$ for z-axis sensor
$\rho_{\alpha_{b\Omega}}, \ldots$	elements of 4×4 matrix $\mathbf{P}$ for single-axis sensor without roll
$\Sigma_{\widehat{\mathbf{c}}}$	covariance matrix of estimated parameter vector $\widehat{\mathbf{c}}$
$\Sigma_{\widehat{\mathbf{v}}}$	2×2 covariance matrix or 3×3 covariance matrix of $\widehat{\mathbf{v}}$
$\Sigma_{\widehat{\mathbf{z}}}$	2×2 covariance matrix of $\widehat{\mathbf{z}}$
σ_b, σ_S	estimated standard errors due to sensor offset and sensitivity drift, respectively
σ_{bias}	estimated standard error due to bias uncertainty
σ_{cal}	estimated standard error due to calibration bias error
σ_E	estimated total standard error
σ_{inv}	root-mean-square value of residuals of inferred angles
σ_{prec}	estimated standard error due to precision uncertainty
σ_R	roll measurement standard deviation
$\sigma_v(\mathbf{z})$	output standard deviation function ($\mathbf{z}$ is omitted when context is clear)
$\sigma_{v_x}(\mathbf{z}), \sigma_{v_y}(\mathbf{z}), \sigma_{v_z}(\mathbf{z}), \sigma_{v_\alpha}(\mathbf{z})$	output standard deviation function of x-, y-, z-, and single-axis sensors without roll
$\sigma_x, \sigma_y, \sigma_z$	output measurement standard deviation of x-, y-, and z-axis sensors
$\sigma_{\widehat{\alpha}}(\mathbf{z}), \sigma_{\widehat{R}}(\mathbf{z})$	standard deviation function of inferred pitch and roll angles
σ_0	standard deviation of new measurement
$\mathbf{\Phi}_c$	$K \times 4$ matrix
$\boldsymbol{\phi}_b, \boldsymbol{\phi}_S, \boldsymbol{\phi}_\Omega, \boldsymbol{\phi}_A$	$K \times 1$ gradient vector; columns of matrix $\mathbf{\Phi}_c$
$\boldsymbol{\phi}_c, \boldsymbol{\phi}_{c_k}$	1×4 gradient vector; kth row of matrix $\mathbf{\Phi}_c$
$\boldsymbol{\phi}_{x_\mathbf{c}}, \boldsymbol{\phi}_{y_\mathbf{c}}, \boldsymbol{\phi}_{z_\mathbf{c}}$	gradient vector with respect to $\mathbf{c}$ for x-, y-, and z-axis sensors
ϕ_{xA}	$= \partial\phi_x/\partial A$
$\phi_{x\Omega}$	$= \partial\phi_x/\partial\Omega$
ϕ_{yA}	$= \partial\phi_y/\partial A$
$\phi_{y\Omega}$	$= \partial\phi_y/\partial\Omega$
ϕ_{zA}	$= \partial\phi_z/\partial A$
$\phi_{z\Omega}$	$= \partial\phi_z/\partial\Omega$
$\phi_{\widehat{\alpha}}$	pitch misalignment angle of single-axis sensor without roll, rad
Ω	coning angle for single-axis sensor, rad (values in text are given in degrees, but radians are required for equations)
$\Omega_x, \Omega_y, \Omega_z$	coning angle for x-, y-, and z-axis sensors, rad (values in text are given in degrees, but radians are required for equations)

Subscripts:

x, y, z	x-, y-, z-axis sensors with roll
α	single-axis sensor without roll
k	kth observation
0	new measurement after calibration

Superscript:

T	transpose

Caret $\hat{}$ denotes least-squares estimated value or inferred value; argument $\mathbf{z}$ is omitted from variance functions $\sigma_v^2(\mathbf{z})$, etc., when context is clear; matrix notation $\mathbf{A}^{-\mathrm{T}}$ denotes $[\mathbf{A}^{\mathrm{T}}]^{-1}$.

Abstract

Statistical tools, previously developed for nonlinear least-squares estimation of multivariate sensor calibration parameters and the associated calibration uncertainty analysis, have been applied to single- and multiple-axis inertial model attitude sensors used in wind tunnel testing to measure angle of attack and roll angle. The analysis provides confidence and prediction intervals of calibrated sensor measurement uncertainty as functions of applied input pitch and roll angles. A comparative performance study of various experimental designs for inertial sensor calibration is presented along with corroborating experimental data. The importance of replicated calibrations over extended time periods has been emphasized; replication provides independent estimates of calibration precision and bias uncertainties, statistical tests for calibration or modeling bias uncertainty, and statistical tests for sensor parameter drift over time. A set of recommendations for a new standardized model attitude sensor calibration method and usage procedures is included. The statistical information provided by these procedures is necessary for the uncertainty analysis of aerospace test results now required by industrial users of wind tunnel test facilities.

1. Introduction

The standard instrumentation used at the Langley Research Center (LaRC) for measuring model attitude in the wind tunnel is the inertial angle of attack (AOA) sensor package described in reference 1. Langley Research Center has employed the inertial sensor as the primary AOA measurement system during the past 30 years. Various aspects of inertial model attitude measurement have been subsequently reported in references 2 to 4. In particular, reference 2 describes data reduction techniques for model attitude measurements in pitch and roll and pitch measurement only at zero roll. Typically, the LaRC AOA package provides static model attitude measurements at accuracies of $\pm 0.01°$.

Because of signal-to-noise ratios as low as -100 dB commonly encountered in wind tunnel test facilities, heavy low-pass filtering in the bandwidth range of 0.3 to 0.6 Hz is necessary for static attitude measurement (ref. 3). Therefore the inertial system is suitable only as a static attitude measurement device and is not useful for dynamic attitude measurement. In addition, the inertial accelerometer has been found to exhibit an offset error due to centrifugal forces developed in the presence of repetitive model motion in yaw and pitch encountered at high dynamic levels during tests, as discussed in reference 4. Although optical sensors, which are insensitive to centrifugal errors, are used increasingly for both static and dynamic model attitude measurement, the inertial sensor remains important for high-precision primary measurement, calibration of optical systems, and optical system backup during poor test section visibility.

Inertial model attitude sensor packages have been calibrated at LaRC by means of four- and six-point tumble tests. The tumble test technique, easy to implement through the use of simple precision leveling devices, has been adequate in the past. It, however, does not provide adequate spatial resolution for modeling precision or statistical uncertainty information now required by test facility users. Also, current calibration procedures do not employ replication, necessary for independent estimation of sensor bias and precision uncertainties and for assessment of long-term drift.

Multiple-point replicated calibration is now feasible and convenient through use of the automatically controlled calibration dividing head and modern computerized control and data acquisition systems. Statistical tools recently developed in reference 5 for general estimation of multivariate sensor calibration parameters and the associated calibration uncertainty analysis are applied in this publication to multiple-point replicated calibration of inertial AOA packages. These statistical tools, applied to one-, two-, and three-axis inertial sensor packages, allow comparison of experimental designs for calibration, computation of calibration confidence intervals, and prediction intervals as functions of applied inputs, independent estimation of calibration bias and precision uncertainties, and detection of long-term parameter drift. Experimental calibration data are presented to demonstrate and verify the efficacy of the technique.

Based on the theoretical analysis and experimental calibration results, a set of recommendations for model attitude sensor calibration and usage is proposed. The recommended procedures may be readily implemented by means of modern automated calibration apparatus. The statistical information thus provided, not previously available to test facility users, is necessary for determination of overall uncertainty of aerospace test results now required by industrial test facility users.

2. Pitch and Roll Measurement

2.1. Angle of Attack Measurement Without Roll

Use of the single-axis inertial angle of attack (AOA) sensor in wind tunnel facilities without roll allows simplified data reduction, as described in reference 2; the uncertainty analysis described briefly in reference 5 is extended here. Misalignment of the accelerometer sensitive axis with respect to the AOA package x-axis is represented by the angle, denoted by ϕ_α, between the projection of the sensitive axis onto the x-z (pitch) plane and the x-axis. Roll angles during calibration and facility usage are assumed to remain zero. The sensor output is given by the following equation:

$$v_\alpha = b_\alpha + S_\alpha \sin(\alpha - \phi_\alpha) \tag{1}$$

where v_α is the sensor output in volts, b_α is the sensor offset in volts, S_α is the sensitivity in volts per g unit, α is the pitch angle in radians, and ϕ_α is the pitch misalignment angle in radians. Note that acceleration of gravity g is normalized to unity in all equations.

2.2. Model Attitude Measurement With Roll

For single-axis or multiple-axis attitude measurement with roll, the inertial sensor axis misalignment must be characterized in three-dimensional (3-D) space. At LaRC the sensitive axis of the x-axis sensor is represented as lying on the surface of a cone, aligned with the x-axis of the sensor package, whose vertex is located at the origin of the package coordinate system. The semivertex angle of the cone, denoted by Ω, is termed the "coning angle." Looking in the positive x direction, the angular position of the pitch sensor axis on the surface of the cone is specified by angle A_x, measured counterclockwise from the positive y-axis to the pitch sensor axis; angle A_x is termed the "azimuth angle." As indicated in appendix A and reference 2, the sensor output equation is given by the following form:

$$v_x = b_x + S_x[\cos\Omega_x \sin\alpha - \sin\Omega_x \cos\alpha \sin(R + A_x)] \tag{2}$$

where R denotes roll angle and subscript x denotes pitch sensor parameters. Angles are in radians. If roll angle R is known, input angle α is inferred by inverting equation (2) to obtain

$$\alpha = \arcsin\left[\frac{(v_x - b_x)/S_x}{\sqrt{\cos^2\Omega_x + \sin^2(R + A_x)\sin^2\Omega_x}}\right] + \arctan[\tan\Omega_x \sin(R + A_x)] \tag{3}$$

Multiple-axis inertial attitude measurement packages, designed for simultaneous measurement of pitch and roll angles, employ two orthogonally placed accelerometers aligned nominally with the x- and y-axes of the model, or three orthogonally placed accelerometers aligned nominally with the x-, y-, and z-axes of the model. Coning angles Ω_y and Ω_z and azimuth angles A_y and A_z for the y-axis and z-axis sensors are defined analogously to Ω_x and A_x. The x-axis sensor output is given by equation (2). The y-axis sensor output, obtained in appendix A, is found to be

$$v_y = b_y - S_y[\cos\Omega_y \sin R \cos\alpha - \sin\Omega_y (\sin A_y \sin\alpha - \cos A_y \cos R \cos\alpha)] \tag{4}$$

Given observed outputs v_x and v_y, the corresponding inputs α and R are inferred by simultaneous solution of equations (2) and (4) via an iterative method. However, as shown later a useful solution does not exist near $\alpha = \pm 90°$ or $R = \pm 90°$, where the 2×2 Jacobian matrix of the system of equations (2) and (4) with respect to α and R becomes singular or poorly conditioned. It can be shown that the Jacobian matrix must be nonsingular for the existence of a solution (ref. 6).

As shown later, the singularities near $R = \pm 90°$ are eliminated by addition of the z-axis sensor, whose output, obtained in appendix A, is found to be

$$v_z = b_z - S_z[\cos\Omega_z \cos R \cos\alpha - \sin\Omega_z (\cos A_z \sin\alpha - \sin A_z \sin R \cos\alpha)] \tag{5}$$

The 3×2 Jacobian matrix of the system of equations (2), (4), and (5) has rank 1 at $\alpha = \pm 90°$, and rank 2 elsewhere for $\Omega < 10°$ as is shown subsequently. Inputs α and R are estimated by least-squares solution of the overdetermined system of equations (2), (4), and (5), provided that the Jacobian matrix has rank 2. At $\alpha = \pm 90°$, estimated pitch angle can be determined within the accuracy of the y-axis and z-axis sensors, although roll angle cannot be determined. Note that calibration parameters b, S, Ω, and A of sensors x, y, and z are independently determined.

3. Experimental Designs for Calibration

Experimental designs for calibration of the single-axis AOA sensor without roll, the single-axis pitch sensor with roll, and the multiple-axis package are now analyzed by using nonlinear multivariate uncertainty analysis techniques and notation developed in reference 5. Let $\mathbf{c}_\alpha$ denote the 3×1 parameter vector for the single-axis sensor without roll as follows:

$$\mathbf{c}_\alpha = [b_\alpha \ S_\alpha \ \phi_\alpha]^{\mathrm{T}} \tag{6}$$

and let $\mathbf{z}$ denote the vector of independent variables, which contains the single element α. The calibration experimental design D consists of K-element set $ß_\alpha = \{\alpha_1, \ldots, \alpha_K\} \subseteq [\alpha_{\min}, \alpha_{\max}]$. The $K \times 1$ design matrix $\mathbf{Z}$ is then

$$\mathbf{Z} = [\alpha_1 \ldots \alpha_K]^{\mathrm{T}} \tag{7}$$

Similarly, let $\mathbf{c}_x$, $\mathbf{c}_y$, and $\mathbf{c}_z$ denote 4×1 vectors of x-, y-, and z-axis sensor parameters with roll; therefore,

$$\left.\begin{aligned} \mathbf{c}_x &= [b_x \ S_x \ \Omega_x \ A_x]^{\mathrm{T}} \\ \mathbf{c}_y &= [b_y \ S_y \ \Omega_y \ A_y]^{\mathrm{T}} \\ \mathbf{c}_z &= [b_z \ S_z \ \Omega_z \ A_z]^{\mathrm{T}} \end{aligned}\right\} \tag{8}$$

and let $\mathbf{z}$ denote the 1×2 vector of independent variables

$$\mathbf{z} = [\alpha \ R] \tag{9}$$

The calibration experimental design contains K pitch-roll angle pairs, where the pitch angle is selected from set $\text{ß}_\alpha \subseteq [\alpha_{\min}, \alpha_{\max}]$ containing N values, and the roll angle is selected from set $\text{ß}_R \subseteq [R_{\min}, R_{\max}]$ containing M values; thus

$$\left.\begin{aligned} \text{ß}_\alpha &= \{\alpha_1, \alpha_2, \ldots, \alpha_N\} \\ \text{ß}_R &= \{R_1, R_2, \ldots, R_M\} \end{aligned}\right\} \tag{10}$$

The experimental design of primary interest, denoted by D, contains $K = MN$ ordered pairs from sets ß_α and ß_R, represented by $K \times 2$ design matrix $\mathbf{Z}$ as

$$\mathbf{Z} = \begin{bmatrix} \alpha_1 & \alpha_1 & \cdots & \alpha_1 & \alpha_2 & \alpha_2 & \cdots & \alpha_2 & \cdots & \alpha_N & \alpha_N & \cdots & \alpha_N \\ R_1 & R_2 & \cdots & R_M & R_1 & R_2 & \cdots & R_M & \cdots & R_1 & R_2 & \cdots & R_M \end{bmatrix}^{\mathrm{T}} \tag{11}$$

Although, as is shown, design D has desirable properties, its possibly large cardinality may become experimentally impractical. Fractional experimental designs constructed as subsets of D are described later and provide more efficient calibration with adequate prediction uncertainties. The considerable available literature on design of efficient experiments is not reviewed in this publication.

Let the corresponding x-, y-, and z-axis sensor output observations be denoted by $K \times 1$ vectors $\mathbf{v}_x$, $\mathbf{v}_y$, and $\mathbf{v}_z$ as follows:

$$\left.\begin{aligned} \mathbf{v}_x &= [\, v_{x1} \quad v_{x2} \quad \cdots \quad v_{xK} \,]^{\mathrm{T}} \\ \mathbf{v}_y &= [\, v_{y1} \quad v_{y2} \quad \cdots \quad v_{yK} \,]^{\mathrm{T}} \\ \mathbf{v}_z &= [\, v_{z1} \quad v_{z2} \quad \cdots \quad v_{zK} \,]^{\mathrm{T}} \end{aligned}\right\} \tag{12}$$

3.1. Observed Sensor Outputs

At the kth calibration point of the single-axis sensor without roll, where $k = 1, \ldots, K$, element k of observation vector $\mathbf{v}_\alpha$ is obtained from equation (1) as

$$v_{\alpha_k} = f_\alpha(\mathbf{c}_\alpha, \mathbf{z}_k) = b_\alpha + S_\alpha[\cos\,\phi_\alpha\ \sin\,\alpha_k - \sin\,\phi_\alpha\ \cos\,\alpha_k] \tag{13}$$

Similarly, for sensors with roll, vectors $\mathbf{v}_x$, $\mathbf{v}_y$, and $\mathbf{v}_z$ are obtained by using equations (2), (4), and (5) as

$$v_{x_k} = f_x(\mathbf{c}_x, \mathbf{z}_k) = b_x + S_x[\cos\,\Omega_x\ \sin\,\alpha_k - \sin\,\Omega_x\ \cos\,\alpha_k\ \sin\,(R_k + A_x)] \tag{14}$$

$$\begin{aligned} v_{y_k} &= f_y(\mathbf{c}_y, \mathbf{z}_k) \\ &= b_y - S_y[\cos\,\Omega_y\ \sin\,R_k \cos\,\alpha_k - \sin\,\Omega_y\,(\sin\,A_y\ \sin\,\alpha_k - \cos\,A_y \cos\,R_k\ \cos\,\alpha_k)] \end{aligned} \tag{15}$$

and

$$\begin{aligned} v_{z_k} &= f_z(\mathbf{c}_z, \mathbf{z}_k) \\ &= b_z - S_z[\cos\,\Omega_z\ \cos\,R_k \cos\,\alpha_k - \sin\,\Omega_z\,(\cos\,A_z\ \sin\,\alpha_k - \sin\,A_z\ \sin\,R_k\ \cos\,\alpha_k)] \end{aligned} \tag{16}$$

Note that equation (13) is a special case of equation (14), where

$$\left.\begin{aligned} \Omega_x &= \phi_\alpha \\ A_x &= \pi/2 \\ R_k &= 0 \end{aligned}\right\} \tag{17}$$

For K observations, equations (13) to (16) are extended to vector function notation as

$$\mathbf{v}_x = \mathbf{f}_x(\mathbf{c}_x,\mathbf{Z}) = [f_x(\mathbf{c}_x,\mathbf{z}_1)\ f_x(\mathbf{c}_x,\mathbf{z}_2)\ \cdots\ f_x(\mathbf{c}_x,\mathbf{z}_K)]^{\mathrm{T}} \tag{18}$$

Vectors $\mathbf{v}_\alpha$, $\mathbf{v}_y$, and $\mathbf{v}_z$ are defined analogously.

3.2. Evaluation of Gradient Matrices

The 3×1 gradient vector of $f_\alpha(\mathbf{c}_\alpha,\mathbf{z})$ with respect to $\mathbf{c}_\alpha$ is given by

$$\mathbf{f}_{\alpha_c} \equiv \frac{\partial f_\alpha(\mathbf{c}_\alpha,\mathbf{z})}{\partial \mathbf{c}_\alpha} \equiv \left[\frac{\partial f_\alpha(\mathbf{c}_\alpha,\mathbf{z})}{\partial b_\alpha}\ \frac{\partial f_\alpha(\mathbf{c}_\alpha,\mathbf{z})}{\partial S_\alpha}\ \frac{\partial f_\alpha(\mathbf{c}_\alpha,\mathbf{z})}{\partial \phi_\alpha}\right]^{\mathrm{T}} \tag{19}$$

The 4×1 gradient vectors— $f_x(\mathbf{c}_x,\mathbf{z})$ with respect to $\mathbf{c}_x$, $f_y(\mathbf{c}_y,\mathbf{z})$ with respect to $\mathbf{c}_y$, and $f_z(\mathbf{c}_z,\mathbf{z})$ with respect to $\mathbf{c}_z$ —are obtained as follows:

$$\mathbf{f}_c \equiv \frac{\partial f(\mathbf{c},\mathbf{z})}{\partial \mathbf{c}} \equiv \left[\frac{\partial f(\mathbf{c},\mathbf{z})}{\partial b}\ \frac{\partial f(\mathbf{c},\mathbf{z})}{\partial S}\ \frac{\partial f(\mathbf{c},\mathbf{z})}{\partial \Omega}\ \frac{\partial f(\mathbf{c},\mathbf{z})}{\partial A}\right]^{\mathrm{T}} \tag{20}$$

Element-by-element evaluation of equation (20) for the x-axis sensor is as follows:

$$f_{xb} \equiv \frac{\partial f_x(\mathbf{c}_x,\mathbf{z})}{\partial b_x} = 1 \tag{21}$$

$$f_{xS} \equiv \frac{\partial f_x(\mathbf{c}_x,\mathbf{z})}{\partial S_x} = \cos\,\Omega_x\,\sin\,\alpha - \sin\,\Omega_x\,\cos\,\alpha\,\sin\,(R + A_x) \tag{22}$$

$$f_{x\Omega} \equiv \frac{\partial f_x(\mathbf{c}_x,\mathbf{z})}{\partial \Omega_x} = -S_x[\sin\,\Omega_x\,\sin\,\alpha + \cos\,\Omega_x\,\cos\,\alpha\,\sin\,(R + A_x)] = S_x\phi_{x\Omega} \tag{23}$$

$$f_{xA} \equiv \frac{\partial f_x(\mathbf{c}_x,\mathbf{z})}{\partial A_x} = -S_x\,\sin\,\Omega_x\,\cos\,\alpha\,\cos\,(R + A_x) = S_x w_x \phi_{xA} \tag{24}$$

where

$$\phi_{x\Omega} \equiv -\sin\,\Omega_x\,\sin\,\alpha - \cos\,\Omega_x\,\cos\,\alpha\,\sin\,(R + A_x) \tag{25}$$

$$\phi_{xA} \equiv -\cos\,\alpha\,\cos\,(R + A_x) \tag{26}$$

$$w_x \equiv \sin\,\Omega_x \tag{27}$$

To evaluate the gradient terms of equation (19) for the single-axis sensor without roll, substitute the values of equation (17) into equations (21) to (23).

Similarly equation (20) is evaluated for the y-axis sensor as follows:

$$f_{yb} \equiv \frac{\partial f_y(\mathbf{c}_y,\mathbf{z})}{\partial b_y} = 1 \tag{28}$$

$$f_{yS} \equiv \frac{\partial f_y(\mathbf{c}_y,\mathbf{z})}{\partial S_y} = -\cos\,\Omega_y\,\cos\,\alpha\,\sin\,R + \sin\,\Omega_y\,(\sin\,A_y\,\sin\,\alpha - \cos\,A_y\,\cos\,\alpha\,\cos\,R) \tag{29}$$

$$\begin{aligned} f_{y\Omega} &\equiv \frac{\partial f_y(\mathbf{c}_y,\mathbf{z})}{\partial \Omega_y} = S_y[\sin\,\Omega_y\,\cos\,\alpha\,\sin\,R + \cos\,\Omega_y\,(\sin\,A_y\,\sin\,\alpha - \cos\,A_y\,\cos\,\alpha\,\cos\,R)] \\ &= S_y\phi_{y\Omega} \end{aligned} \tag{30}$$

$$f_{y_A} \equiv \frac{\partial f_y(\mathbf{c}_y,\mathbf{z})}{\partial A_y} = S_y \sin\,\Omega_y(\cos\,A_y \sin\,\alpha + \sin\,A_y \cos\,R \cos\,\alpha) = S_y w_y \phi_{yA} \tag{31}$$

where

$$\phi_{y\Omega} \equiv \sin\,\Omega_y \cos\,\alpha \sin\,R + \cos\,\Omega_y\,(\sin\,A_y \sin\,\alpha - \cos\,A_y \cos\,\alpha \cos\,R) \tag{32}$$

$$\phi_{yA} \equiv \cos\,A_y \sin\,\alpha + \sin\,A_y \cos\,R \cos\,\alpha \tag{33}$$

$$w_y \equiv \sin\,\Omega_y \tag{34}$$

Evaluation of equation (20) is similar for the z-axis sensor as follows:

$$f_{zb} \equiv \frac{\partial f_z(\mathbf{c}_z,\mathbf{z})}{\partial b_z} = 1 \tag{35}$$

$$f_{zS} \equiv \frac{\partial f_z(\mathbf{c}_z,\mathbf{z})}{\partial S_z} = -\cos\,\Omega_z \cos\,\alpha \cos\,R + \sin\,\Omega_z\,(\cos\,A_z \sin\,\alpha - \sin\,A_z \cos\,\alpha \sin\,R) \tag{36}$$

$$\begin{aligned} f_{z\Omega} &\equiv \frac{\partial f_z(\mathbf{c}_z,\mathbf{z})}{\partial \Omega_z} = S_z[\sin\,\Omega_y \cos\,\alpha \cos\,R + \cos\,\Omega_z\,(\cos\,A_z \sin\,\alpha - \sin\,A_z \cos\,\alpha \sin\,R)] \\ &= S_z \phi_{z\Omega} \end{aligned} \tag{37}$$

$$f_{zA} \equiv \frac{\partial f_z(\mathbf{c}_z,\mathbf{z})}{\partial A_z} = -S_z \sin\,\Omega_z\,(\sin\,A_z \sin\,\alpha + \cos\,A_z \sin\,R \cos\,\alpha) = S_z w_z \phi_{zA} \tag{38}$$

where

$$\phi_{z\Omega} \equiv \sin\,\Omega_z \cos\,\alpha \cos\,R + \cos\,\Omega_z(\cos\,A_z \sin\,\alpha - \sin\,A_z \cos\,\alpha \sin\,R) \tag{39}$$

$$\phi_{zA} \equiv -(\sin\,A_z \sin\,\alpha + \cos\,A_z \sin\,R \cos\,\alpha) \tag{40}$$

$$w_z \equiv \sin\,\Omega_z \tag{41}$$

For calibration of sensor packages with roll, define $K \times 4$ gradient matrices $\mathbf{F}_{x_\mathbf{c}}$, $\mathbf{F}_{y_\mathbf{c}}$, and $\mathbf{F}_{z_\mathbf{c}}$, obtained from equation (20) as

$$\mathbf{F}_\mathbf{c} = \frac{\partial \mathbf{f}(\mathbf{c}, \mathbf{Z})}{\partial \mathbf{c}} = \begin{bmatrix} \mathbf{f}_{\mathbf{c}_1}^{\mathrm{T}} \\ \mathbf{f}_{\mathbf{c}_2}^{\mathrm{T}} \\ \vdots \\ \mathbf{f}_{\mathbf{c}_K}^{\mathrm{T}} \end{bmatrix} = \left[\mathbf{f}_b \mid \mathbf{f}_S \mid \mathbf{f}_\Omega \mid \mathbf{f}_A \right] \tag{42}$$

where $\mathbf{f}_b$, $\mathbf{f}_S$, $\mathbf{f}_\Omega$, and $\mathbf{f}_A$ denote columns 1, 2, 3, and 4, respectively, of matrix $\mathbf{F}_\mathbf{c}$. The $K \times 3$ matrix $\mathbf{F}_{\alpha\mathbf{c}}$ is similarly defined for the single-axis sensor without roll.

Reference 5 shows that the least-squares estimate of $\mathbf{c}$, denoted by $\widehat{\mathbf{c}}$, is individually obtained for sensor x, y, or z by solving the following $K \times 1$ system of nonlinear equations for $\mathbf{c}$:

$$\mathbf{h}(\mathbf{v},\mathbf{c}) \equiv [\mathbf{v} - \mathbf{f}(\mathbf{c},\mathbf{Z})]^{\mathrm{T}}\, \mathbf{U}_\mathbf{Y}^{-1} \left[\frac{\partial \mathbf{f}}{\partial \mathbf{c}}(\mathbf{c},\mathbf{Z}) \right] = 0 \tag{43}$$

where $\mathbf{v}$ is the $K \times 1$ vector of observed outputs, and $\sigma_E^2 \mathbf{U}_\mathbf{Y}$ is the $K \times K$ output uncertainty covariance matrix, where σ_E^2 is the measurement variance. The $L \times L$ moment matrix $\mathbf{R}$ (ref. 5) is given by the following equation:

$$\mathbf{R} \equiv \frac{\partial \mathbf{h}(\mathbf{v}, \mathbf{c})}{\partial \mathbf{c}} = \mathbf{F}_\mathbf{c}^{\mathrm{T}}\, \mathbf{U}_\mathbf{Y}^{-1}\, \mathbf{F}_\mathbf{c} + \mathbf{H}_E \tag{44}$$

where the ij^{th} element of $L \times L$ matrix $\mathbf{H}_E$ is given by

$$h_{e_{ij}} = [\mathbf{v} - \mathbf{f}(\mathbf{c},\mathbf{Z})]^{\mathrm{T}}\mathbf{U}_{\mathbf{Y}}^{-1}\mathbf{f}_{\mathbf{cc}_{ij}} \tag{45}$$

where $\mathbf{f}_{\mathbf{cc}_{ij}}$ is the ijth column vector of length K contained in $L \times L \times K$ array $\mathbf{F}_{\mathbf{cc}}$ defined by

$$\mathbf{F}_{\mathbf{cc}} \equiv \frac{\partial \mathbf{F}_{\mathbf{c}}(\mathbf{c},\mathbf{Z})}{\partial \mathbf{c}} = \frac{\partial^2 \mathbf{f}(\mathbf{c},\mathbf{Z})}{\partial \mathbf{c}^2} \tag{46}$$

where $1 \leq i,\ j \leq L$, $L = 3$ without roll; and $L = 4$ with roll. Matrix $\mathbf{H}_E$, evaluated in appendix B, is negligible unless the least-squares residuals are large. Indeed, note that term $\widehat{\mathbf{e}} \equiv [\mathbf{v} - \mathbf{f}(\widehat{\mathbf{c}},\mathbf{Z})]$ in equation (45) equals the vector of residuals following least-squares estimation of $\mathbf{c}$. The norm of $\widehat{\mathbf{e}}$, equal to the root sum of squares of its elements, is defined as

$$\|\widehat{\mathbf{e}}\| \equiv \left(\sum_{k=1}^{K} \widehat{e}_k^2\right)^{1/2} = (\widehat{\mathbf{e}}^{\mathrm{T}}\widehat{\mathbf{e}})^{1/2} \tag{47}$$

Reference 5 shows that the expected value of $\|\widehat{\mathbf{e}}\|$ equals $(K-L)^{1/2}\sigma_E$, where σ_E is the standard deviation of the measurement error. Therefore, if σ_E is small, matrix $\mathbf{H}_E$ can be neglected in equation (44) for uncertainty analysis. See appendix B for details.

The standard error S_E, defined individually for sensor x, y, or z as

$$S_E = \frac{(\widehat{\mathbf{e}}^{\mathrm{T}}\widehat{\mathbf{e}})^{1/2}}{\sqrt{K - L}} \tag{48}$$

provides an unbiased estimate of σ_E. For the special case where $\mathbf{U}_Y = \mathbf{I}$ and where $\mathbf{H}_E$ can be neglected, moment matrix $\mathbf{R}$ becomes

$$\mathbf{R} = \mathbf{F}_{\mathbf{c}}^{\mathrm{T}}\mathbf{F}_{\mathbf{c}} \tag{49}$$

The covariance matrix of estimated parameter vector $\widehat{\mathbf{c}}$ is then given by (ref. 5)

$$\Sigma_{\mathbf{c}} = \sigma_E^2 \mathbf{R}^{-1} \tag{50}$$

A confidence ellipsoid for $\widehat{\mathbf{c}}$ at confidence level $1-\alpha$ is defined by the following inequality (ref. 5):

$$(\mathbf{c} - \widehat{\mathbf{c}})^{\mathrm{T}}\mathbf{R}^{-1}(\mathbf{c} - \widehat{\mathbf{c}}) \leq (K - L)S_E^2 F_{L,K-L}(\alpha) \tag{51}$$

where $F_{L,K-L}(\alpha)$ is the α-percentile value of the F-distribution with L, $K-L$ degrees of freedom.

3.3. Sensor Output Variance Function

In reference 5, the variance function $\sigma_v^2(\mathbf{z})$ of predicted outputs $\widehat{v}_x$, $\widehat{v}_y$, and $\widehat{v}_z$, respectively, for sensor x, y, and z is given by the following quadratic form:

$$\frac{\sigma_v^2(\mathbf{z})}{\sigma_E^2} = \frac{\mathbf{f}_{\mathbf{c}}^{\mathrm{T}}(\mathbf{z})\Sigma_{\mathbf{c}}\mathbf{f}_{\mathbf{c}}(\mathbf{z})}{\sigma_E^2} \approx \mathbf{f}_{\mathbf{c}}^{\mathrm{T}}(\mathbf{z})\mathbf{R}^{-1}\mathbf{f}_{\mathbf{c}}(\mathbf{z}) \tag{52}$$

The following three theorems, proved in appendix C, show that the output variance functions of the x-, y-, and z-axis sensors are independent of the corresponding parameter vector $\mathbf{c}$ for any calibration experimental design.

Theorem I: Sensor output variance function $\sigma_v^2(\mathbf{z})$ is independent of calibration parameters b and S

Theorem II: Sensor output variance function $\sigma_v^2(\mathbf{z})$ is independent of calibration parameter Ω

Theorem III: Sensor output variance function $\sigma_v^2(\mathbf{z})$ is independent of calibration parameter A

Note in equation (127), proof of Theorem 1 in appendix C, that variance function $\sigma_v^2(\mathbf{z})$ is well-defined whenever matrix $\mathbf{P}$ (eq. (129)) is nonsingular. Thus $\sigma_v^2(\mathbf{z})$ exists for $w \equiv \sin\,\Omega = 0$ where matrix $\mathbf{R}$ is singular. Matrix $\mathbf{R}$ is evaluated analytically in appendix D.

From Theorems I to III, the conclusion is drawn that variance function $\sigma_v^2(\mathbf{z})$ of predicted output $\widehat{v}$ is independent of calibration parameters b, S, Ω, and A for the x-, y-, and z-axis sensors. Hence, sensor output uncertainty depends only upon experimental design values of α and R and measurement variance σ_E^2.

3.4. Experimental Design Figure of Merit

Box (ref. 7) defines a figure of merit V for any experimental design as the mean value of the output variance function over test volume $\Im$, normalized by the number of calibration points and the measurement variance. (See also ref. 5.) The value of V for experimental design D is obtained with the help of equation (147) as

$$V = \frac{K\displaystyle\int_{\Im} \sigma_v^2(\mathbf{z})\, d\mathbf{x}}{\sigma_E^2 \displaystyle\int_{\Im} d\mathbf{x}} = \frac{MN \displaystyle\int_{\alpha_{\min}}^{\alpha_{\max}} \int_{R_{\min}}^{R_{\max}} \boldsymbol{\phi}_c \mathbf{P}^{-1} \boldsymbol{\phi}_c^{\mathrm{T}}\, dR\, d\alpha}{\displaystyle\int_{\alpha_{\min}}^{\alpha_{\max}} \int_{R_{\min}}^{R_{\max}} dR\, d\alpha} \tag{53}$$

Design figures of merit are equal for x-, y-, and z-axis sensor output uncertainties. The numerator of equation (53), which contains integrals of cross products of the elements of gradient vector $\boldsymbol{\phi}_c$, is evaluated in appendix E as

$$V_N \equiv \int_{\Im} q_R(\mathbf{z})\, d\mathbf{x} = \int_{\alpha_{\min}}^{\alpha_{\max}} \int_{R_{\min}}^{R_{\max}} \boldsymbol{\phi}_c \mathbf{P}^{-1} \boldsymbol{\phi}_c^{\mathrm{T}}\, dR\, d\alpha = \sum_{i=1}^{4} \sum_{j=1}^{4} \mathbf{P}_{ij}^{-1} \mathbf{I}_{\phi ij} \tag{54}$$

where $\mathbf{P}_{ij}^{-1}$ is the ijth element of the inverse of matrix $\mathbf{P}$ defined in equation (129) and terms $\mathbf{I}_{\phi ij}$ are defined in appendix E. The figure-of-merit expression

$$V = \frac{MNV_N}{I_{bb}} \tag{55}$$

is obtained in appendix E. Definite integral I_{bb} is defined for the x-axis sensor in equation (214). Values of V for selected experimental designs are given later.

4. Evaluation of Variance Function for Special Experimental Designs

4.1. Experimental Designs

Three special calibration experimental designs, denoted by D_0, D_1, and T, are considered as follows:

Minimal design D_0: A special case of design D

1. Pitch angle set $ß_\alpha$ contains N points in the closed interval $[\alpha_{\min},\ \alpha_{\max}]$
2. Roll angle set $ß_R$ contains M unique principal angle valued points, uniformly distributed over closed interval $[-\pi,\ \pi - \Delta R]$, where $\Delta R = 2\pi/M$

Minimal design D_1: A special case of design D_0

1. Pitch angle set $ß_\alpha$ contains N unique principal angle valued points uniformly distributed and centered about zero over the closed interval $[-\alpha_{\max},\ \alpha_{\max}]$, although $\alpha_{\max}$ may equal π, where $\Delta\alpha = 2\alpha_{\max}/(N-1)$.

2. Roll angle set $ß_R$ equals that of design D_0

Parts 1 of designs D_0 and D_1 apply for calibration without roll. Designs D_0 and D_1 may also be constructed of multiple copies of a minimal D_0 or D_1 design, respectively. For example, a typical pitch calibration proceeds from $\alpha_{\min}$ to $\alpha_{\min}$, followed the same points in reverse order from $\alpha_{\max}$ to $\alpha_{\min}$. The properties of design D variance functions derived in sections 4.2 and 4.3 are preserved under reordering, randomization, and replication.

Design T

1. Six-point "tumble" calibration with roll

   The single-axis or multiple-axis sensor package with roll is calibrated only at cardinal angles; experimental design matrix $\mathbf{Z}$ is as follows:

$$\mathbf{Z} = \begin{bmatrix} -\frac{\pi}{2} & 0 & \frac{\pi}{2} & \pi & 0 & 0 \\ 0 & 0 & 0 & 0 & -\frac{\pi}{2} & \frac{\pi}{2} \end{bmatrix} \tag{56}$$

2. Four-point tumble calibration without roll

   The single-axis sensor package without roll is calibrated only at cardinal angles; experimental design matrix $\mathbf{Z}$ is as follows:

$$\mathbf{Z} = \begin{bmatrix} -\frac{\pi}{2} & 0 & \frac{\pi}{2} & \pi \end{bmatrix} \tag{57}$$

Moment matrix $\mathbf{R}$ and its related matrix $\mathbf{P}$ are evaluated analytically in appendix D in equations (206) to (213) for computation of variance function $\sigma_v^2(\mathbf{z})$. Because $\sigma_v^2(\mathbf{z})$ is independent of parameters b, S, Ω, and A, the following parameter values are chosen for simplification:

$$\left. \begin{aligned} & b = \Omega = A = 0 \\ & S = 1 \end{aligned} \right\} \tag{58}$$

The values listed in equations (17) are selected for computation of variance function $\sigma_v^2(\mathbf{z})$ without roll.

4.2. Variance Function for Design D_0

Sensor output variance $\sigma_{vx}^2(\mathbf{z}_k)$ for design D_0 depends only on the number of pitch calibration points N, the number of roll calibration points M, the pitch angle calibration range $\alpha_{\max}$, and the pitch angle α_k as shown by the following. The output variance for x-, y-, and z-axis sensors is given by equation (147) as

$$\frac{\sigma_v^2(\mathbf{z}_k)}{\sigma_E^2} \equiv \boldsymbol{\phi}_c^{\mathrm{T}}(\mathbf{z}_k)\mathbf{P}^{-1}\boldsymbol{\phi}_c(\mathbf{z}_k) \tag{59}$$

where $\boldsymbol{\phi}_c$ is defined in equation (128) and matrix $\mathbf{P}$ is evaluated in appendix D (eq. (129)). The following theorem, proved in appendix C, shows, for calibration with roll, that the pitch angle sensor output uncertainty is independent of roll angle R for design D_0.

Theorem IV: Let roll angle calibration set ß_R, defined in equation (10), contain $K = NM$ points uniformly spaced over the interval $[-\pi,\ \pi - \Delta R]$, where M and N are integers, $\Delta R = 2\pi/M$, and the principal value of each angle contained in ß_R occurs with the same frequency; then the pitch sensor output variance is independent of roll angle R.

For calibration without roll, equations (21), (22), and (25), evaluated by using the parameter values of equations (17), become

$$\left.\begin{aligned} f_{xb} &= 1 \\ f_{xS} &= \sin\ \alpha \\ \phi_{x\Omega} &= -\cos\ \alpha \end{aligned}\right\} \tag{60}$$

With the help of equations (176) to (203),

$$\mathrm{P}_x = \begin{bmatrix} r_{\alpha_{bb}} & r_{\alpha_{bS}} & \rho_{\alpha_{b\Omega}} \\ r_{\alpha_{bS}} & r_{\alpha_{SS}} & \rho_{\alpha_{S\Omega}} \\ \rho_{\alpha_{b\Omega}} & \rho_{\alpha_{S\Omega}} & \rho_{\alpha_{\Omega\Omega}} \end{bmatrix} \tag{61}$$

where

$$\left.\begin{aligned} r_{\alpha_{bb}} &= N \\ r_{\alpha_{bS}} &= S_A \\ \rho_{\alpha_{b\Omega}} &= -C_\alpha \\ r_{\alpha_{SS}} &= \frac{1}{2}(N - C_{2\alpha}) \\ \rho_{\alpha_{S\Omega}} &= -\frac{1}{2}S_{2\alpha} \\ \rho_{\alpha_{\Omega\Omega}} &= \frac{1}{2}(N + C_{2\alpha}) \end{aligned}\right\} \tag{62}$$

and where S_A, C_α, $S_{2\alpha}$, and $C_{2\alpha}$ are defined in equations (165) and (166).

4.3. Variance Function for Design D_1

For design D_1, matrix $\mathbf{P}$ for the x-, y-, and z-axis sensors simplifies to the following diagonal form for calibration with roll:

$$\mathbf{P} = \begin{bmatrix} r_{bb} & 0 & 0 & 0 \\ 0 & r_{SS} & 0 & 0 \\ 0 & 0 & \rho_{\Omega\Omega} & 0 \\ 0 & 0 & 0 & \rho_{AA} \end{bmatrix} \tag{63}$$

Inverse matrix $\mathbf{P}^{-1}$ is given by

$$\mathbf{P}^{-1} = \begin{bmatrix} \frac{1}{r_{bb}} & 0 & 0 & 0 \\ 0 & \frac{1}{r_{SS}} & 0 & 0 \\ 0 & 0 & \frac{1}{\rho_{\Omega\Omega}} & 0 \\ 0 & 0 & 0 & \frac{1}{\rho_{AA}} \end{bmatrix} \tag{64}$$

Combine equations (59) and (64) to obtain x-, y-, and z-axis sensor output variances as

$$\frac{\sigma_v^2(\mathbf{z})}{\sigma_E^2} = \frac{1}{r_{bb}} + \frac{f_S^2}{r_{SS}} + \frac{\phi_\Omega^2}{\rho_{\Omega\Omega}} + \frac{\phi_A^2}{\rho_{AA}} \tag{65}$$

Equation (65) is evaluated for design D_1 with the help of equations (148) and equations (176) to (203); after simplification the normalized x-axis sensor variance is obtained as

$$\frac{\sigma_{vx}^2(\mathbf{z})}{\sigma_x^2} = \frac{1}{MN} + \frac{2\left[N + C_{2\alpha} + (N - 3C_{2\alpha})\cos^2\alpha\right]}{M(N^2 - C_{2\alpha}^2)} \tag{66}$$

where $C_{2\alpha}$ is defined in appendix D (eqs. (172)). It is shown in appendix D that $\sigma_{vy}(\mathbf{z}) = \sigma_{vz}(\mathbf{z}) = \sigma_{vx}(\mathbf{z})$. Equation (66) shows that the variation of $\sigma_{vx}^2(\mathbf{z}_k)$ with α_k is concave upward about zero pitch for $C_{2\alpha} > N/3$ and concave downward about zero pitch for $C_{2\alpha} < N/3$. Normally, maximum attitude measurement accuracy is desired near zero pitch.

For calibration without roll via design D_1, variables $S_A = 0$ and $S_{2\alpha} = 0$; equations (62) change accordingly. The variance function is shown to be given by

$$\frac{\sigma_{vx}^2(\mathbf{z})}{\sigma_x^2} = \frac{(1/2)(N + C_{2\alpha}) - 2C_\alpha \cos\alpha + N\cos^2\alpha}{(1/2)N(N + C_{2\alpha}) - C_\alpha^2} + \frac{2\sin^2\alpha}{N - C_{2\alpha}} \tag{67}$$

4.4. Variance Function for Design T

For single-axis or multiple-axis six-point tumble calibration with roll, matrix $\mathbf{P}$ (eq. (129)) simplifies to the following diagonal form for x-, y-, and z-axis sensors:

$$\mathbf{P} = \begin{bmatrix} 6 & 0 & 0 & 0 \\ 0 & 2 & 0 & 0 \\ 0 & 0 & 2 & 0 \\ 0 & 0 & 0 & 2 \end{bmatrix} \tag{68}$$

From equations (154) and (65), the variance function is

$$\frac{\sigma_{vx}^2(\mathbf{z})}{\sigma_x^2} = \frac{2}{3} \tag{69}$$

After multiplying by the number of calibration points, the normalized standard deviation is found to be equal to 2.

For single-axis four-point tumble calibration without roll, matrix $\mathbf{P}$ becomes

$$\mathbf{P} = \begin{bmatrix} 4 & 0 & 0 \\ 0 & 2 & 0 \\ 0 & 0 & 2 \end{bmatrix} \tag{70}$$

The variance function is

$$\frac{\sigma_{v\alpha}^2(\mathbf{z})}{\sigma_x^2} = \frac{3}{4} \tag{71}$$

After multiplying the variance function by the number of calibration points, the normalized standard deviation is found to be equal to $3^{1/2}$.

5. Confidence and Prediction Intervals

5.1. Multiple-Axis Sensor Uncertainty

For arbitrary input $\mathbf{z}_0$, the calibration confidence interval of the corresponding predicted sensor output $\widehat{v}_0$, for sensor x, y, or z, is defined by the following expression:

$$\delta\widehat{v}_0 = |\widehat{v}_0 - v_0| \leq t_{K-4}(\alpha) S_E \left[\mathbf{f}_\mathbf{c}^\mathrm{T}(\mathbf{z}_0)\mathbf{R}^{-1}\mathbf{f}_\mathbf{c}(\mathbf{z}_0)\right]^{1/2} \tag{72}$$

where S_E is the standard error of the regression and $t_k(a)$ is the a-percentile value of the two-tailed t-distribution with k degrees of freedom, denoted the precision index (ref. 8); x, y, and z subscripts are elided. The corresponding prediction interval (ref. 5) of a single new measured output is defined as

$$\delta\widehat{v}_{P_0} \leq t_{K-4}(\alpha) S_E \left[\mathbf{f}_\mathbf{c}^\mathrm{T}(\mathbf{z}_0)\mathbf{R}^{-1}\mathbf{f}_\mathbf{c}(\mathbf{z}_0) + \frac{\sigma_0^2}{\sigma_E^2}\right]^{1/2} \tag{73}$$

where σ_0^2 is the variance of the new measurement and σ_E^2 is the calibration measurement variance.

5.2. Single-Axis Pitch Sensor Uncertainty With Roll

New measurement data reduction for the single-axis pitch sensor with roll requires independent measurement of roll angle R whose variance, denoted by σ_R^2, is independent of the calibration uncertainties and the pitch sensor output measurement uncertainty. The calibration confidence interval is given by equation (72). The prediction interval is given by

$$\delta\widehat{v}_{P_0} \leq t_{K-4}(\alpha) S_E \left[\mathbf{f}_\mathbf{c}^\mathrm{T}(\mathbf{z}_0)\mathbf{R}^{-1}\mathbf{f}_\mathbf{c}(\mathbf{z}_0) + \frac{\sigma_0^2 + f_{xR}^2\sigma_R^2}{\sigma_y^2}\right]^{1/2} \tag{74}$$

where

$$f_{xR} \equiv \frac{\partial f_x}{\partial R} = S_x \sin\Omega_x \cos\alpha_0 \cos(R_0 + A_x) \tag{75}$$

and where α_0 and R_0 are the new pitch and roll angles, respectively.

5.3. Parametric Studies of Experimental Designs

Figures 1 to 5 illustrate the variation of sensor output uncertainty with pitch at selected parameter values for various experimental designs. Recall that uncertainties for x-, y-, and z-axis sensor output are identical. Uncertainties are shown as standard deviation functions normalized by sensor measurement uncertainty σ_E and $(MN)^{1/2}$, where M and N are the number of roll and pitch calibration points, respectively. Note that calibrations without roll are normalized by $N^{1/2}$. Confidence intervals are readily obtained from normalized standard deviation curves. For comparison, normalized tumble test uncertainty curves are shown with those of the higher order experimental design in each of figures 1 and 2. Note that the low cardinality of tumble calibrations causes high calibration uncertainties compared with higher order calibration. Although the normalized tumble calibration uncertainties are comparable with those of the higher order designs, the unnormalized tumble calibration uncertainties will increase by the factor $(65/4)^{1/2}$ in figure 1 and by $(65/6)^{1/2}$ in figure 2 compared with the uncertainties of the higher order designs.

For comparison, table 1 presents the normalized mean standard deviations $V^{1/2}$, where V is the figure of merit defined in equation (53), for calibration designs with roll from figures 2 to 5, evaluated over the calibration range. In addition, the normalized mean standard deviations evaluated over reduced usage ranges, denoted by $V_R^{1/2}$, are shown.

5.3.1 Single-axis pitch sensor without roll. Figure 1 illustrates the variation of normalized sensor output standard deviation with pitch angle for design D_1 for calibrations over the ranges from $-30°$ to $30°$, $-45°$ to $45°$, $-90°$ to $90°$, and $-180°$ to $180°$, respectively, for $N = 65$. The constant normalized standard deviation for the four-point tumble calibration is shown in each figure for comparison. Note in figures 1(a), (b), and (c) that sensor uncertainty is low within the center 50 percent of the calibration range and increases rapidly outside the center range. Calibration from $-180°$ to $180°$ produces nearly constant uncertainty approximately equal to that for the four-point tumble calibration and at a level 17 percent greater than that in the center ranges of the calibration designs from $-90°$ to $90°$ and less.

5.3.2. Single- or multiple-axis attitude sensor with roll. Some effects of spacing test points uniformly and nonuniformly on the mean normalized standard deviation using designs D_0 and D_1 are illustrated in figures 2 through 5 and summarized in table 1. Figure 2 illustrates the variation of sensor output standard deviation σ_{vx} with pitch angle for design D_1, for maximum pitch calibration angles of $30°$, $45°$, $90°$, and $180°$, respectively, and for values of N from the set $\{5, 9, 17, 33, 65\}$. For comparison, the constant normalized standard deviation for the six-point tumble calibration design T is indicated in each figure. As shown in Theorem IV in section 4.2, σ_{vx} is independent of roll with design D_0 and, hence, with design D_1. From equation (66), the normalized curves are independent of M. Note in figures 2(a) and (b) that the uncertainty curves concave upward about $0°$ for calibration designs with $\alpha_{\max} \leq 45°$.

Figures 2(c) and (d) show that calibration for $\alpha = -90°$ to $90°$ and $-180°$ to $180°$ produce uncertainty curves concaved downward about $0°$ with significantly greater uncertainty at $0°$ than at $\pm 90°$. Indeed, equations (172) of appendix D shows that $C_{2\alpha} < 0$ for $\alpha_{\max} = 90°$ and $C_{2\alpha} = 1$ for $\alpha_{\max} = 180°$. In these cases from equation (66) the pitch sensor uncertainty curve should concave downward for all N over from $-90°$ to $90°$.

The results illustrated in figure 2 are summarized in columns 2 to 5 of table 1. Row 3 indicates the pitch angle calibration range, row 4 contains the mean normalized standard deviation over this range, row 5 indicates the reduced "usage range" over which measurements are to be made, and the final row contains the mean normalized standard deviation over the reduced "usage range." Note that calibration over $-45°$ to $45°$ slightly reduces the mean normalized standard deviation $V^{1/2}$ within the usage range over $-30°$ to $30°$ compared with calibration over $-30°$ to $30°$. However, calibration over $-90°$ to $90°$ worsens $V^{1/2}$ by 12 percent within the usage range from $-30°$ to $30°$ compared with calibration over $-30°$ to $30°$. For calibration over $-45°$ to $45°$ or less, figures 2(a) and (b) demonstrate that the normalized curve shapes do not change significantly as N varies from 5 to 65. The results of figure 2 suggest that the AOA sensor should be calibrated over $-45°$ to $45°$ degrees for use in the normal $-30°$ to $30°$ range.

The effects of unequally spaced pitch angle points within design D_0 are illustrated in figures 3 and 4 and in columns 6 to 8 of table 1. Each calibration is conducted over a pitch range from $-30°$ to $30°$ with $5.63°$ roll increments, $M = 64$, and $N = 33$. In top plot of figure 3 pitch angle calibration points, shown as circles, are closely spaced at $1°$ increments within a range from $-10°$ to $10°$ and are more widely spaced at $4°$ increments for $|\alpha| > 14°$. In bottom plot of figure 3, pitch angle calibration points are closely spaced at $1°$ increments for $|\alpha| > 20°$ and are more widely spaced with $4°$ increments for $|\alpha| < 16°$. Note that the normalized standard deviation curve of bottom plot of figure 3 is significantly flattened, although the minimum value is greater when compared with top plot of figure 3. Table 1 indicates that the design of bottom plot of figure 3 reduces $V^{1/2}$ by 10 percent compared with that of figure 3 over a usage range from $-30°$ to $30°$; however, the latter design increases $V^{1/2}$ by only 1 percent over a usage range from $-10°$ to $10°$. The design of bottom plot of figure 3 reduces $V^{1/2}$ by 9 percent over a usage range of $-10°$ to $10°$ compared with design D_1 of figure 2(a).

Figure 4 illustrates a design wherein all calibration points are located at $\pm 30°$ boundaries except for a single center point at $0°$; there is less variation of normalized standard deviation over the calibration interval compared with figure 3. As discussed in reference 5, designs containing a preponderance of boundary points reduce overall precision uncertainty at the expense of increased bias uncertainty due to modeling error.

The results of figures 2 to 4 show that only small uncertainty reductions result from the use of nonuniformly spaced pitch calibration sets compared with design D_1. If minimum uncertainty is required over $-10°$ to $10°$ the design of top plot of figure 3 provides a modest 9-percent average uncertainty reduction compared with design D_1.

Figure 5 illustrates pitch sensor uncertainty for a modified D_1 design with $N = 33$ and $M = 65$, with pitch angle uniformly spaced over $-30°$ to $30°$, and roll angle uniformly spaced over $-180°$ to $180°$ with a repeated roll point at $180°$. A family of normalized standard deviation curves is dependent on roll angle results, although deviation is small from the corresponding single uncertainty curve of figure 1 with design D_1. Curves are shown for 13 uniformly spaced roll values ranging over $-180°$ to $180°$. This modified design, convenient for experimental use, has insignificant disadvantage compared with design D_1. The mean normalized standard deviation for this case is listed in the last column of table 1.

6. Computation of Inferred Inputs and Confidence Intervals

6.1. Single-Axis Sensor Without Roll

Given observed pitch sensor output v_α, the corresponding inferred pitch angle $\widehat{\alpha}$ is estimated by inverting equation (1) so that

$$\widehat{\alpha} = \arcsin\left(\frac{v_\alpha - b_\alpha}{S_\alpha}\right) + \phi_\alpha \tag{76}$$

The uncertainty of $\widehat{\alpha}$ is given by

$$\delta\widehat{\alpha} = \frac{\delta v_\alpha}{S_\alpha \cos(\alpha - \phi_\alpha)} \tag{77}$$

Then the standard deviation of $\widehat{\alpha}$ is given by

$$\sigma_{\widehat{\alpha}}(\mathbf{z}) = \frac{\sigma_{v\alpha}(\mathbf{z})}{S_\alpha|\cos(\alpha - \phi_\alpha)|} \tag{78}$$

Figure 6 illustrates the normalized standard deviation of $\widehat{\alpha}$ versus pitch angle and shows that inferred pitch angle uncertainty is unbounded near the extremes, $\alpha = \pm 90°$.

6.2. Measurements With Roll

Given observed model attitude sensor outputs v_x, v_y, and v_z, the corresponding inferred applied pitch and roll angles, $\widehat{\alpha}$ and $\widehat{R}$, are estimated by simultaneously inverting nonlinear equations (2), (4), and (5) as appropriate by means of Newton-Raphson iteration or other iterative procedure.

6.3. Single-Axis Sensor Package With Independent Roll Measurement

For the single-axis pitch sensor with independently measured roll angle, inferred pitch angle $\widehat{\alpha}$ is computed from observed sensor output v_x with equation (3) as follows:

$$\widehat{\alpha} = \arcsin\left[\frac{(v_x - \widehat{b}_x)/\widehat{S}_x}{\sqrt{\cos^2\widehat{\Omega}_x + \sin^2(R + \widehat{A}_x)\sin^2\widehat{\Omega}_x}}\right] + \arctan\left[\tan\widehat{\Omega}_x \sin(R + \widehat{A}_x)\right] \tag{79}$$

Thus from equation (2) and reference 5, the uncertainty of inferred pitch angle $\widehat{\alpha}$ at known roll angle R is given by

$$\delta\widehat{\alpha} = \frac{\delta v_x - S_x \sin\Omega_x \cos\alpha \cos(R + A_x)\,\delta R}{S_x[\cos\Omega_x \cos\alpha + \sin\Omega_x \sin\alpha \sin(R + A_x)]} \tag{80}$$

where δR is the uncertainty of R. The standard deviation of $\widehat{\alpha}$ is found to be

$$\sigma_{\widehat{\alpha}}(\mathbf{z}) = \frac{\{\sigma_{vx}^2(\mathbf{z})/S_x^2 + [\sin\Omega_x \cos\alpha \cos(R + A_x)]^2\sigma_R^2\}^{1/2}}{|\cos\Omega_x \cos\alpha + \sin\Omega_x \sin\alpha \sin(R + A_x)|} \tag{81}$$

where σ_R^2 is the variance of independently measured roll angle R. If misalignment parameter Ω is zero, the standard deviation of $\widehat{\alpha}$ simplifies to the following equation:

$$\sigma_{\widehat{\alpha}}(\mathbf{z}) = \frac{\sigma_{vx}(\mathbf{z})}{S_x \cos\alpha} \tag{82}$$

The inferred pitch angle uncertainty is minimum at $\alpha = 0°$ and unbounded near $\alpha = \pm 90°$. Normalized standard deviation curves, $\sigma_{\widehat{\alpha}}/\sigma_{vx}$, for $\Omega_x = 1°$ and $A_x = 90°$, appear in figure 7 as functions of α over $-90°$ to $90°$ and in figure 8 as functions of R over $0°$ to $180°$. Figure 7 contains two curves with measured roll angle uncertainties of 1 times and 10 times pitch sensor uncertainty, respectively. For these cases, inferred pitch angle uncertainty does not vary significantly with roll angle. Figure 8 contains three curves with measured roll angle uncertainties of 1 times, 10 times, and 100 times pitch sensor uncertainty, respectively. Inferred pitch angle uncertainty varies significantly with roll only for the latter case. Note that the inferred pitch angle uncertainty is approximately 15 percent greater at $\alpha = 30°$ than at $\alpha = 0°$.

6.4. Two-Axis Sensor Package

The two-axis model attitude sensor package containing accelerometers aligned with the x- and y-axes is suitable for simultaneous pitch and roll measurement within limits. As is shown, measurement singularities exist at $\pm 90°$ pitch and near $\pm 90°$ roll. Let $\widehat{\mathbf{z}}$ denote the 1×2 vector of inferred inputs corresponding to 1×2 observed output vector $\mathbf{v}$, obtained by simultaneous solution of equations (2) and (4), where

$$\left.\begin{aligned} \widehat{\mathbf{z}} &= [\widehat{\alpha} \quad \widehat{R}] \\ \mathbf{v} &= [v_x \quad v_y] \end{aligned}\right\} \tag{83}$$

In addition, let $\mathbf{f}(\mathbf{C},\mathbf{z})$ denote the 1×2 vector of functions defined by transducer equations (14) and (15) as follows:

$$\mathbf{f}(\mathbf{C},\mathbf{z}) = [f_x(\mathbf{c}_x,\mathbf{z})\; f_y(\mathbf{c}_y,\mathbf{z})] \tag{84}$$

where 4×2 parameter matrix $\mathbf{C}$ is defined as

$$\mathbf{C} = \left[\mathbf{c}_x \,\vdots\, \mathbf{c}_y\right] \tag{85}$$

The 2×2 Jacobian matrix of equation (84) with respect to input vector $\mathbf{z}$ is given by

$$\mathbf{F}_z \equiv \left[\frac{\partial \mathbf{f}(\mathbf{C},\widehat{\mathbf{z}})}{\partial \mathbf{z}}\right] = \begin{bmatrix} f_{x\alpha} & f_{y\alpha} \\ f_{xR} & f_{yR} \end{bmatrix} \tag{86}$$

where

$$\left.\begin{aligned} f_{x_\alpha} &= S_x[\cos\,\Omega_x\,\cos\,\alpha_k + \sin\,\Omega_x\,\sin\,\alpha_k\,\sin\,(R_k + A_x)] \\ f_{x_R} &= -S_x\,\sin\,\Omega_x\,\cos\,\alpha_k\,\cos(R_k + A_x) \end{aligned}\right\} \tag{87}$$

and

$$\left.\begin{aligned} f_{y_\alpha} &= S_y[\cos\,\Omega_y\,\sin\,\alpha_k\,\sin\,R_k + \sin\,\Omega_y\,(\sin\,A_y\,\cos\,\alpha_k + \cos\,A_y\,\sin\,\alpha_k\,\cos\,R_k)] \\ f_{y_R} &= -S_y\,\cos\,\alpha_k(\cos\,\Omega_y\,\cos\,R_k - \sin\,\Omega_y\,\cos\,A_y\,\sin\,R_k) \end{aligned}\right\} \tag{88}$$

A solution to $\mathbf{f}(\mathbf{C},\mathbf{z}) = 0$ exists only if Jacobian matrix $\mathbf{F}_z$ is nonsingular at $\mathbf{z}$ (ref. 5). The singularity loci of matrix $\mathbf{F}_z$ are obtained by setting the determinant of equation (86) to zero. Note that $\mathbf{F}_z$ is singular at $\alpha = \pm 90°$. Figures 9(a) and (b) show the singularity loci as functions of α and R where coning angles $\Omega_x = \Omega_y$ equal 0.1° and 1°, respectively, for $A_x = 0°$ and $A_y = 90°$; these loci nearly coincide with $\alpha = \pm 90°$ and $R = \pm 90°$ for $|\Omega| \leq 1°$. Figures 9(c) and (d) illustrate the previous case repeated for $A_x = 90°$ and $A_y = 90°$. Note the significant departure from $R = \pm 90°$ as α approaches $\pm 90°$ for $|\Omega| \geq 0.1°$. Parametric studies show that the singularity loci are dependent upon A_x and nearly independent of A_y for $|\Omega| \leq 1°$. Figure 9 illustrates the extreme cases.

As shown in reference 5, the uncertainty $\delta\widehat{\mathbf{z}}$ of inferred input vector $\widehat{\mathbf{z}}$, corresponding to observed output vector $\mathbf{v}$, is obtained from the following equation:

$$\delta\widehat{\mathbf{z}} = \delta\widehat{\mathbf{v}}\,\mathbf{F}_z^{-1} \tag{89}$$

where $\boldsymbol{\delta}\widehat{\mathbf{z}} = [\delta\widehat{\alpha} \quad \delta\widehat{R}]$, and $\boldsymbol{\delta}\widehat{\mathbf{v}} = [\delta v_x \quad \delta v_y]$ is the uncertainty of predicted output vector $\widehat{\mathbf{v}}$. Thus the 2×2 covariance matrix of $\widehat{\mathbf{z}}$ is given by

$$\Sigma_{\widehat{\mathbf{z}}} = \mathbf{F}_z^{-\mathrm{T}}\Sigma_{\widehat{\mathbf{v}}}\mathbf{F}_z^{-1} \tag{90}$$

Matrix $\Sigma_{\widehat{\mathbf{v}}}$ is the 2×2 covariance matrix of $\widehat{\mathbf{v}}$, whose diagonal elements $\sigma^2_{\widehat{\alpha}}$ and $\sigma^2_{\widehat{R}}$ are estimated by means of equation (52). Confidence and prediction intervals for $\widehat{\mathbf{z}}$ are obtained from equation (90).

The normalized standard deviations of $\widehat{\alpha}$ and $\widehat{R}$, shown as $\sigma_{\widehat{\alpha}}/\sigma_{vx}$ and $\sigma_{\widehat{R}}/\sigma_{vy}$, are presented for comparison in figure 10 as functions of R for selected x- and y-axis sensor output uncertainties as R varies from $-180°$ to 180° at pitch angles of 0°, 20°, 40°, 60°, and 80° and at coning angles of 0.1° and 1°. Sensor x and y outputs are assumed to be uncorrelated; hence, $\Sigma_{\widehat{\mathbf{v}}}$ is diagonal. As seen in the figures, inferred roll angle is singular near $R = \pm 90°$. Consequently, x-axis sensor misalignment correction accuracy is limited in this region, causing inferred pitch angle uncertainty to increase sharply near $R = \pm 90°$, although the maximum pitch error is bounded by coning angles Ω. Roll certainties reach minima near $R = 0°$ and 180°.

In figure 10(a), x-axis sensor output uncertainty equals y-axis sensor output uncertainty, that is, $\sigma_x = \sigma_y$; however, $\sigma_y = 10\sigma_x$ in figures 10(b), (c), and (d). The x-axis sensor azimuth $A_x = 90°$ in figures 10(a), (b), and (c); $A_x = 0°$ in figure 10(d). Comparison of figures 10(a), (b), and (c) shows that, for $\Omega \leq 1°$ and $|\alpha| < 60°$ or $120° < |\alpha| < 240°$, the ten times less accurate y-axis sensor does not significantly worsen inferred pitch angle uncertainty in the ranges $|R| < 85°$ and $95° < |R| < 265°$. However comparison of figures 10(a), (b), and (c) shows that the inferred pitch angle uncertainty singularity near 90° widens as coning angle increases from 0.1° to 1° for $\sigma_y = 10\sigma_x$. Figures 10(b) and (d) show that pitch angle uncertainty is least affected by roll for $A_x = 0°$.

The x-y package is suitable for pitch-roll measurement in the range $[|\alpha| < 80^\circ$ **or** $100^\circ < |\alpha| < 260^\circ]$ **and** $[|R| < 60^\circ$ **or** $120^\circ < |R| < 240^\circ]$. Note that **and** and **or** are logical operators in the above statement.

6.5. Two-Axis Sensor Package

The two-axis model attitude sensor package containing accelerometers aligned with the x- and z-axes is not suitable for simultaneous pitch and roll measurement at typical wind tunnel model test attitudes, since singularities exist near roll of 0° and $\pm 180^\circ$, as well as at pitch of $\pm 90^\circ$, as shown later. Let $\widehat{\mathbf{z}}$ denote the 1×2 vector of inferred inputs corresponding to 1×2 observed output vector $\mathbf{v}$, obtained by simultaneous solution of equations (2) and (5), where

$$\left.\begin{aligned} \widehat{\mathbf{z}} &= [\widehat{\alpha} \quad \widehat{R}] \\ \mathbf{v} &= [v_x \quad v_z] \end{aligned}\right\} \tag{91}$$

In addition, let $\mathbf{f}(\mathbf{C},\mathbf{z})$ denote the 1×2 vector of functions defined by transducer equations (14) and (16) as follows:

$$\mathbf{f}(\mathbf{C},\mathbf{z}) = [f_x(\mathbf{c}_x,\mathbf{z}) \ f_z(\mathbf{c}_z,\mathbf{z})] \tag{92}$$

where 4×2 parameter matrix $\mathbf{C}$ is defined as

$$\mathbf{C} = \left[\mathbf{c}_x \,\middle|\, \mathbf{c}_z\right] \tag{93}$$

The 2×2 Jacobian matrix of equation (92) with respect to input vector $\mathbf{z}$ is given by

$$\mathbf{F}_\mathbf{z} \equiv \left[\frac{\partial \mathbf{f}(\mathbf{C},\widehat{\mathbf{z}})}{\partial \mathbf{z}}\right] = \begin{bmatrix} f_{x_\alpha} & f_{z_\alpha} \\ f_{x_R} & f_{z_R} \end{bmatrix} \tag{94}$$

where

$$\left.\begin{aligned} f_{z_\alpha} &= S_z[\cos\,\Omega_z \,\sin\,\alpha_k\,\cos\,R_k + \sin\,\Omega_z\,(\cos\,A_z\,\cos\,\alpha_k + \sin\,A_z\,\sin\,\alpha_k\,\sin\,R_k)] \\ f_{z_R} &= S_z\,\cos\,\alpha_k\,(\cos\,\Omega_z\,\sin\,R_k - \sin\,\Omega_z\,\sin\,A_z\,\cos\,R_k) \end{aligned}\right\} \tag{95}$$

Figures 11(a) and (b) show the singularity loci of matrix $\mathbf{F}_\mathbf{z}$ as functions of α and R for $A_x = 90^\circ$ and $A_z = 0^\circ$, where $\Omega_x = \Omega_z$ ranges from 0.1° to 1°; the singularity loci nearly coincide with the lines $\alpha = \pm 90^\circ$, and the lines $R = 0^\circ$ and $R = 180^\circ$ for $|\Omega| \leq 1^\circ$. Figures 11(c) and (d) illustrate the previous case repeated for $A_x = 0^\circ$ and $A_z = 0^\circ$; note the significant departure from $R = \pm 90^\circ$ as α approaches $\pm 90^\circ$, for $|\Omega| \geq 0.1^\circ$. Parametric studies show that the singularity loci are dependent upon A_x and nearly independent of A_z for $|\Omega| \leq 1^\circ$.

The x-z package is useful for pitch measurement from $\alpha = -180^\circ$ to 180° with independently measured roll R except for the points $\{\alpha,R\} = \{\pm 90^\circ, \pm\, 90^\circ\}$, as is now shown. Given observed package output $\mathbf{v}$ at known roll R, α is estimated by least-squares solution of overdetermined system (eq. (92)), where the uncertainty of the estimate is

$$\delta\widehat{\alpha} = \delta\mathbf{v}\;\mathbf{f}_\alpha^\mathrm{T}\left(\mathbf{f}_\alpha\mathbf{f}_\alpha^\mathrm{T}\right)^{-1} \tag{96}$$

and where

$$\mathbf{f}_\alpha \equiv \left[\frac{\partial \mathbf{f}(\mathbf{C},\widehat{\mathbf{z}})}{\partial \alpha}\right] = [f_{x_\alpha} \ f_{z_\alpha}] \tag{97}$$

It is readily shown for $\Omega_z = \Omega_z = 0^\circ$ that

$$\mathbf{f}_\alpha\mathbf{f}_\alpha^\mathrm{T} = (1 - \cos^2 R)\cos^2\alpha + \cos^2 R \tag{98}$$

for which case the estimated pitch angle uncertainty is unbounded only at the points $\{\alpha, R\} = \{\pm 90°, \pm 90°\}$.

It is seen that the x-z package is satisfactory for pitch measurement from $\alpha = -180°$ to $180°$, where roll R is measured independently, except for the points $\{\alpha, R\} = \{\pm 90°, \pm 90°\}$. Although it is capable of simultaneous pitch-roll measurement, the usable range, limited to $[|\alpha| < 80°$ **or** $100° < |\alpha| < 260°]$ **and** $[30° < |R| < 150°]$, excludes typical wind tunnel model attitudes.

6.6. Three-Axis Sensor Package

The three-axis sensor package, with accelerometers aligned with the x-, y-, and z-axes, is suitable for simultaneous pitch-roll measurement at all attitudes, except $\alpha = \pm 90°$ where R cannot be determined, as shown subsequently. Let $\widehat{\mathbf{z}}$ denote the 1×2 vector of inferred inputs corresponding to 1×3 observed output vector $\mathbf{v}$, estimated by least-squares solution of overdetermined equation system (eqs. (2), (4), and (5)), where

$$\left.\begin{aligned} \widehat{\mathbf{z}} &= [\widehat{\alpha} \quad \widehat{R}] \\ \mathbf{v} &= [v_x \quad v_y \quad v_z] \end{aligned}\right\} \tag{99}$$

In addition, let $\mathbf{f}(\mathbf{C},\mathbf{z})$ denote the 1×3 vector of functions defined by transducer equations (14) to (16) as follows:

$$\mathbf{f}(\mathbf{C},\mathbf{z}) = [f_x(\mathbf{c}_x,\mathbf{z}) \; f_y(\mathbf{c}_y,\mathbf{z}) \; f_z(\mathbf{c}_z,\mathbf{z})] \tag{100}$$

where 4×3 parameter matrix $\mathbf{C}$ is defined as

$$\mathbf{C} = \left[\mathbf{c}_x \,\vdots\, \mathbf{c}_y \,\vdots\, \mathbf{c}_z\right] \tag{101}$$

The 2×3 Jacobian matrix of equation (100) with respect to input vector $\mathbf{z}$ is given by

$$\mathbf{F}_z \equiv \left[\frac{\partial \mathbf{f}(\mathbf{C},\widehat{\mathbf{z}})}{\partial \mathbf{z}}\right] = \begin{bmatrix} f_{x\alpha} & f_{y\alpha} & f_{z\alpha} \\ f_{xR} & f_{yR} & f_{zR} \end{bmatrix} \tag{102}$$

where the elements of $\mathbf{F}_z$ are defined in equations (87), (88), and (95).

A least-squares estimated solution to the 3×1 system $\mathbf{f}(\mathbf{C},\mathbf{z}) = 0$ exists only if $\mathbf{F}_z$ has rank 2, or equivalently, if 2×2 moment matrix $\mathbf{F}_z\mathbf{F}_z^{\mathrm{T}}$ is nonsingular. Clearly, $\mathbf{F}_z\mathbf{F}_z^{\mathrm{T}}$ is singular for $\alpha = \pm 90°$. General analytic computation of the remaining zeros of det $(\mathbf{F}_z\mathbf{F}_z^{\mathrm{T}})$ is unmanageable. However, parametric computations show that $\mathbf{F}_z\mathbf{F}_z^{\mathrm{T}}$ is nonsingular for all values of R, A, and $\alpha \neq \pm 90°$ whenever $|\Omega| < 10°$. The singularity locus of $\mathbf{F}_z\mathbf{F}_z^{\mathrm{T}}$ for $\Omega_x = \Omega_y = \Omega_z = 45°$ and $A_x = A_y = A_z = 90°$ is shown in figure 12; this case is primarily of academic interest since typically $|\Omega| < 1°$.

It is shown in reference 5 that the uncertainty $\delta\widehat{\mathbf{z}}$ of inferred input vector $\widehat{\mathbf{z}}$, relative to observed output vector $\mathbf{v}$, is obtained from the following equation as

$$\delta\widehat{\mathbf{z}} = \delta\widehat{\mathbf{v}}\mathbf{F}_z^{\mathrm{T}}\left(\mathbf{F}_z\mathbf{F}_z^{\mathrm{T}}\right)^{-1} \tag{103}$$

where $\delta\widehat{\mathbf{z}} = [\delta\widehat{\alpha} \quad \delta\widehat{R}]$. Note that $\delta\widehat{\mathbf{v}} = [\delta v_x \quad \delta v_y \quad \delta v_z]$ is the uncertainty of predicted output vector $\widehat{\mathbf{v}}$. It follows that the 2×2 covariance matrix of $\widehat{\mathbf{z}}$ is given by

$$\Sigma_{\widehat{\mathbf{z}}} = \left(\mathbf{F}_z\mathbf{F}_z^{\mathrm{T}}\right)^{-1}\mathbf{F}_z\Sigma_{\widehat{\mathbf{v}}}\mathbf{F}_z^{\mathrm{T}}\left(\mathbf{F}_z\mathbf{F}_z^{\mathrm{T}}\right)^{-1} \tag{104}$$

where $\Sigma_{\widehat{\mathbf{v}}}$ is the 3×3 covariance matrix of $\widehat{\mathbf{v}}$. Confidence and prediction intervals for $\widehat{\mathbf{z}}$ are obtained from equation (104).

To determine closed-form variance functions of inferred inputs $\widehat{\alpha}$ and $\widehat{R}$ for the three-axis sensor without misalignment errors, evaluate gradient matrix $\mathbf{F}_z$ using the parameter values of equation (58) as follows:

$$\mathbf{F}_z = \begin{bmatrix} \cos\,\alpha & \sin\,R\,\sin\,\alpha & \cos\,R\,\sin\,\alpha \\ 0 & -\cos\,R\,\cos\,\alpha & \sin\,R\,\cos\,\alpha \end{bmatrix} \tag{105}$$

Moment matrix $\mathbf{F}_z\mathbf{F}_z^{\mathrm{T}}$ is then given by

$$\mathbf{F}_z\mathbf{F}_z^{\mathrm{T}} = \begin{bmatrix} 1 & 0 \\ 0 & \cos^2\,\alpha \end{bmatrix} \tag{106}$$

Let the y- and z-axis sensors have equal measurement variance σ_y^2 and let the three measurement errors be uncorrelated; then measurement covariance matrix $\Sigma_{\hat{\mathbf{v}}}$ is of the form

$$\Sigma_{\hat{\mathbf{v}}} = \begin{bmatrix} \sigma_x^2 & 0 & 0 \\ 0 & \sigma_y^2 & 0 \\ 0 & 0 & \sigma_y^2 \end{bmatrix} \tag{107}$$

Combine equations (104) to (107) to obtain variance functions $\sigma_{\hat{\alpha}}^2(\mathbf{z})$ and $\sigma_{\hat{R}}^2(\mathbf{z})$ of the inferred inputs, as follows:

$$\left.\begin{aligned} \sigma_{\hat{\alpha}}^2 &= \sigma_x^2\,\cos^2\,\alpha + \sigma_y^2\,\sin^2\,\alpha \\ \sigma_{\hat{R}}^2 &= \frac{\sigma_y^2}{\cos^2\,\alpha} \end{aligned}\right\} \tag{108}$$

Note from equations (108) that $\sigma_{\hat{\alpha}}(\mathbf{z}) = \sigma_x$ whenever $\sigma_x = \sigma_y$. If $\sigma_y > \sigma_x$ then $\sigma_{\hat{\alpha}}(\mathbf{z})$ reaches a minimum of σ_x at $\alpha = 0°$, and reaches a maximum of σ_y at $\alpha = \pm 90°$. Thus, the three-axis sensor eliminates inferred pitch angle uncertainty singularities at $\alpha = \pm 90°$ seen for the single-axis sensor with independently measured roll in equation (81) and for the two-axis x-y sensor package. However, inferred roll angle is unbounded at $\alpha = \pm 90°$. Both uncertainties are independent of roll.

Curves of relative standard deviations $\sigma_{\hat{\alpha}}(\mathbf{z})/\sigma_{vx}(\mathbf{z})$ and $\sigma_{\hat{R}}(\mathbf{z})/\sigma_{vy}(\mathbf{z})$ appear in figures 12 to 20 as α varies from $-90°$ to $90°$, as R varies from $0°$ to $180°$, and for $\sigma_y = \sigma_z$. Weighted least-squares estimation is assumed, where output component squared errors are weighted by the inverse of the associated output variances. Figures 13 and 14 illustrate inferred pitch and roll angle uncertainties plotted versus pitch and roll, respectively, for $\sigma_y = \sigma_z = 10\sigma_x$, $\Omega_x = \Omega_y = \Omega_z = 0.1°$, $A_x = \pi/2$, and $A_y = A_z = 0°$. There is negligible deviation from the misalignment-free curves of equations (108).

Figures 15 and 16 repeat the case of figures 13 and 14 with $\sigma_y = \sigma_z = 10\sigma_x$ except that $\Omega_x = \Omega_y = \Omega_z = 1°$; there is insignificant change from figures 13 and 14. Figures 17 and 18 repeat the case of figures 15 and 16 with $\Omega_x = \Omega_y = \Omega_z = 1°$ except that $\sigma_y = \sigma_z = \sigma_x$; inferred pitch uncertainty is nearly constant over pitch and roll in spite of 1° misalignment angles. Figures 19 and 20 repeat the case of figures 15 and 16 with $\sigma_y = \sigma_z = 10\sigma_x$, except that $\Omega_x = \Omega_y = \Omega_z = 5°$; pitch angle uncertainty worsens by approximately 50 percent at roll of 90°.

6.7. Summary of Pitch Measurement With Roll

Comparison of figures 13 to 20 with figures 10 and 11 confirms that the three-axis sensor package is required for general purpose pitch-roll measurement. To obtain the most accurate pitch measurement over the full pitch and roll angle ranges, high-precision sensors are required on all three axes. However, inferred pitch angle measurement accuracy can be maintained within the typical ranges of $-60°$ to $60°$ for pitch and $-180°$ to $180°$ for roll angles using y- and z-axis sensors whose uncertainties are up to 10 times greater than the x-axis sensor uncertainty, and with sensor misalignment angles as large as $2°$. Thus, accurate pitch measurement with roll can be obtained from $-60°$ to $60°$ with a high-precision x-axis sensor in two- and three-axis packages with significantly less accurate y- and z-axis sensors and in a single-axis package with significantly less accurate independent roll measurement. Note that roll measurement at $\alpha = \pm 90°$ is not possible with the three-axis sensor. The x-y axis sensor is useful primarily for pitch measurement from $-180°$ to $180°$ with independently measured roll for $R \neq \pm 90°$.

7. Fractional Experimental Designs

Fractional experimental designs constructed as subsets of larger type D experimental designs can provide more efficient calibration while maintaining adequate prediction uncertainties. Test point placement for fractional designs includes the following considerations:

1. Comprehensive test point coverage throughout the area of ß including boundaries
2. Sufficient incremental resolution to define functional variation
3. Limited number of experimental design points to maintain affordable calibration

The number of points for experimental design D can be reduced while maintaining coverage over its full area by decimation of selected interior rows and columns. This procedure also maintains full incremental resolution within the nondecimated rows and columns. Figure 21(a) illustrates an $N \times M$ type D design, where $N = 19$ and $M = 13$. Figure 21(b) illustrates the same design wherein every K_Rth row is decimated by a factor of $K_a = 3$, and every K_ath column is decimated by a factor of $K_R = 4$. Boundaries are not decimated. The number of points, denoted by C', of the fractional design is thereby reduced from $C = NM = 247$ to $C' = 139$, where

$$C' = N\left(\frac{M-1}{K_R} + 1\right) + (M-1)\left(1 - \frac{1}{K_R}\right)\left(\frac{N-1}{K_a} + 1\right) \tag{109}$$

8. Replicated Calibration

As discussed in reference 5, up to 10 replicated calibrations over an extended time period are necessary to obtain adequate statistical sampling over time, to estimate bias and precision uncertainties, and to test for nonstationarity and drift of the estimated parameters. The following analysis of variance techniques developed in reference 5 are applied to experimental calibration data presented below:

1. Test of significance for presence of bias uncertainty
2. Estimated bias and precision uncertainties
3. Tests of significance for estimated offset and sensitivity drift

Typically six replicated calibrations are obtained.

9. Experimental Calibration Data

Calibration residual plots are shown figures 22 to 54 for the experimental calibration data sets described in this section, with 95 percent calibration confidence intervals indicated as dotted curves and 95 percent prediction intervals indicated as dash-dotted curves. Residual sets for each replication are indicated by a unique symbol. Numerical statistics for selected figures are listed in table 2 as follows. The standard error of the regression is denoted by σ_E. Analyses of variance (ref. 5) provide estimates of standard error σ_{bias} due to calibration bias error and standard error

σ_{prec} due to calibration measurement precision error. Symbol T_{bias} denotes the test value for the calibration bias error test of significance; $(F_{\text{bias}})_{95}$ denotes the corresponding F-distributed limit at 95 percent confidence level. In addition, standard errors and tests of significance are indicated for variation between replications of estimated sensor offset and sensitivity. Variables σ_b and σ_S denote the estimated standard errors due to drift in b and S, respectively. Symbols T_b and T_S denote test values for significant offset drift and sensitivity drift, respectively; $(F_{bS})_{95}$ denotes the corresponding F-distributed limit for both test values. Note that the tests are statistically significant if test value T exceeds limit F.

Inferred residual plots are also provided for each data set, obtained by back-computation of inferred calibration inputs using the observed calibration output data and estimated calibration parameters. The corresponding inferred calibration confidence intervals and prediction intervals are shown as dotted curves and dash-dotted curves, respectively.

9.1. Single-Axis Calibration Without Roll

Figures 22, 24, and 26 present calibration residual plots with 95 percent confidence and prediction intervals for six replicated calibrations without roll of a high-precision single-axis AOA sensor, without temperature correction. Inferred calibration inputs are back-calculated by using equation (76). The corresponding inferred residual plots appear in figures 23, 25, and 27.

The calibration of figures 22 and 23 employs design D_1 from $\alpha = -36°$ to $36°$ with $2°$ increments. The standard error of regression of figure 22, listed in table 2, is 0.000160°; no significant calibration bias error or sensor sensitivity drift over the six replications is detected. Slightly significant sensor offset drift is detected. The rms value of the residuals of the inferred angles, denoted by σ_{inv}, equals 0.000174°.

The calibration of figures 24 and 25 employs design D_1 from $\alpha = -180°$ to $180°$ with $5°$ increments. The calibration residuals disclose a systematic sinusoidal error pattern with two periods from $\alpha = -180°$ to $180°$. Note in table 2 that the larger standard error of regression for figure 24 is 0.000317°, compared with figure 22, and significant calibration bias uncertainty is detected. Significant sensor offset and sensitivity drift are not detected. At $\pm 90°$ where inferred confidence and prediction intervals become unbounded, most residuals of the inferred angles fall outside the boundaries of figure 25. The observed sinusoidal systematic error in figure 24 is due to static deflection of isolation pads within the sensor package.

Figures 26 and 27 illustrate residuals for six replicated four-point tumble calibrations with a standard error of regression for figure 36 of 0.000284° listed in table 2. The large calibration confidence intervals are caused by the reduced number of degrees of freedom. Note also that significant calibration bias uncertainty is detected although without significant sensor parameter drift. Most residuals of the inferred angles fall outside the chart boundaries at $\alpha = \pm 90°$ in figure 27.

9.2. Single-Axis Calibration With Roll

Two single-axis AOA sensors were simultaneously calibrated with roll over multiple replications. Sensor 1 is a high-precision unit; sensor 2 is a less expensive unit of lower accuracy. Experimental design D_1 with an extra roll point at 180°, as in the design of figure 5, was employed with pitch angle limits of $\pm 30°$ and $\pm 180°$.

9.2.1. Full calibration from $-30°$ to $30°$. Pitch and roll angle step sizes are 5° and 15°, respectively, and the resultant design contains 325 calibration points per replication over six calibrations. Temperature variation did not exceed 1°C during calibration.

Figure 28(a) illustrates calibration residuals of sensor 1 computed without temperature correction; residuals are plotted versus pitch angle. As seen in table 2, the standard error of the regression is 0.000776° with only minimally significant indicated calibration bias uncertainty. However, very significant sensor sensitivity drift, with $T_S = 919$, and less significant sensor offset drift are detected, which is also apparent from slope variations seen in the residual pattern.

Figures 28(b) and 29 illustrate calibration residuals and residuals of the inferred angles, respectively, for the data of figure 28(a) recomputed with temperature corrections for sensor offset and sensitivity. Standard error reduces to 0.000387° compared with that in figure 28(a), as shown in table 2; significant calibration bias uncertainty is detected. After temperature correction, sensor offset drift and sensitivity drift are greatly reduced, with $T_S = 5.14$. Figure 30 illustrates individual residual curves for the first replication only plotted versus pitch and parameterized by calibration roll angles from 180° to 0° by using calibration parameters estimated over six replications. The systematic error pattern produces minimum error dispersion at $-5°$ pitch and greatest dispersion at $\pm 30°$ pitch. Figures 31 and 32 illustrate calibration residuals and residuals of the inferred angles, respectively, plotted versus roll angle. Minimum dispersion is apparent near $\pm 90°$ roll, with maximum dispersion near 0° and $\pm 180°$ roll. Statistics for figure 31 are identical to those for figure 28(b). Figure 33 illustrates individual inferred residual curves for the first replication only plotted versus roll angle and parameterized by calibration pitch angles over $-30°$ to 30°, using parameters estimated over six replications.

Figure 34 illustrates calibration residuals for less accurate sensor 2 plotted versus pitch with temperature correction. The standard error of the regression is 0.00166° as listed in table 2; calibration bias uncertainty is insignificant. Strongly significant sensor offset and sensitivity drifts are indicated, which are apparent in the residual patterns.

9.2.2. Fractional calibration from −30° to 30°. The design cardinality of the 325-point calibration D design in section 9.2.1 is reduced to 53 points as follows: overall pitch and roll angle resolutions are reduced from 3° to 15° and from 15° to 30°, respectively. Alternate rows and columns are then decimated by factors of 2. Figure 35 illustrates the fractional calibration residuals for sensor 1. Note the enlarged calibration confidence intervals, caused by reduced degrees of freedom, and the larger prediction intervals compared with the full calibration data of figure 28(b). As seen in table 2, the standard error is increased from 0.000387° in figure 28(b) to 0.000427°; the test for calibration bias error is significant.

Figure 36 illustrates the data residuals computed from the full data set by using parameter vector $\widehat{\mathbf{c}}$ and confidence intervals obtained from the fractional calibration. The standard error of the residuals equals 0.000389° compared with the standard error of 0.000387° obtained for the full data set of figure 28(b). For sensor 1, calibration by this particular fractional design provides a fit nearly equivalent to that provided by the complete design.

9.2.3. Calibration from −180° to 180°. Pitch and roll angle step sizes are 15° and 30°, respectively, with 325 calibration points per replication. Temperature variation during calibration did not exceed 1°C.

Figures 37 and 38 illustrate sensor 1 calibration residuals and residuals of the inferred angles, respectively, computed with temperature correction over four replications; residuals are plotted against pitch angle. The standard error of the regression is 0.000489° with significant indicated calibration bias uncertainty, as seen in table 2. Slightly significant sensor offset drift is detected without significant sensor sensitivity drift. Figure 39 illustrates individual residual curves for the first replication only using calibration parameters estimated over four replications; curves are plotted versus pitch angle and parameterized by calibration roll angles from 0° to 180°. The systematic residual pattern is dependent on both pitch and roll; error variation with pitch angle is sinusoidal with two periods over $\alpha = -180°$ to 180°.

Figure 40 illustrates calibration residuals plotted versus roll angle. Figure 41 illustrates individual residual curves for the first replication using calibration parameters estimated over four replications; curves are plotted versus roll angle and parameterized by calibration pitch angles from 0° to 180°. The systematic error pattern is dependent on both pitch and roll; error variation with roll angle is sinusoidal with one period over $R = -180°$ to 180°.

Figures 42 and 43 illustrate sensor 2 calibration residuals and residuals of the inferred angles, respectively, with temperature correction over six replications; residuals are plotted versus pitch angle. The standard error of the regression is 0.00134°. Other statistics appear in table 2. Calibration bias uncertainty is insignificant. Strongly significant sensor offset and sensitivity drift are detected between replications.

9.3. Three-Axis Calibration With Roll

A three-axis model attitude sensor package containing identical high-precision sensors was calibrated with roll for six replications. Experimental design D_1 with an extra roll point at 180°, as in the design of figure 5, was employed with pitch angle limits of ±90° and ±180°. Sensor data are temperature corrected; confidence and prediction intervals appear in each figure. Residuals of the inferred angles are obtained by subtracting true angle values from the back-computed angle values.

9.3.1. Calibration from −90° to 90°. Pitch and roll angle step sizes are 10° and 30°, respectively, with 247 calibration points per replication over six calibrations. Total calibration time was approximately 13 hr with temperature variation no greater than ±1°C. Figures 44(a), (b), and (c) illustrate calibration residuals plotted versus pitch angle for the x-, y-, and z-axis sensors, respectively, over six replications. The regression standard errors of the three sensors are 0.000434°, 0.000444°, and 0.000355°, respectively. As seen in table 2 significant calibration bias uncertainty and significant offset drift are detected for each of the three sensors. However, significant sensitivity drift is detected only for the x- and z-axis sensors.

Figures 45 and 46 illustrate residuals of the inferred pitch and roll angles, respectively, for the first replication only; curves are plotted versus pitch angle. Prediction intervals for inferred roll angle uncertainty, shown as functions of pitch angle, are significantly greater than those for inferred pitch angle uncertainty.

9.3.2. Calibration from −180° to 180°. Step sizes for pitch and roll angles are 10° and 30°, respectively, with six replications. Total calibration time was approximately 28 hr. Figures 47(a), (b), and (c) illustrate calibration residuals for the x-, y-, and z-axis sensors, respectively, over the six replications; curves are plotted versus pitch angle. Statistics are given in table 2. The regression standard errors of the three sensors are 0.000409°, 0.000523°, and 0.000479°, respectively. Significant calibration bias uncertainty is detected for each of the three sensors. Two periods of a sinusoidal error pattern over $\alpha = -180°$ to 180° are apparent in figure 44(c) for the x-axis sensor. However, significant sensitivity drift and significant offset drift are detected only for the x- and z-axis sensors. Figures 48 and 49 illustrate inferred pitch and roll angle residuals, respectively, for the first replication only; curves are plotted versus pitch angle. A sinusoidal error pattern is also apparent in the inferred pitch angle residuals of figure 48, with unusually large scatter at $\alpha = -90°$. The observed sinusoidal systematic error is due to static deflection of isolation pads within the sensor package as observed also in figure 24.

9.3.3. Six-point tumble calibration. Six replicated six-point tumble calibrations using design T are obtained from the previous data set in section 9.3.2. Figure 50 illustrates x-, y-, and z-axis sensor calibration residual curves over the six replications; individual curves are plotted versus pitch angle. Statistics appear in table 2. The regression standard errors are 0.000433°, 0.000197°, and 0.000279°, respectively. Significant calibration bias uncertainty is detected for the x- and y-axis sensors. However, neither significant offset drift nor sensitivity drift is detected for the x- and y-axis sensors. Figure 51 illustrates inferred pitch angle residuals and roll angle residuals, respectively, for all six replications; curves are plotted versus pitch angle.

Figure 52 illustrates sensor output residuals for the entire calibration data set computed by using parameters estimated from the six-point tumble calibration data. The indicated confidence and prediction intervals are obtained from the tumble calibration regression analysis. Standard residual errors are 0.00104°, 0.00095°, and 0.00084°, respectively. The corresponding regression standard errors appear in the previous paragraph. Comparison with figure 44 shows that the replicated six-point tumble test significantly underestimates prediction intervals. At the same time it suffers greater calibration uncertainty compared with the full calibration, as evidenced by the larger calibration confidence intervals. Compared with figure 47(a), figure 52(a) illustrates increased standard residual error (0.00104° compared with 0.000433°), as indicated by the systematic error pattern, caused primarily by the limited spatial resolution of the T experimental design compared with the multipoint D_0 design.

9.3.4. Fractional calibration from −180° to 180°. The design cardinality of the 481-point calibration of section 9.3.4 is reduced to 73 points as follows: overall pitch and roll angle resolutions are reduced from 10° to 30° and from 30° to 60°, respectively. Alternate rows and columns are then decimated each by a factor of 2. Statistics are given in table 2. Comparison of the x-axis sensor fractional calibration residuals, shown in figure 53, with the full calibration residuals of figure 47(a) shows nearly the same prediction intervals, although the calibration confidence intervals are enlarged due to fewer degrees of freedom. The standard errors and tests for calibration bias error are nearly unchanged. However, the fractional calibration fails to detect significant offset drift and indicates considerably reduced sensitivity drift significance. Figure 54 illustrates the data residuals computed from the full data set by using the parameter vector $\widehat{\mathbf{c}}$ and confidence intervals estimated by fractional calibration. The standard error of the residuals shown in figure 54 equals 0.000410° compared with a residual standard error of 0.000409° obtained in figure 47(a). Except for offset drift detection, the 73-point fractional calibration performs equivalently to the full 481-point calibration.

10. Concluding Remarks

Statistical tools, developed in NASA/TP-1999-209545 for nonlinear least-squares estimation of multivariate sensor calibration parameters and the associated calibration uncertainty analysis, have been applied to single- and multiple-axis inertial model attitude sensors with and without roll. These techniques provide confidence and prediction intervals of calibrated sensor uncertainty as functions of applied input angle values. They also provide a comparative performance study of various experimental designs for inertial sensor calibration. The importance of replicated calibrations over extended time periods has been emphasized; replication provides estimates of calibration precision and bias uncertainties, statistical tests for calibration or modeling bias uncertainty, and statistical tests for sensor offset and sensitivity drift during replicated calibrations.

The techniques developed herein properly account for correlation among estimated calibration parameters and among multisensor signal conditioning channels, allow inclusion of calibration standard uncertainties, and account for uncertainty of independently measured roll angle. Previous empirical techniques for treating correlations among estimated parameters may overestimate, or in certain cases significantly underestimate, uncertainty magnitudes.

The sensor output variance function, and hence calibration confidence intervals and prediction intervals, have been shown to be identical for x-, y-, and z-axis sensors. Moreover, the output variance function is independent of the inertial sensor parameters $\mathbf{c} = [b\,S\,\Omega\,A]^{\mathrm{T}}$. Hence, the design figure of merit is independent of the sensor under calibration. In addition, the sensor output variance function is independent of roll angle R for experimental design D_0, wherein roll angle test points are uniformly spaced over the roll angle range without repeated principal angle values.

Parametric studies show that the pitch sensor figure of merit, computed within a limited usage range, can be reduced by limiting pitch angle test points to a range approximately 1.5 times the usage range. For example, calibration over a pitch range from $-45°$ to $45°$ is appropriate for a pitch usage range of $-30°$ to $30°$. Additional modest variance reduction within a limited test range is possible by concentrating pitch angle test points near the center of the range of interest. However, as discussed in NASA/TP-1999-209545, uniformly spaced designs minimize the mean normalized error variance due to systematic bias errors. For this reason, design D_1 with uniformly spaced pitch and roll angle test points is preferable. Experimental results show that calibration over a pitch range from $-180°$ to $180°$ detects systematic bias errors not seen in pitch calibrations from $-45°$ to $45°$.

Experimental results show that fractional multipoint D designs can provide adequate statistical uncertainty and uncertainty characterization with increased calibration efficiency. However, experimental results show that tumble test T calibration designs, limited to cardinal angles, provide insufficient spatial resolution to adequately characterize systematic modeling uncertainty. As a result, prediction intervals tended to be significantly underestimated in spite of increased calibration uncertainty due to fewer degrees of freedom evidenced by larger calibration confidence intervals.

Simple closed-form rational trigonometric polynomial expressions are obtained for computation of confidence and prediction intervals for design D_1. In any case, numerical point-by-point calculation of confidence and prediction intervals for any design is readily programmed for on-line computation or posttest data reduction.

Inferred input pitch and roll angle uncertainties are dependent upon independent variables, pitch angle α and roll angle R, for any experimental design, even if the variance function is independent of R.

Single- and two-axis model attitude sensors do not provide accurate pitch angle or roll angle measurements near pitch of $\pm 90°$. Neither does the two-axis sensor provide accurate roll measurement near roll of $\pm 90°$ at any pitch angle. Within the range of typical sensor parameters the three-axis sensor eliminates measurement singularities except for roll angle measurement near pitch of $\pm 90°$. By using identical x-, y-, and z-axis sensors, full pitch angle precision is maintained over a pitch range from $-180°$ to $180°$. Adequate pitch angle measurement precision with roll can be maintained within a pitch angle range from $-60°$ to $60°$ by use of a precision x-axis sensor with significantly less accurate y- and z-axis sensors, such as $\sigma_y = \sigma_z = 10\sigma_x$, and $\Omega < 2°$.

Recommendations for model attitude sensor calibration and usage are as follows:

1. The pitch angle calibration range should be approximately 150 percent of the usage range.
2. The roll angle calibration range should be from $-180°$ to $180°$.
3. Test points should be uniformly spaced in both pitch and roll.
4. Pitch angle should vary from minimum angle to maximum angle and back to minimum angle.
5. Fractional D calibration experimental designs may be employed for calibration efficiency, provided that statistical adequacy is established experimentally.
6. Calibrations should be replicated at least 6 times, and preferably 10 times, for estimation of bias and precision uncertainty and for detection of parameter nonstationarity.

7. Four-point and six-point tumble calibration experimental designs are not recommended for laboratory calibration.
8. The single-axis package may be used for pitch angle measurement with adequate uncertainty whenever the uncertainty of the independently measured roll angle does not exceed 10 times the desired pitch angle uncertainty.
9. The three-axis sensor package is suitable for general pitch-roll measurement with adequate accuracy except for roll measurement near pitch of $\pm 90°$. The y- and z-axis sensor uncertainties should not exceed 10 times the x-axis sensor uncertainty.
10. The x-y axis sensor package is suitable only for measurements away from pitch of $\pm 90°$ and roll of $\pm 90°$. The y-axis sensor uncertainties should not exceed 10 times the x-axis sensor uncertainty.

The recommended calibration experimental designs may be readily implemented by means of modern automated calibration apparatus.

Appendix A

Derivation of x-, y-, and z-Axis Sensor Outputs for Measurement With Roll

The inertial attitude sensor output is obtained in reference 2 by computation of the projection of the gravitational force vector onto the sensor sensitive axis. The effects of package rotations in pitch, roll, and yaw, as well as package misalignments Ω and A, are computed by means of coordinate transformations.

Consider a three-dimensional right-hand coordinate system with axes x, y, and z, where negative z represents the direction of gravity in gravitational coordinates, shown in figure A1. Let x denote the direction of the model axis in model coordinates at zero pitch, roll, and yaw. Then $\mathbf{g} = [0\;0\;{-1}]^{\mathrm{T}}$ denotes the normalized gravitational force vector in gravitational coordinates, and let $\mathbf{g_q} = [g_{q_x}\;g_{q_y}\;g_{q_z}]^{\mathrm{T}}$ denote $\mathbf{g}$ transformed into sensor coordinates.

Transformation from gravity coordinates to model axis coordinates, and thence to sensor coordinates, consists of an ordered sequence of rotations, defined by the following coordinate transformations:

1. Pitch α—left-hand rotation about y-axis:

$$\mathbf{T}_{\alpha}(\alpha) = \begin{bmatrix} \cos\alpha & 0 & -\sin\alpha \\ 0 & 1 & 0 \\ \sin\alpha & 0 & \cos\alpha \end{bmatrix} \tag{110}$$

2. Roll R—left-hand rotation about x-axis:

$$\mathbf{T}_{R}(R) = \begin{bmatrix} 1 & 0 & 0 \\ 0 & \cos R & \sin R \\ 0 & -\sin R & \cos R \end{bmatrix} \tag{111}$$

3. Yaw Y—left-hand rotation about z-axis:

$$\mathbf{T}_{Y}(Y) = \begin{bmatrix} \cos Y & \sin Y & 0 \\ -\sin Y & \cos Y & 0 \\ 0 & 0 & 1 \end{bmatrix} \tag{112}$$

Model Attitude Transformation

Let the model be oriented at pitch angle α and roll angle R. Transformation from gravity coordinates to model coordinates is represented by pitch rotation $\mathbf{T}_{\alpha}(\alpha)$ followed by roll rotation $\mathbf{T}_{R}(R)$. Gravity vector $\mathbf{g}$ transformed to model coordinates becomes

$$\mathbf{g}_{M} = \mathbf{T}_{R}(R)\,\mathbf{T}_{\alpha}(\alpha)\mathbf{g} \tag{113}$$

Transformation to x-Axis Sensor Coordinates

The sensitive axis of the x-axis sensor is nominally aligned with the model x-axis. Sensor misalignment is represented as transformation from model coordinates to sensor coordinates as positive roll rotation $\mathbf{T}_{R}(A)$ followed by positive yaw rotation $\mathbf{T}_{Y}(\Omega)$. In x-sensor coordinates the gravity vector is given by

$$\mathbf{g}_{\mathbf{q}_x} = \mathbf{T}_{Y}(\Omega_x)\,\mathbf{T}_{R}(A_x)\,\mathbf{g}_{M} \tag{114}$$

The x-component of $\mathbf{g}_{\mathbf{q}_x}$, corrected for sensor sensitivity S_x and offset b_x, yields equation (2).

Transformation to y-Axis Sensor Coordinates

Transformation to the sensitive axis of the y-axis sensor, nominally aligned with the model y-axis, is represented by the y-component of vector $\mathbf{g}_M$. Sensor misalignment is represented by a model-to-sensor coordinate transformation as positive pitch rotation $\mathbf{T}_\alpha(A)$ followed by positive roll rotation $\mathbf{T}_R(\Omega)$. In y-axis sensor coordinates, the gravity vector is given by

$$\mathbf{g}_{\mathbf{q}_y} = \mathbf{T}_R(\Omega_y)\,\mathbf{T}_\alpha(A_y)\,\mathbf{g}_M \tag{115}$$

The y-component of $\mathbf{g}_{\mathbf{q}_y}$, corrected for sensor sensitivity S_y and offset b_y, yields equation (4).

Transformation to z-Axis Sensor Coordinates

Transformation to the sensitive axis of the z-axis sensor, nominally aligned with the model z-axis, is represented by the z-component of vector $\mathbf{g}_M$. Sensor misalignment is represented by a model-to-sensor coordinate transformation as positive yaw rotation $\mathbf{T}_Y(A)$ followed by positive pitch rotation $\mathbf{T}_\alpha(\Omega)$. In z-axis sensor coordinates the gravity vector is given by

$$\mathbf{g}_{\mathbf{q}_z} = \mathbf{T}_\alpha(\Omega_z)\,\mathbf{T}_Y(A_z)\,\mathbf{g}_M \tag{116}$$

The z-component of $\mathbf{g}_{\mathbf{q}_z}$, corrected for sensor sensitivity S_z and offset b_z, yields equation (5).

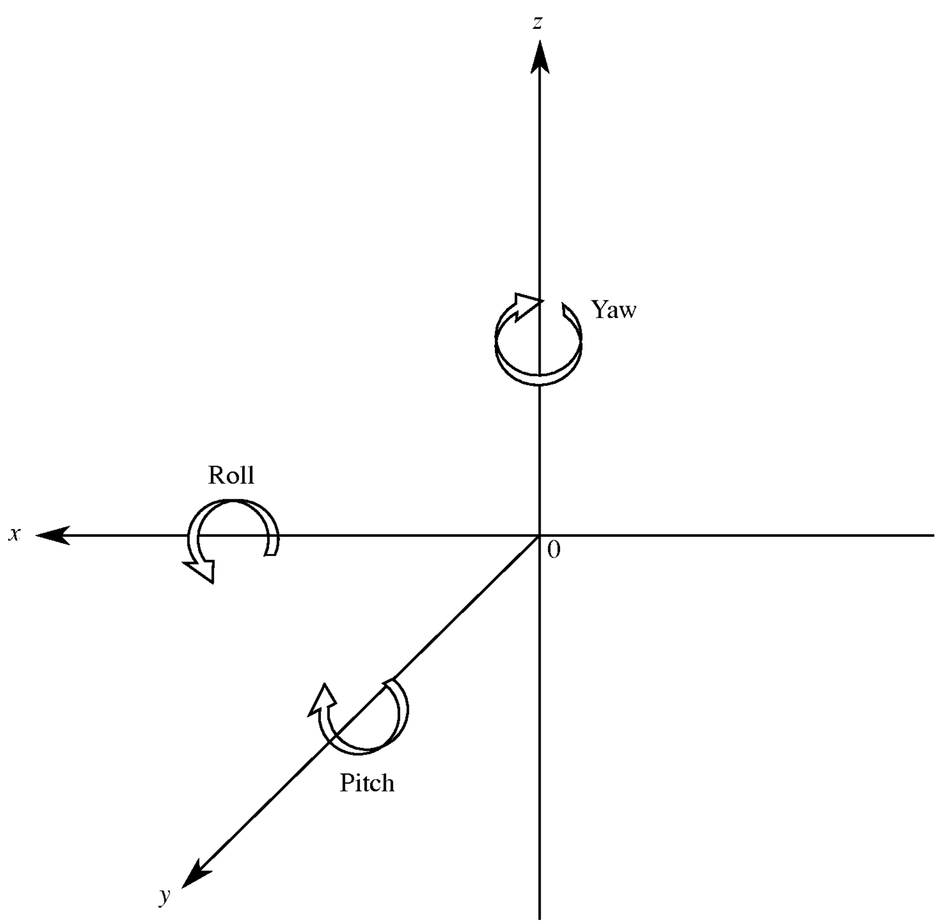

Figure A1. Cartesian coordinate system.

Appendix B

Evaluation of Matrix $\mathbf{H}_E$

Matrix $\mathbf{H}_E$ of equation (45) is evaluated for the pitch sensor. The kth 4×4 matrix contained in $4 \times 4 \times K$ array $\mathbf{F}_{cc}$ defined in equation (46) is equal to the Jacobian matrix of equation (2) evaluated at the kth element of experimental design ß. The elements of $\mathbf{F}_{cc}$ are obtained for the pitch sensor by differentiating equations (21) to (24) as follows:

$$f_{bb} = f_{bS} = f_{b\Omega} = f_{bA} = f_{SS} \equiv 0 \tag{117}$$

$$f_{S\Omega_k} = -\sin\Omega \sin\alpha_k - \cos\Omega \cos\alpha_k \sin(R_k + A) \tag{118}$$

$$f_{SA_k} = -\sin\Omega \cos\alpha_k \cos(R_k + A) \tag{119}$$

$$f_{\Omega\Omega_k} = -S[(\cos\Omega \sin\alpha_k - \sin\Omega \cos\alpha_k \sin(R_k + A)] \tag{120}$$

$$f_{\Omega A_k} = -S \cos\Omega \cos\alpha_k \cos(R_k + A) \tag{121}$$

$$f_{AA_k} = S \sin\Omega \cos\alpha_k \sin(R_k + A) \tag{122}$$

Similar expressions result for the roll sensor. Matrix $\mathbf{F}_{cc_k}$ is therefore of the form

$$\mathbf{F}_{cck} = \begin{bmatrix} 0 & 0 & 0 & 0 \\ 0 & 0 & f_{S\Omega_k} & f_{SA_k} \\ 0 & f_{S\Omega_k} & f_{\Omega\Omega_k} & f_{\Omega A_k} \\ 0 & f_{SA_k} & f_{\Omega A_k} & f_{AA_k} \end{bmatrix} \tag{123}$$

If measurement covariance matrix $\mathbf{U}_Y$ equals $\sigma^2\mathbf{I}$, then matrix $\mathbf{H}_E$ is given by

$$\mathbf{H}_E = \frac{1}{\sigma^2} \begin{bmatrix} 0 & 0 & 0 & 0 \\ 0 & 0 & \sum_{k=1}^{K} \widehat{e}_k f_{S\Omega_k} & \sum_{k=1}^{K} \widehat{e}_k f_{SA_k} \\ 0 & \sum_{k=1}^{K} \widehat{e}_k f_{S\Omega_k} & \sum_{k=1}^{K} \widehat{e}_k f_{\Omega\Omega_k} & \sum_{k=1}^{K} \widehat{e}_k f_{\Omega A_k} \\ 0 & \sum_{k=1}^{K} \widehat{e}_k f_{SA_k} & \sum_{k=1}^{K} \widehat{e}_k f_{\Omega A_k} & \sum_{k=1}^{K} \widehat{e}_k f_{AA_k} \end{bmatrix} \tag{124}$$

where $\widehat{e}_k$ is the kth element of residual vector $\widehat{\mathbf{e}}$.

Simulation studies show that among the experimental designs evaluated above the prediction uncertainty is unaffected by matrix $\mathbf{H}_E$ for values of measurement error standard deviation $\sigma \leq 0.01|\mathbf{v}|$, where $\mathbf{v}$ is the observed output vector. Moreover, only insignificant random effects are evident for $\sigma \leq 0.1|\mathbf{v}|$; this confirms that $\mathbf{H}_E$ may be neglected for typical levels of measurement error.

Appendix C

Properties of Sensor Variance Functions

The proofs of Theorems I to IV are given in this appendix.

Theorem I: Sensor output variance function $\sigma_v^2(\mathbf{z})$ is independent of calibration parameters b and S.

Proof: It is shown in appendix D, in the general evaluation of elements of matrix $\mathbf{R}_x$ for the x-axis sensor with roll, that matrix $\mathbf{R}_x$ is of the form

$$\mathbf{R} = \begin{bmatrix} r_{bb} & r_{bS} & r_{b\Omega} & r_{bA} \\ r_{bS} & r_{SS} & r_{S\Omega} & r_{SA} \\ r_{b\Omega} & r_{S\Omega} & r_{\Omega\Omega} & r_{\Omega A} \\ r_{bA} & r_{SA} & r_{\Omega A} & r_{AA} \end{bmatrix} = \begin{bmatrix} r_{bb} & r_{bS} & S\rho_{b\Omega} & Sw\rho_{bA} \\ r_{bS} & r_{SS} & S\rho_{S\Omega} & Sw\rho_{SA} \\ S\rho_{b\Omega} & S\rho_{S\Omega} & S^2\rho_{\Omega\Omega} & S^2 w\rho_{\Omega A} \\ Sw\rho_{bA} & Sw\rho_{SA} & S^2 w\rho_{\Omega A} & S^2 w^2 \rho_{AA} \end{bmatrix} \tag{125}$$

The terms denoted by r and ρ are obtained by means of equations (130) to (135) and are explicitly evaluated in appendix D by equations (176) to (205). It follows from equations (28) to (40) for sensors y and z that matrices $\mathbf{R}_y$ and $\mathbf{R}_z$ may be expressed in the same form. For the x-, y-, and z-axis sensors, vector $\mathbf{f}_c$ is of the form

$$\mathbf{f}_{\mathbf{c}}^{\mathrm{T}} = [f_b\, f_S\, f_\Omega\, f_A] = [f_b\, f_S\, S\boldsymbol{\phi}_\Omega\, Sw\boldsymbol{\phi}_A] \tag{126}$$

where $\boldsymbol{\phi}_\Omega$ and $\boldsymbol{\phi}_A$ are independent of b and S; presubscripts x, y, and z are elided for convenience. It is shown by Lemma 1, appendix D, that if matrix $\mathbf{R}^{-1}$ exists, then

$$\frac{\sigma_v^2(\mathbf{z}_k)}{\sigma_E^2} \approx q_R \equiv \mathbf{f}_{\mathbf{c}}^{\mathrm{T}}\, \mathbf{R}^{-1}\, \mathbf{f}_{\mathbf{c}} = \boldsymbol{\phi}_c^{\mathrm{T}}\, \mathbf{P}^{-1}\, \boldsymbol{\phi}_c \tag{127}$$

where

$$\boldsymbol{\phi}_c = [f_b\, f_S\, \phi_\Omega\, \phi_A]^{\mathrm{T}} \tag{128}$$

and

$$\mathbf{P} = \begin{bmatrix} r_{bb} & r_{bS} & \rho_{b\Omega} & \rho_{bA} \\ r_{bS} & r_{SS} & \rho_{S\Omega} & \rho_{SA} \\ \rho_{b\Omega} & \rho_{S\Omega} & \rho_{\Omega\Omega} & \rho_{\Omega A} \\ \rho_{bA} & \rho_{SA} & \rho_{\Omega A} & \rho_{AA} \end{bmatrix} \tag{129}$$

Because the elements of $\boldsymbol{\phi}_c$, and those of $\mathbf{P}$ as shown, are independent of parameters b and S, variance function q_R is independent of b and S. In particular, matrix $\mathbf{P}$ is obtained as

$$\mathbf{P} = \boldsymbol{\Phi}_c^{\mathrm{T}}\, \boldsymbol{\Phi}_c \tag{130}$$

where $K \times 4$ matrix $\boldsymbol{\Phi}_c$ is defined as

$$\boldsymbol{\Phi}_c = \begin{bmatrix} \boldsymbol{\phi}_{\mathbf{c}_1}^{\mathrm{T}} \\ \boldsymbol{\phi}_{\mathbf{c}_2}^{\mathrm{T}} \\ \vdots \\ \boldsymbol{\phi}_{\mathbf{c}_K}^{\mathrm{T}} \end{bmatrix} = \left[\boldsymbol{\phi}_b \,\vdots\, \boldsymbol{\phi}_S \,\vdots\, \boldsymbol{\phi}_\Omega \,\vdots\, \boldsymbol{\phi}_A\right] \tag{131}$$

where

$$\boldsymbol{\phi}_b = [f_{b_1} \cdots f_{b_K}]^{\mathrm{T}} \tag{132}$$

$$\boldsymbol{\phi}_S = [f_{S_1} \cdots f_{S_K}]^{\mathrm{T}} \tag{133}$$

$$\boldsymbol{\phi}_\Omega = [\phi_{\Omega_1} \cdots \phi_{\Omega_K}]^{\mathrm{T}} \tag{134}$$

$$\boldsymbol{\phi}_A = [\phi_{A_1} \cdots \phi_{A_K}]^{\mathrm{T}} \tag{135}$$

Therefore matrix $\mathbf{P}$ is independent of parameters b and S because $\mathbf{P}$ is computed by using equations (130) to (135). The proof for the single-axis sensor without roll is analogous.

QED

Theorem II: Sensor output variance function $\sigma_v^2(\mathbf{z})$ is independent of calibration parameter Ω.

Proof: For x-, y-, and z-axis sensors define vectors

$$\left.\begin{array}{llll}
\mathbf{g}_{xc}^{\mathrm{T}} = [1 & \sin\alpha & \cos\alpha\,(\sin R\cos A_x + \cos R\sin A_x) & -\cos\alpha\,(\cos R\cos A_x - \sin R\sin A_x)] \\
\mathbf{g}_{yc}^{\mathrm{T}} = [1 & -\cos\alpha\sin R & -\sin A_y\sin\alpha + \cos A_y\cos\alpha\cos R & \cos A_y\sin\alpha + \sin A_y\cos\alpha\cos R \quad] \\
\mathbf{g}_{zc}^{\mathrm{T}} = [1 & -\cos\alpha\cos R & -\cos A_z\cos\alpha + \sin A_z\cos\alpha\sin R & -\sin A_z\sin\alpha - \cos A_z\cos\alpha\sin R \quad]
\end{array}\right\} \tag{136}$$

and matrix

$$\mathbf{\Gamma}_W = \begin{bmatrix} 1 & 0 & 0 & 0 \\ 0 & \cos\Omega & -\sin\Omega & 0 \\ 0 & -\sin\Omega & -\cos\Omega & 0 \\ 0 & 0 & 0 & 1 \end{bmatrix} \tag{137}$$

Matrix Γ_W is orthogonal; that is,

$$\mathbf{\Gamma}_W^{\mathrm{T}}\,\mathbf{\Gamma}_W = \mathbf{\Gamma}_W\,\mathbf{\Gamma}_W^{\mathrm{T}} = \mathbf{I} \tag{138}$$

For sensors x, y, and z, gradient vector $\boldsymbol{\phi}_c$, defined in equation (128), equals the product of vector $\mathbf{g}_c$ and matrix $\mathbf{\Gamma}_W$ as follows:

$$\boldsymbol{\phi}_c^{\mathrm{T}} = \mathbf{g}_c^{\mathrm{T}}\,\mathbf{\Gamma}_W \tag{139}$$

Similarly, $K \times 4$ matrix $\mathbf{\Phi}_c$ defined in equation (131) may be written as

$$\mathbf{\Phi}_c = \mathbf{G}_c\,\mathbf{\Gamma}_W \tag{140}$$

where $K \times 4$ matrix $\mathbf{G}_c$ is defined as

$$\mathbf{G}_c = \begin{bmatrix} \mathbf{g}_{\mathbf{c}_1}^{\mathrm{T}} \\ \vdots \\ \mathbf{g}_{\mathbf{c}_K}^{\mathrm{T}} \end{bmatrix} = \left[\mathbf{g}_b \,\vdots\, \mathbf{g}_S \,\vdots\, \mathbf{g}_\Omega \,\vdots\, \mathbf{g}_A\right] \tag{141}$$

where for sensor x

$$\mathbf{g}_{x_b} = [1 \cdots 1]^{\mathrm{T}} \tag{142}$$

$$\mathbf{g}_{x_S} = [\sin\alpha_1 \cdots \sin\alpha_K]^{\mathrm{T}} \tag{143}$$

$$\mathbf{g}_{x_\Omega} = \begin{bmatrix} \cos\alpha_1\,\sin(R_1 + A_x) \\ \vdots \\ \cos\alpha_K\,\sin(R_K + A_x) \end{bmatrix} \tag{144}$$

$$\mathbf{g}_{x_A} = \begin{bmatrix} \cos\,\alpha_1\,\cos\,(R_1 + A_x) \\ \vdots \\ \cos\,\alpha_K\,\cos\,(R_K + A_x) \end{bmatrix} \tag{145}$$

Vectors $\mathbf{g}_{y_b}$, $\mathbf{g}_{y_S}$, $\mathbf{g}_{y_\Omega}$, $\mathbf{g}_{y_A}$ and $\mathbf{g}_{z_b}$, $\mathbf{g}_{z_S}$, $\mathbf{g}_{z_\Omega}$, $\mathbf{g}_{z_A}$ are defined similarly. After noting that

$$\mathbf{P}^{-1} = \mathbf{\Gamma}_W^{\mathrm{T}} \left(\mathbf{G}_c^{\mathrm{T}}\,\mathbf{G}_c\right)^{-1} \mathbf{\Gamma}_W \tag{146}$$

it follows that the gradient vector $\boldsymbol{\phi}_c$ obtained in equation (128) may be combined with equations (139), (140), and (146) to yield

$$\frac{\sigma_v^2}{\sigma_E^2} \approx \boldsymbol{\phi}_c^{\mathrm{T}}\,\mathbf{P}^{-1}\,\boldsymbol{\phi}_c = \mathbf{g}_c^{\mathrm{T}} \left(\mathbf{G}_c^{\mathrm{T}}\,\mathbf{G}_c\right)^{-1} \mathbf{g}_c \tag{147}$$

Therefore, $\sigma_v^2(\mathbf{z})$ is independent of Ω for sensors x, y, and z. The proof for the single-axis sensor without roll is analogous.

QED

Theorem III: Sensor output variance function $\sigma_v^2(\mathbf{z})$ is independent of calibration parameter A.

Proof: Define vectors

$$\left.\begin{array}{llllll} \mathbf{h}_{x_c} = [1 & \sin\,\alpha & \cos\,\alpha\,\sin\,R & -\cos\,\alpha\cos\,R]^{\mathrm{T}} \\ \mathbf{h}_{y_c} = [1 & -\cos\,\alpha\sin\,R & \cos\,\alpha\cos\,R & \sin\,\alpha\quad]^{\mathrm{T}} \\ \mathbf{h}_{z_c} = [1 & -\cos\,\alpha\,\cos\,R & -\sin\,\alpha & -\cos\,\alpha\cos\,R]^{\mathrm{T}} \end{array}\right\} \tag{148}$$

and matrix

$$\mathbf{\Gamma}_A = \begin{bmatrix} 1 & 0 & 0 & 0 \\ 0 & 1 & 0 & 0 \\ 0 & 0 & \cos\,A & -\sin\,A \\ 0 & 0 & \sin\,A & \cos\,A \end{bmatrix} \tag{149}$$

Note that matrix $\mathbf{\Gamma}_A$ is unitary and that

$$\mathbf{g}_c^{\mathrm{T}} = \mathbf{h}_c^{\mathrm{T}}\,\mathbf{\Gamma}_A \tag{150}$$

for sensors x, y, and z. Define $K \times 4$ matrix $\mathbf{H}_c$ similarly to $\mathbf{G}_c$ as

$$\mathbf{H}_c = \begin{bmatrix} \mathbf{h}_{c_1}^{\mathrm{T}} \\ \vdots \\ \mathbf{h}_{c_K}^{\mathrm{T}} \end{bmatrix} \tag{151}$$

After noting from equations (141) and (149) that

$$\left[\mathbf{G}_c^{\mathrm{T}}\,\mathbf{G}_c\right]^{-1} = \mathbf{\Gamma}_A^{\mathrm{T}} \left[\mathbf{H}_c^{\mathrm{T}}\,\mathbf{H}_c\right]^{-1} \mathbf{\Gamma}_A \tag{152}$$

it follows that

$$\frac{\sigma_v^2}{\sigma_E^2} \approx \boldsymbol{\phi}_c^{\mathrm{T}}\,\mathbf{P}^{-1}\,\boldsymbol{\phi}_c = \mathbf{g}_c^{\mathrm{T}} \left[\mathbf{G}_c^{\mathrm{T}}\,\mathbf{G}_c\right]^{-1} \mathbf{g}_c = \mathbf{h}_c^{\mathrm{T}} \left[\mathbf{H}_c^{\mathrm{T}}\,\mathbf{H}_c\right]^{-1} \mathbf{h}_c \tag{153}$$

for sensors x, y, and z. Therefore, $\sigma_v^2(\mathbf{z})$ is independent of azimuth A since $\mathbf{h}_c$ and $\mathbf{H}_c$ are independent of A.

QED

Theorem IV: Let roll angle calibration set ß_R, defined in equations (10), contain $K = NM$ points uniformly spaced over the interval $[-\pi, \pi - \Delta R]$, where M and N are integers, $\Delta R = 2\pi/M$, and the principal value of each angle contained in ß_R occurs with the same frequency, then the pitch sensor output variance $\sigma_v^2(\mathbf{z})$ is independent of roll angle R.

Proof: Since variance function $\sigma_v^2(\mathbf{z})$ is independent of calibration parameters b, S, Ω, and R, evaluation of equations (21) to (26) using the parameter values of equations (58) yields the following equations:

$$\left.\begin{aligned} f_{x_b} &= 1 \\ f_{x_S} &= \sin\,\alpha \\ \phi_{x_\Omega} &= -\cos\,\alpha\,\sin\,R \\ \phi_{x_A} &= -\cos\,\alpha\,\cos\,R \end{aligned}\right\} \tag{154}$$

Evaluation of equations (173) and (174) in appendix D yields

$$\left.\begin{aligned} C_{MR} &= 0 \\ C_{2R} &= 0 \end{aligned}\right\} \tag{155}$$

It follows from equations (176) to (203) that

$$\mathbf{P}_x = \begin{bmatrix} r_{x_{bb}} & r_{x_{bS}} & 0 & 0 \\ r_{x_{bS}} & r_{x_{SS}} & 0 & 0 \\ 0 & 0 & \rho_{x_{\Omega\Omega}} & 0 \\ 0 & 0 & 0 & \rho_{x_{AA}} \end{bmatrix} \tag{156}$$

where

$$\left.\begin{aligned} r_{x_{bb}} &= MN \\ r_{x_{bS}} &= MS_\alpha \\ r_{x_{SS}} &= \frac{1}{2}M(N - C_{2\alpha}) \\ \rho_{x_{\Omega\Omega}} &= \rho_{x_{AA}} = \frac{1}{4}M(N + C_{2\alpha}) \end{aligned}\right\} \tag{157}$$

It then follows that

$$\mathbf{P}_x^{-1} = \begin{bmatrix} \frac{r_{x_{SS}}}{D} & \frac{-r_{x_{bS}}}{D} & 0 & 0 \\ \frac{-r_{x_{bS}}}{D} & \frac{r_{x_{bb}}}{D} & 0 & 0 \\ 0 & 0 & \frac{1}{\rho_{x_{AA}}} & 0 \\ 0 & 0 & 0 & \frac{1}{\rho_{x_{AA}}} \end{bmatrix} \tag{158}$$

where $D = r_{x_{bb}} r_{x_{SS}} - r^2_{x_{bS}}$. Evaluate equation (59), with the help of equations (128), (154), and (158) to obtain

$$\begin{aligned} \frac{\sigma_v^2(\mathbf{z})}{\sigma_E^2} &\approx \boldsymbol{\phi}_c(\mathbf{z})\,\mathbf{P}^{-1}\,\boldsymbol{\phi}_c^{\mathrm{T}}(\mathbf{z}) \\ &= \frac{r_{x_{SS}} - 2r_{s_{bS}}\ \sin\ \alpha + r_{x_{bb}}\ \sin^2\ \alpha}{D + \cos^2\ \alpha/(\rho_{x_{AA}})} \end{aligned} \tag{159}$$

which is seen to be independent of roll R.

QED

Appendix D

Evaluation of the Moment Matrix

Lemma 1: Proof of equation (127).

Define matrix Ξ as

$$\Xi = \begin{bmatrix} 1 & 0 & 0 & 0 \\ 0 & 1 & 0 & 0 \\ 0 & 0 & S & 0 \\ 0 & 0 & 0 & Sw \end{bmatrix} \tag{160}$$

It follows from equations (126) and (128) that

$$\mathbf{f}_c = \Xi \boldsymbol{\phi}_c \tag{161}$$

and from equations (125) and (129) that

$$\mathbf{R} = \Xi \mathbf{P} \Xi \tag{162}$$

If $\mathbf{R}^{-1}$ and Ξ^{-1} exist, then

$$\mathbf{R}^{-1} = \Xi^{-1} \mathbf{P}^{-1} \Xi^{-1} \tag{163}$$

Hence,

$$q_R = \mathbf{f}_c^{\mathrm{T}}\, \mathbf{R}^{-1} \mathbf{f}_c = \boldsymbol{\phi}_c^{\mathrm{T}}\, \Xi \Xi^{-1}\, \mathbf{P}^{-1}\, \Xi^{-1} \Xi\, \boldsymbol{\phi}_c = \boldsymbol{\phi}_c^{\mathrm{T}}\, \mathbf{P}^{-1}\, \boldsymbol{\phi}_c \tag{164}$$

QED

The following definitions and relations are used in the subsequent development:

1. Pitch angle set ß$_\alpha$ contains N points in the closed interval $[\alpha_{\min} \alpha_{\max}]$

a.

$$\left. \begin{aligned} S_A &\equiv \sum_{n=1}^{N} \sin\ \alpha_n \\ C_\alpha &\equiv \sum_{n=1}^{N} \cos\ \alpha_n \end{aligned} \right\} \tag{165}$$

b.

$$\left. \begin{aligned} S_{2\alpha} &\equiv \sum_{n=1}^{N} \sin\ 2\alpha_n \\ C_{2\alpha} &\equiv \sum_{n=1}^{N} \cos\ 2\alpha_n \end{aligned} \right\} \tag{166}$$

c. With these definitions,

$$\left. \begin{aligned} \sum_{n=1}^{N} \sin^2\ \alpha_n &= \frac{1}{2}(N - C_{2\alpha}) \\ \sum_{n=1}^{N} \cos^2\ \alpha_n &= \frac{1}{2}(N + C_{2\alpha}) \end{aligned} \right\} \tag{167}$$

2. Roll angle set ß_R contains M points in the closed interval $[R_{\min} R_{\max}]$

a.

$$\left.\begin{aligned} S_R &\equiv \sum_{m=1}^{M} \sin\ R_m \\ C_R &\equiv \sum_{m=1}^{M} \cos\ R_m \end{aligned}\right\} \tag{168}$$

b.

$$\left.\begin{aligned} S_{2R} &\equiv \sum_{m=1}^{M} \sin\ 2R_m \\ C_{2R} &\equiv \sum_{m=1}^{M} \cos\ 2R_m \end{aligned}\right\} \tag{169}$$

c. Using these definitions gives

$$\left.\begin{aligned} \sum_{m=1}^{M} \sin^2\ R_m &= \frac{1}{2}(M - C_{2R}) \\ \sum_{m=1}^{M} \cos^2\ R_m &= \frac{1}{2}(M + C_{2R}) \end{aligned}\right\} \tag{170}$$

Special Experimental Designs

Minimal design D_0: Roll angle set ß_R contains M points uniformly distributed over the closed interval $[-\pi + \Delta R, \pi]$ where the principal value of each angle contained in ß_R occurs only once and $\Delta R = 2\pi/M$.

Minimal design $D_1 \subset D_0$: Pitch angle set ß_α contains N points uniformly distributed over the closed interval $[-\alpha_{\max} \alpha_{\max}]$ where the principal value of each angle contained in ß_α occurs only once unless $\alpha_{\max} = \pi$; $\Delta\alpha = 2\alpha_{\max}/(N-1)$. Roll angle set ß_R is the same as in design D_0.

For D_0 and D_1 designs containing M_D copies of a minimal design, the expressions obtained below are multiplied by M_D.

For design $D_1 \subset D_0$.

1.

$$\left.\begin{aligned} S_A &\equiv \sum_{n=1}^{N} \sin\ \alpha_n = 0 \\ C_\alpha &\equiv \sum_{n=1}^{N} \cos\ \alpha_n = \frac{\sin[N\alpha_{\max}/(N-1)]}{\sin[\alpha_{\max}/(N-1)]} \end{aligned}\right\} \tag{171}$$

2.

$$\left.\begin{aligned} S_{2\alpha} &\equiv \sum_{n=1}^{N} \sin\ 2\alpha_n = 0 \\ C_{2\alpha} &\equiv \sum_{n=1}^{N} \cos\ 2\alpha_n = \frac{\sin[2N\alpha_{\max}/(N-1)]}{\sin[2\alpha_{\max}/(N-1)]} \end{aligned}\right\} \tag{172}$$

The following expressions are evaluated for ß$_R$ containing M points uniformly distributed over the closed interval $[-R_{\max}+\Delta R, R_{\max}]$, where $\Delta R = 2R_{\max}/M$. Evaluation at $R_{\max} = \pi$ for design D_0 yields zero in each case.

1.

$$\left.\begin{aligned} S_R &\equiv \sum_{m=1}^{M} \sin\ R_m = \sin\ R_{\max} = 0 \\ C_R &\equiv \sum_{m=1}^{M} \cos\ R_m = \cot \frac{R_{\max}}{M} \sin\ R_{max} = 0 \end{aligned}\right\} \tag{173}$$

2.

$$\left.\begin{aligned} S_{2R} &\equiv \sum_{m=1}^{M} \sin\ 2R_m = \sin\ 2R_{\max} = 0 \\ C_{2R} &\equiv \sum_{m=1}^{M-1} \cos\ 2R_m = \cot \frac{2R_{\max}}{M} \sin\ 2R_{max} = 0 \end{aligned}\right\} \tag{174}$$

Evaluation of x-Axis Sensor Moment Matrix

Moment matrix $\mathbf{R}_x$, defined in equation (44) and required for computation of variance function $\sigma_v^2(\mathbf{z})$, is now evaluated in general using the approximation in equation (49) showing that $\mathbf{R}_x$ may be expressed in the form of equation (125), as needed for proof of Theorem I. Since $\sigma_v^2(\mathbf{z})$ is independent of parameters b, S, Ω, and A, matrix $\mathbf{R}_x$ is then simplified by using the values given in equations (58) for later evaluation of $\sigma_v^2(\mathbf{z})$. Further simplifications are obtained for designs D, D_0, and/or D_1.

With the values of equations (58), the elements of gradient vector $\boldsymbol{\phi}_{x_c}$ become

$$\left.\begin{aligned} f_{x_b} &= 1 \\ f_{x_S} &= \sin\ \alpha \\ \boldsymbol{\phi}_{x_\Omega} &= -\cos\ \alpha\ \sin\ R \\ \boldsymbol{\phi}_{x_A} &= -\cos\ \alpha\ \cos R \end{aligned}\right\} \tag{175}$$

Element-by-element evaluation proceeds as follows:

1. r_{bb}

General evaluation using equations (58):

$$\left.\begin{aligned} r_{x_{bb}} &= \mathbf{f}_b^{\mathrm{T}} \mathbf{f}_b \\ &= \sum_{k=1}^{K} 1 = K \end{aligned}\right\} \tag{176}$$

Specific evaluation for design D:

$$r_{x_{bb}} = MN \tag{177}$$

2. $r_{bS} = r_{Sb}$

General evaluation using equations (58):

$$r_{x_bS} = \mathbf{f}_{xb}^{\mathrm{T}}\mathbf{f}_{xS} = \sum_{k=1}^{K} f_{x_{Sk}} = \sum_{k=1}^{K} \sin\ \alpha_k \tag{178}$$

Specific evaluation for design D:

$$r_{x_bS} = \sum_{m=1}^{M}\sum_{n=1}^{N} \sin\ \alpha_n = MS_\alpha \tag{179}$$

Specific evaluation for design D_1: $r_{x_bS} = 0$.

3. $r_{b\Omega} = r_{\Omega b}$

General evaluation:

$$r_{x_b\Omega} = \mathbf{f}_{xb}^{\mathrm{T}}\mathbf{f}_{x\Omega} = S_x \sum_{k=1}^{K} \phi_{x_{\Omega k}} = S_x \rho_{x_{b\Omega}} \tag{180}$$

Using equations (58) gives

$$\rho_{x_{b\Omega}} \equiv \sum_{k=1}^{K} \phi_{x_{\Omega k}} = -\sum_{k=1}^{K} \cos\ \alpha_k\ \sin\ R_k \tag{181}$$

Specific evaluation for design D:

$$\rho_{x_{b\Omega}} \equiv -\sum_{m=1}^{M} \sin\ R_m \sum_{n=1}^{N} \cos\ \alpha_n = -S_R C_\alpha \tag{182}$$

Specific evaluation for design D_0:

$$\rho_{x_{b\Omega}} = 0$$

4. $r_{bA} = r_{Ab}$

General evaluation:

$$r_{x_{bA}} = \mathbf{f}_{xb}^{\mathrm{T}}\mathbf{f}_{xA} = S_x w_x \sum_{k=1}^{K} \phi_{x_{Ak}} = S_x w_x \rho_{x_{bA}} \tag{183}$$

Using equations (58) gives

$$\rho_{x_{bA}} \equiv \sum_{k=1}^{K} \phi_{x_{Ak}} = -\sum_{k=1}^{K} \cos\ \alpha_k\ \cos\ R_k \tag{184}$$

Specific evaluation for design D:

$$\rho_{x_{bA}} = -\sum_{n=1}^{N} \cos\ \alpha_n \sum_{m=1}^{M} \cos\ R_m = -C_\alpha C_R \tag{185}$$

Specific evaluation for design D_0:

$$\rho_{x_{bA}} = 0$$

5. r_{SS}

General evaluation:

$$r_{x_{SS}} = \mathbf{f}_{x_S}^{\mathrm{T}}\mathbf{f}_{x_S} \tag{186}$$

Using equations (58) gives

$$r_{x_{SS}} \equiv \sum_{k=1}^{K} f_{x_{Sk}}^2 = \sum_{k=1}^{K} \sin^2 \alpha_k \tag{187}$$

Specific evaluation for designs D and D_0:

$$r_{x_{SS}} = \sum_{m=1}^{M} \sum_{n=1}^{N} \sin^2 \alpha_n = \frac{1}{2}M(N - C_{2\alpha}) \tag{188}$$

6. $r_{S\Omega} = r_{\Omega S}$

General evaluation:

$$r_{x_{S\Omega}} = \mathbf{f}_{x_S}^{\mathrm{T}}\mathbf{f}_{x_\Omega} = S_x \sum_{k=1}^{K} f_{x_{Sk}}\, \boldsymbol{\phi}_{x_{\Omega k}} = S_x \rho_{x_{S\Omega}} \tag{189}$$

Using equations (58) gives

$$\rho_{x_{S\Omega}} \equiv \sum_{k=1}^{K} f_{x_{Sk}}\, \boldsymbol{\phi}_{x_{\Omega k}} = -\sum_{k=1}^{K} \sin\, \alpha_k\, \cos \alpha_k\, \sin\, R_k \tag{190}$$

Specific evaluation for design D:

$$\rho_{x_{S\Omega}} = -\frac{1}{2} \sum_{m=1}^{M} \sin\, R_m \sum_{n=1}^{N} \sin\, 2\alpha_n = -\frac{1}{2} S_R S_{2\alpha} \tag{191}$$

Specific evaluation for design D_0:

$$\rho_{x_{S\Omega}} = 0$$

7. $r_{SA} = r_{AS}$

General evaluation:

$$r_{x_{SA}} = \mathbf{f}_{x_S}^{\mathrm{T}}\mathbf{f}_{x_A} = S_x w_x \sum_{k=1}^{K} f_{x_{Sk}}\, \boldsymbol{\phi}_{x_{Ak}} = S_x w_x \rho_{x_{SA}} \tag{192}$$

Using equations (58) gives

$$\rho_{x_{SA}} \equiv \sum_{k=1}^{K} f_{x_{Sk}}\, \boldsymbol{\phi}_{x_{Ak}} = -\frac{1}{2} \sum_{k=1}^{K} \sin\, 2\alpha_k \cos\, R_k \tag{193}$$

Specific evaluation for design D:

$$\rho_{x_{SA}} = -\frac{1}{2} \sum_{n=1}^{N} \sin\, 2\alpha_n \sum_{m=1}^{M} \cos\, R_m = -\frac{1}{2} S_{2\alpha} C_R \tag{194}$$

Specific evaluation for design D_0:

$$\rho_{x_{SA}} = 0$$

8. $r_{\Omega\Omega}$

General evaluation:

$$r_{x\Omega\Omega} = \mathbf{f}_{x_\Omega}^{\mathrm{T}}\mathbf{f}_{x_\Omega} = S_x^2 \sum_{k=1}^{K} \boldsymbol{\phi}_{x\Omega k}^2 = S_x^2 \rho_{x\Omega\Omega} \tag{195}$$

Using equations (58) gives

$$\rho_{x\Omega\Omega} \equiv \sum_{k=1}^{K} \boldsymbol{\phi}_{x\Omega k}^2 = \sum_{k=1}^{K} \cos^2 \alpha_k \sin^2 R_k \tag{196}$$

Specific evaluation for design D:

$$\rho_{x\Omega\Omega} = \sum_{m=1}^{M} \sin^2 R_m \sum_{n=1}^{N} \cos^2 \alpha_n = \frac{1}{4}(M - C_{2R})(N + C_{2\alpha}) \tag{197}$$

Specific evaluation for design D_0:

$$\rho_{x\Omega\Omega} = \frac{1}{4}M(N + C_{2\alpha}) \tag{198}$$

9. $r_{\Omega A} = r_{A\Omega}$

General evaluation:

$$r_{x\Omega A} = \mathbf{f}_{x_\Omega}^{\mathrm{T}}\mathbf{f}_{xA} = S_x^2 w_x \sum_{k=1}^{K} \boldsymbol{\phi}_{x\Omega k}\boldsymbol{\phi}_{xAk} = S_x^2 w_x \rho_{x\Omega A} \tag{199}$$

Using equations (58) gives

$$\rho_{x\Omega A} \equiv \sum_{k=1}^{K} \boldsymbol{\phi}_{x\Omega k}\boldsymbol{\phi}_{xAk} = \frac{1}{2}\sum_{k=1}^{K} \cos^2 \alpha_k \sin 2R_k \tag{200}$$

Specific evaluation for design D:

$$\rho_{x\Omega A} = \frac{1}{2}\sum_{n=1}^{N} \cos^2 \alpha_n \sum_{m=1}^{M} \sin 2R_m = \frac{1}{4}(N + C_{2\alpha})S_{2R} \tag{201}$$

Specific evaluation for design D_0:

$$\rho_{x\Omega A} = 0$$

10. r_{AA}

General evaluation:

$$r_{xAA} = \mathbf{f}_{x_A}^{\mathrm{T}}\mathbf{f}_{xA} = S_x^2 w_x^2 \sum_{k=1}^{K} \boldsymbol{\phi}_{xAk}^2 = S_x^2 w_x^2 \rho_{xAA} \tag{202}$$

Using equations (58) gives

$$\rho_{x_{AA}} \equiv \sum_{k=1}^{K} \phi_{x_{Ak}}^2 = \sum_{k=1}^{K} \cos^2\,\alpha_k\,\cos^2\,R_k \tag{203}$$

Specific evaluation for design D:

$$\rho_{x_{AA}} = \sum_{n=1}^{N} \cos^2\,\alpha_n \sum_{m=1}^{M} \cos^2\,R_m = \frac{1}{4}(N + C_{2\alpha})(M + C_{2R}) \tag{204}$$

Specific evaluation for design D_0:

$$\rho_{x_{AA}} = \frac{1}{4}M\,(N + C_{2\alpha}) \tag{205}$$

Evaluation of R Matrix for *y*- and *z*-Axis Sensors

By using the values of equations (58), the simplified elements of gradient vector $\boldsymbol{\phi}_{yc}$ for the y-axis sensor are given by

$$\left.\begin{aligned} f_{y_b} &= 1 \\ f_{y_S} &= -\cos\,\alpha\,\sin\,R = \phi_{x_\Omega} \\ \phi_{y_\Omega} &= -\cos\,\alpha\,\cos\,R = \phi_{x_A} \\ \phi_{y_A} &= \sin\,\alpha = f_{x_S} \end{aligned}\right\} \tag{206}$$

and the elements of gradient vector $\boldsymbol{\phi}_{z_c}$ for the z-axis sensor are given by

$$\left.\begin{aligned} f_{z_b} &= 1 \\ f_{z_S} &= -\cos\,\alpha\,\cos\,R = \phi_{x_A} \\ \phi_{z_\Omega} &= \sin\,\alpha = f_{x_S} \\ \phi_{z_A} &= -\cos\,\alpha\,\sin\,R = \phi_{x_\Omega} \end{aligned}\right\} \tag{207}$$

Equation sets (175), (206), and (207) show that the elements of vectors $\boldsymbol{\phi}_{y_c}$ and $\boldsymbol{\phi}_{z_c}$ are permutations of vector $\boldsymbol{\phi}_{x_c}$. Since matrices $\mathbf{P}_y$ and $\mathbf{P}_z$ are obtained from vectors $\boldsymbol{\phi}_{y_c}$ and $\boldsymbol{\phi}_{z_c}$, their rows and columns are permutations of matrix $\mathbf{P}_x$, and are the same permutations as those of vectors $\boldsymbol{\phi}_{y_c}$ and $\boldsymbol{\phi}_{z_c}$, respectively, relative to vector $\boldsymbol{\phi}_{x_c}$. Therefore, it follows from equation (127) that quadratic forms $q_{R_x} = q_{R_y} = q_{R_z}$ and thus variance functions $\boldsymbol{\phi}_{v_x}(\mathbf{z}) = \sigma_{v_y}(\mathbf{z}) = \sigma_{v_z}(\mathbf{z})$.

$\mathbf{R}_y$ Matrix for *y*-Axis Sensor

The elements of gradient matrix $\mathbf{R}_y$ are obtained from equations (206) and (176) to (205) in terms of $\mathbf{R}_x$ as follows:

$$\left.\begin{aligned} r_{y_{bb}} &= r_{x_{bb}} \\ r_{y_{bS}} &= \rho_{x_{b\Omega}} \\ \rho_{y_{b\Omega}} &= \rho_{x_{bA}} \\ \rho_{y_{bA}} &= r_{x_{bS}} \end{aligned}\right\} \tag{208}$$

Similarly

$$\left.\begin{aligned} r_{y_{SS}} &= \rho_{x_{\Omega\Omega}} \\ \rho_{y_{S\Omega}} &= \rho_{x_{\Omega A}} \\ \rho_{y_{SA}} &= \rho_{x_{S\Omega}} \end{aligned}\right\} \tag{209}$$

and

$$\left.\begin{aligned} \rho_{y_{\Omega\Omega}} &= \rho_{x_{AA}} \\ \rho_{y_{\Omega A}} &= \rho_{x_{SA}} \\ \rho_{y_{AA}} &= r_{x_{SS}} \end{aligned}\right\} \tag{210}$$

$\mathbf{R}_z$ Matrix for z-Axis Sensor

The elements of gradient matrix $\mathbf{R}_z$ are obtained from equations (207) and (176) to (205) in terms of $\mathbf{R}_x$ as follows:

$$\left.\begin{aligned} r_{z_{bb}} &= r_{x_{bb}} \\ r_{z_{bS}} &= \rho_{x_{bA}} \\ \rho_{z_{b\Omega}} &= r_{x_{bS}} \\ \rho_{z_{bA}} &= \rho_{x_{b\Omega}} \end{aligned}\right\} \tag{211}$$

Similarly

$$\left.\begin{aligned} r_{z_{SS}} &= \rho_{x_{AA}} \\ \rho_{z_{S\Omega}} &= \rho_{x_{SA}} \\ \rho_{z_{SA}} &= \rho_{x_{\Omega A}} \end{aligned}\right\} \tag{212}$$

and

$$\left.\begin{aligned} \rho_{z_{\Omega\Omega}} &= r_{x_{SS}} \\ \rho_{z_{\Omega A}} &= \rho_{x_{S\Omega}} \\ \rho_{z_{AA}} &= \rho_{x_{\Omega\Omega}} \end{aligned}\right\} \tag{213}$$

Appendix E

Evaluation of Figure of Merit of Experimental Design

The design figure of merit V for experimental design D is given by equation (53). The numerator of equation (53) contains integrals of cross products of the elements of gradient vector $\boldsymbol{\phi}_c$, which are now evaluated by using the parameter values of equations (58).

The design figure of merit for the x-axis sensor is obtained from equations (21) to (26) and (58) as follows:

1. $f_{x_b} f_{x_b} = 1$

$$I_{x_{bb}} = \int_{\alpha_{\min}}^{\alpha_{\max}} \int_{R_{\min}}^{R_{\max}} dR\, d\alpha = \Delta\alpha\, \Delta R \tag{214}$$

2. $f_{x_b} f_{x_S} = \sin\,\alpha$

$$I_{x_{bS}} = \int_{\alpha_{\min}}^{\alpha_{\max}} \int_{R_{\min}}^{R_{\max}} \sin\,\alpha\, dR\, d\alpha = -\Delta R\, \Delta\,\cos\,\alpha \tag{215}$$

3. $f_{x_b} \boldsymbol{\phi}_{x_\Omega} = -\cos\,\alpha\,\sin\,R$

$$I_{x_{b\Omega}} = -\int_{\alpha_{\min}}^{\alpha_{\max}} \int_{R_{\min}}^{R_{\max}} \cos\,\alpha\,\sin R\, dR\, d\alpha = \Delta\,\sin\alpha\,\Delta\,\cos\,R \tag{216}$$

4. $f_{x_b} \boldsymbol{\phi}_{x_A} = -\cos\,\alpha\,\cos\,R$

$$I_{x_{bA}} = -\int_{\alpha_{\min}}^{\alpha_{\max}} \int_{R_{\min}}^{R_{\max}} \cos\,\alpha\,\cos R\, dR\, d\alpha = -\Delta\,\sin\alpha\,\Delta\,\sin R \tag{217}$$

5. $f_{x_S} f_{x_S} = \sin^2\,\alpha$

$$I_{x_{SS}} = \int_{\alpha_{\min}}^{\alpha_{\max}} \int_{R_{\min}}^{R_{\max}} \sin^2\alpha\, dR\, d\alpha = \frac{1}{2}\Delta\, R \left(\Delta\alpha - \frac{1}{2}\Delta\,\sin 2\alpha\right) dR\, d\alpha \tag{218}$$

6. $f_{x_S} \boldsymbol{\phi}_{x_\Omega} = -\frac{1}{2}\sin\,2\alpha\,\sin\,R$

$$I_{x_{S\Omega}} = \frac{1}{2}\int_{\alpha_{\min}}^{\alpha_{\max}} \int_{R_{\min}}^{R_{\max}} \sin\,2\alpha\,\sin\,R\, dR\, d\alpha = -\frac{1}{4}\Delta\,\cos\,2\alpha\,\Delta\,\cos\,R \tag{219}$$

7. $f_{x_S} \boldsymbol{\phi}_{x_A} = -\frac{1}{2}\sin\,2\alpha\,\cos\,R$

$$I_{x_{SA}} = -\frac{1}{2}\int_{\alpha_{\min}}^{\alpha_{\max}} \int_{R_{\min}}^{R_{\max}} \sin\,2\alpha\,\cos\,R\, dR\, d\alpha = \frac{1}{2}\Delta\,\cos\,2\alpha\,\Delta\,\sin\,R \tag{220}$$

8. $\boldsymbol{\phi}_{x_\Omega} \boldsymbol{\phi}_{x_\Omega} = \cos^2\alpha\,\sin^2 R$

$$I_{x_{\Omega\Omega}} = \int_{\alpha_{\min}}^{\alpha_{\max}} \int_{R_{\min}}^{R_{\max}} \cos^2\,\alpha\,\sin^2\,R\, dR\, d\alpha = \frac{1}{4}\left(\Delta\alpha + \frac{1}{2}\Delta\,\sin\,2\alpha\right)\left(\Delta R - \frac{1}{2}\Delta\,\sin\,2R\right) \tag{221}$$

9. $\boldsymbol{\phi}_{x_\Omega}\boldsymbol{\phi}_{x_A} = \dfrac{1}{2}\cos^2\,\alpha\,\sin\,2R$

$$I_{x_{\Omega A}} = \frac{1}{2}\int_{\alpha_{\min}}^{\alpha_{\max}}\int_{R_{\min}}^{R_{\max}} \cos^2\,\alpha\,\sin 2R\,dR\,d\alpha = \frac{1}{8}\left(\Delta\alpha + \frac{1}{2}\Delta\,\sin\,2\alpha\right)(\Delta\,\cos\,2R) \qquad (222)$$

10. $\boldsymbol{\phi}_{x_A}\boldsymbol{\phi}_{x_A} = \cos^2\alpha\,\cos^2 R$

$$I_{x_{AA}} = \int_{\alpha_{\min}}^{\alpha_{\max}}\int_{R_{\min}}^{R_{\max}} \cos^2\,\alpha\,\cos^2\,R\,dR\,d\alpha = \frac{1}{4}\left(\Delta\alpha + \frac{1}{2}\Delta\,\sin\,2\alpha\right)\left(\Delta R + \frac{1}{2}\Delta\,\sin\,2R\right) \qquad (223)$$

where

$$\left.\begin{aligned}\Delta\alpha &= \alpha_{\max} - \alpha_{\min}\\ \Delta R &= R_{\max} - R_{\min}\end{aligned}\right\} \qquad (224)$$

$$\left.\begin{aligned}\Delta\,\sin\,\alpha &= \sin\,\alpha_{\max} - \sin\,\alpha_{\min}\\ \Delta\,\sin\,R &= \sin\,R_{\max} - \sin\,R_{\min}\end{aligned}\right\} \qquad (225)$$

and

$$\left.\begin{aligned}\Delta\,\sin\,2\alpha &= \sin\,2\alpha_{\max} - \sin\,2\alpha_{\min}\\ \Delta\,\sin\,2R &= \sin\,2R_{\max} - \sin\,2R_{\min}\end{aligned}\right\} \qquad (226)$$

Similar definitions apply for $\Delta\,\cos\,\alpha$, $\Delta\,\cos\,R$, $\Delta\,\cos\,2\alpha$, and $\Delta\,\cos\,2R$.

Define the following matrix where subscript x is omitted:

$$\mathbf{I}_\phi = \begin{bmatrix} I_{bb} & I_{bS} & I_{b\Omega} & I_{bA} \\ I_{bS} & I_{SS} & I_{S\Omega} & I_{SA} \\ I_{b\Omega} & I_{S\Omega} & I_{\Omega\Omega} & I_{\Omega A} \\ I_{bA} & I_{SA} & I_{\Omega A} & I_{AA} \end{bmatrix} \qquad (227)$$

It follows that

$$V_N \equiv \int_{\Im} q_R(\mathbf{z})\,d\mathbf{x} = \int_{\alpha_{\min}}^{\alpha_{\max}}\int_{R_{\min}}^{R_{\max}} \boldsymbol{\phi}_c\,\mathbf{P}^{-1}\,\boldsymbol{\phi}_c^{\mathrm{T}}\,dR\,d\alpha \;= \sum_{i=1}^{4}\sum_{j=1}^{4} \mathbf{P}_{ij}^{-1}\,\mathbf{I}_{\phi_{ij}} \qquad (228)$$

The figure-of-merit expression follows from equations (213), (214), and (228) as

$$V = \frac{MNV_N}{I_{bb}} \qquad (229)$$

The final expression applies to x-, y-, and z-axis sensors.

References

1. Finley, T.; and Tcheng, P.: Model Attitude Measurements at NASA Langley Research Center. AIAA-92-0763, Jan. 1992.

2. Tripp, John S.; Wong, Douglas T.; Finley, Tom D.; and Tcheng, Ping: An Improved Calibration Technique for Wind Tunnel Model Attitude Sensors. *Proceedings of the 39th International Instrumentation Symposium*, ISA, 1993, p. 89.

3. Tripp, John S.; Hare, David A.; and Tcheng, Ping: *High-Precision Buffer Circuit for Suppression of Regenerative Oscillation*. NASA TM-4658, 1995.

4. Tcheng, Ping; Tripp, John S.; and Finley, Tom D.: *Effects of Yaw and Pitch Motion on Model Attitude Measurements*. NASA TM-4641, 1995.

5. Tripp, John S.; and Tcheng, Ping: *Uncertainty Analysis of Instrument Calibration and Application*. NASA/TP-1999-209545, 1999.

6. Brand, Louis: Advanced Calculus. John Wiley & Sons, Inc., 1955.

7. Box, G. E. P.: A Basis for the Selection of a Response Surface Design. *J. American Statist. Assoc.*, vol. 54, Sept. 1959, pp. 622–654.

8. Coleman, Hugh W.; and Steele, W. Glenn, Jr.: *Experimentation and Uncertainty Analysis for Engineers*. John Wiley & Sons, 1989.

Table 1. Mean Normalized Standard Deviation Plotted in Figures 2 to 5

$[M = 64; N = 33]$

1	2	3	4	5	6	7	8	9
	Figure 2(a)	Figure 2(b)	Figure 2(c)	Figure 2(d)	Figure 3 (top)	Figure 3 (bottom)	Figure 4	Figure 5
Experimental design	D_1	D_1	D_1	D_1	D_0 (a)	D_0 (b)	D_0 (c)	D_1 (d)
α calibration range	$-30°$ to $30°$	$-45°$ to $45°$	$-90°$ to $90°$	$-180°$ to $180°$	$-30°$ to $30°$	$-30°$ to $30°$	$-30°$ to $30°$	$-30°$ to $30°$
$V^{1/2}$	1.989	1.993	2.008	1.993	2.127	1.937	1.941	1.989
α usage range		$-30°$ to $30°$	$-30°$ to $30°$	$-30°$ to $30°$	$-10°$ to $10°$	$-10°$ to $10°$	$-10°$ to $10°$	
$V_R^{1/2}$		1.927	2.222	2.174	1.811	1.834	1.912	

[a] α points concentrated between $-10°$ and $10°$.

[b] α points concentrated between $-30°$ to $-20°$ and $20°$ to $30°$.

[c] α points concentrated at $-30°$ and $30°$.

[d] Roll repeated at 180°

Table 2. Summary of Statistical Parameters of Predicted Sensor Calibration Outputs

Figure	α range	Number of points	σ_E $\times 10^4$	σ_{bias} $\times 10^4$	σ_{prec} $\times 10^4$	T_{bias}	$(F_{\text{bias}})_{95}$	σ_b $\times 10^4$	σ_S $\times 10^4$	T_b	T_S	$(F_{bS})_{95}$	Remarks
22	−36° to 36°	325	1.60	0.431	1.54	0.407	1.33	1.69	0.347	5.82	0.245	1.35	1-axis without roll, 6 replications, no temperature correlation[a,b]
24	−180° to 180°	325	3.17	2.62	1.79	11.0	1.23	0.955	0.622	0.124	0.060	1.24	1-axis without roll, 6 replications, no temperature correlation
26		4	2.84	2.20	1.79	30.0	4.35	0.940	0.698	0.052	0.029	4.75	Tumble calibration, 1-axis without roll, 6 replications, no temperature correlation
28(a)	−30° to 30°	365	7.76	3.54	6.90	1.33	1.15	41.0	123	102	919	2.22	1-axis with roll, 6 replications, sensor 1, no temperature correlation
28(b)	−30° to 30°	365	3.87	3.54	1.56	26.2	1.15	24.0	8.22	44.0	5.14	2.22	1-axis with roll, 6 replications, sensor 1
34	−30° to 30°	365	16.6	2.45	1.64	0.113	1.15	281	145	5850	1570	2.22	1-axis with roll, 6 replications, sensor 2[c]
35	−30° to 30°	53	4.27	3.97	1.54	36.2	1.40	9.35	3.96	5.01	0.899	2.24	Fractional design, 1-axis with roll, 6 replications, sensor 1
36	−30° to 30°	365	3.89										Standard error using figure 35 coefficient with figure 28(a) data
37	−180° to 180°	325	4.89	4.71	1.31	39.4	1.16	13.4	4.70	7.66	0.944	2.61	1-axis with roll, 4 replications, sensor 1
42	−180° to 180°	325	14.2	4.17	13.5	0.289	1.16	170	201	717	1000	2.61	1-axis with roll, 6 replications, sensor 2
44(a)	−90° to 90°	247	4.34	4.10	1.42	42.1	1.17	12.5	17.5	9.08	17.8	2.22	3-axis, 6 replications, x-axis
44(b)	−90° to 90°	247	4.44	4.17	1.54	37.3	1.17	15.2	5.79	12.8	1.84	2.22	3-axis, 6 replications, y-axis
44(c)	−90° to 90°	247	3.55	3.11	1.71	16.8	1.17	8.10	22.0	6.36	46.9	2.22	3-axis, 6 replications, z-axis
47(a)	−180° to 180°	481	4.09	3.72	1.71	23.9	1.12	14.7	33.2	15.0	76.7	2.22	3-axis, 6 replications, x-axis
47(b)	−180° to 180°	481	5.23	5.08	1.23	85.9	1.12	8.96	8.96	2.98	2.98	2.22	3-axis, 6 replications, y-axis
47(c)	−180° to 180°	481	4.79	4.28	2.15	20.0	1.12	23.2	33.0	27.0	54.6	2.22	3-axis, 6 replications, z-axis

[a]Standard errors are shown in degrees.

[b]Calibrations are temperature corrected unless otherwise indicated.

[c]All sensors are AOA instrument grade quality except sensor 2.

Table 2. Concluded

Figure	α range	Number of points	$\sigma_E \times 10^4$	$\sigma_{\rm bias} \times 10^4$	$\sigma_{\rm prec} \times 10^4$	$T_{\rm bias}$	$(F_{\rm bias})_{95}$	$\sigma_b \times 10^4$	$\sigma_S \times 10^4$	T_b	T_S	$(F_{bS})_{95}$	Remarks
50		6	4.33	4.06	1.70	85.0	3.32	1.29	3.15	0.037	0.223	3.11	Tumble calibration, 3-axis, 6 replications, x-axis
		6	1.97	1.50	1.33	19.1	3.32	1.76	1.48	0.435	0.305	3.11	Tumble calibration, 3-axis, 6 replications, y-axis
		6	2.79	1.34	2.50	4.28	3.32	3.26	4.60	1.87	3.72	3.11	Tumble calibration, 3-axis, 6 replications, z-axis
53	$-180°$ to $180°$	73	4.12	3.78	1.65	27.3	1.33	5.61	12.3	2.03	9.73	1.59	Fractional design, 3-axis, 6 replications, x-axis
	$-180°$ to $180°$	73	5.64	5.51	1.23	104	1.33	3.74	3.34	0.43	0.34	1.59	Fractional design, 3-axis, 6 replications, y-axis
	$-180°$ to $180°$	73	4.79	4.23	2.24	18.5	1.33	8.53	1.35	3.52	8.89	1.59	Fractional design, 3-axis, 6 replications, z-axis
54	$-180°$ to $180°$	481	4.10										Standard error using figure 53 coefficient with figure 47(a) data, x-axis
	$-180°$ to $180°$	481	5.28										Standard error using figure 53 coefficient with figure 47(b) data, y-axis
	$-180°$ to $180°$	481	4.82										Standard error using figure 53 coefficient with figure 47(c) data, z-axis

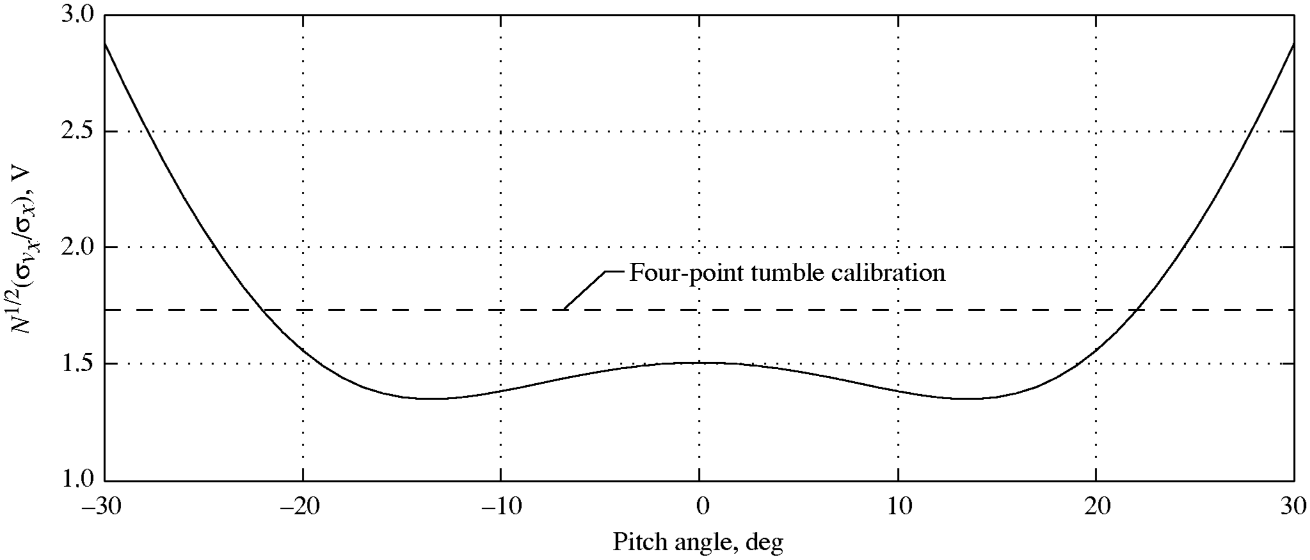

(a) Calibrated from $-30°$ to $30°$.

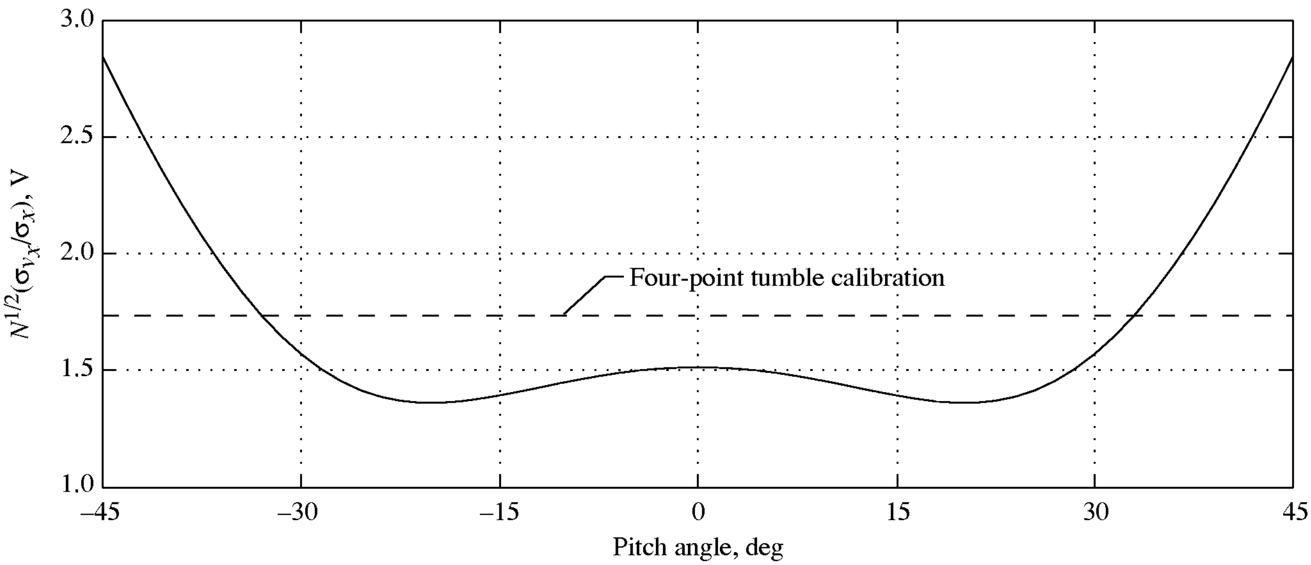

(b) Calibrated from $-45°$ to $45°$.

Figure 1. Normalized standard deviation of predicted output of single-axis AOA sensor without roll.

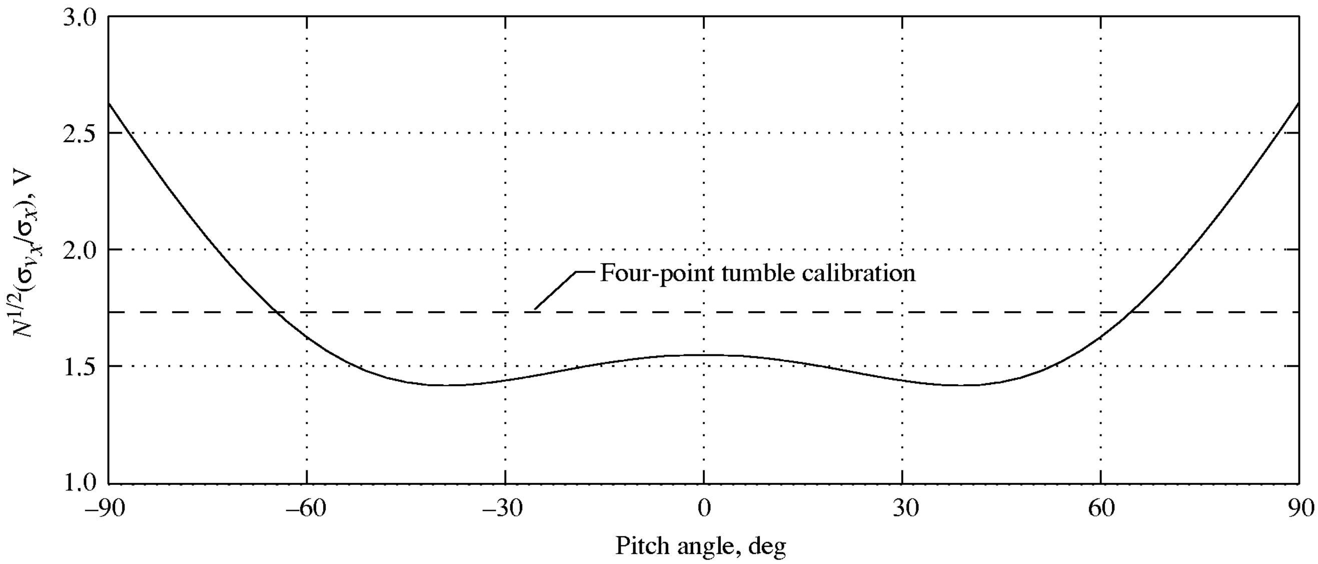

(c) Calibrated from $-90°$ to $90°$.

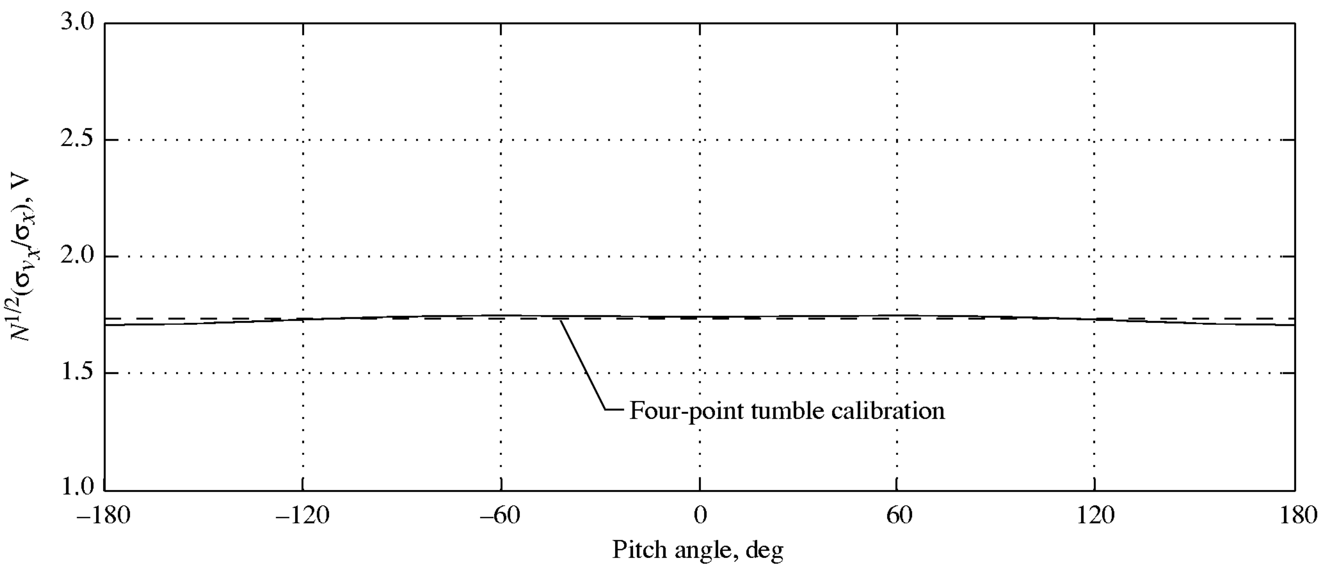

(d) Calibrated from $-180°$ to $180°$.

Figure 1. Concluded.

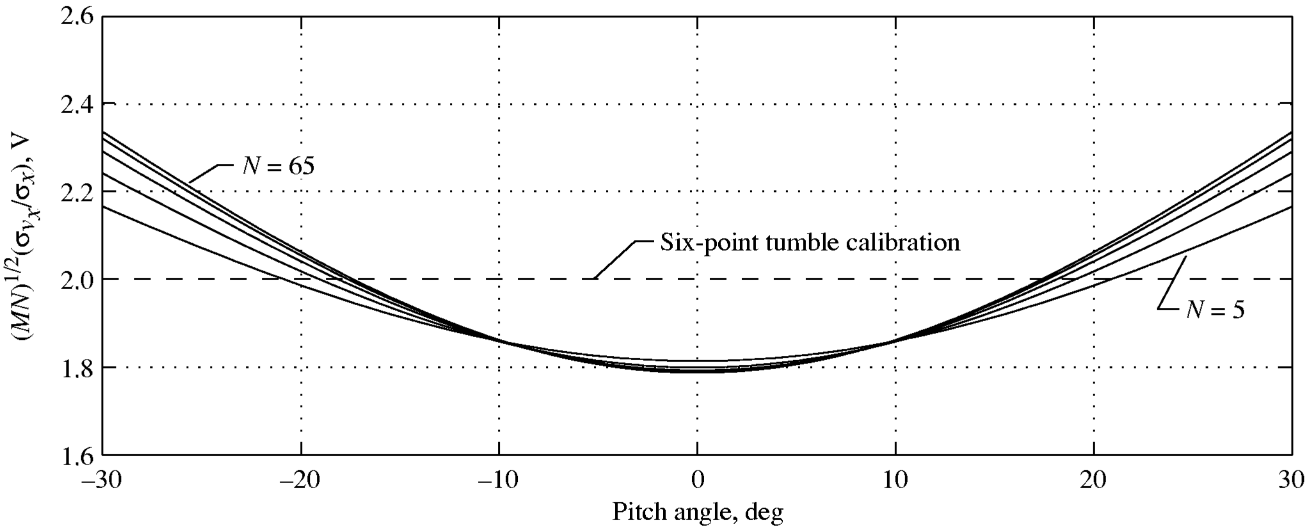

(a) Calibrated from $-30°$ to $30°$.

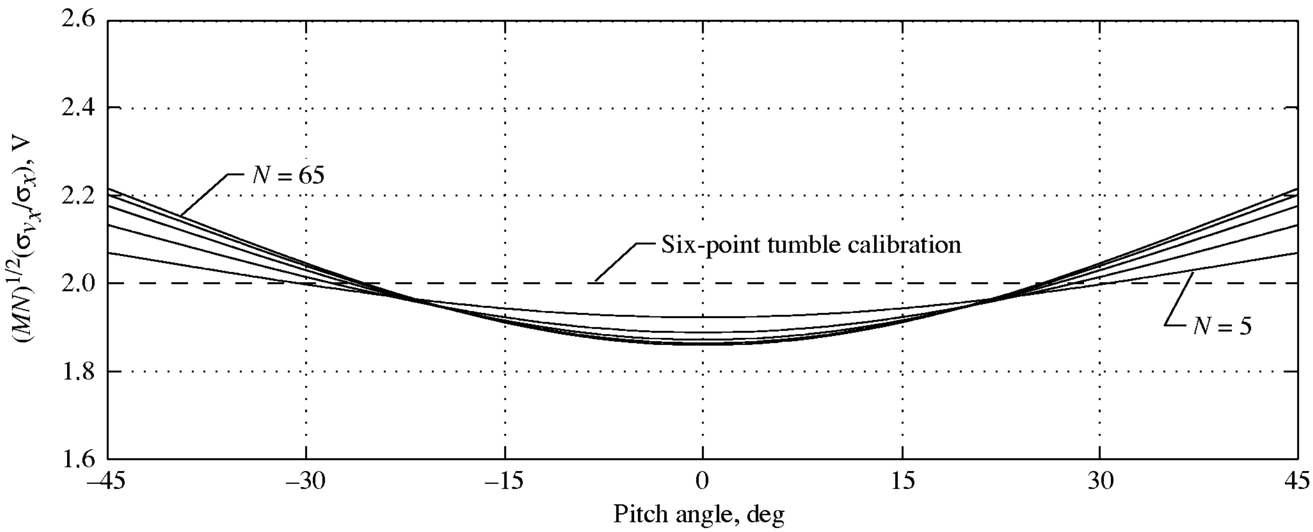

(b) Calibrated from $-45°$ to $45°$.

Figure 2. Normalized standard deviation of predicted output of single-axis AOA sensor with roll.

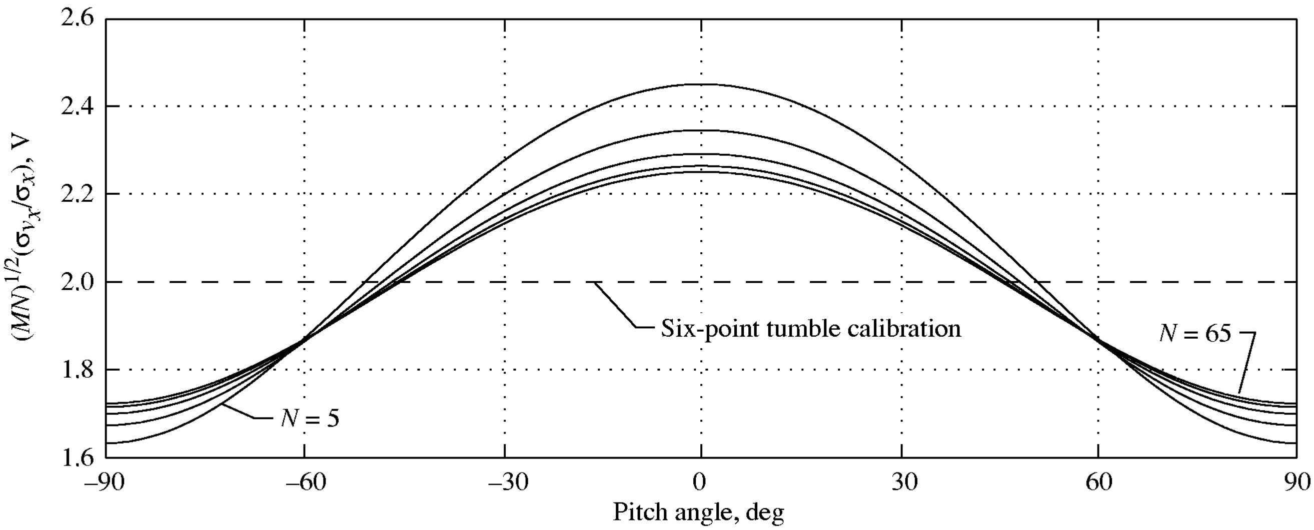

(c) Calibrated from −90° to 90°.

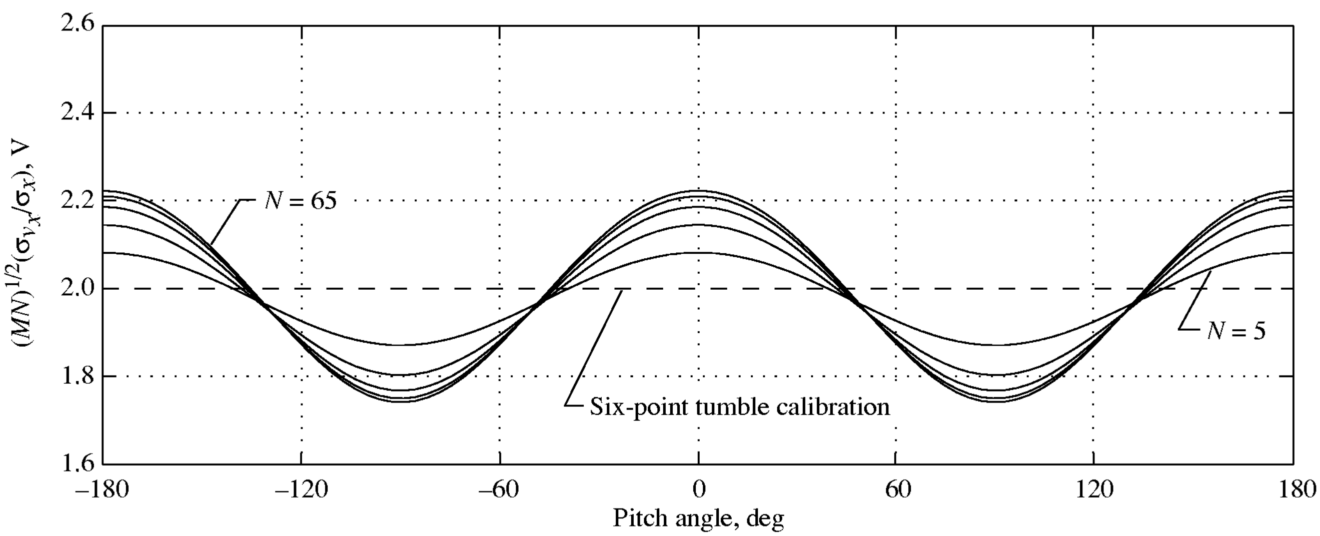

(d) Calibrated from −180° to 180°.

Figure 2. Concluded.

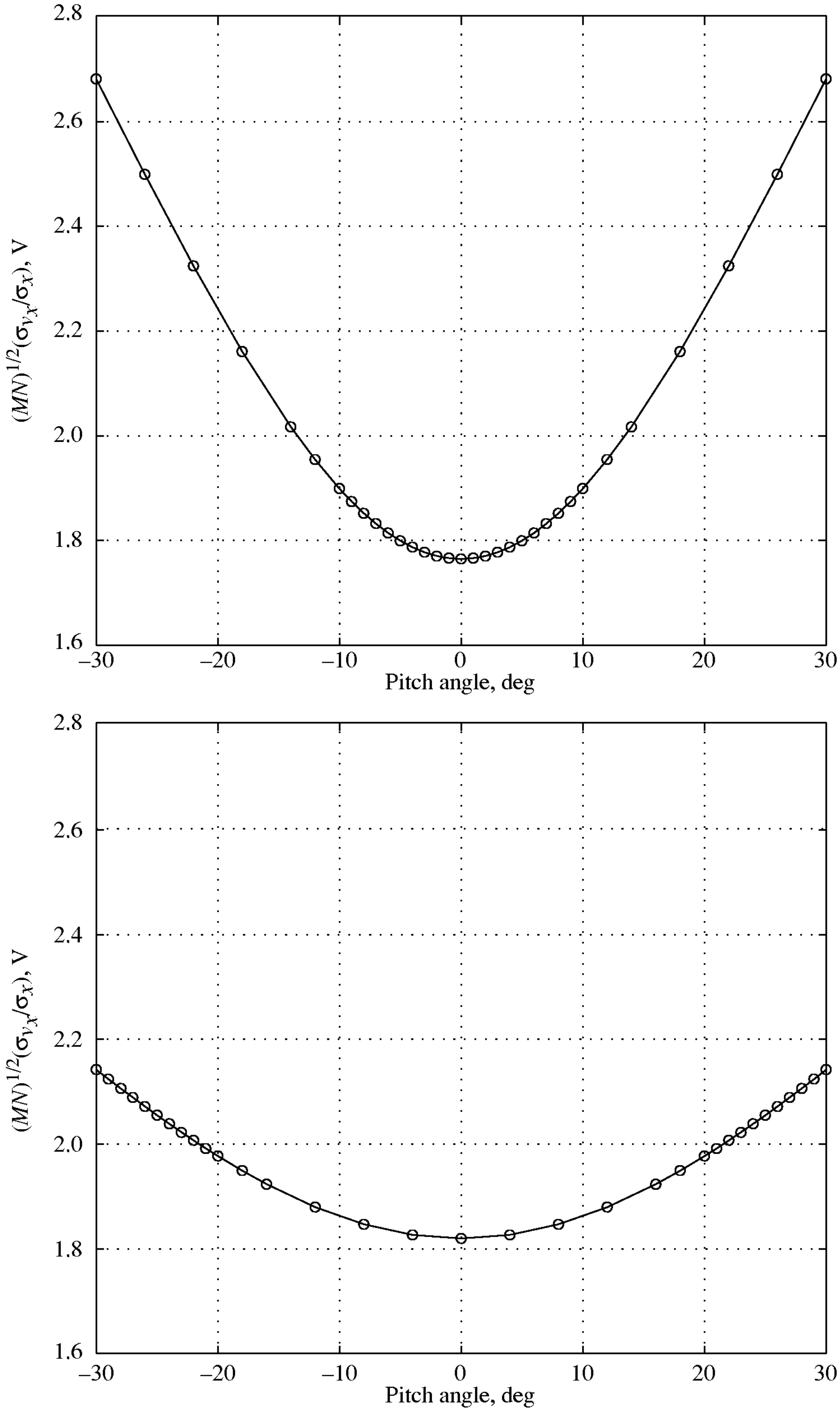

Figure 3. Normalized standard deviation of predicted output of single-axis AOA sensor with roll for calibration points unequally spaced from $-30°$ to $30°$.

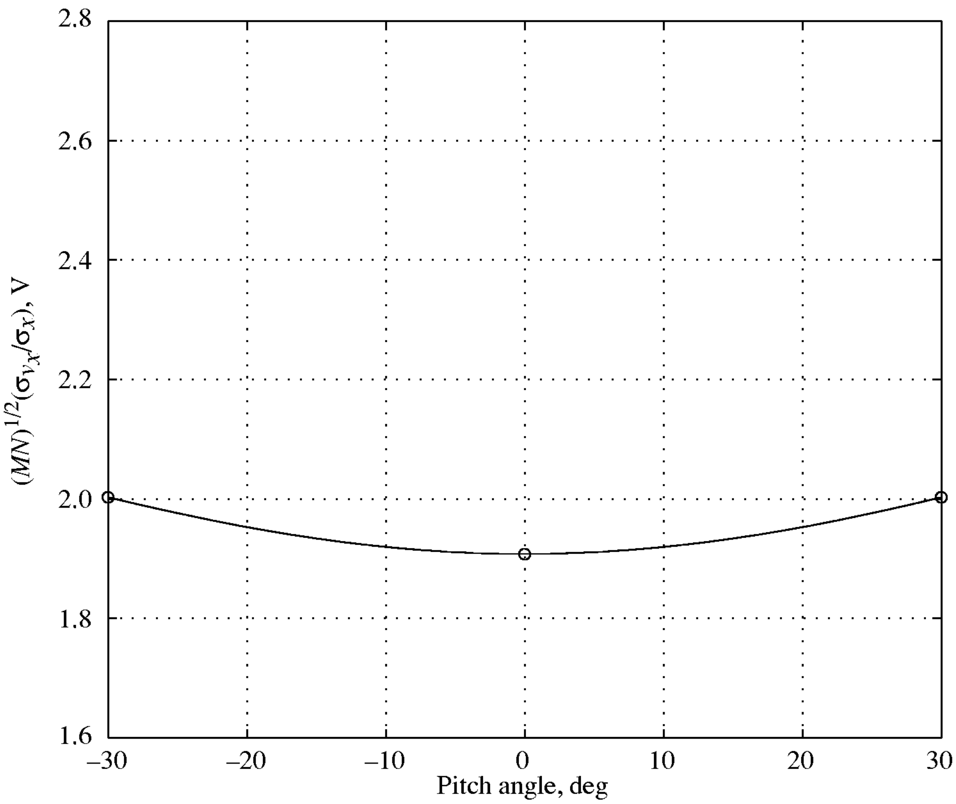

Figure 4. Normalized standard deviation of predicted output of single-axis AOA sensor with roll for calibration repeated at end points (±30°) and once at 0°.

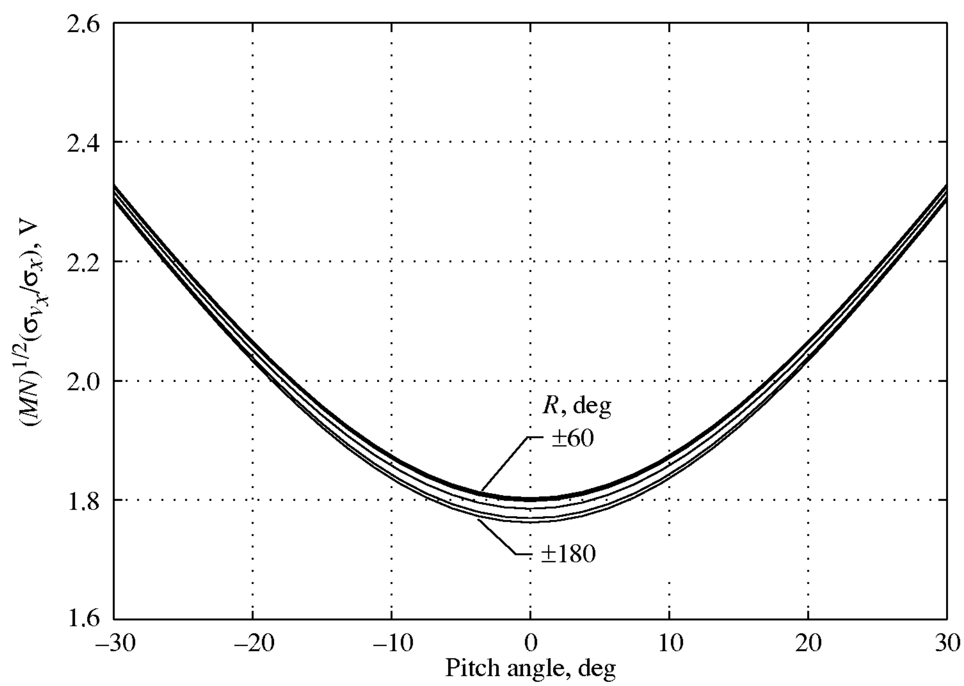

Figure 5. Normalized standard deviation of predicted output of single-axis AOA sensor with roll.

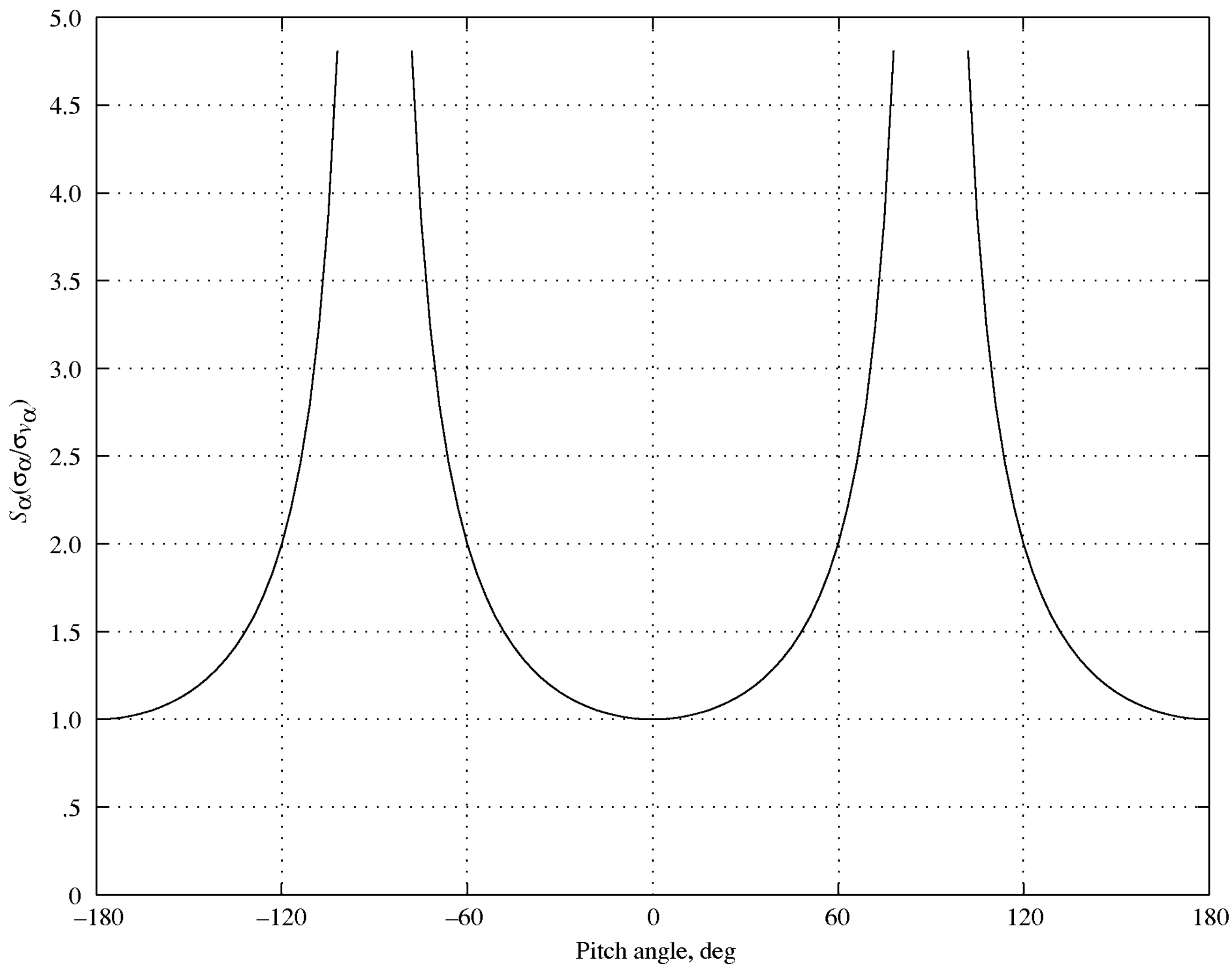

Figure 6. Normalized standard deviation of inferred pitch angle of single-axis AOA sensor without roll for $\phi_\alpha = 0°$.

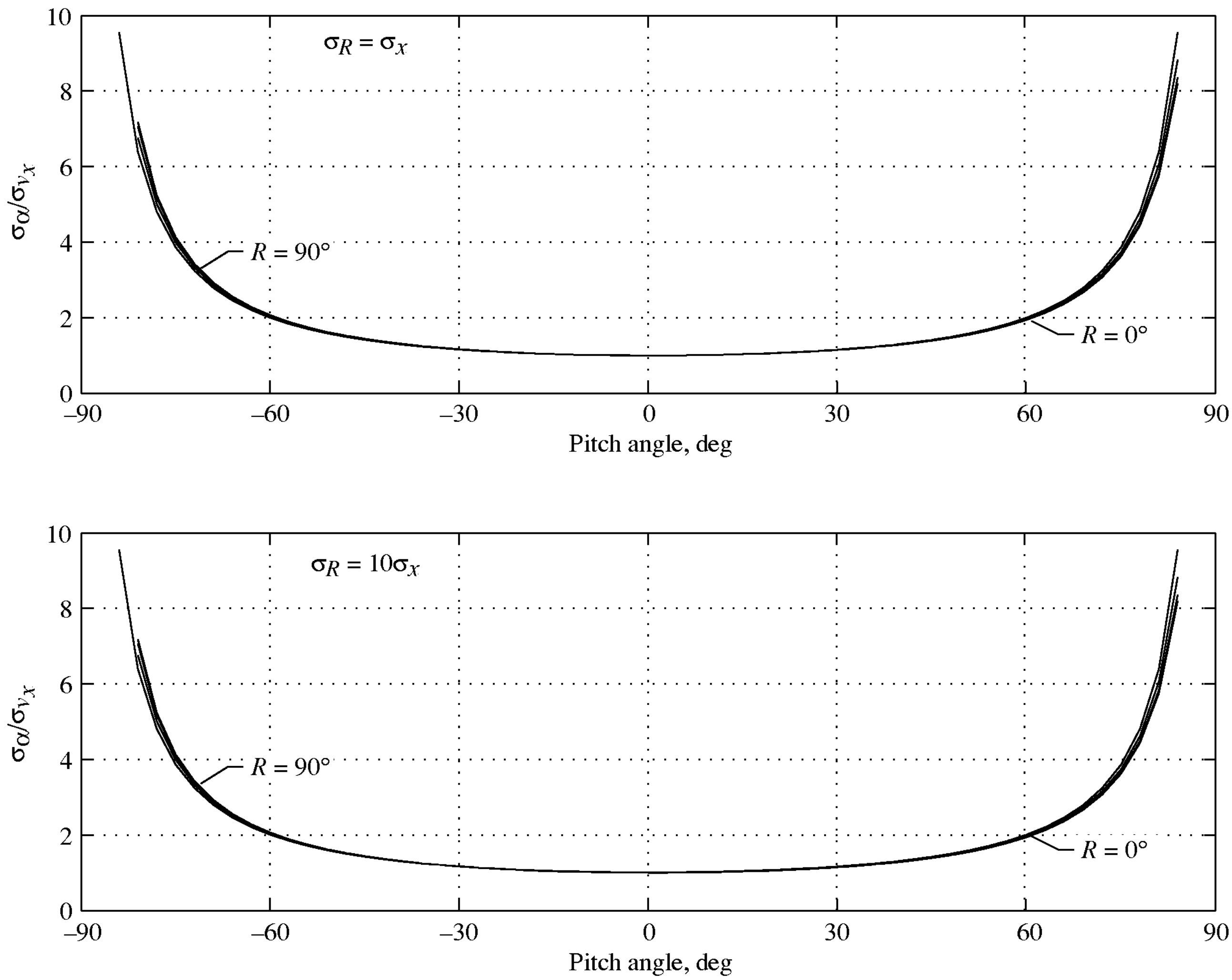

Figure 7. Normalized standard deviation of inferred pitch angle of single-axis AOA sensor with independent roll measurements for $\Omega_x = 1°$ and $A_x = 90°$.

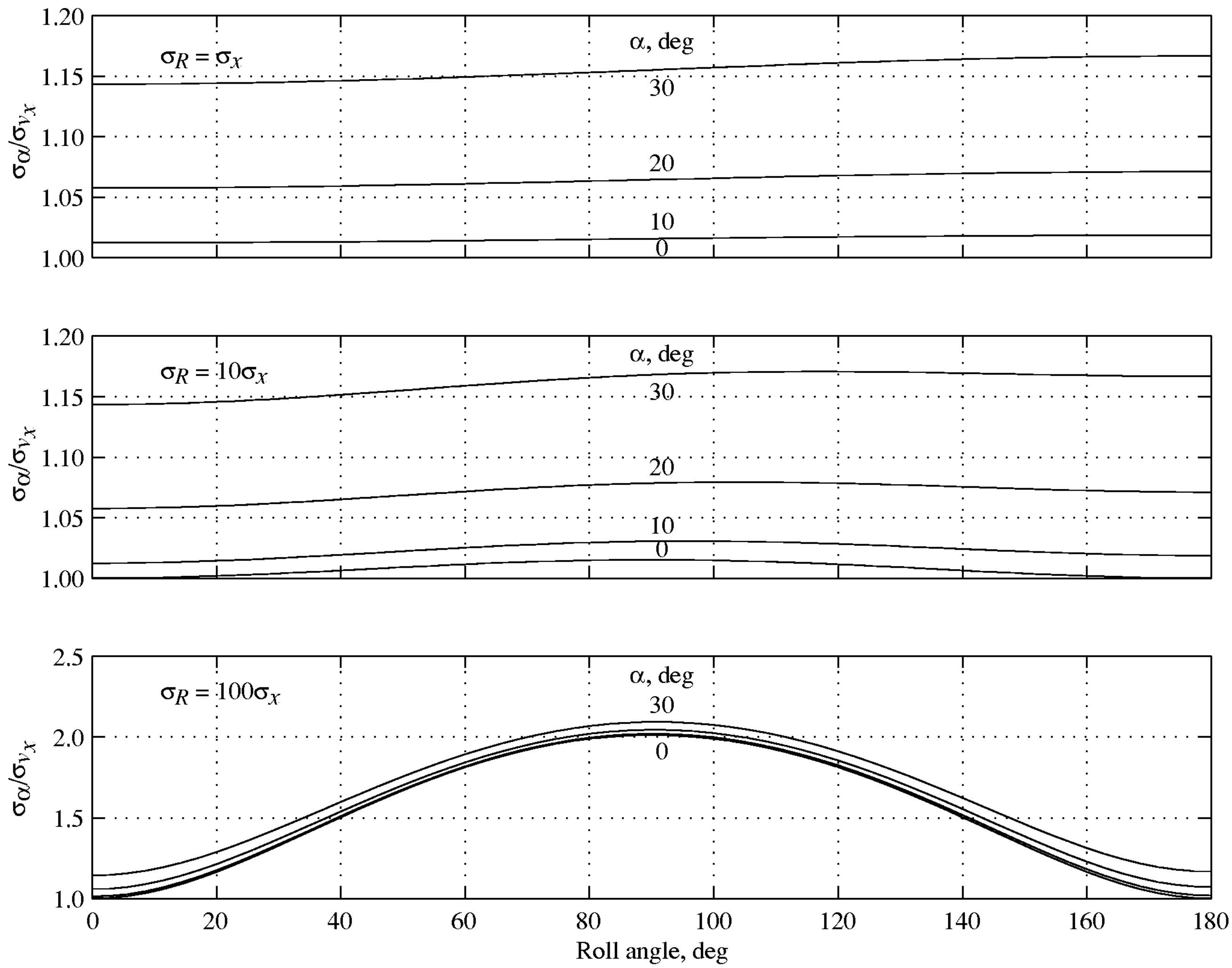

Figure 8. Normalized standard deviation of inferred pitch angle versus roll angle of single-axis AOA sensor with independent roll measurements for $\Omega_x = 1°$ and $A_x = 90°$.

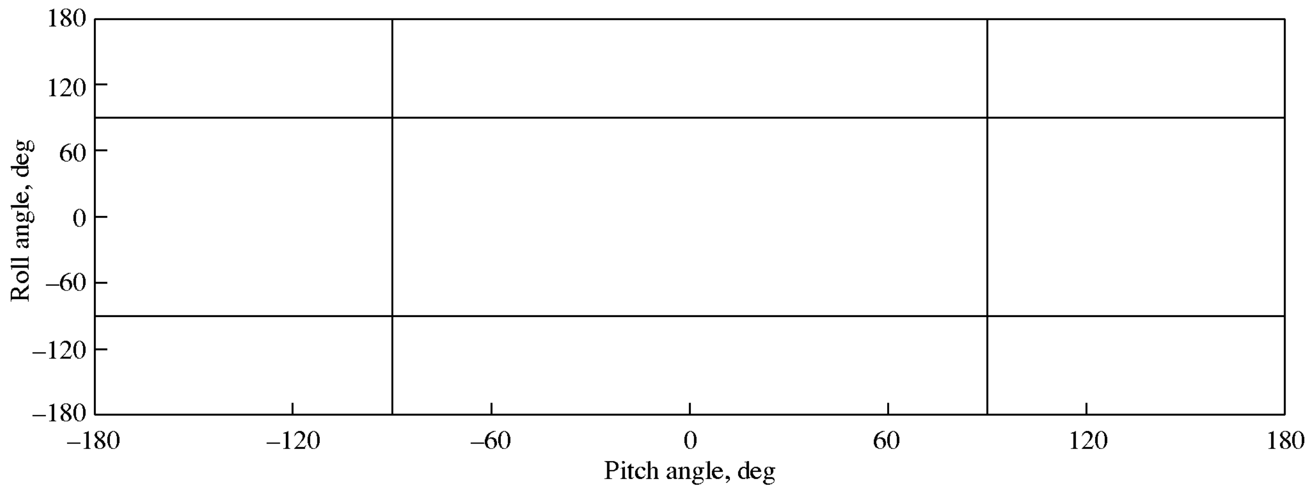

(a) $\Omega = 0.1°$; $A_x = 20°$; $A_y = 90°$.

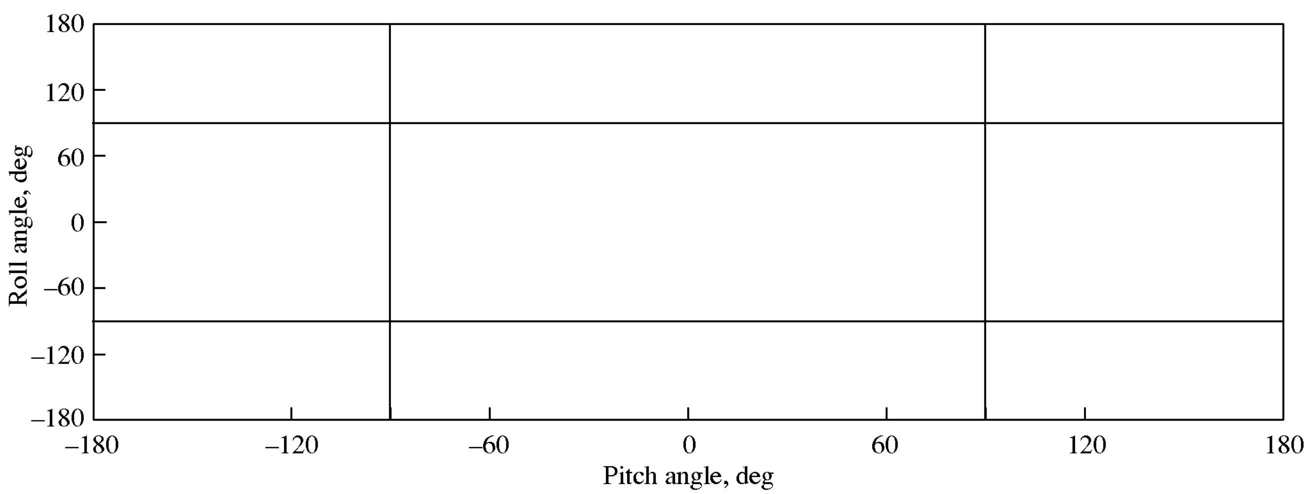

(b) $\Omega = 1°$; $A_x = 20°$; $A_y = 90°$.

Figure 9. Singularity loci of Jacobian matrix $\mathbf{F}_z$ of x-y axis AOA eensor.

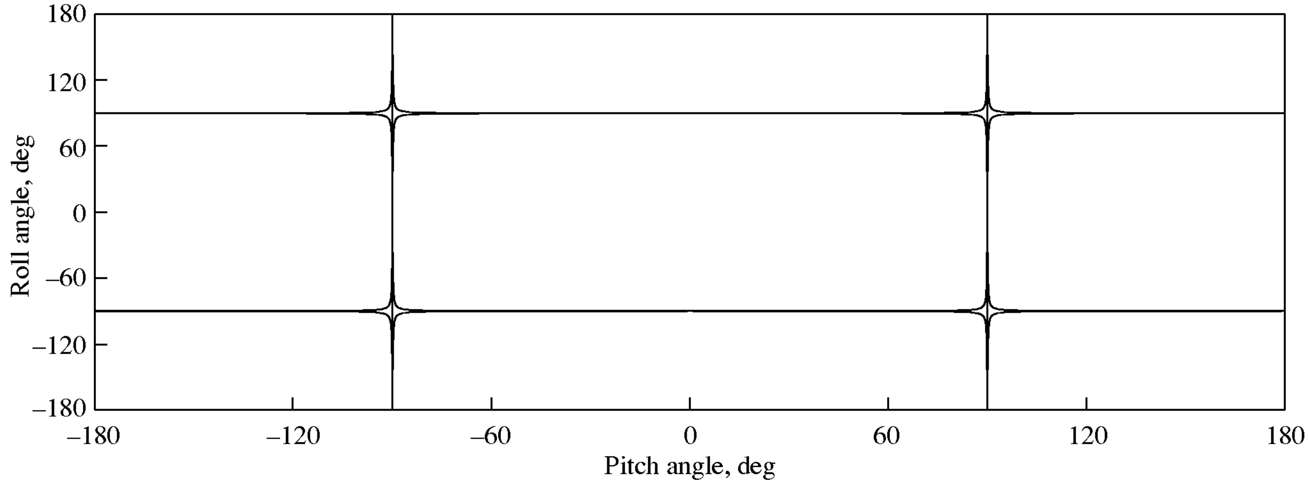

(c) $\Omega = 0.1°$; $A_x = 90°$; $A_y = 90°$.

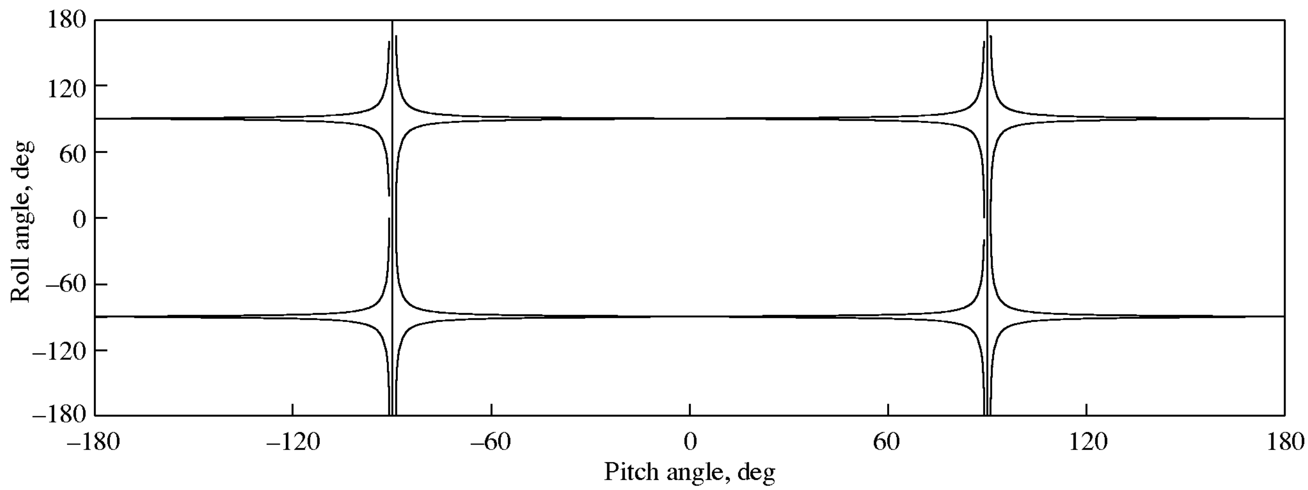

(d) $\Omega = 1°$; $A_x = 90°$; $A_y = 90°$.

Figure 9. Concluded.

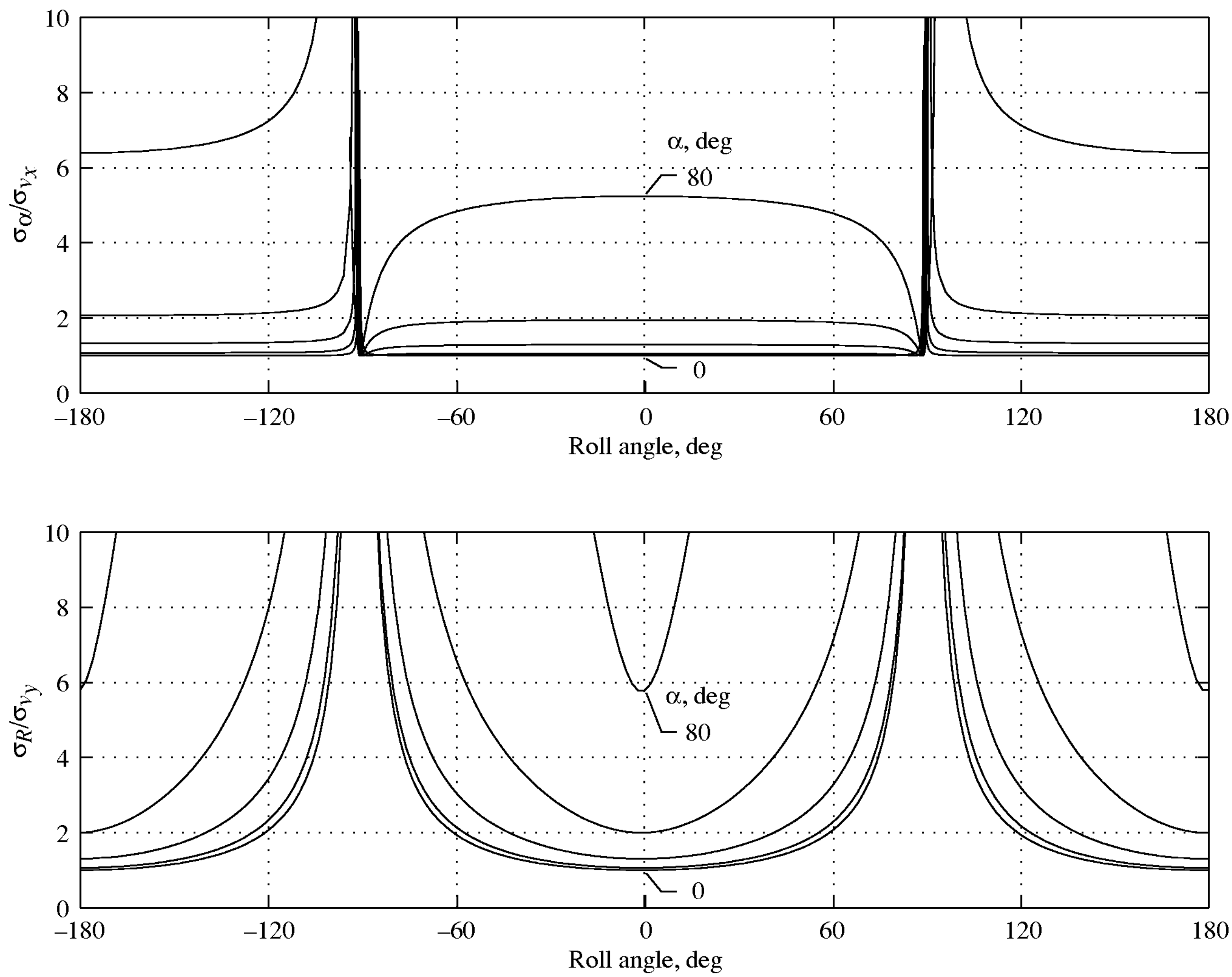

(a) $\sigma_x = 1$; $\Omega_x = 1^\circ$; $A_x = 90^\circ$; $\sigma_y = 1$; $\Omega_y = 1^\circ$; $A_y = 0^\circ$.

Figure 10. Normalized standard deviations of inferred pitch and roll angles of x-y axis AOA sensor.

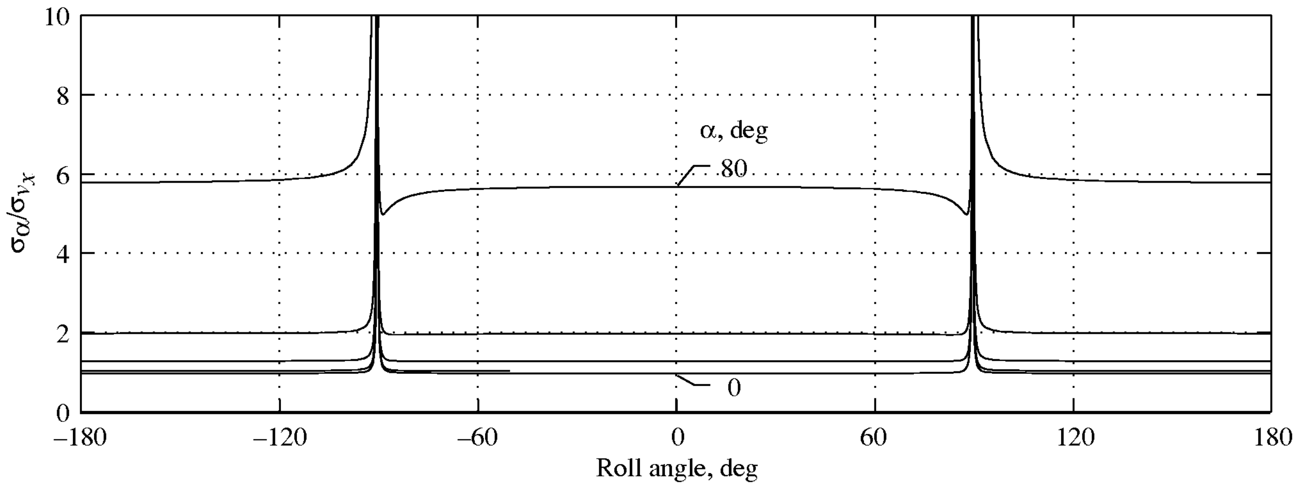

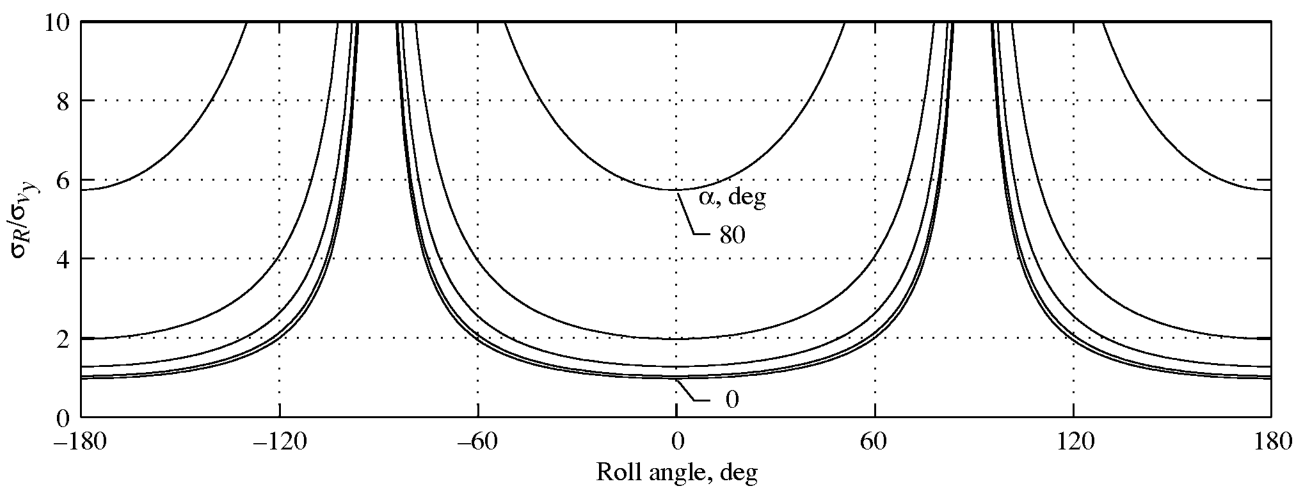

(b) $\sigma_x = 1$; $\Omega_x = 0.1°$; $A_x = 90°$; $\sigma_y = 10$; $\Omega_y = 0.1°$; $A_y = 0°$.

Figure 10. Continued.

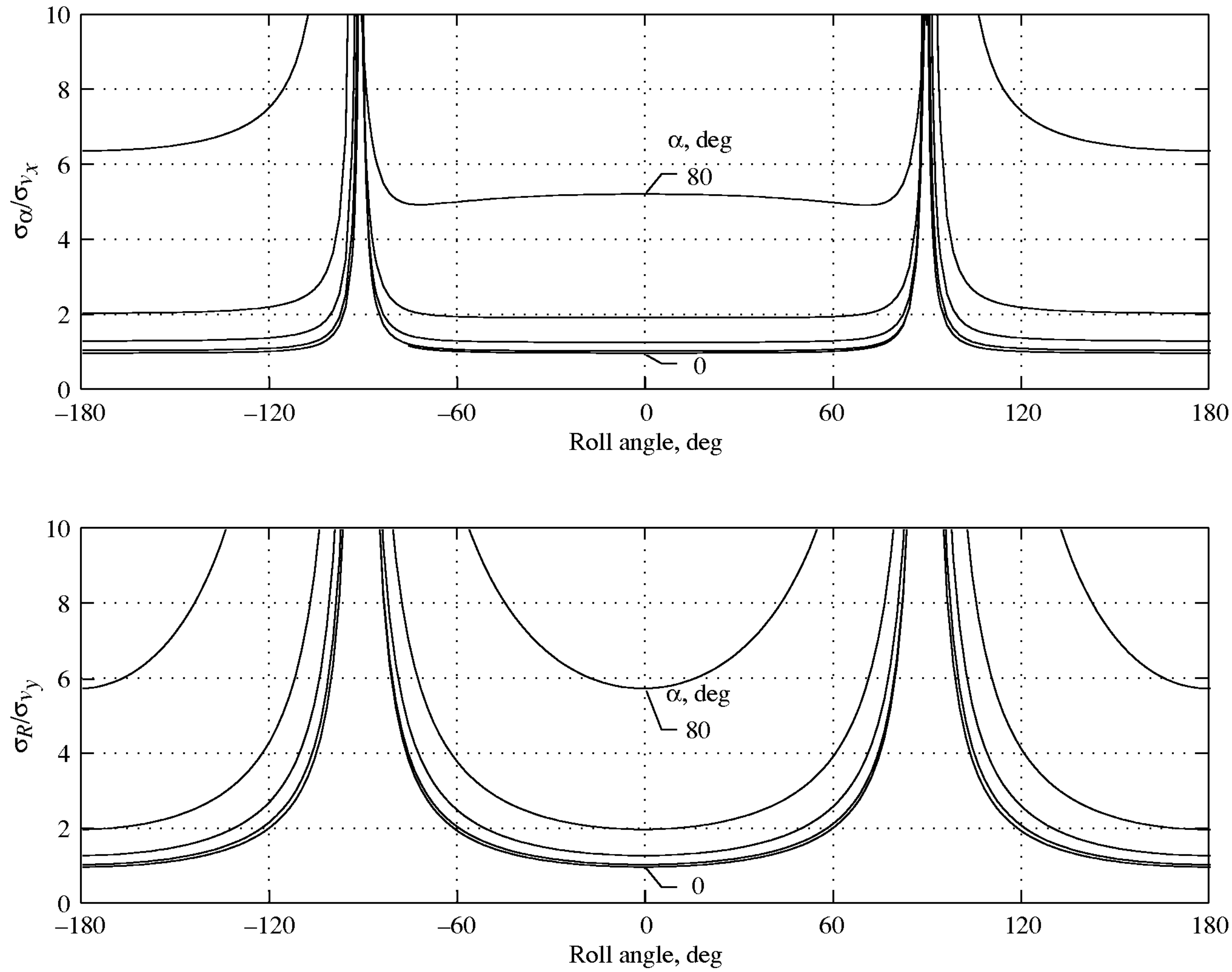

(c) $\sigma_x = 1$; $\Omega_x = 1°$; $A_x = 90°$; $\sigma_y = 10$; $\Omega_y = 1°$; $A_y = 0°$.

Figure 10. Continued.

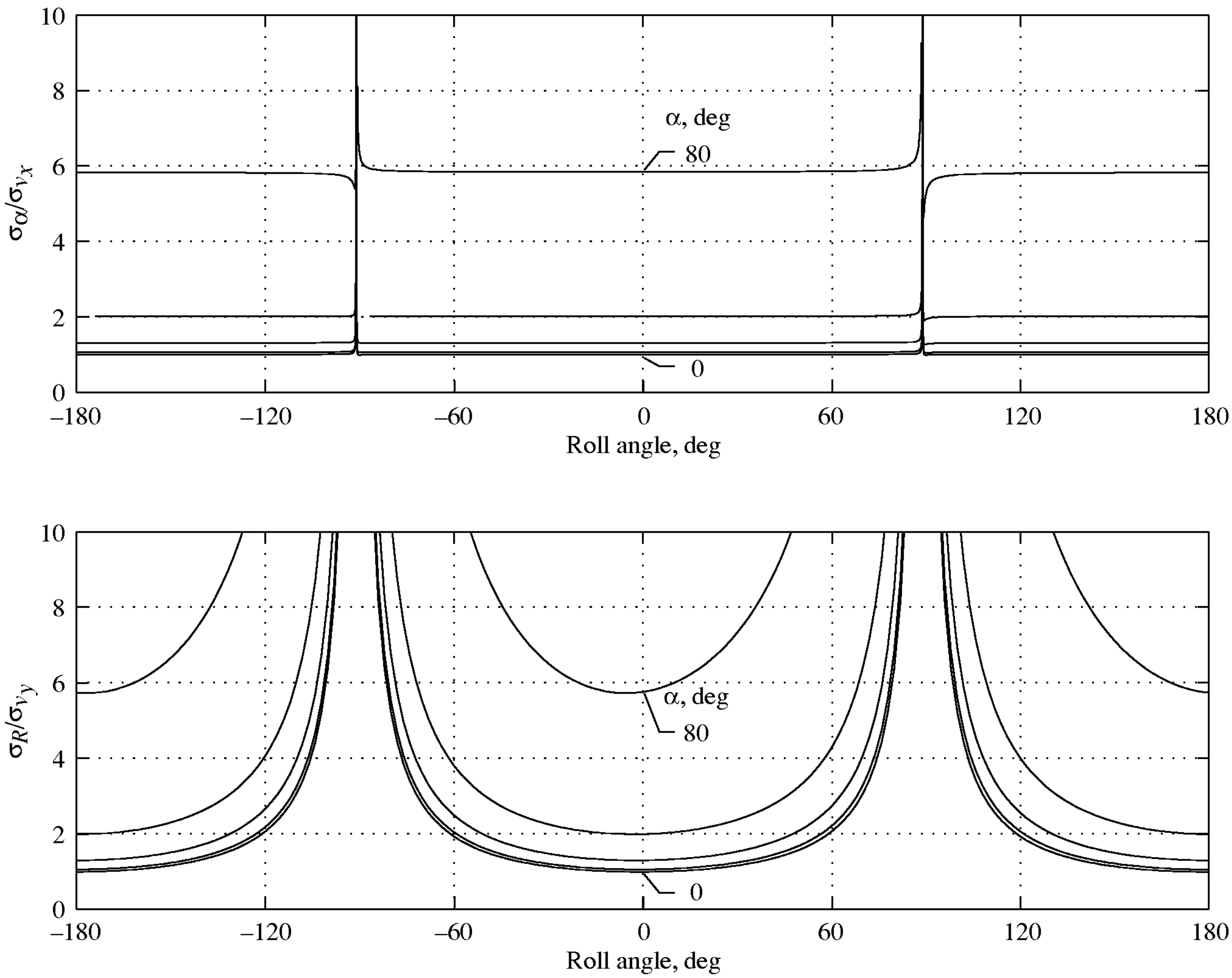

(d) $\sigma_x = 1$; $\Omega_x = 1°$; $A_x = 0°$; $\sigma_y = 10$; $\Omega_y = 0.1°$; $A_y = 0°$.

Figure 10. Concluded.

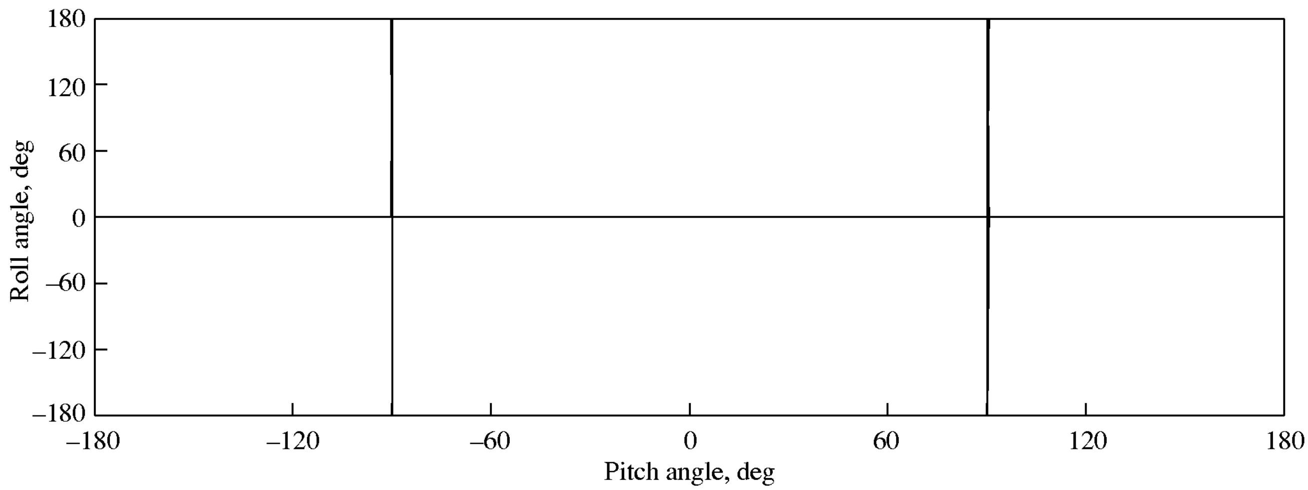

(a) $\Omega = 0.1°$; $A_x = 90°$; $A_z = 0°$.

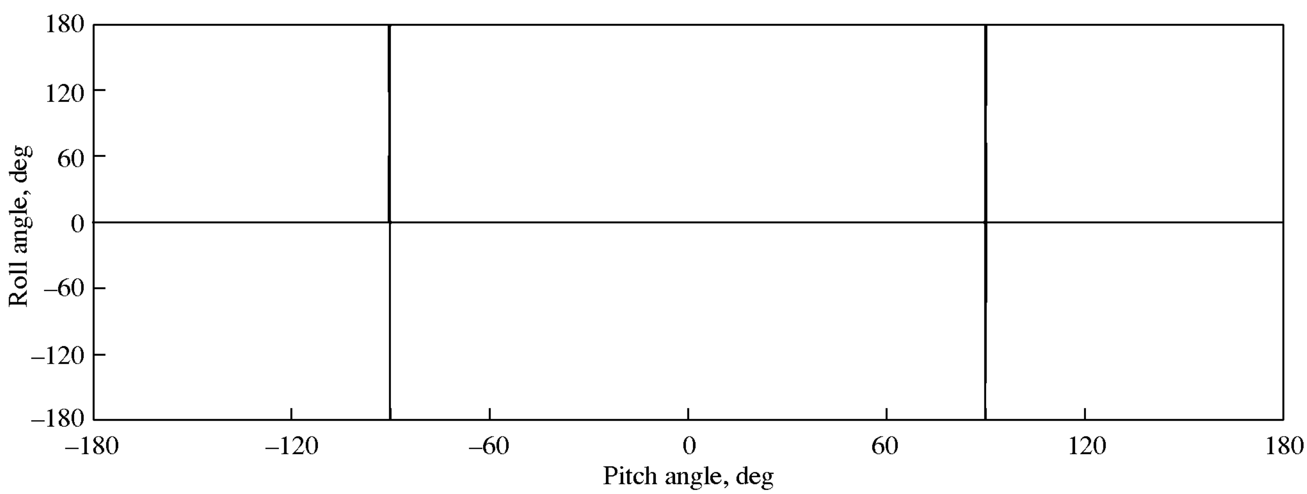

(b) $\Omega = 1°$; $A_x = 90°$; $A_z = 0°$.

Figure 11. Singularity loci of Jacobian matrix $\mathbf{F}_z$ for x-z axis AOA sensor.

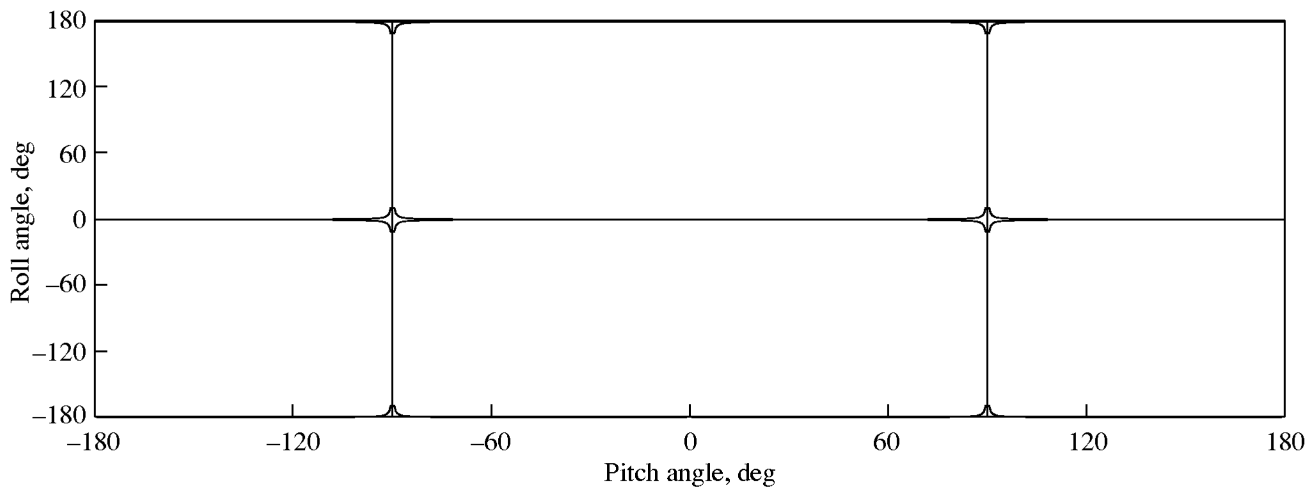

(c) $\Omega = 0.1°$; $A_x = 0°$; $A_z = 0°$.

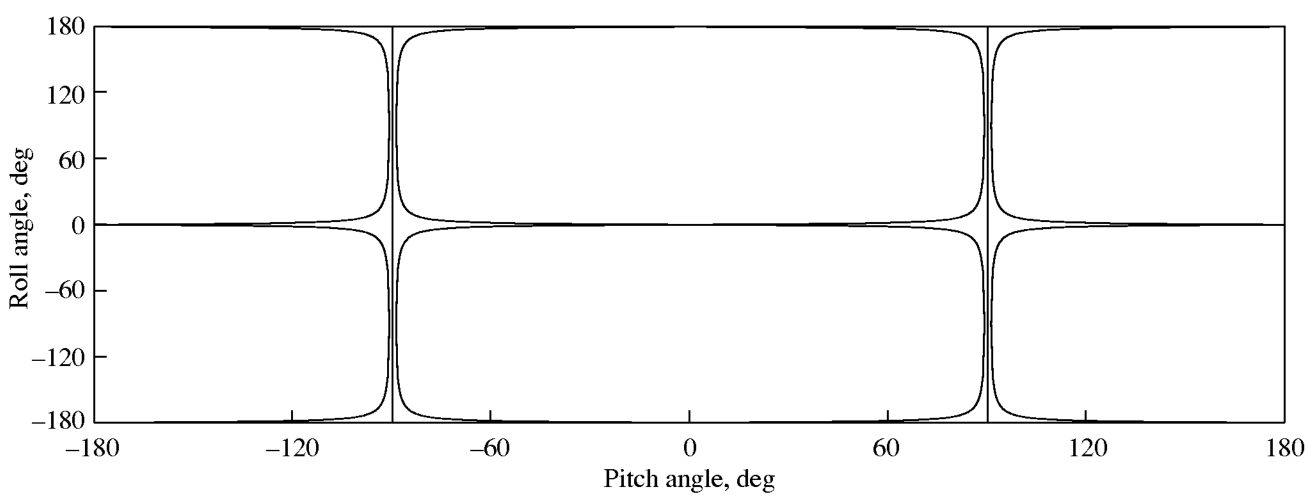

(d) $\Omega = 1°$; $A_x = 0°$; $A_z = 0°$.

Figure 11. Concluded.

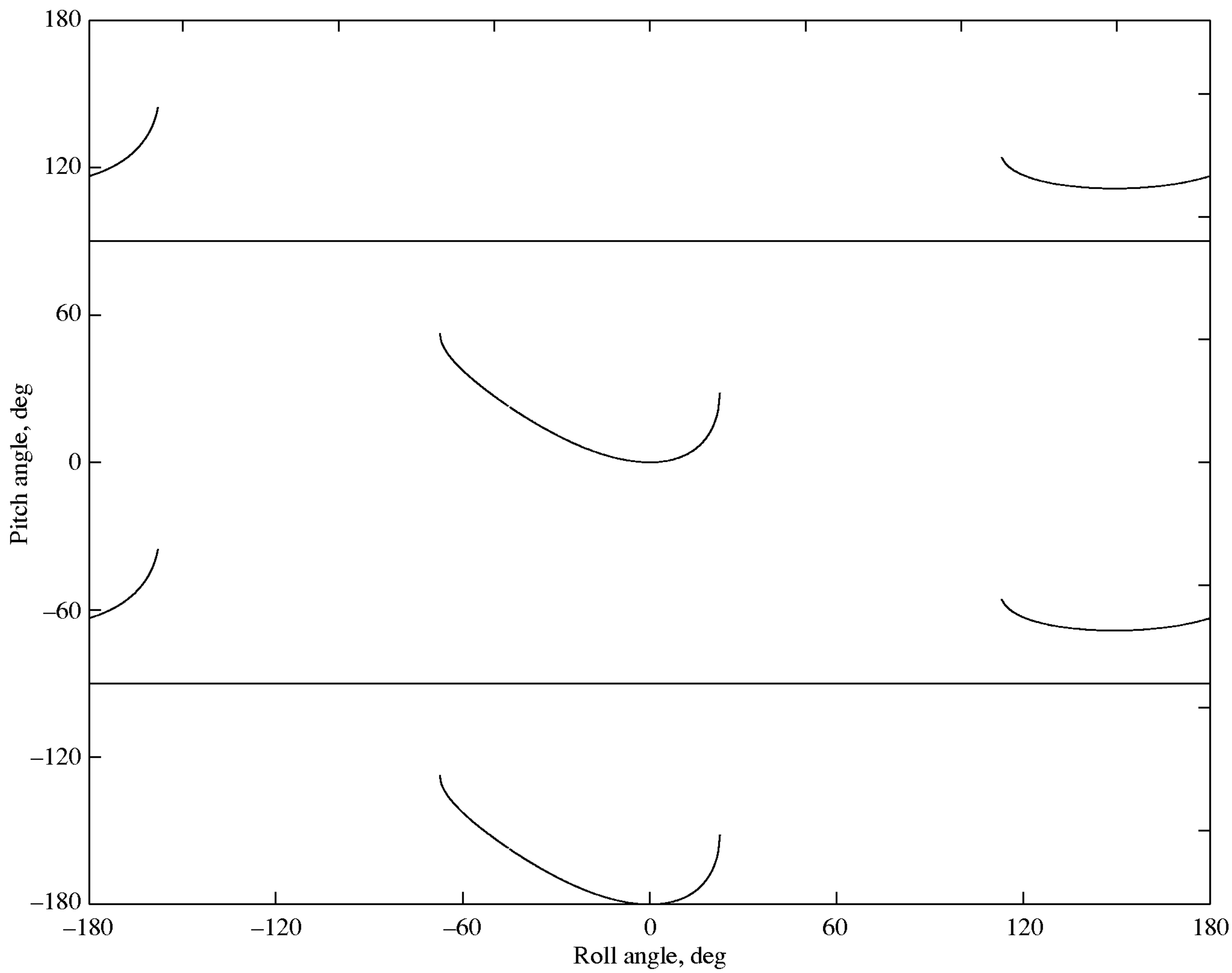

Figure 12. Singularity loci of Jacobian matrix $\mathbf{F}_z\mathbf{F}_z^{\mathrm{T}}$ for three-axis AOA sensor for $\Omega_x = \Omega_y = \Omega_z = 45°$ and $A_x = A_y = A_z = 90°$.

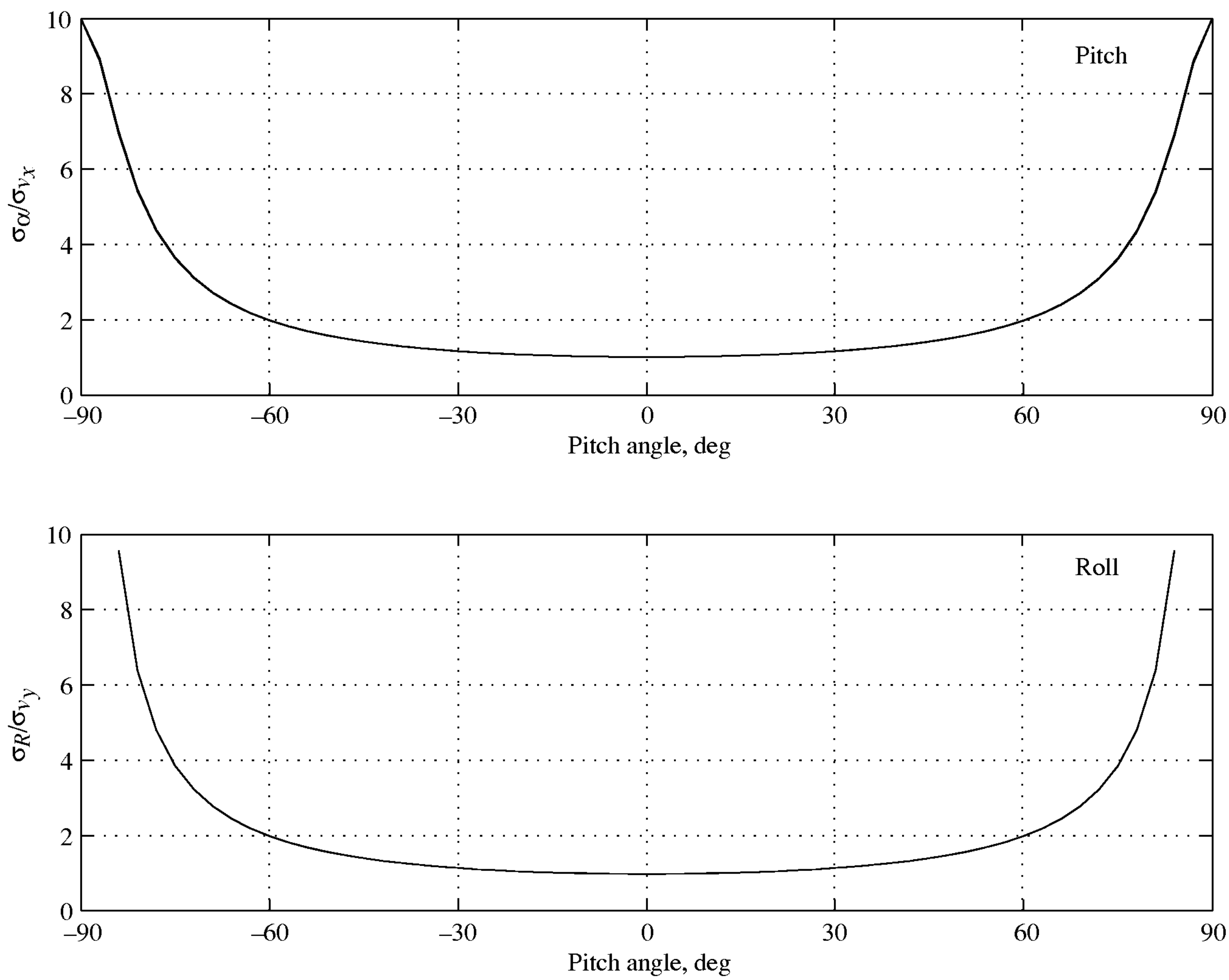

Figure 13. Normalized standard deviations of inferred pitch and roll angles versus pitch angle for three-axis AOA sensor for $\sigma_y = \sigma_z = 10\sigma_x$, $\Omega_x = \Omega_y = \Omega_z = 0.1°$, and $A_x = 90°$, $A_y = A_z = 0°$.

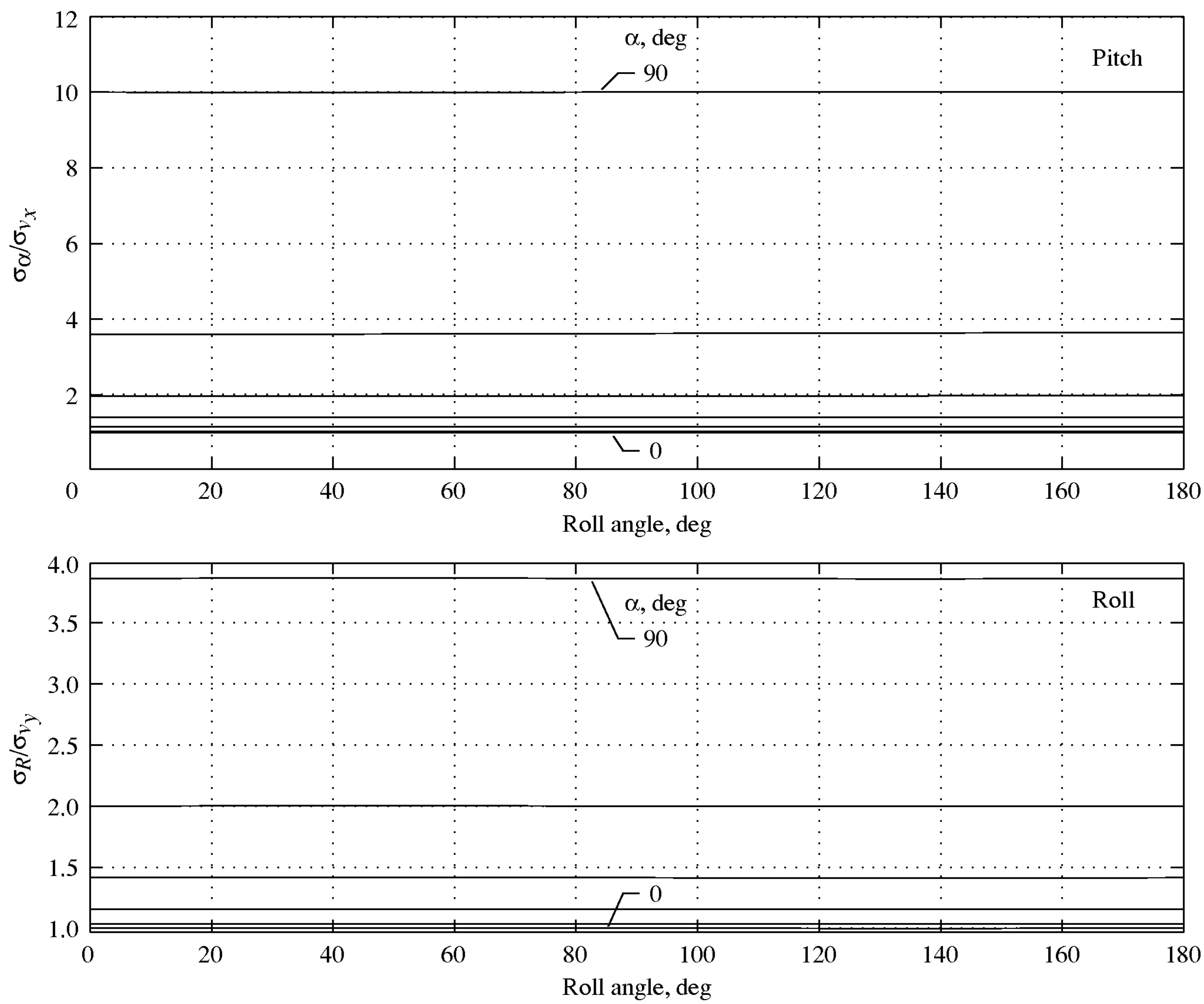

Figure 14. Normalized standard deviations of inferred pitch and roll angles versus roll angle for three-axis AOA sensor for $\sigma_y = \sigma_z = 10\sigma_x$, $\Omega_x = \Omega_y = \Omega_z = 0.1°$, and $A_x = 90°$, $A_y = A_z = 0°$.

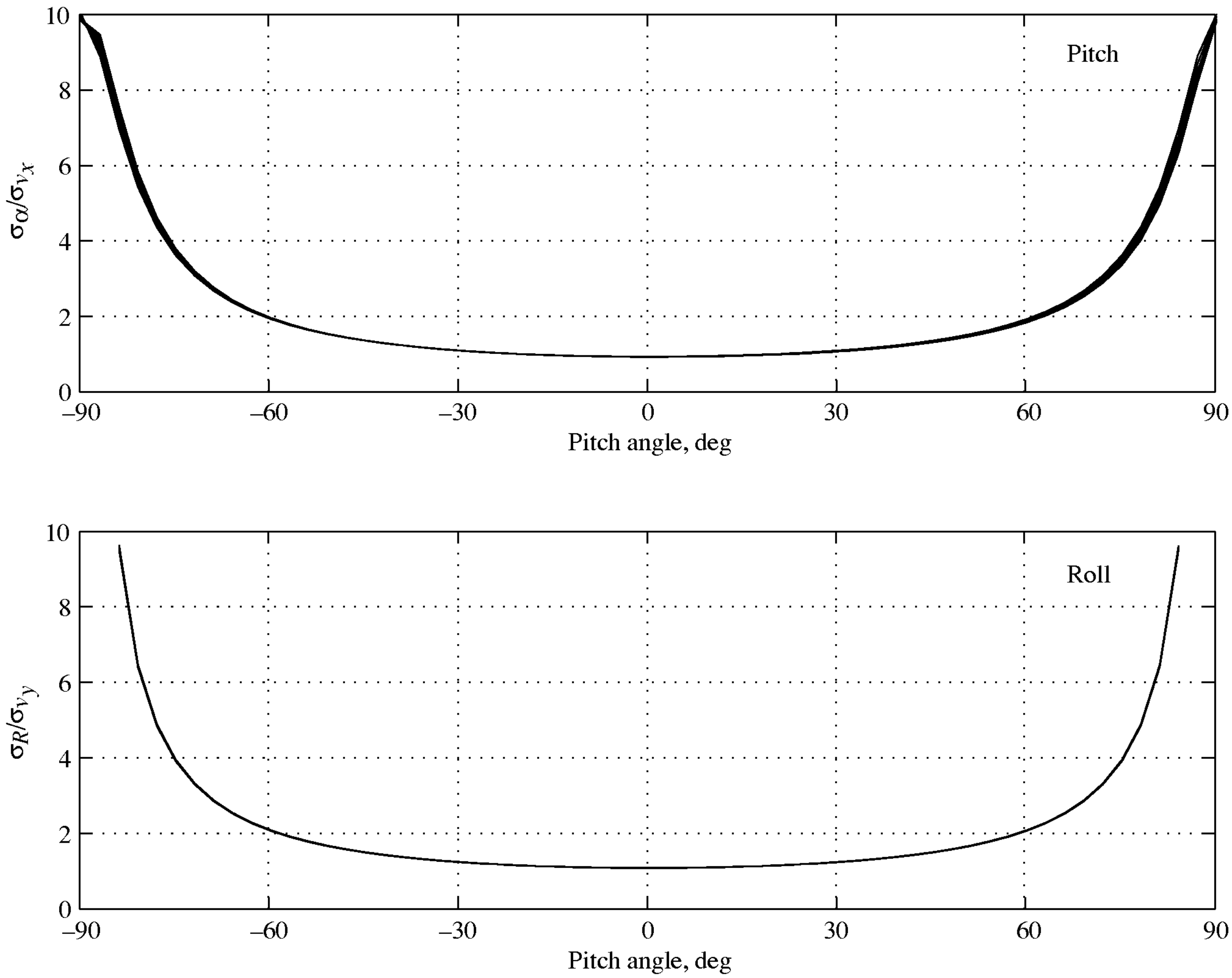

Figure 15. Normalized standard deviations of inferred pitch and roll angles versus pitch angle for three-axis AOA sensor for $\sigma_y = \sigma_z = 10\sigma_x$, $\Omega_x = \Omega_y = \Omega_z = 1°$, and $A_x = 90°$, $A_y = A_z = 0°$.

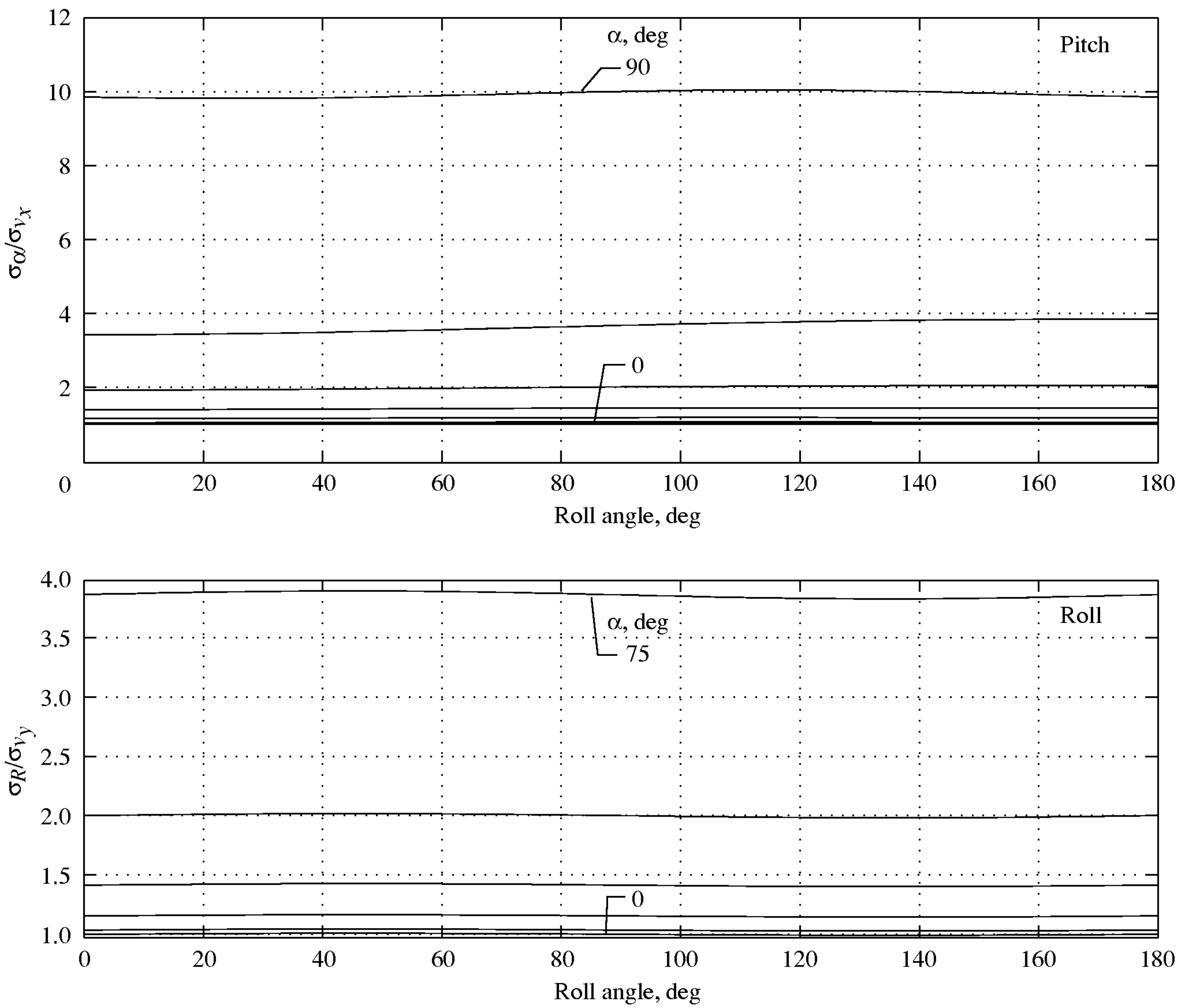

Figure 16. Normalized standard deviations of inferred pitch and roll angles versus roll angle for three-axis AOA sensor for $\sigma_y = \sigma_z = 10\sigma_x$, $\Omega_x = \Omega_y = \Omega_z = 1°$, and $A_x = 90°$, $A_y = A_z = 0°$.

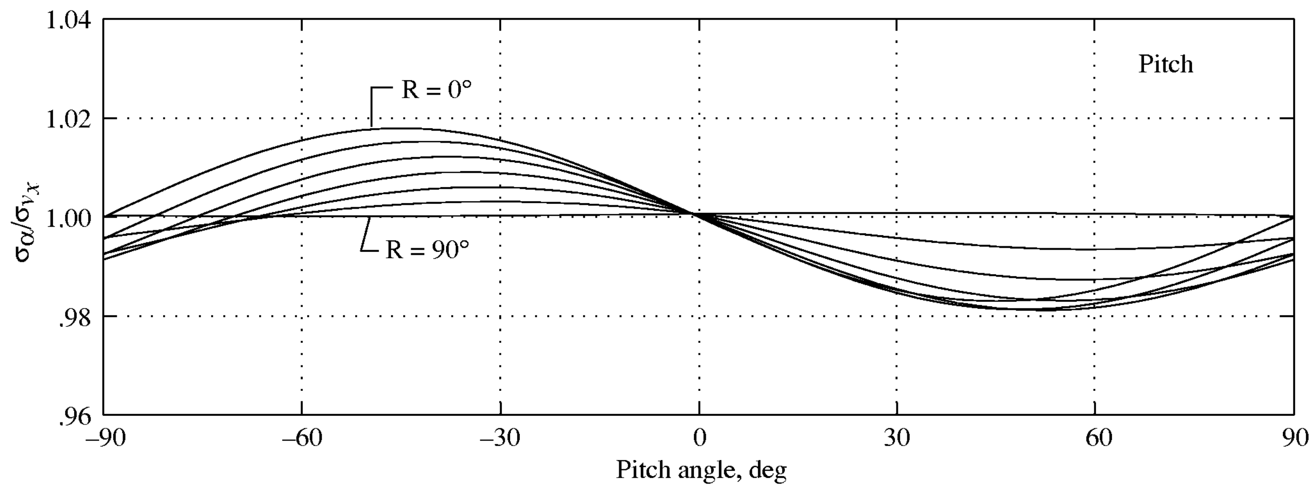

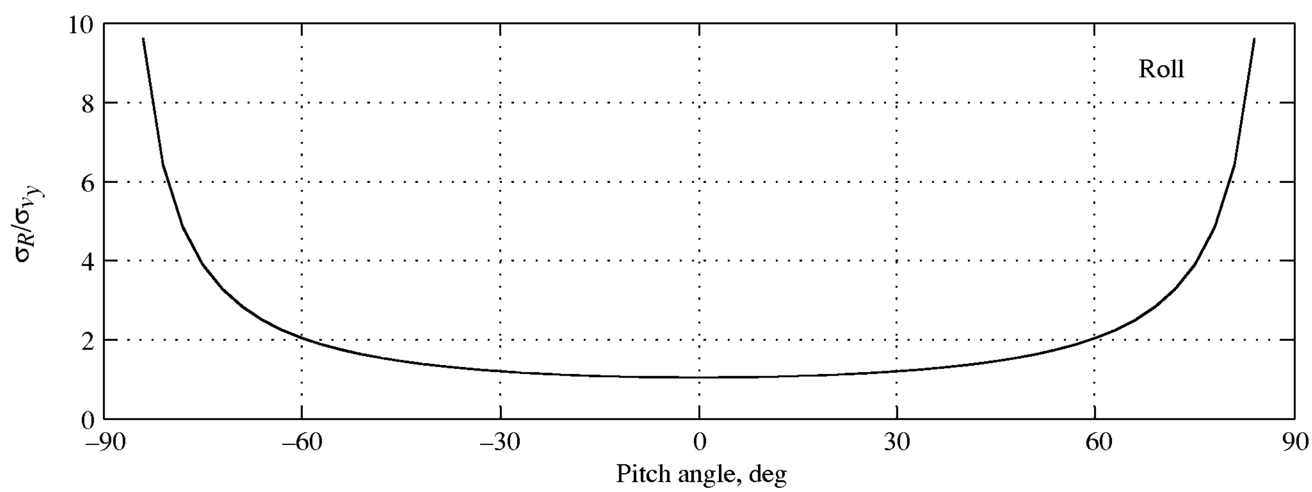

Figure 17. Normalized standard deviations of inferred pitch and roll angles versus pitch angle for three-axis AOA sensor for $\sigma_y = \sigma_z = \sigma_x = 1$, $\Omega_x = \Omega_y = \Omega_z = 1°$, and $A_x = 90°$, $A_y = A_z = 0°$.

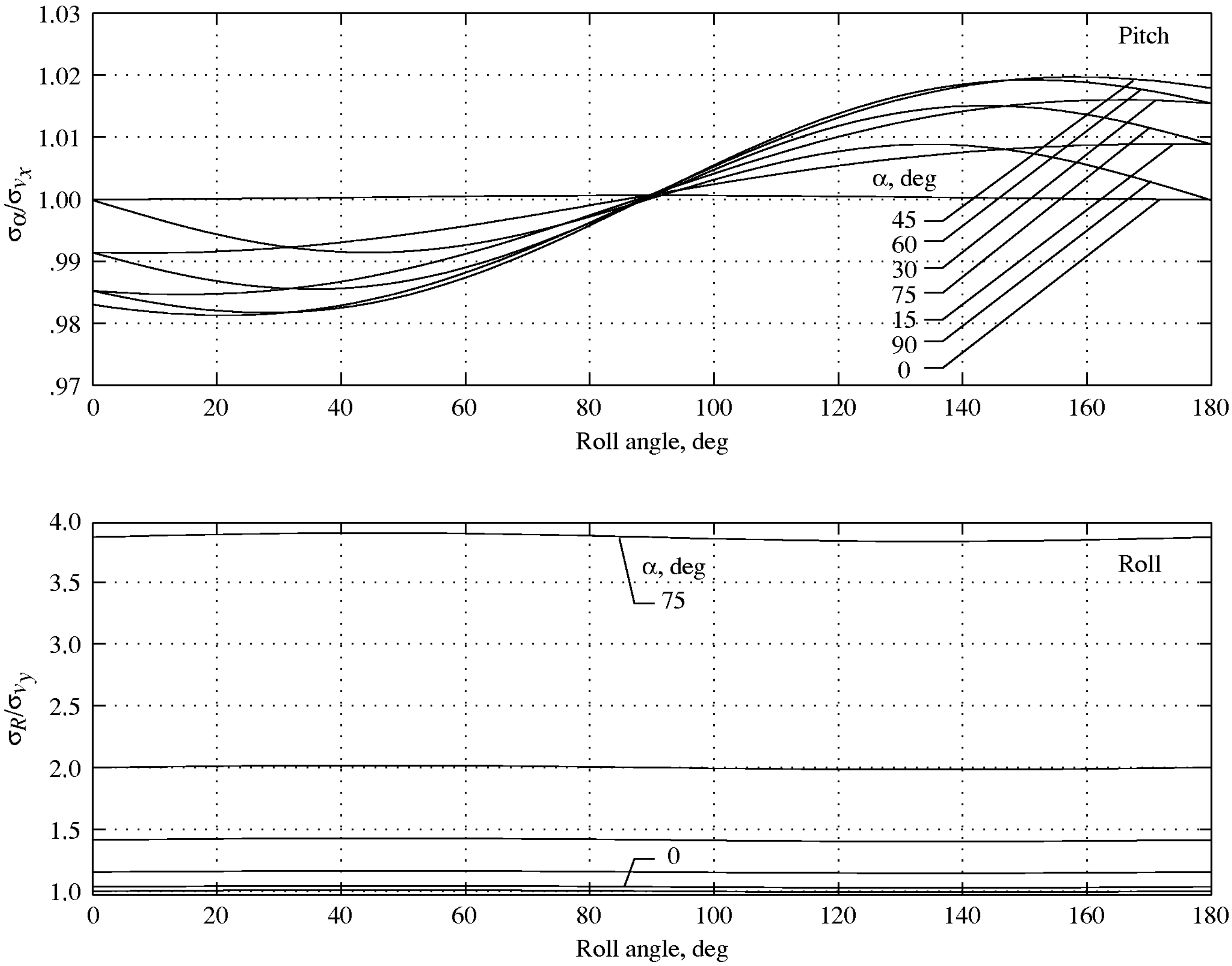

Figure 18. Normalized standard deviations of inferred pitch and roll angles versus roll angle for three-axis AOA sensor for $\sigma_y = \sigma_z = \sigma_x = 1$, $\Omega_x = \Omega_y = \Omega_z = 1°$, and $A_x = 90°$, $A_y = A_z = 0°$.

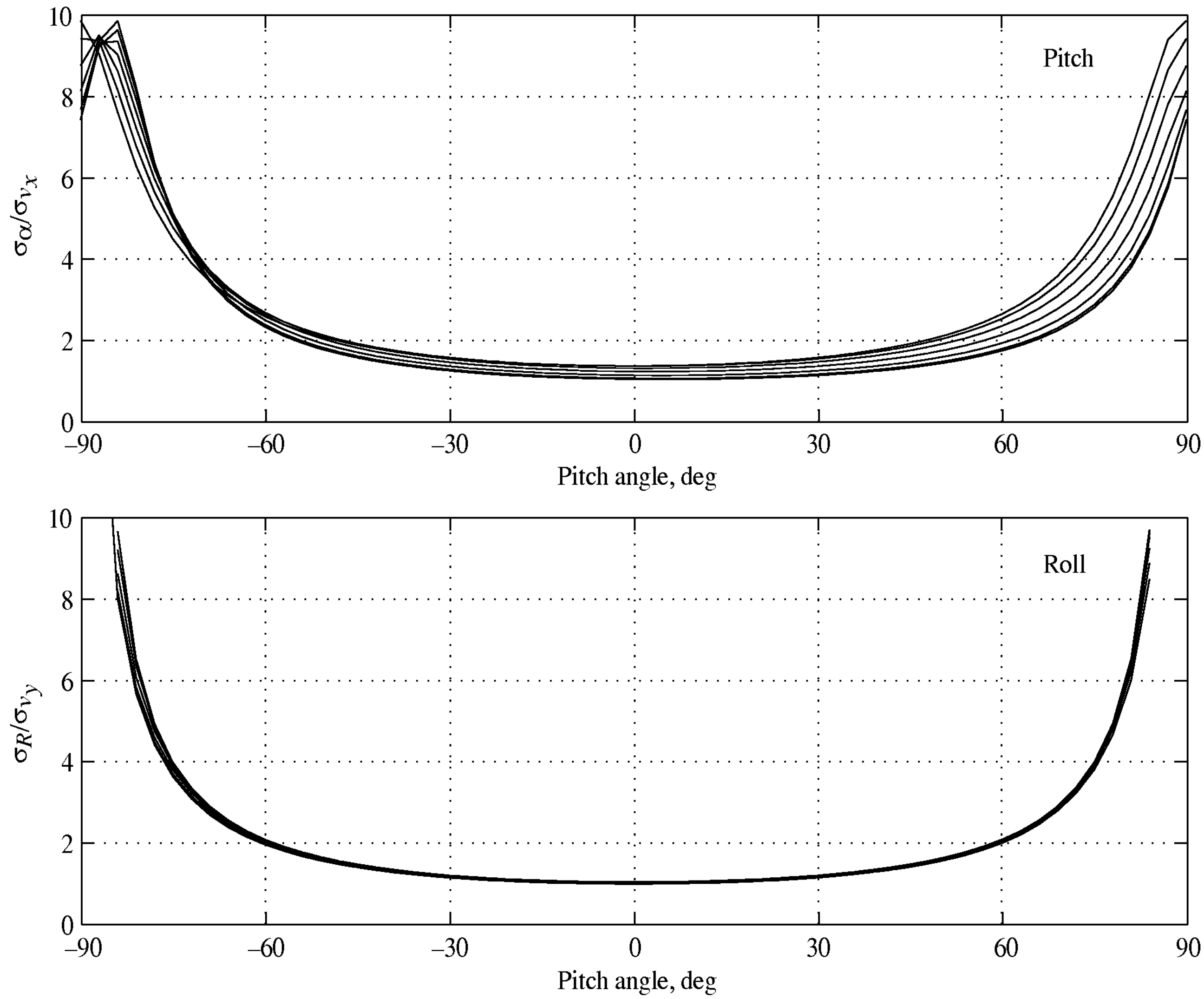

Figure 19. Normalized standard deviations of inferred pitch and roll angles versus pitch angle for three-axis AOA sensor for $\sigma_y = \sigma_z = 10\sigma_x$, $\Omega_x = \Omega_y = \Omega_z = 5°$, and $A_x = 90°$, $A_y = A_z = 0°$.

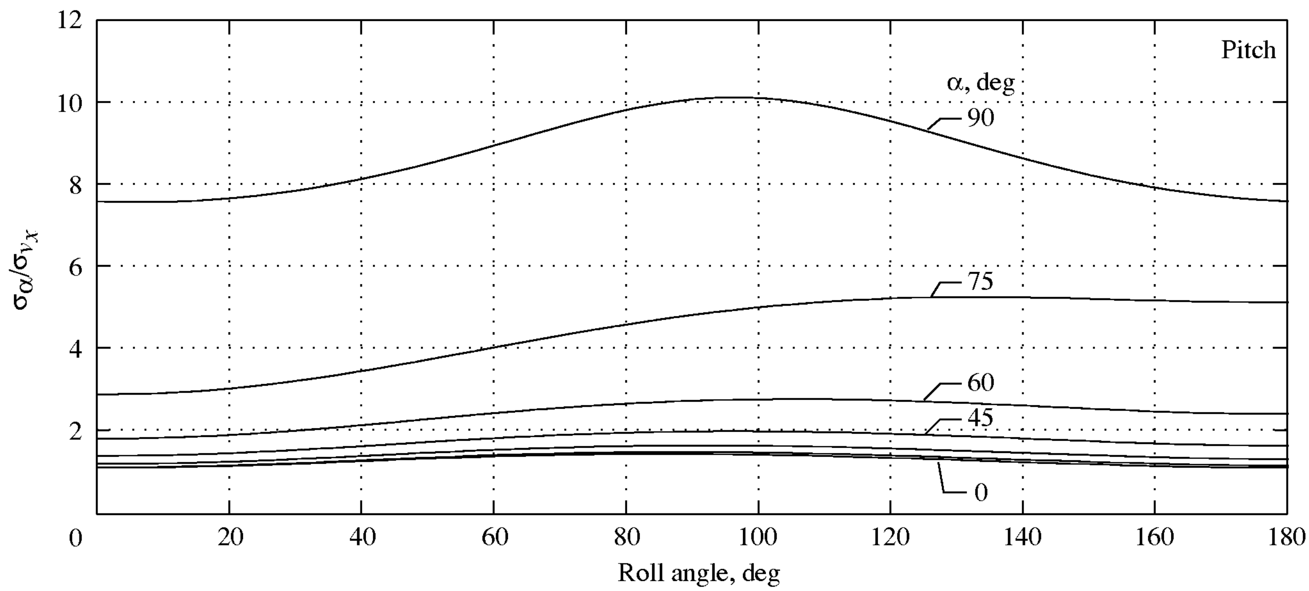

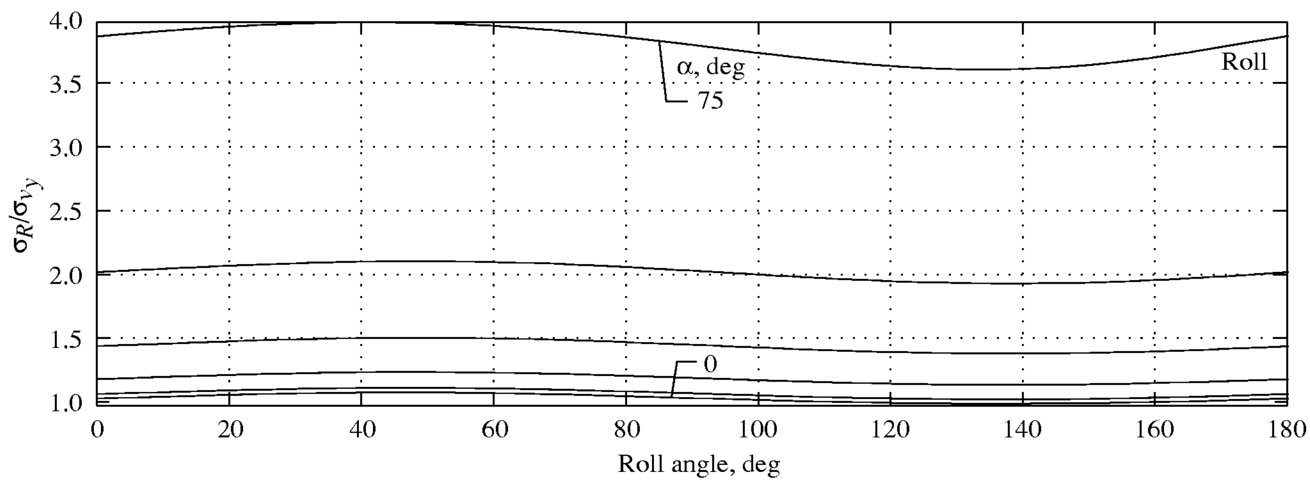

Figure 20. Normalized standard deviations of inferred pitch and roll angles versus roll angle for three-axis AOA sensor for $\sigma_y = \sigma_z = 10\sigma_x$, $\Omega_x = \Omega_y = \Omega_z = 5°$, and $A_x = 90°$, $A_y = A_z = 0°$.

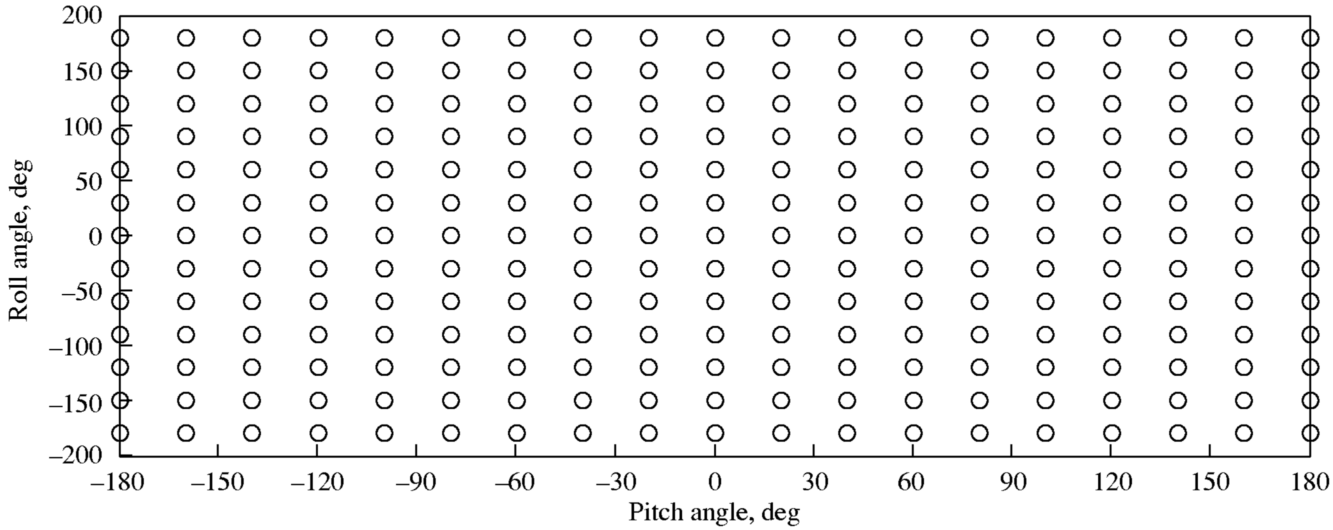

(a) Full 247-point (19 × 13) D design.

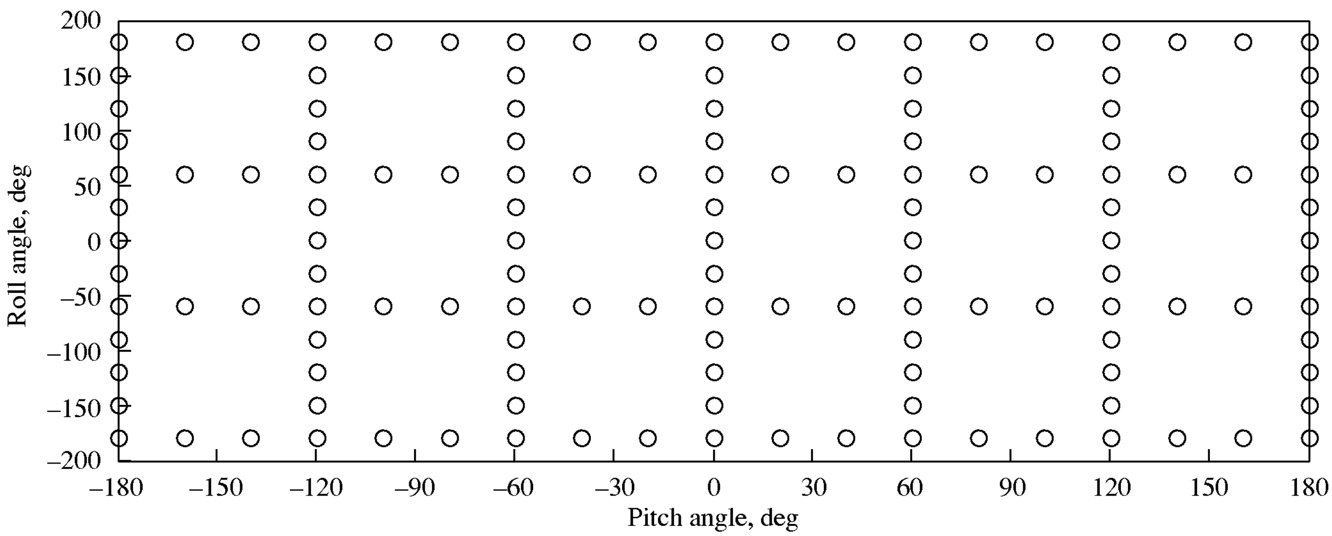

(b) Fractional 139-point D design.

Figure 21. Experimental designs.

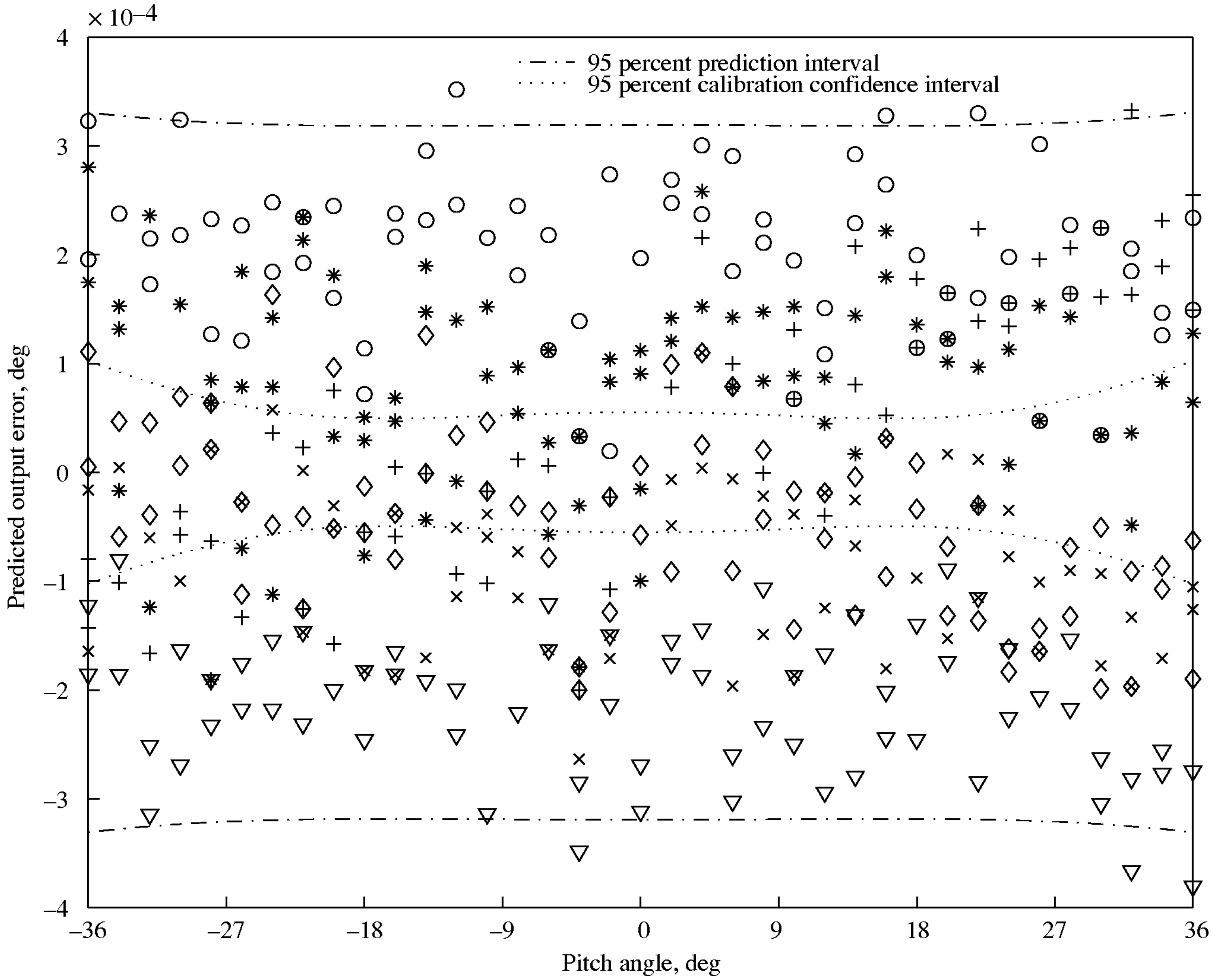

Figure 22. Residuals of predicted output of single-axis AOA sensor without roll for six replications from −36° to 36°.

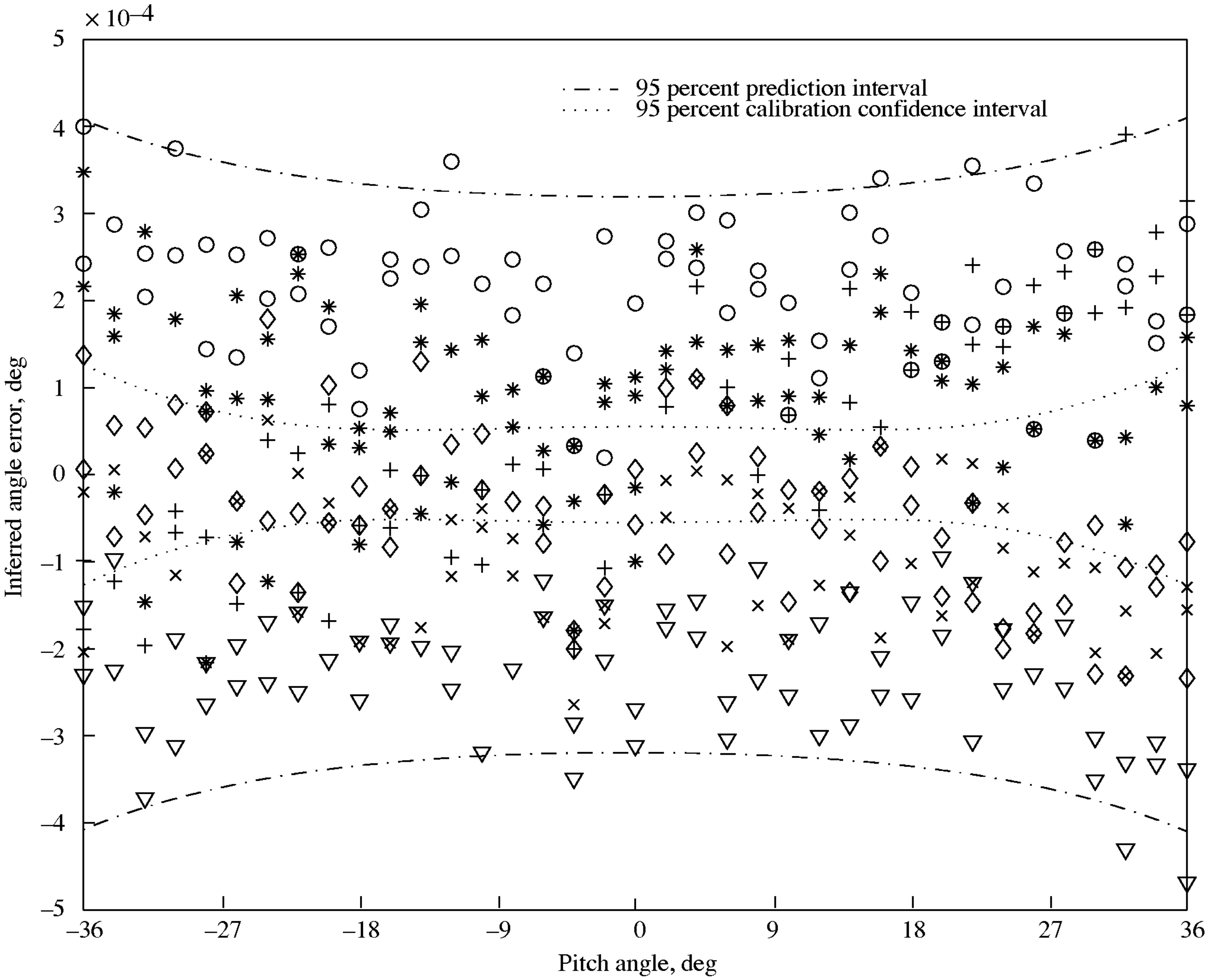

Figure 23. Errors of inferred pitch angles of single-axis AOA sensor without roll for six replications from $-36°$ to $36°$.

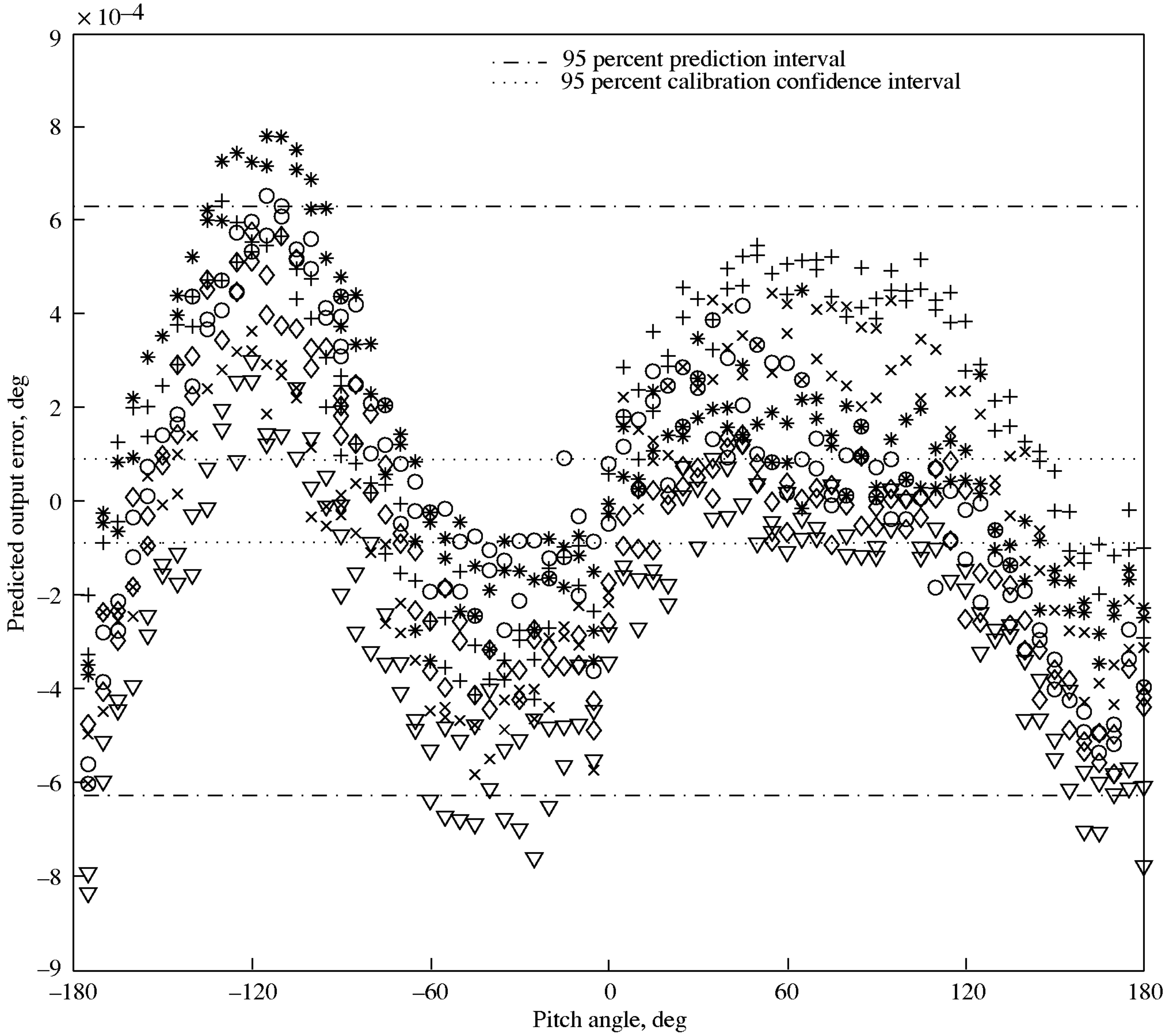

Figure 24. Residuals of predicted output of single-axis AOA sensor without roll for single-axis AOA sensor for six replications from −180° to 180°.

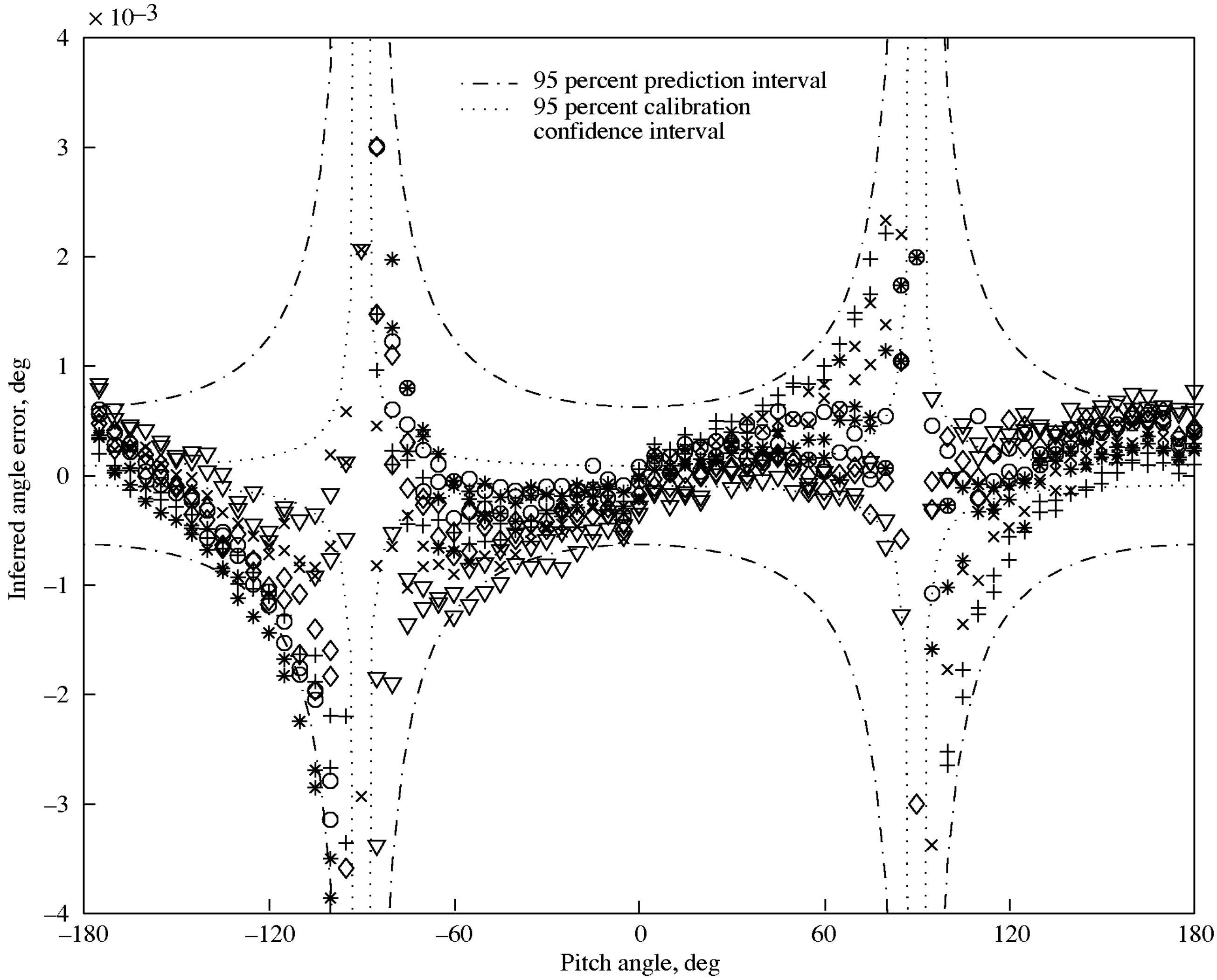

Figure 25. Errors of inferred pitch angles of single-axis AOA sensor without roll for six replications from −180° to 180°.

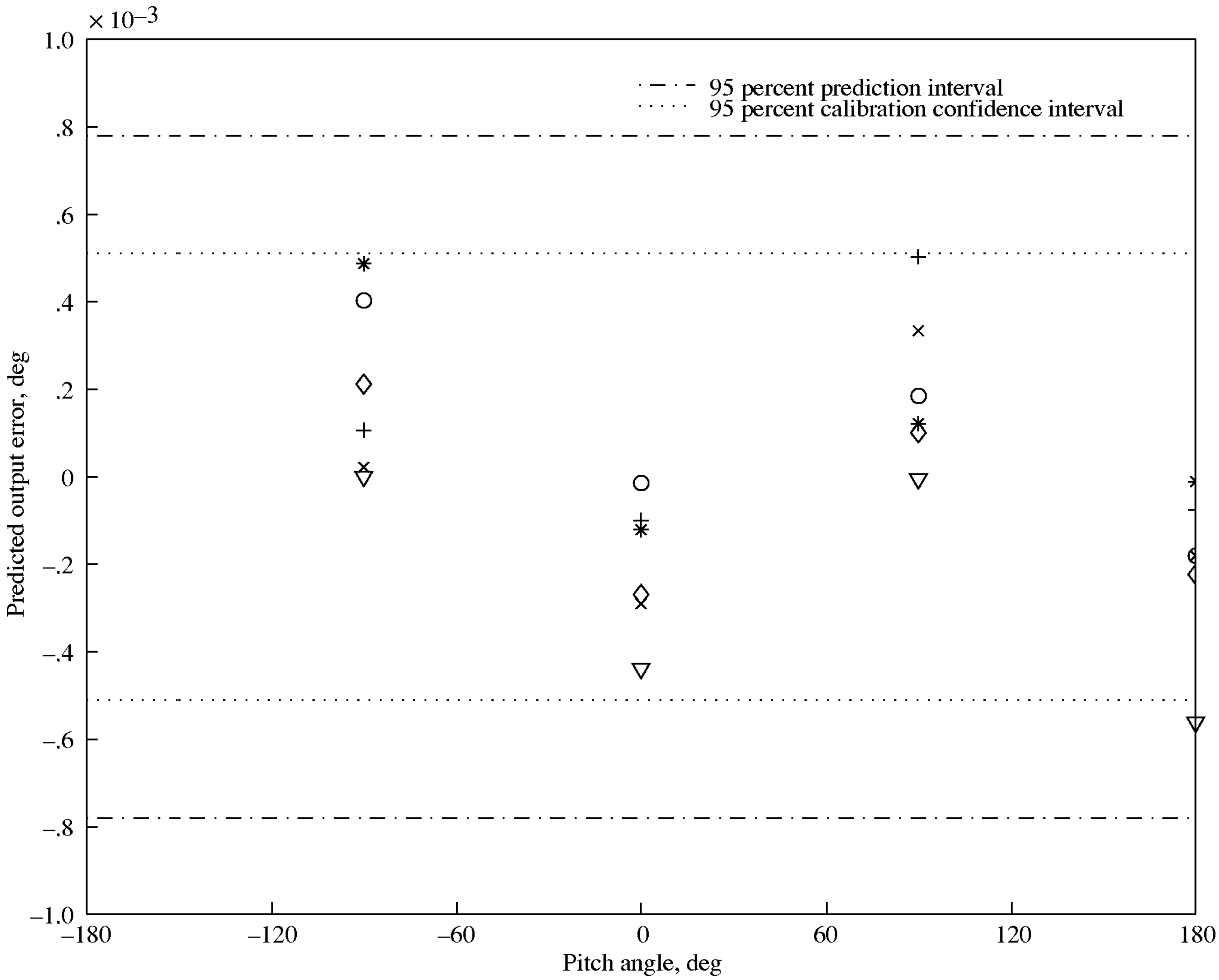

Figure 26. Residuals of predicted output of single-axis AOA sensor without roll for six replications and four-point tumble test.

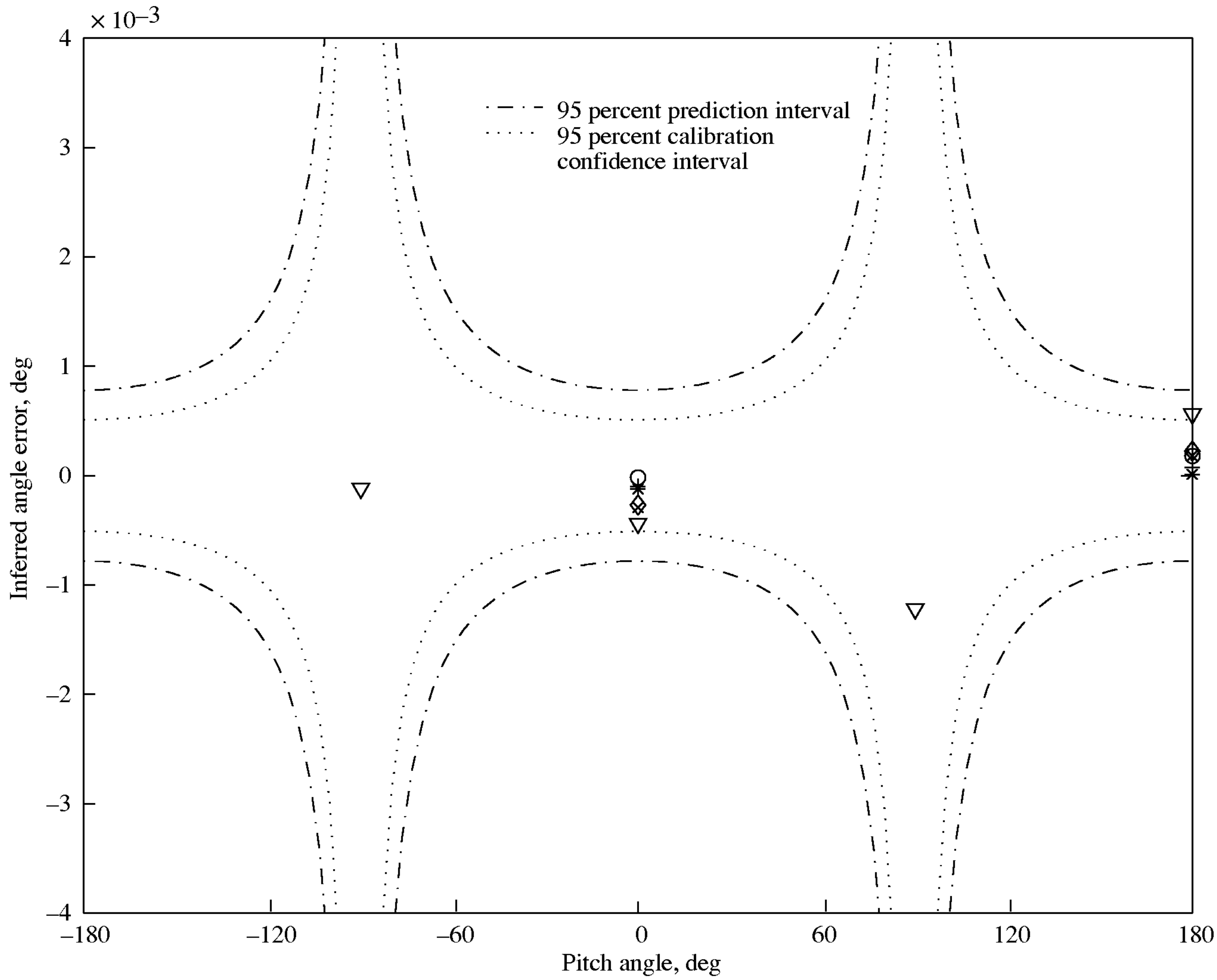

Figure 27. Errors of inferred pitch angle of single-axis AOA sensor without roll for six replications and four-point tumble test.

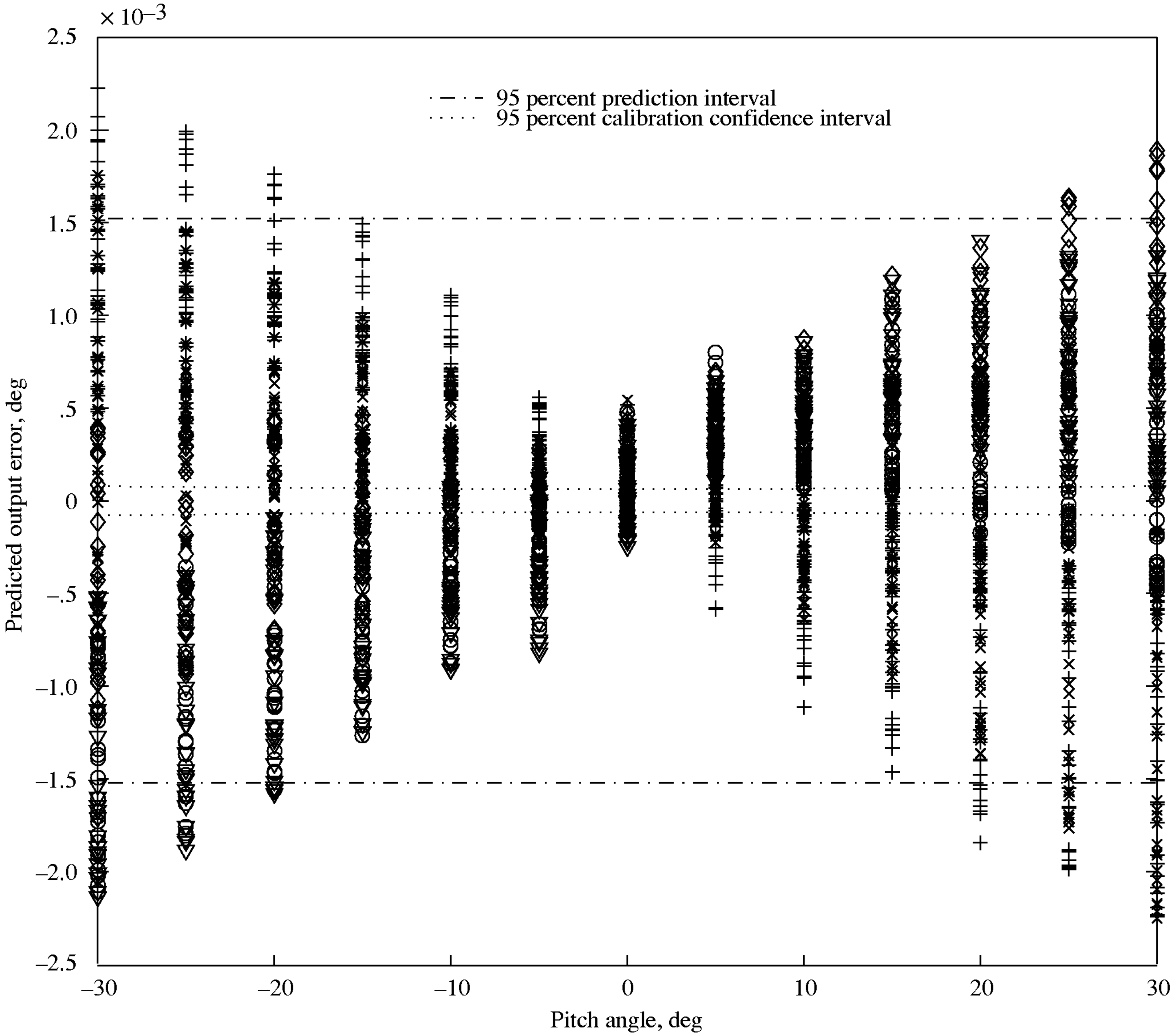

(a) Without temperature correction.

Figure 28. Residuals of predicted output of single-axis AOA sensor with roll for six replications from $-30°$ to $30°$.

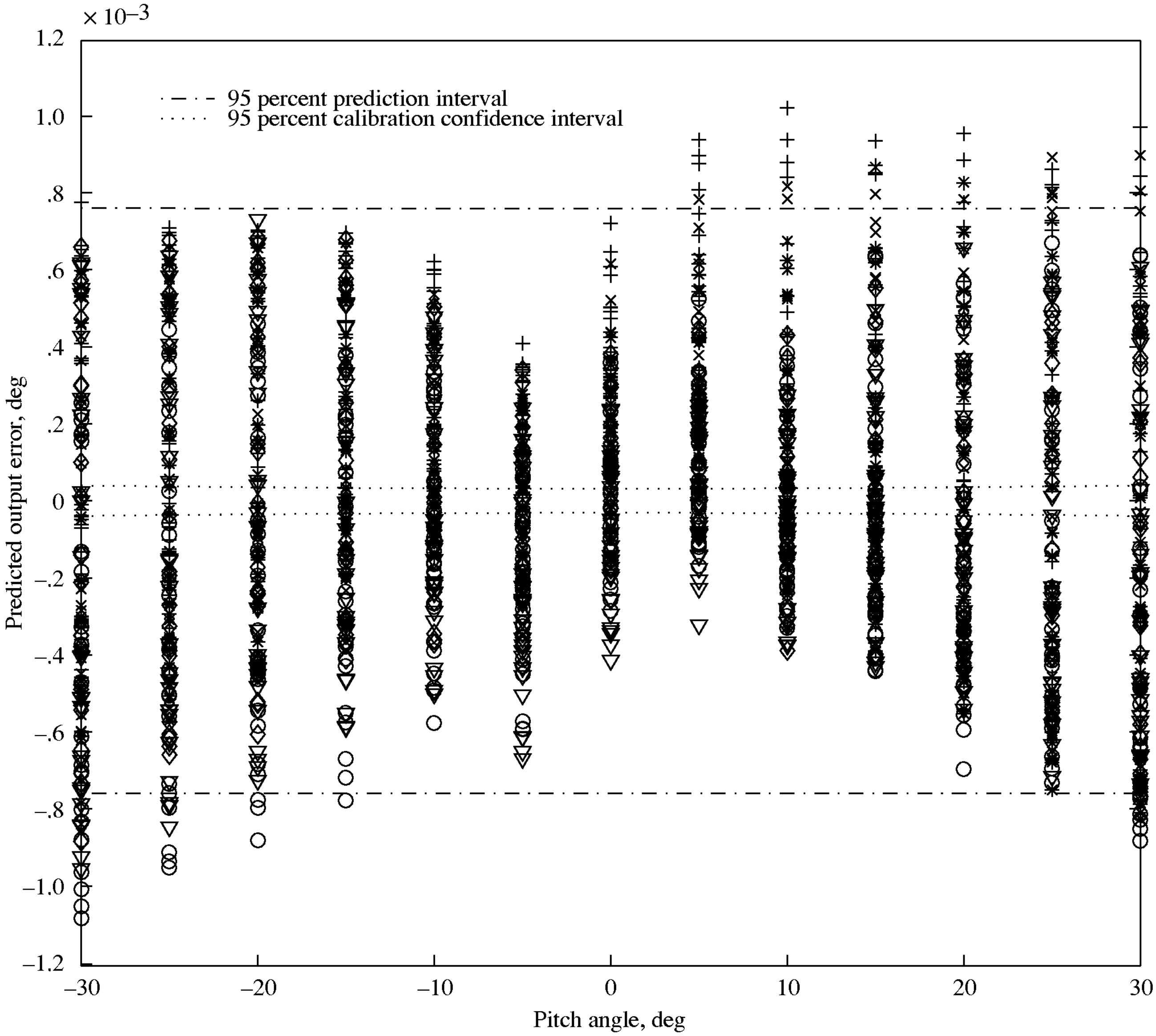

(b) With temperature correction.

Figure 28. Concluded.

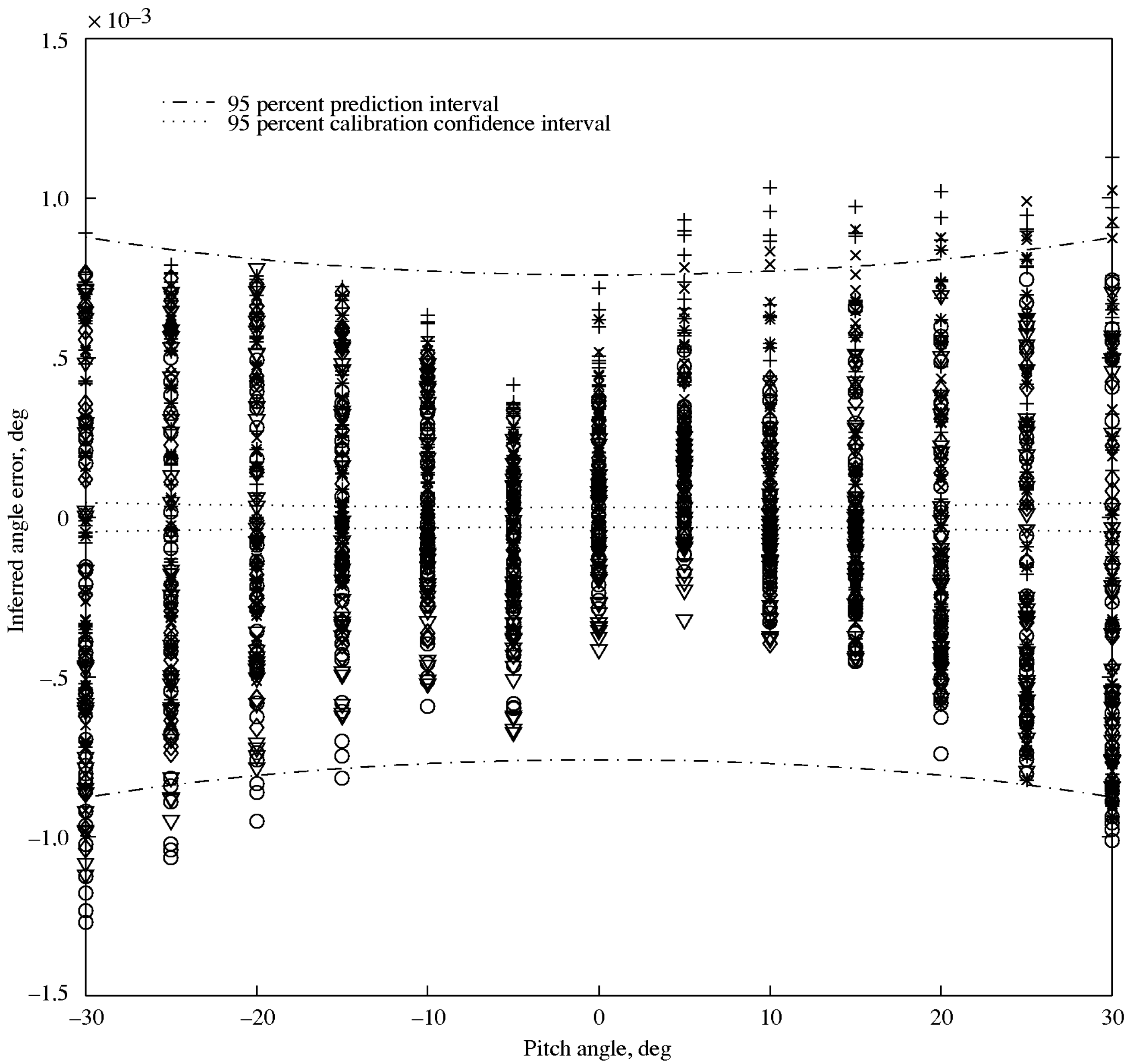

Figure 29. Errors of inferred pitch angle of single-axis AOA sensor with roll for six replications from $-30°$ to $30°$. With temperature correction.

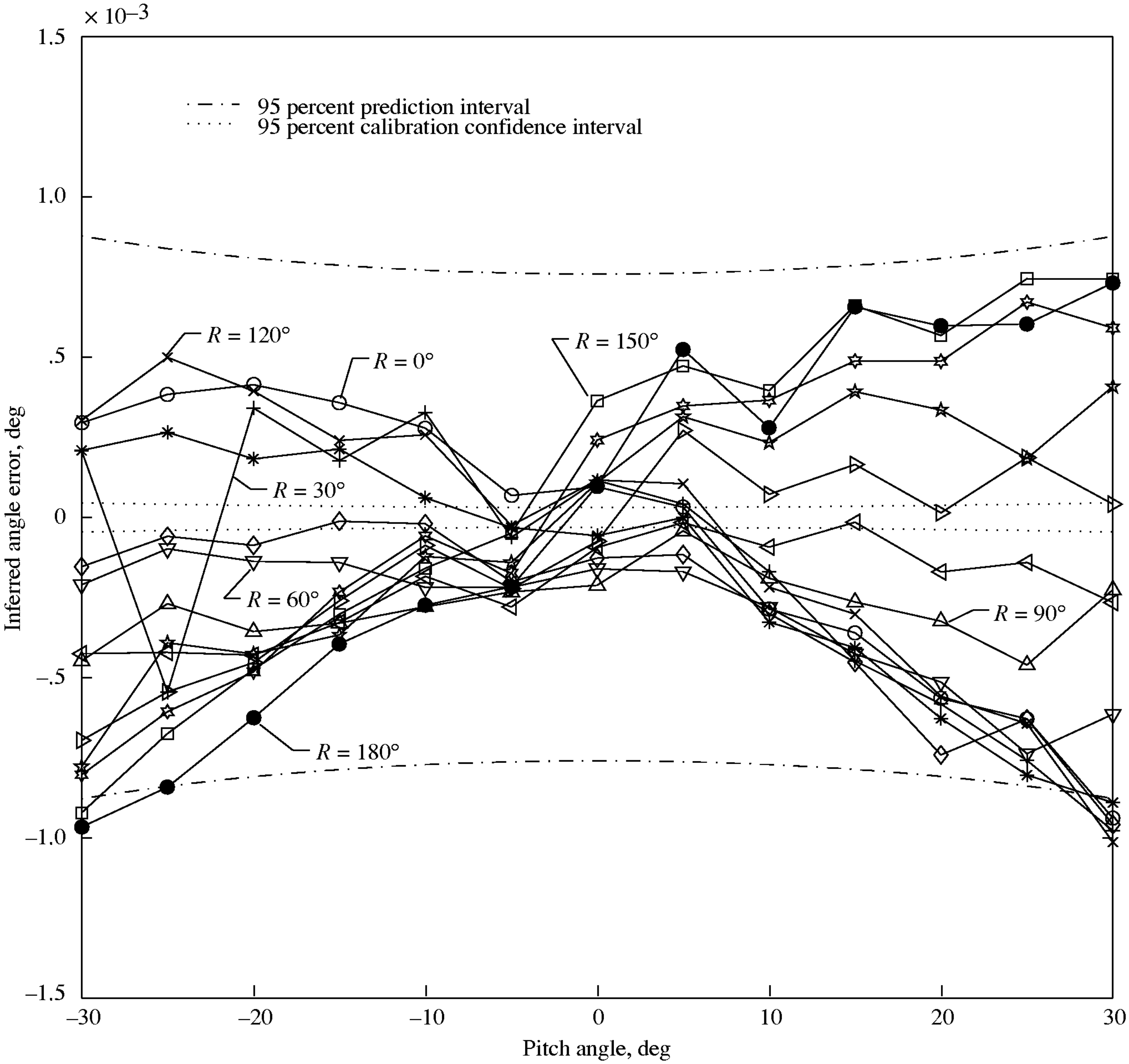

Figure 30. Errors of inferred pitch angle of single-axis AOA sensor with roll for one replication from $-30°$ to $30°$. With temperature correction.

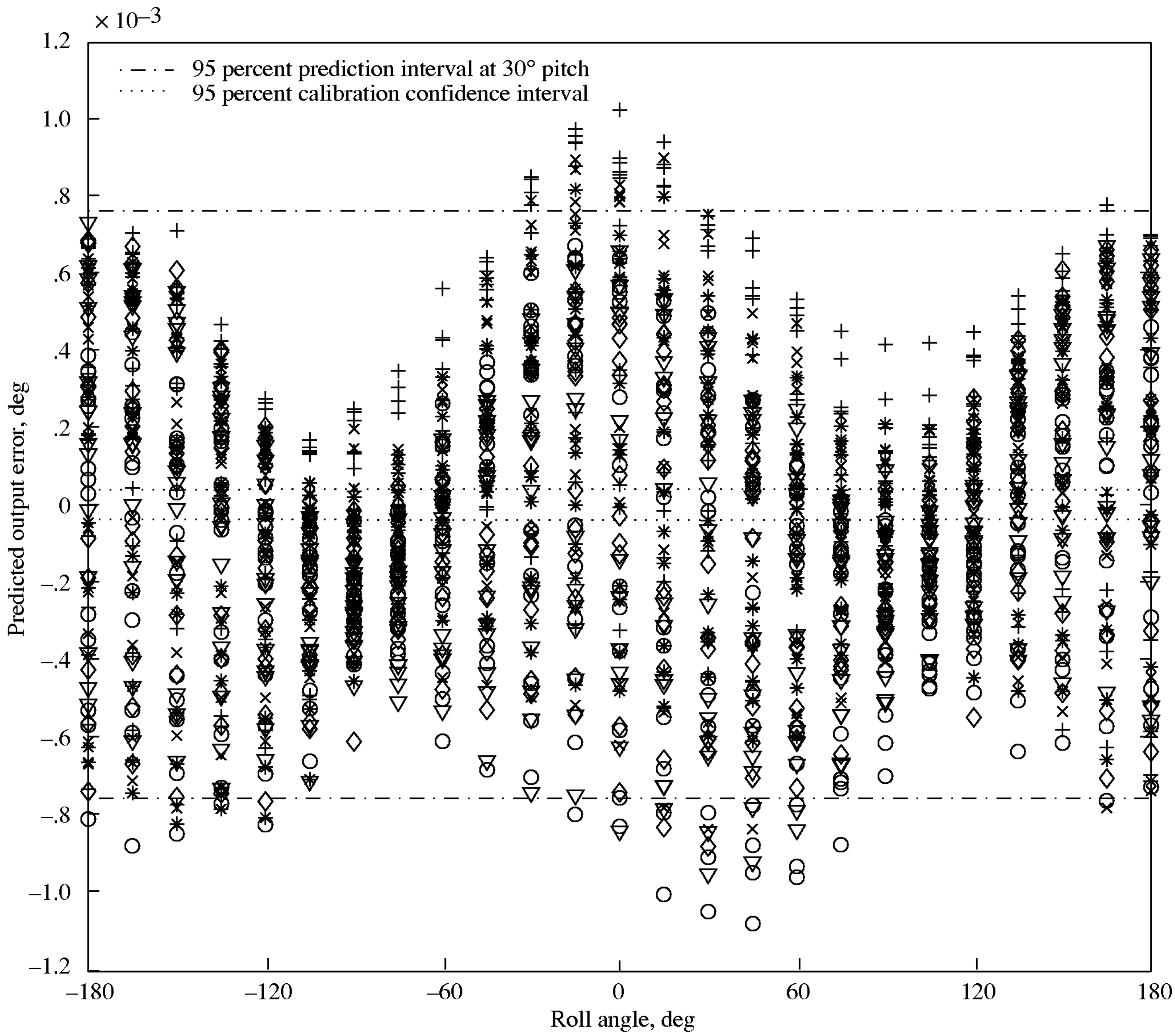

Figure 31. Residuals of predicted output versus roll angle of single-axis AOA sensor with roll for six replications from −180° to 180°. With temperature correction.

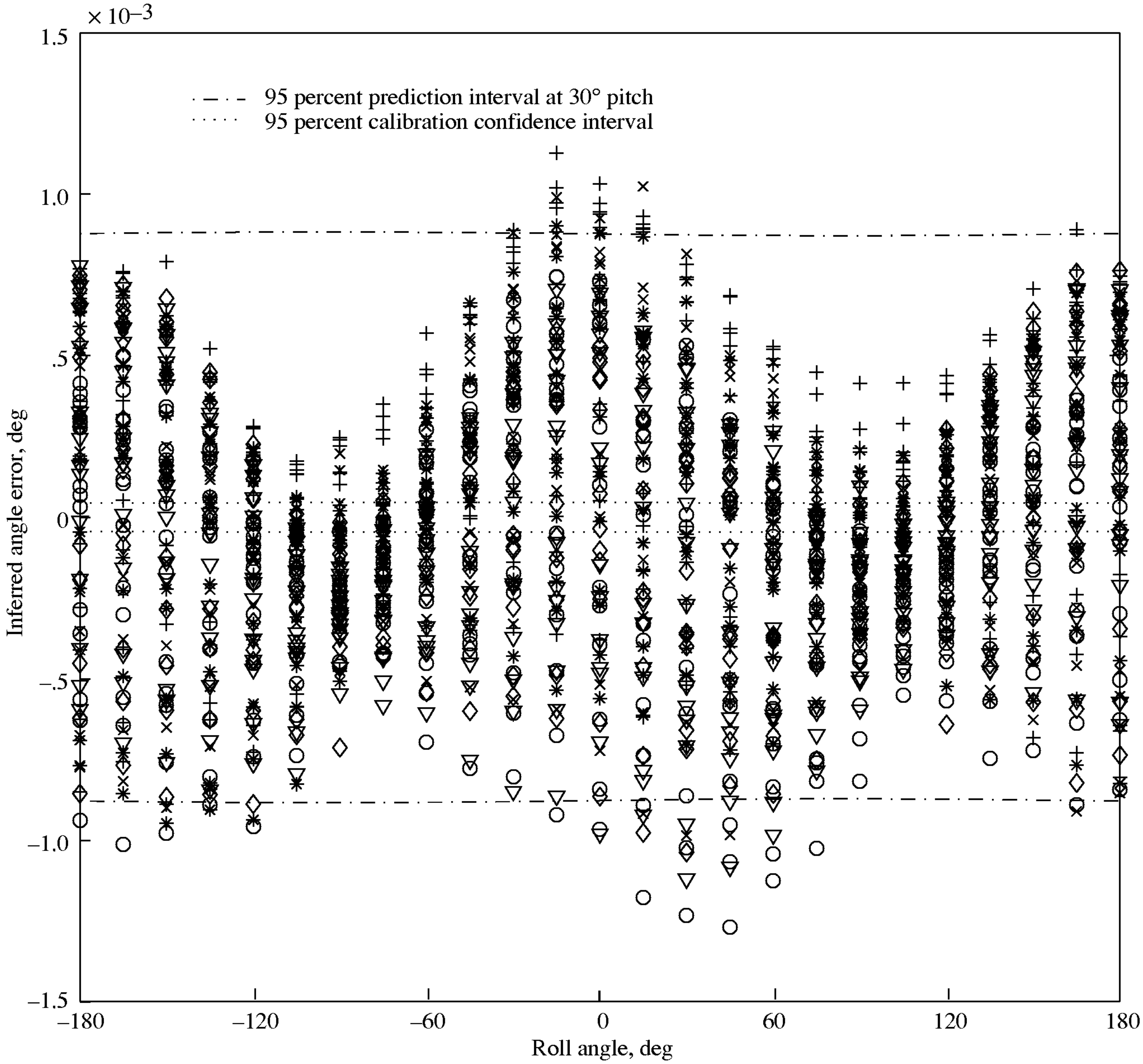

Figure 32. Errors of inferred pitch angle versus roll angle of single-axis AOA sensor with roll for six replications from −180° to 180°. With temperature correction.

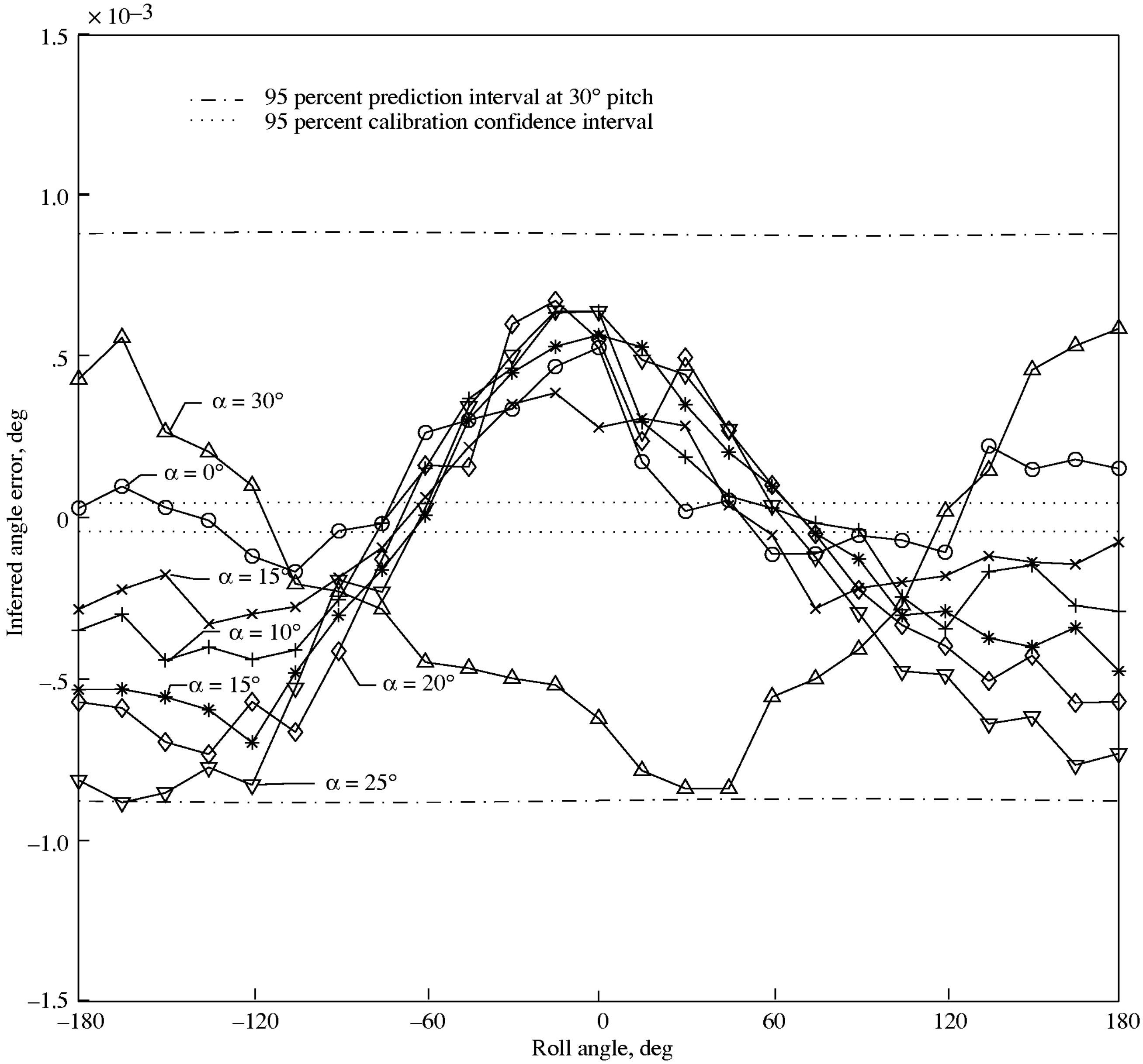

Figure 33. Errors of inferred pitch angle versus roll angle of single-axis AOA sensor with roll for one replication from $-180°$ to $180°$. With temperature correction.

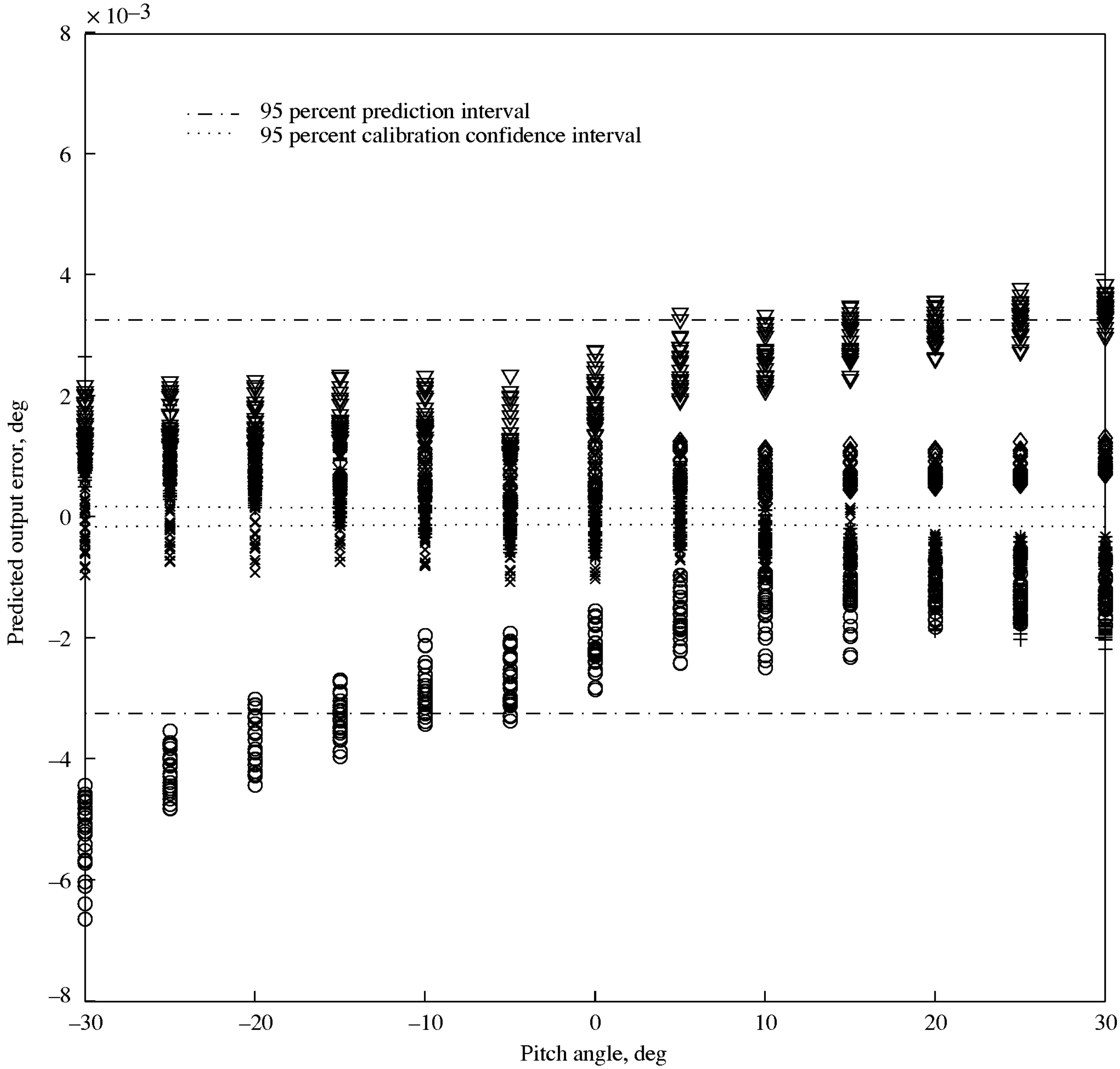

Figure 34. Residuals of predicted output of single-axis AOA sensor 2 for six replications from $-30°$ to $30°$. With temperature correction.

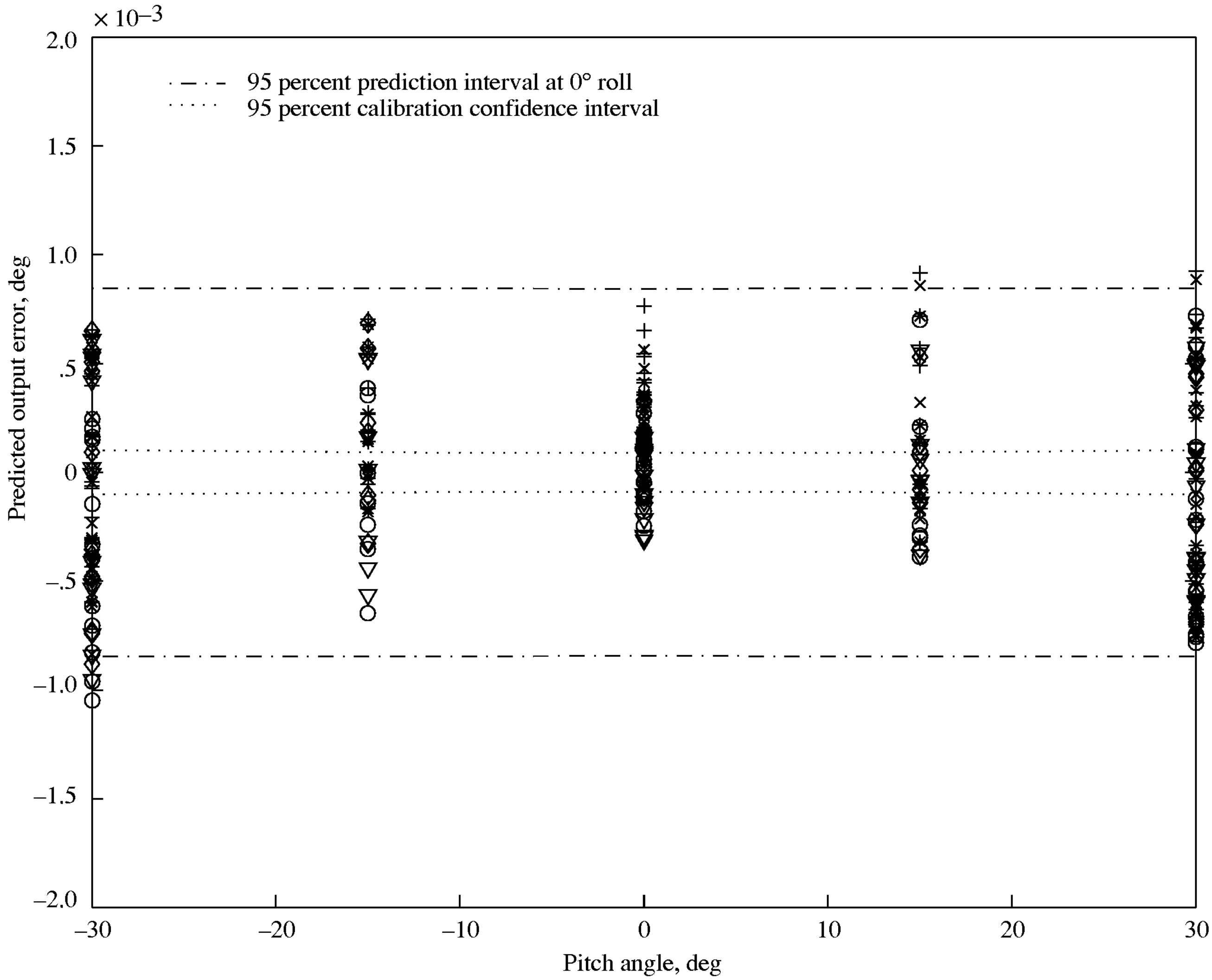

Figure 35. Residuals of predicted output of single-axis AOA sensor with roll for fractional design and six replications from $-30°$ to $30°$. With temperature correction.

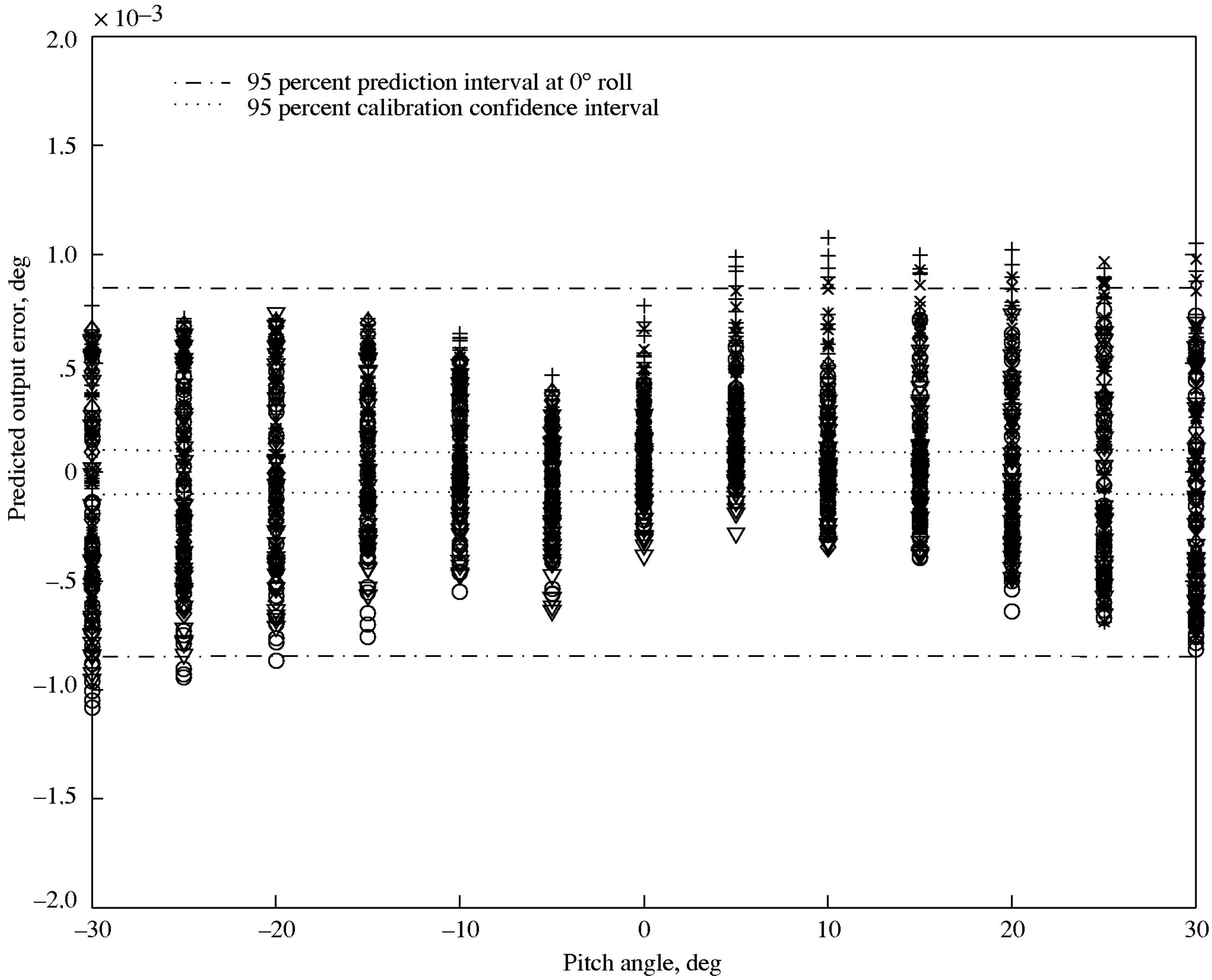

Figure 36. Residuals of predicted output of single-axis AOA sensor with roll that were recomputed by using parameters estimated from fractional design. With temperature correction.

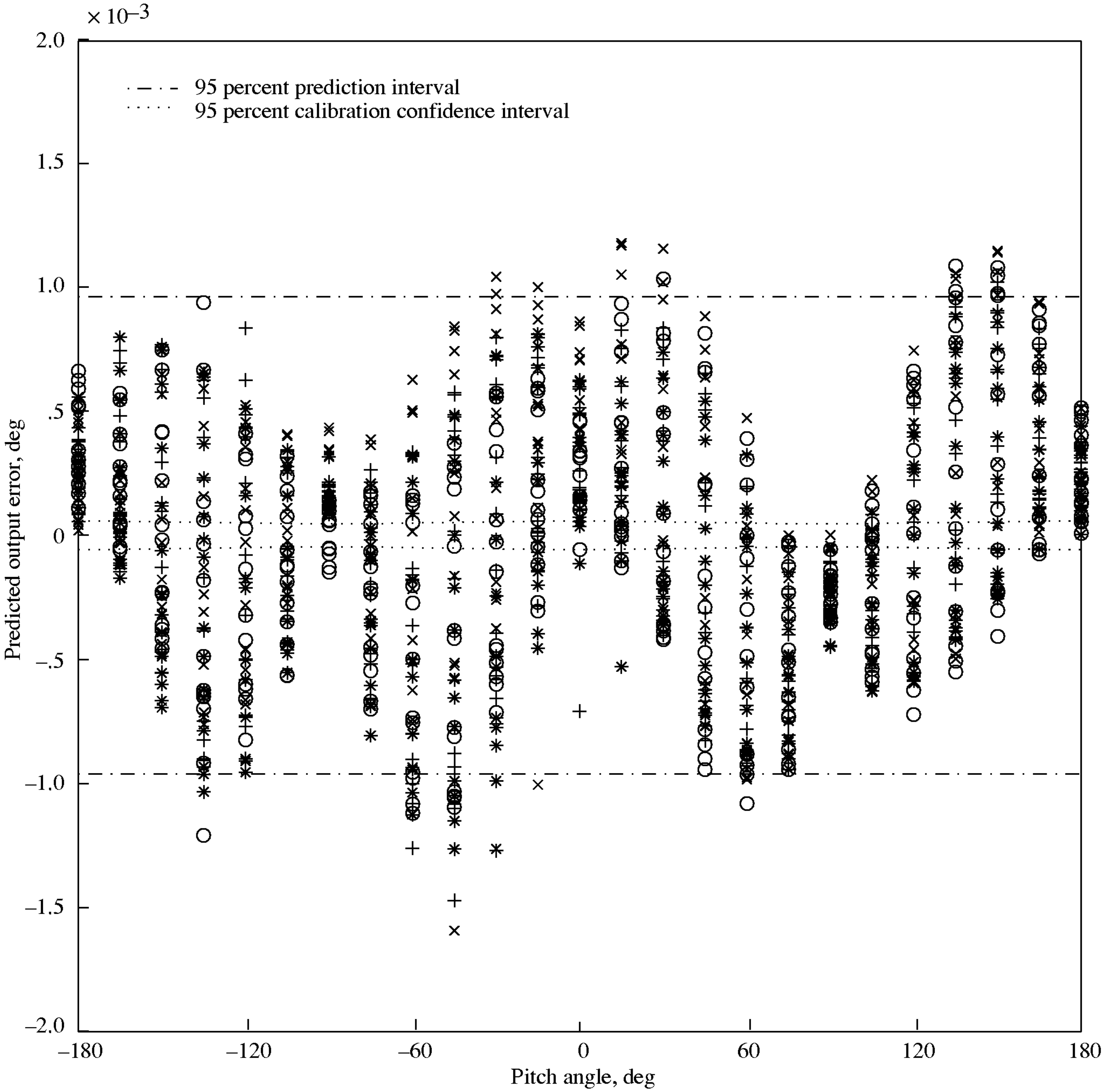

Figure 37. Residuals of predicted output of single-axis AOA sensor with roll for four replications from $-180°$ to $180°$. With temperature correction.

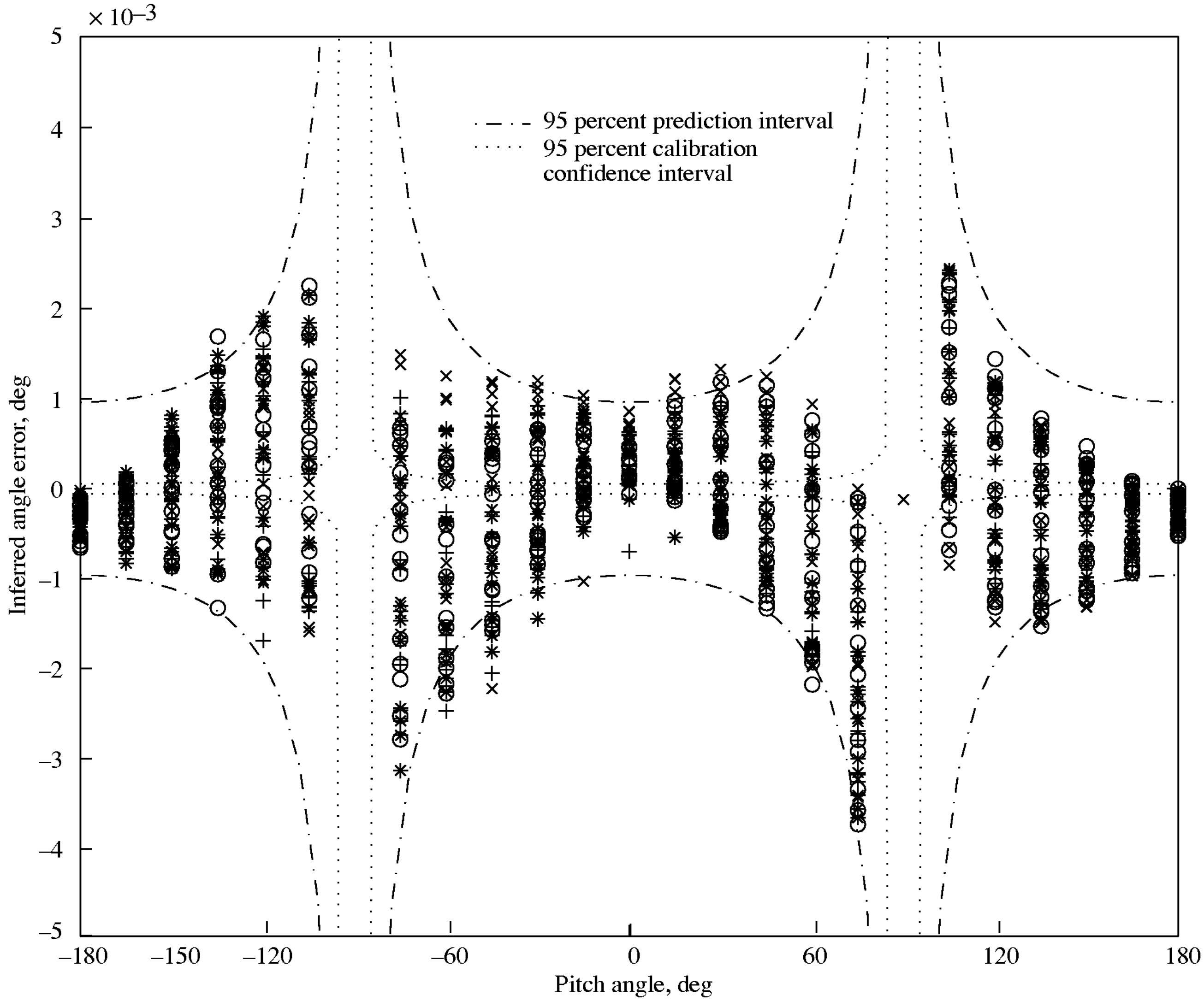

Figure 38. Errors of inferred pitch angle of single-axis AOA sensor with roll for four replications from $-180°$ to $180°$. With temperature correction.

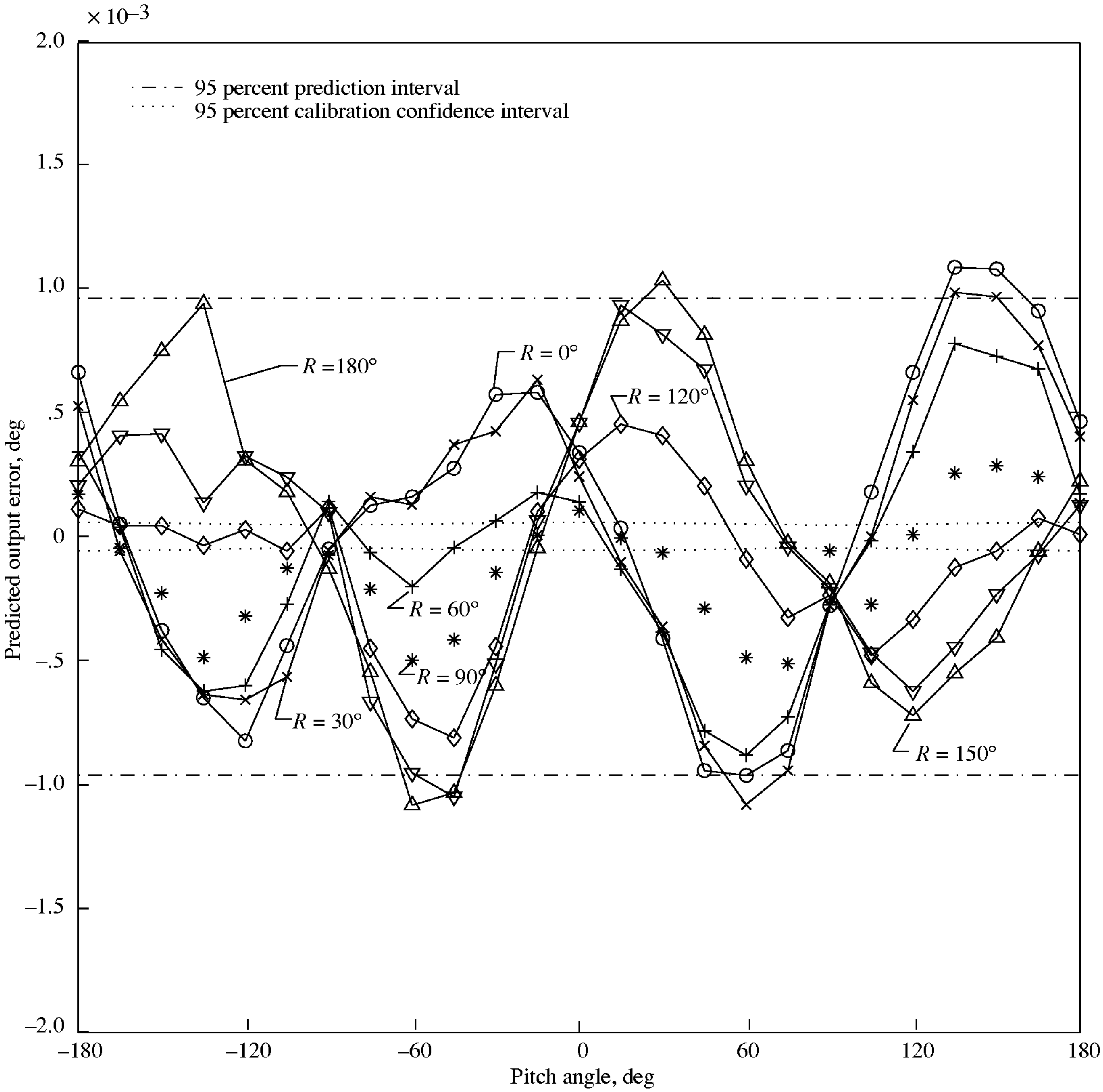

Figure 39. Residuals of predicted output of single-axis AOA sensor with roll for one replication from −180° to 180°. With temperature correction.

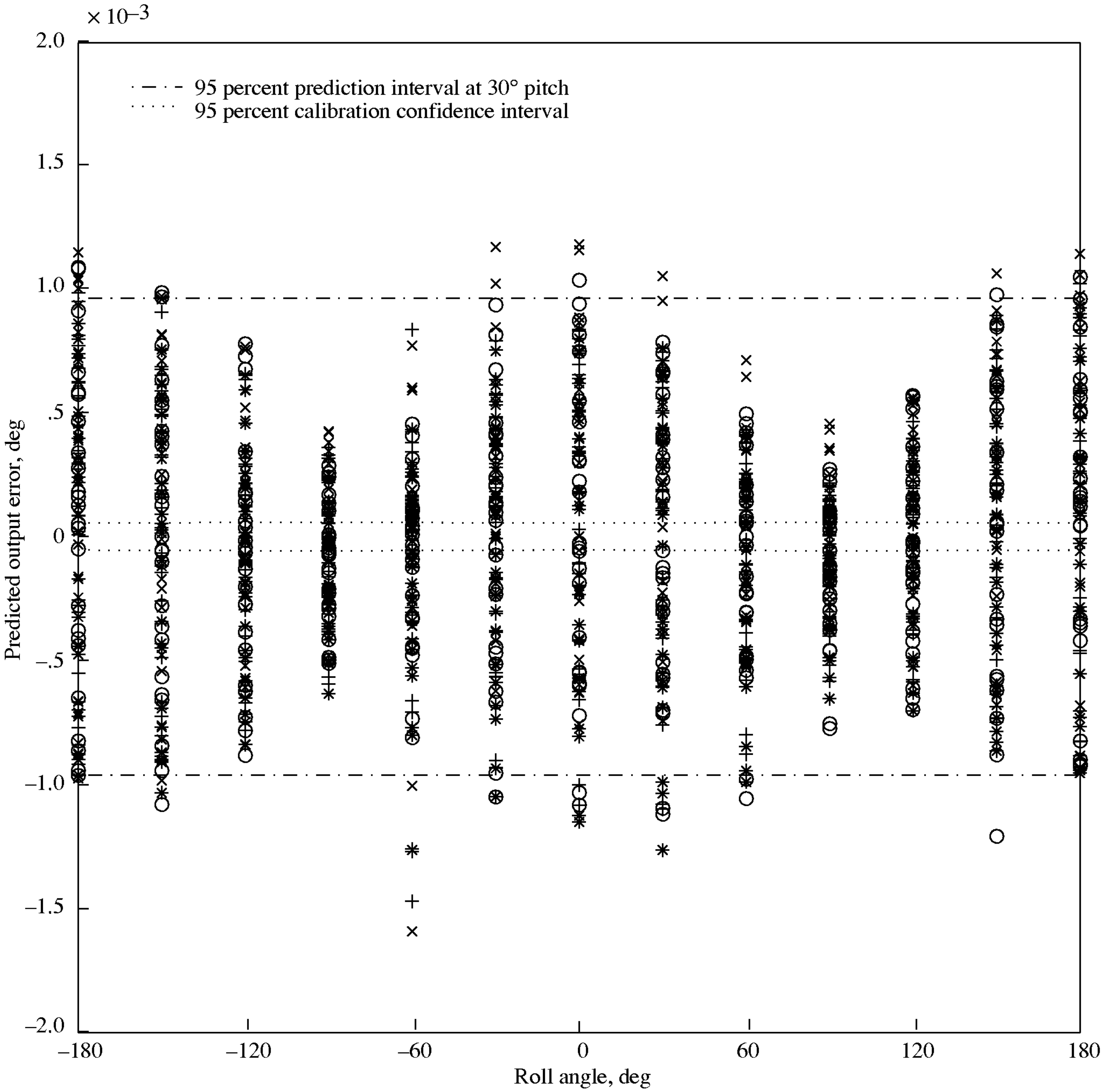

Figure 40. Residuals of predicted output versus roll angle of single-axis AOA sensor with roll for four replications from $-180°$ to $180°$. With temperature correction.

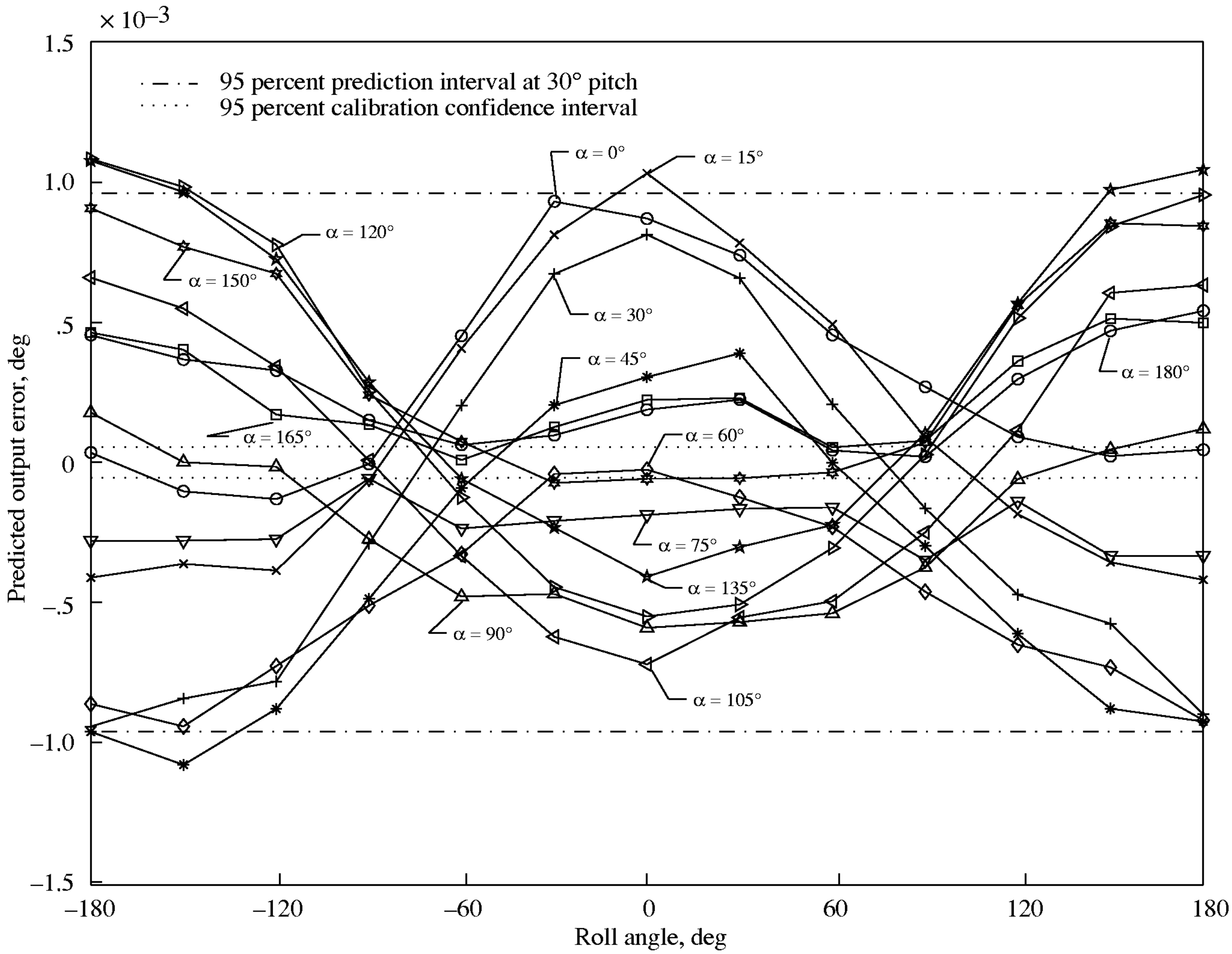

Figure 41. Residuals of predicted output versus roll angle of single-axis AOA sensor with roll for one replication from −180° to 180°. With temperature correction.

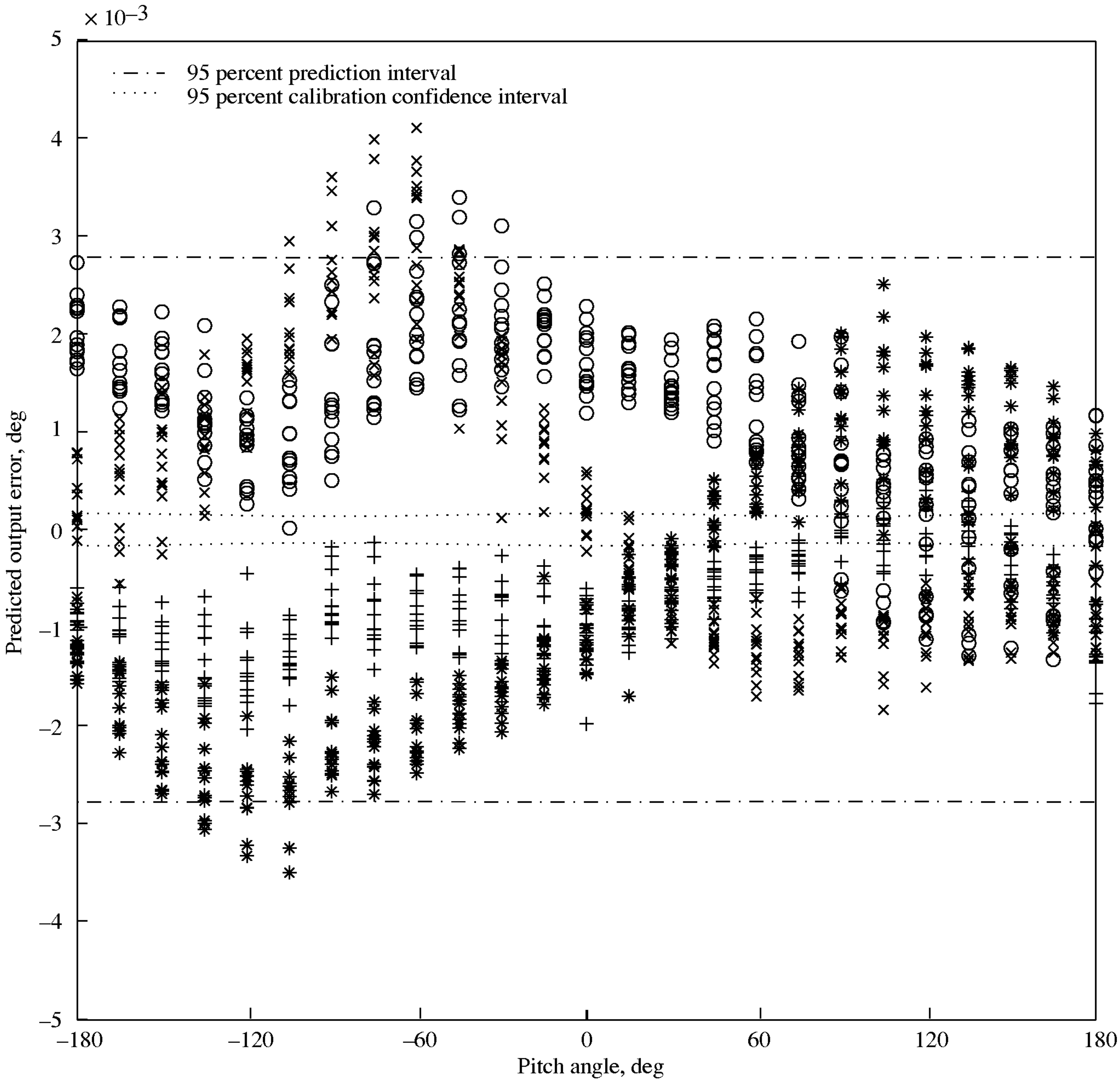

Figure 42. Residuals of predicted output of single-axis AOA sensor 2 with roll for six replications from -180° to 180°. With temperature correction.

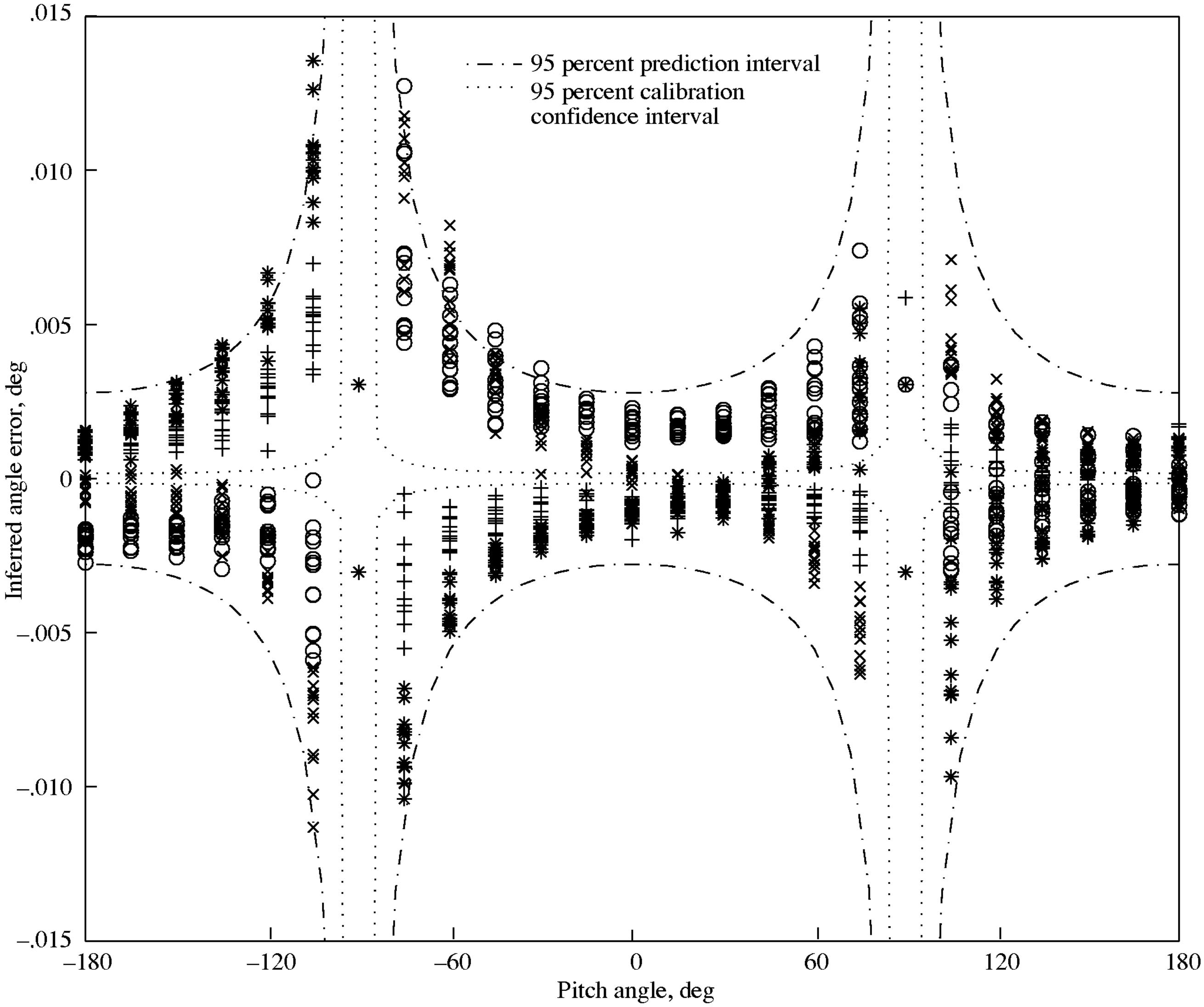

Figure 43. Errors of inferred pitch angle of single-axis AOA sensor 2 with roll for six replications from $-180°$ to $180°$. With temperature correction.

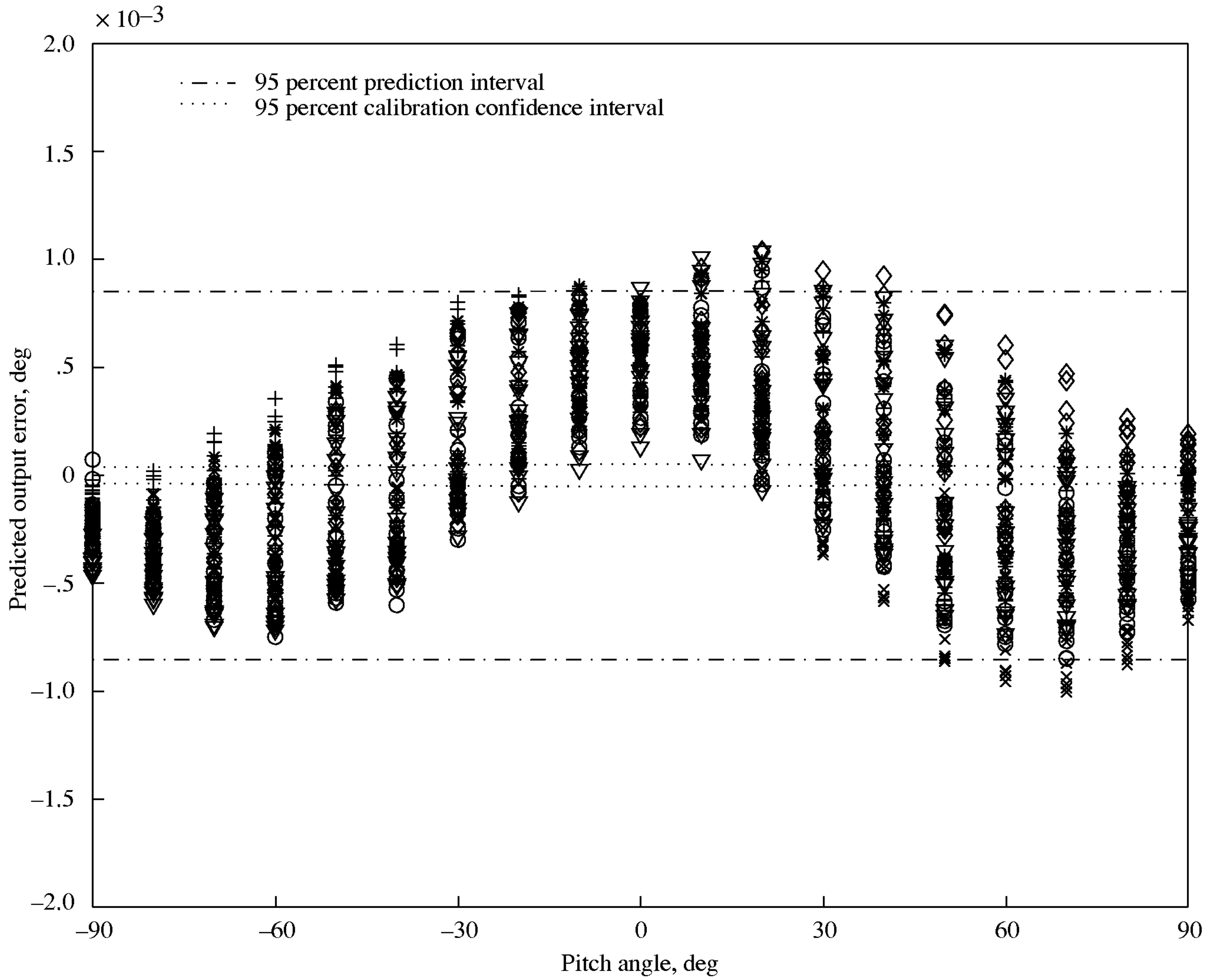

(a) x-axis sensor.

Figure 44. Predicted output residuals of three-axis AOA package with roll for six replications from $-90°$ to $90°$. With temperature correction.

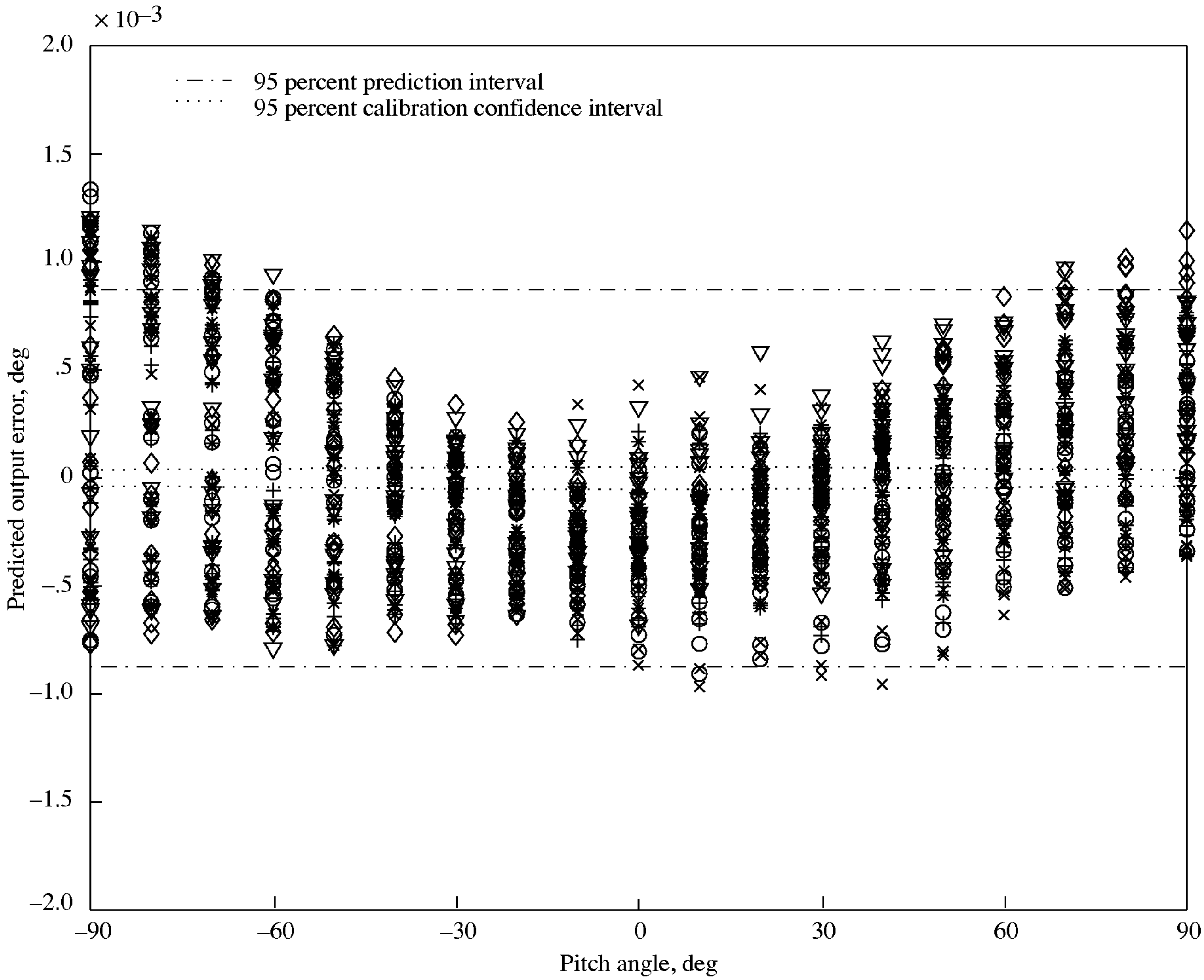

(b) y-axis sensor.

Figure 44. Continued.

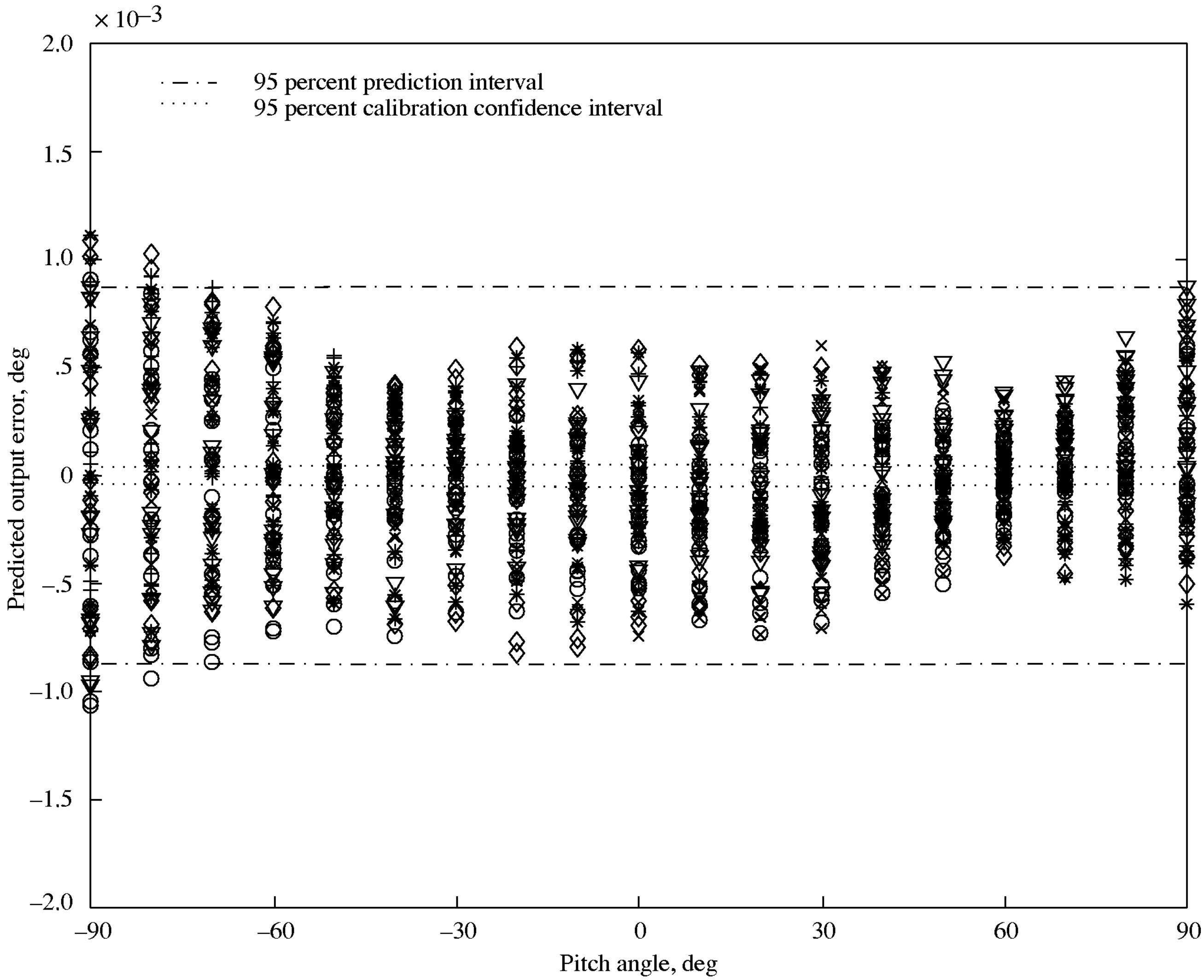

(c) z-axis sensor.

Figure 44. Concluded.

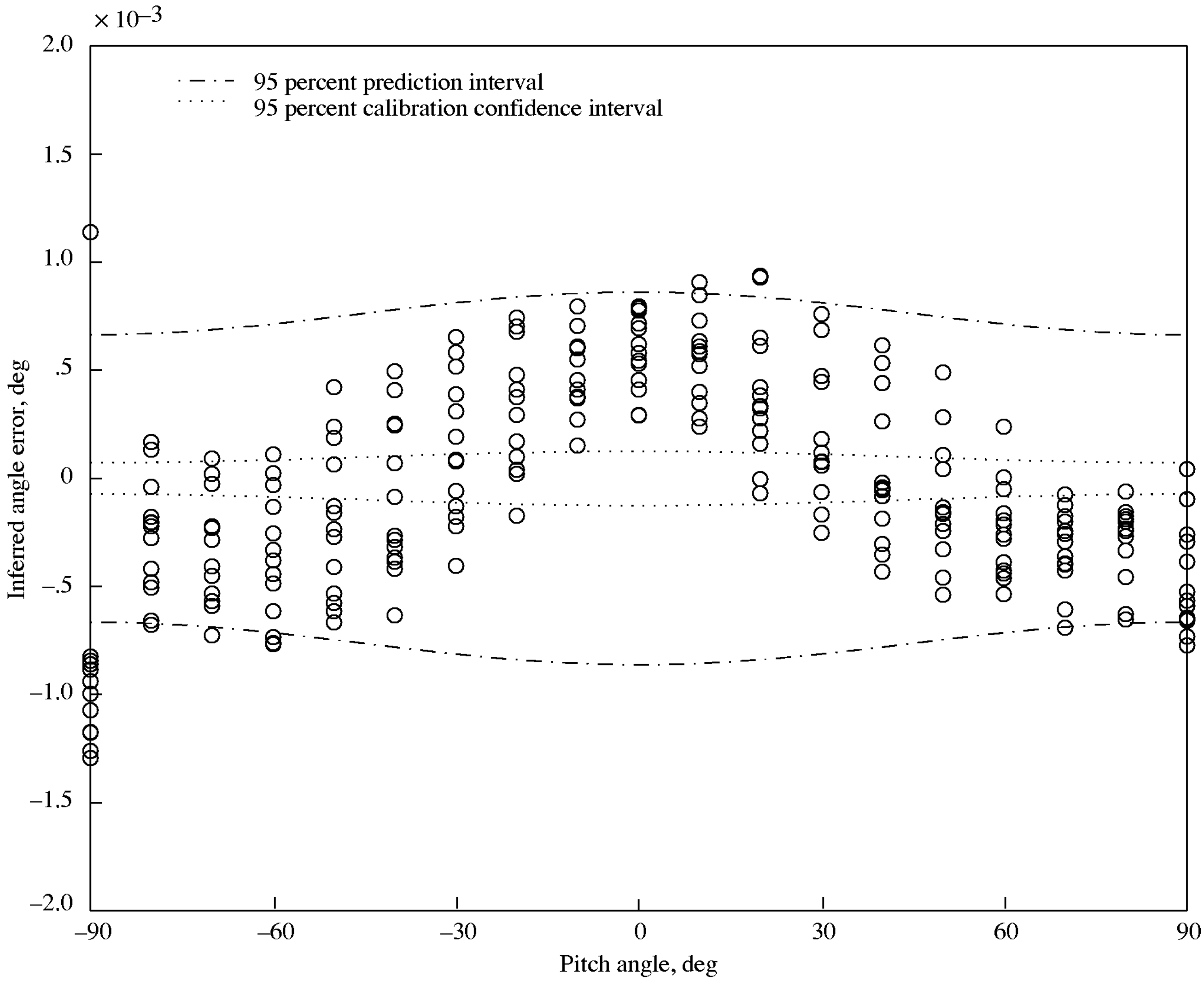

Figure 45. Errors of inferred pitch angles of three-axis AOA package with roll for one replication from $-90°$ to $90°$. With temperature correction.

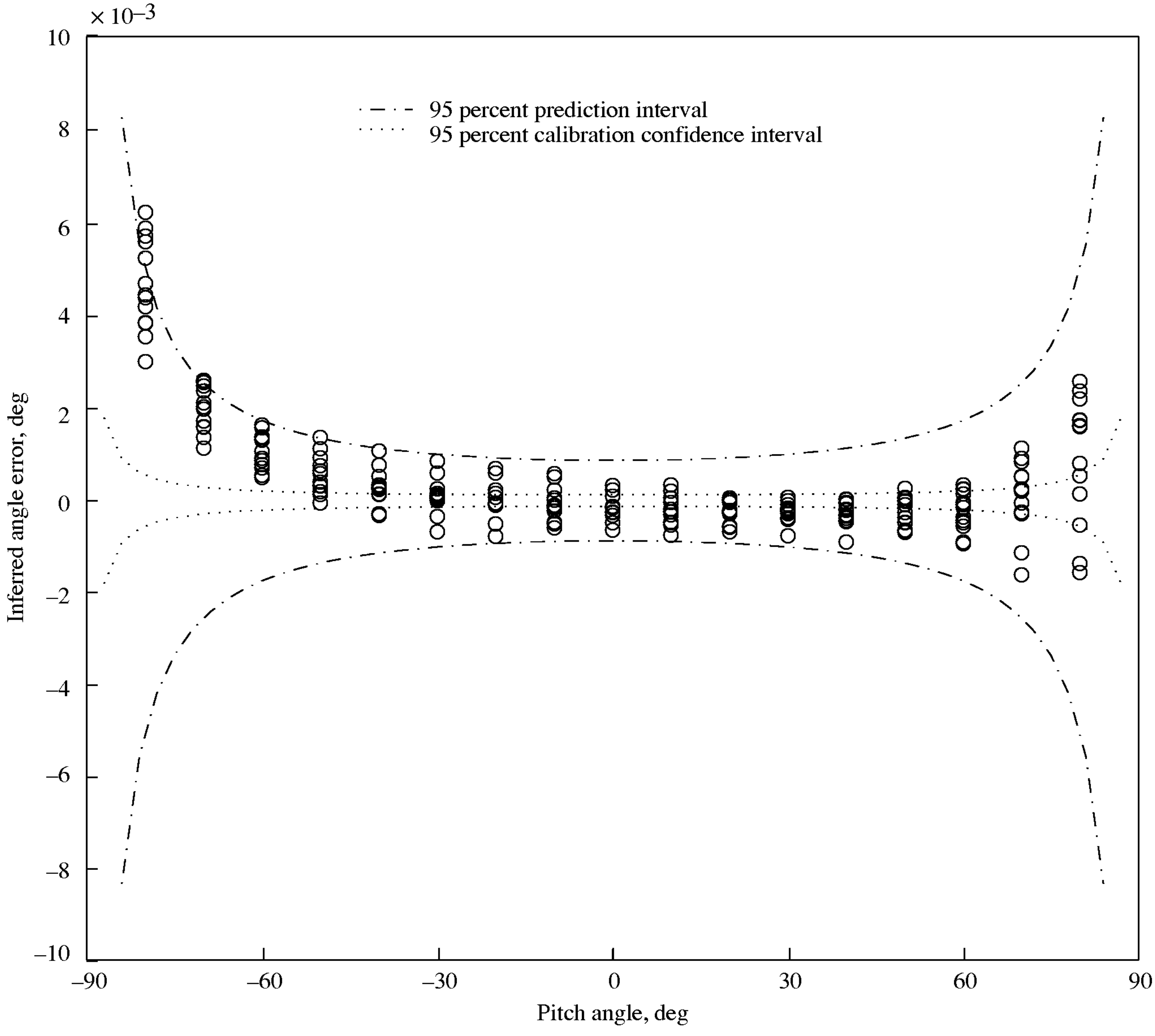

Figure 46. Errors of inferred roll angles of three-axis AOA package with roll for one replication from -90° to 90°. With temperature correction.

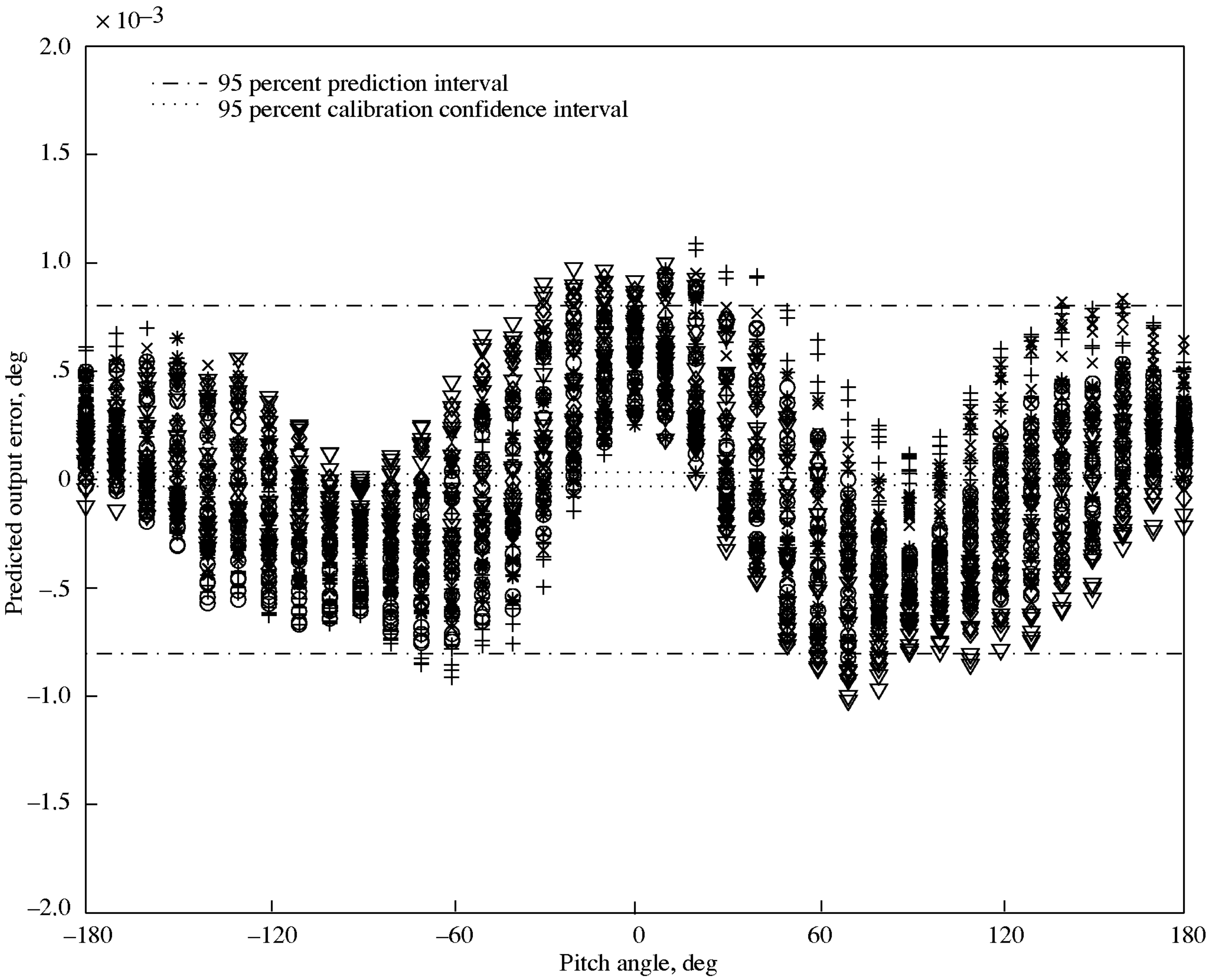

(a) x-axis sensor.

Figure 47. Predicted output residuals of three-axis AOA package with roll for six replications from $-180°$ to $180°$. With temperature correction.

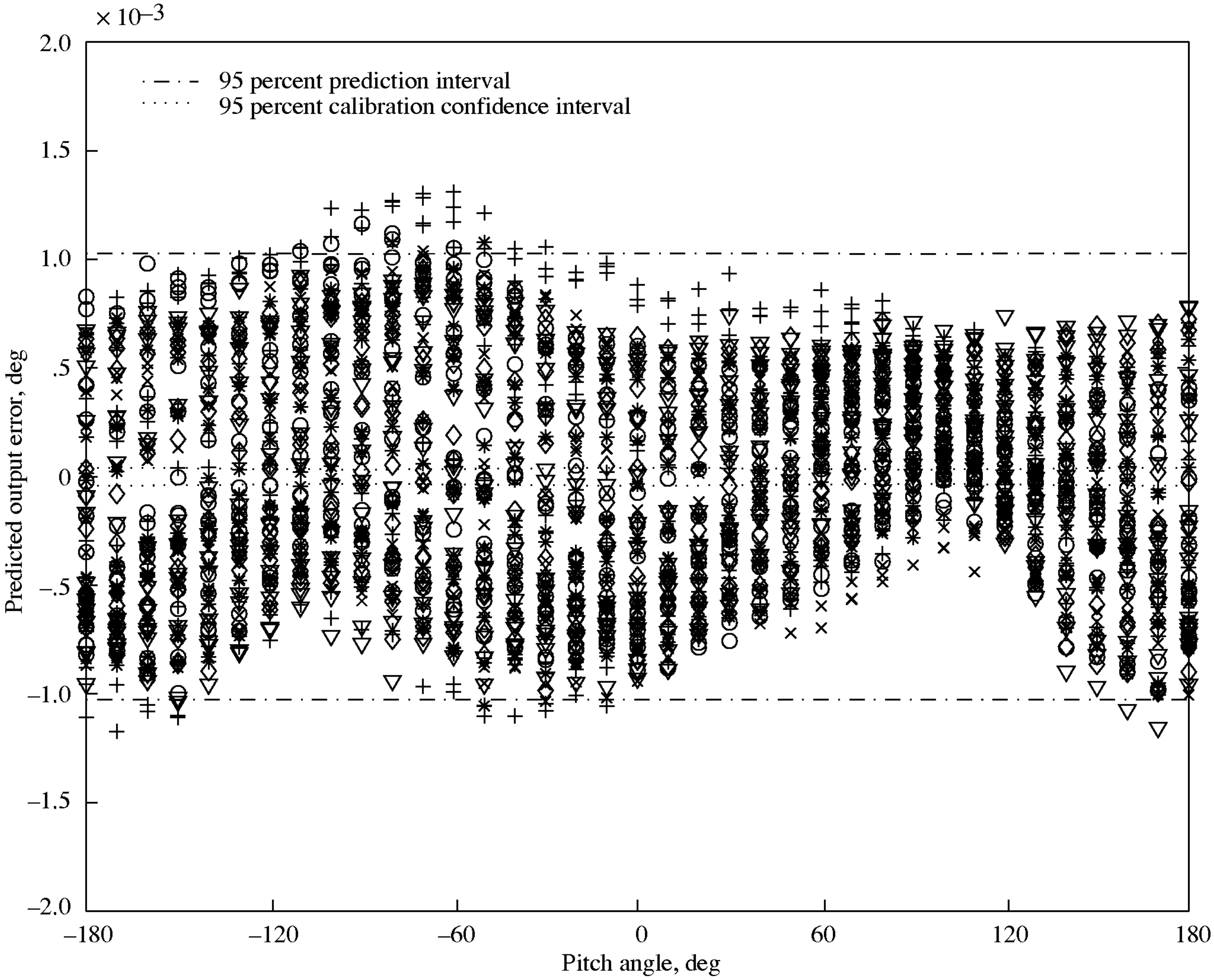

(b) y-axis sensor.

Figure 47. Continued.

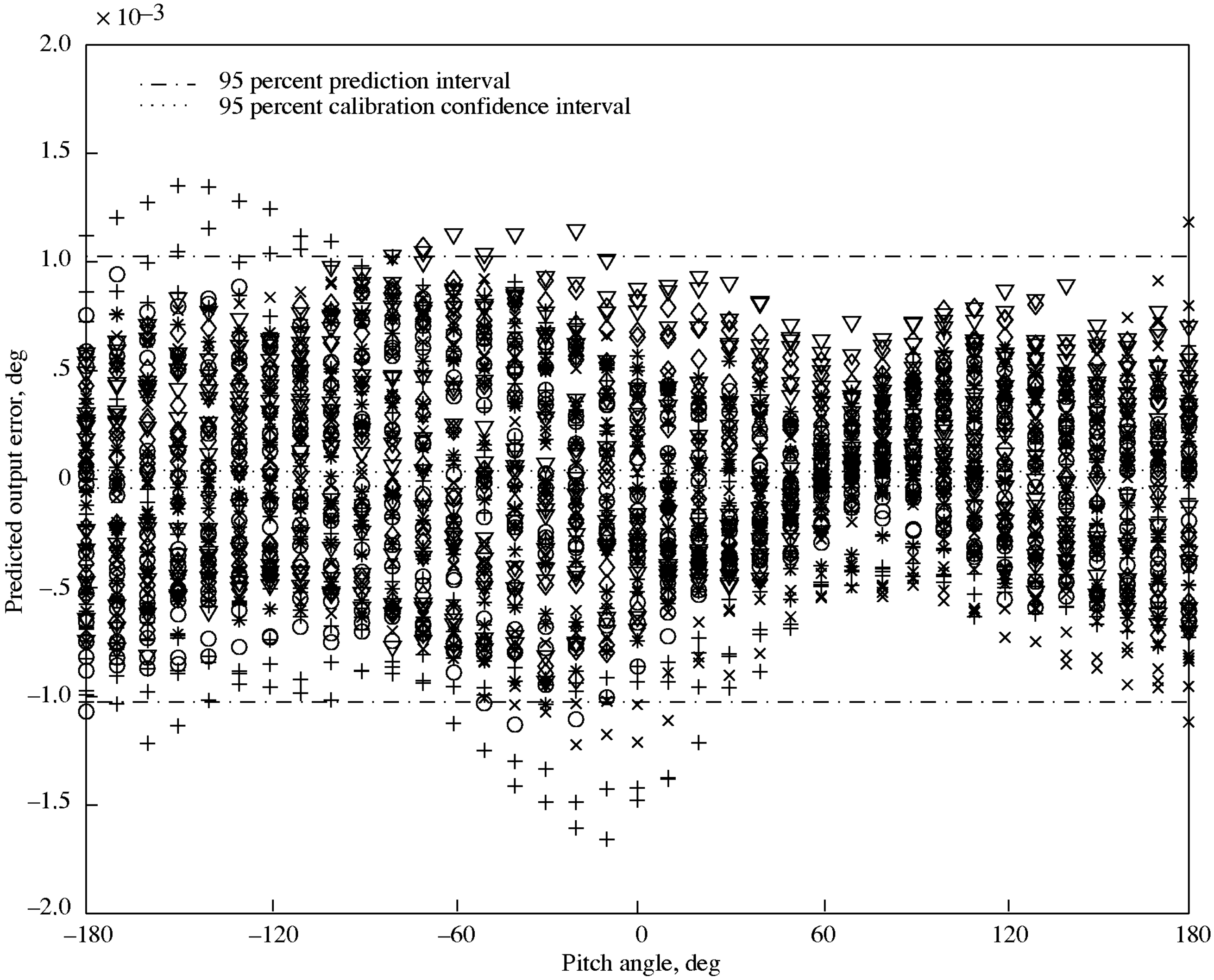

(c) z-axis sensor.

Figure 47. Concluded.

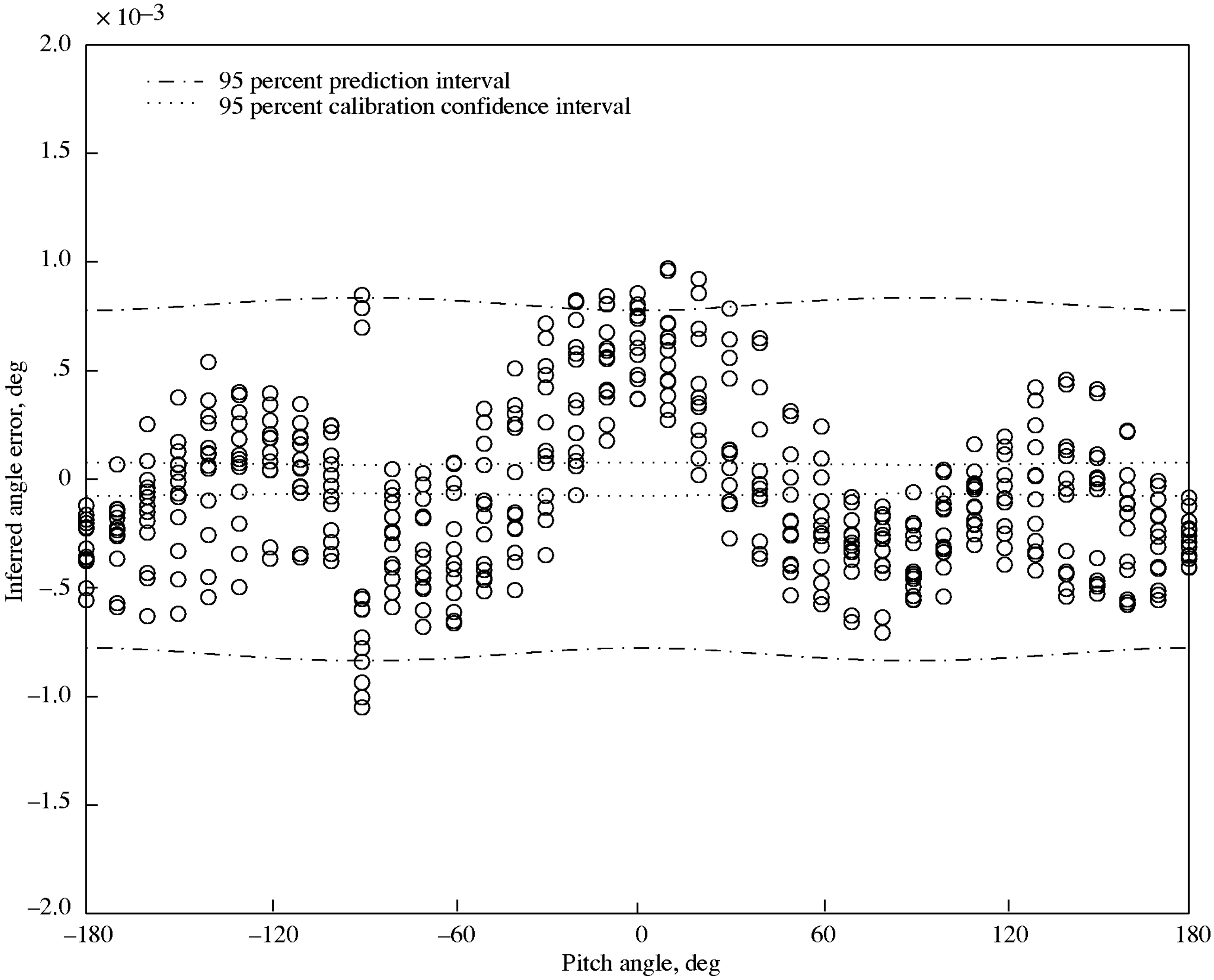

Figure 48. Errors of inferred pitch angles of three-axis AOA package with roll for one replication from $-180°$ to $180°$. With temperature correction.

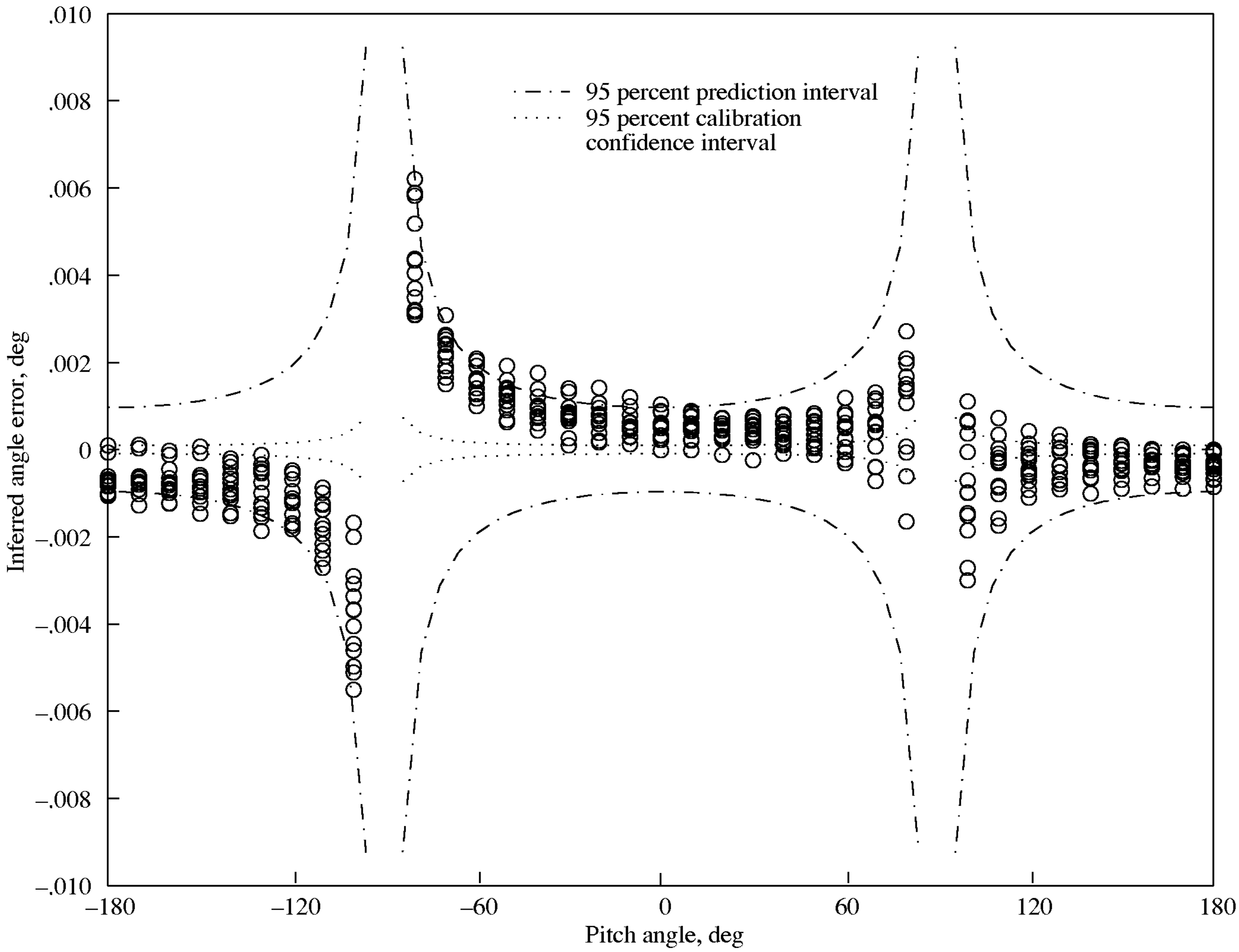

Figure 49. Errors of inferred roll angles of three-axis AOA package with roll for one replication from $-180°$ to $180°$. With temperature correction.

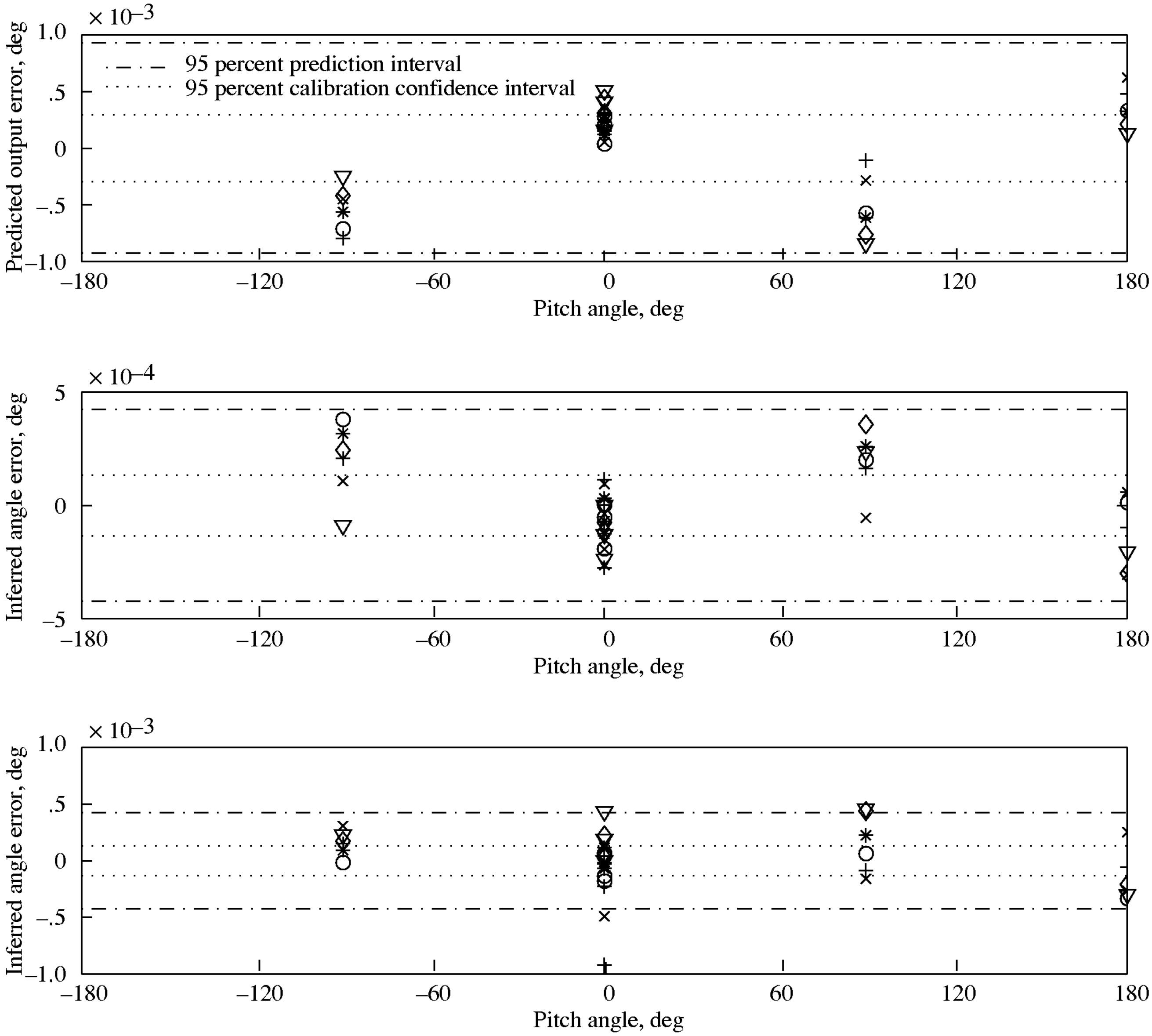

Figure 50. Errors of predicted output residuals of x-, y-, and z-axis sensors of three-axis AOA package with roll for four-point tumble test with six replications. With temperature correction.

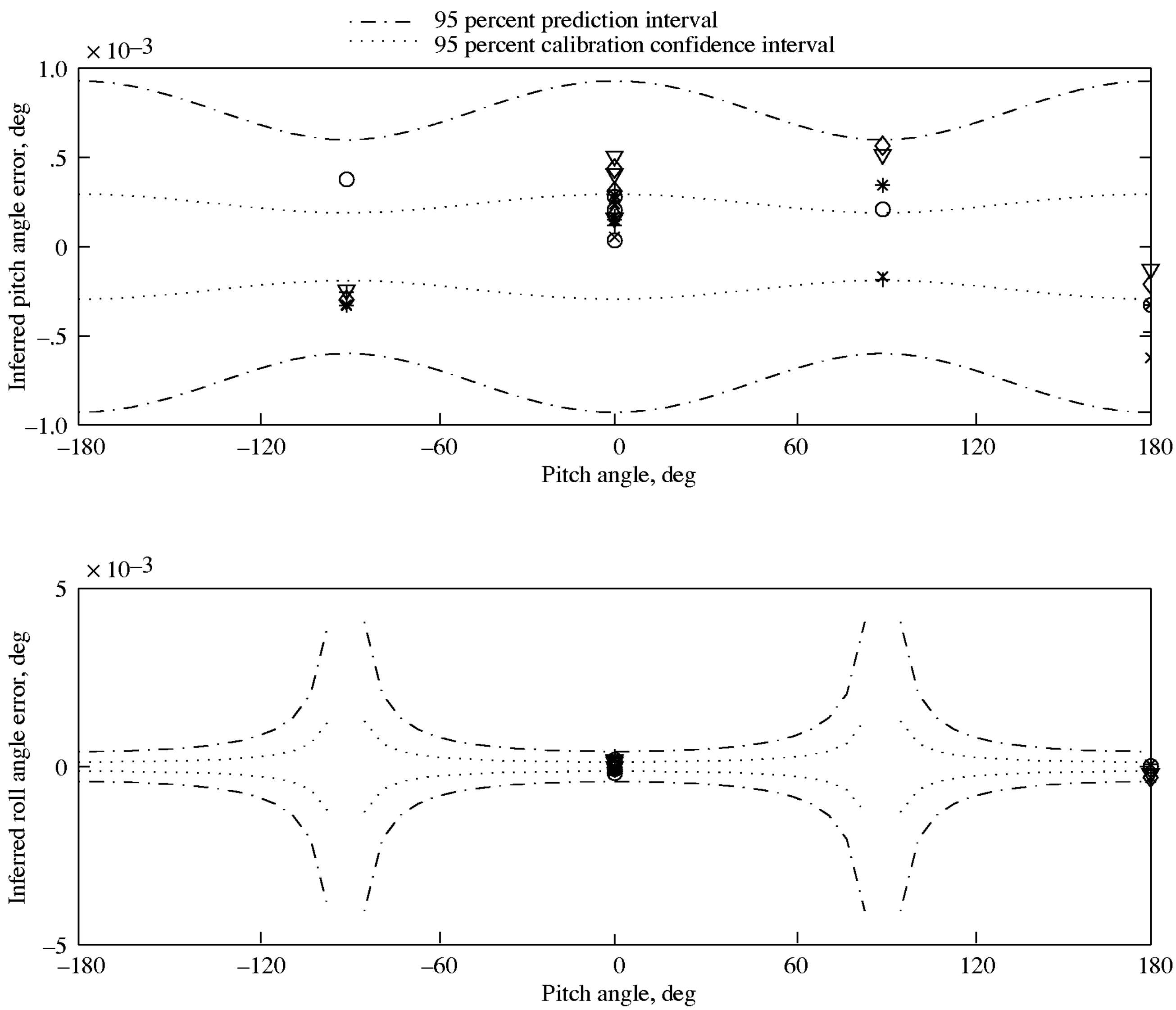

Figure 51. Errors of inferred pitch and roll angles of three-axis AOA package with roll for six-point tumble test with six replications. With temperature correction.

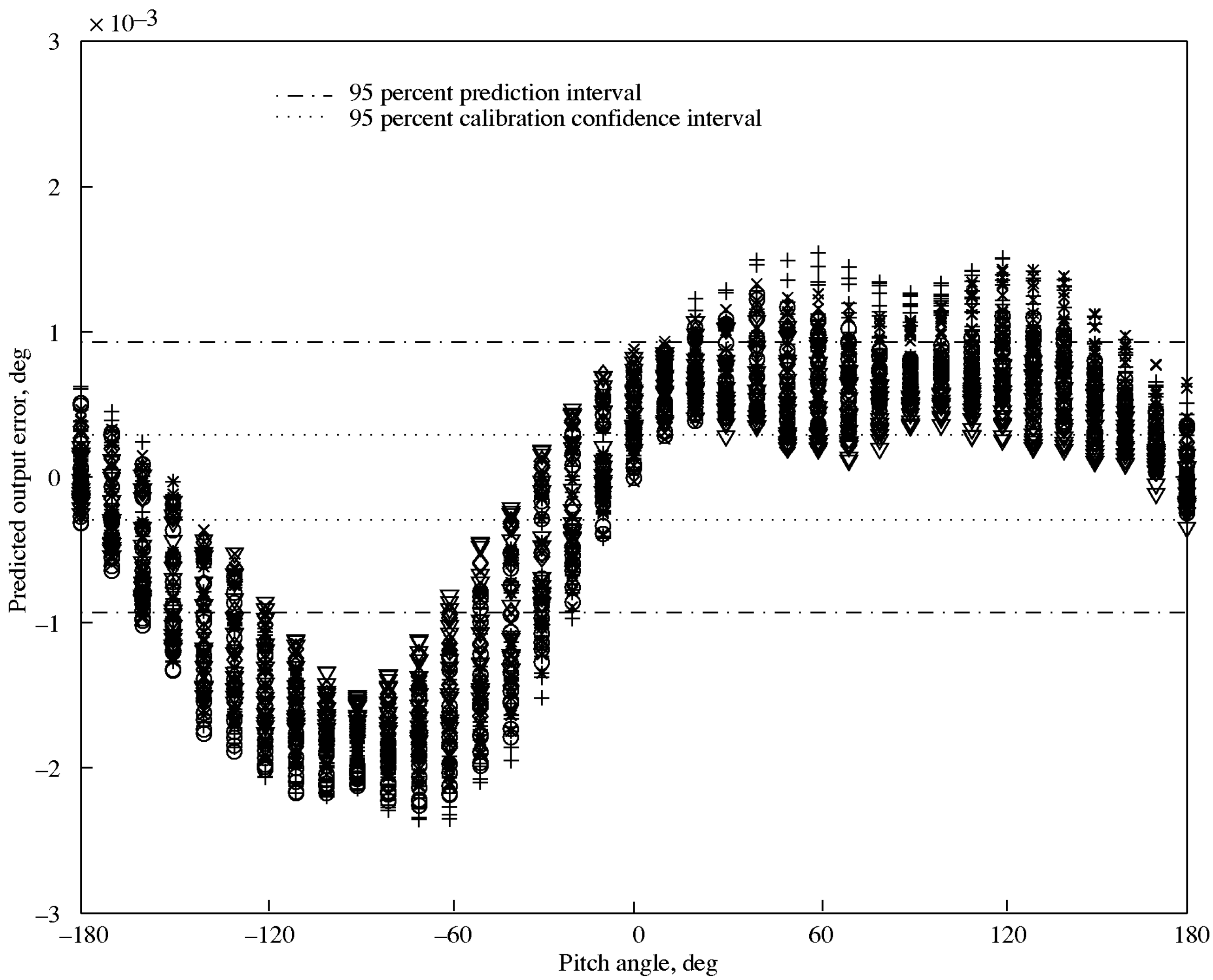

(a) x-axis sensor.

Figure 52. Predicted output residuals of three-axis AOA package with roll calculated by using parameters estimated from six-point tumble test. With temperature correction.

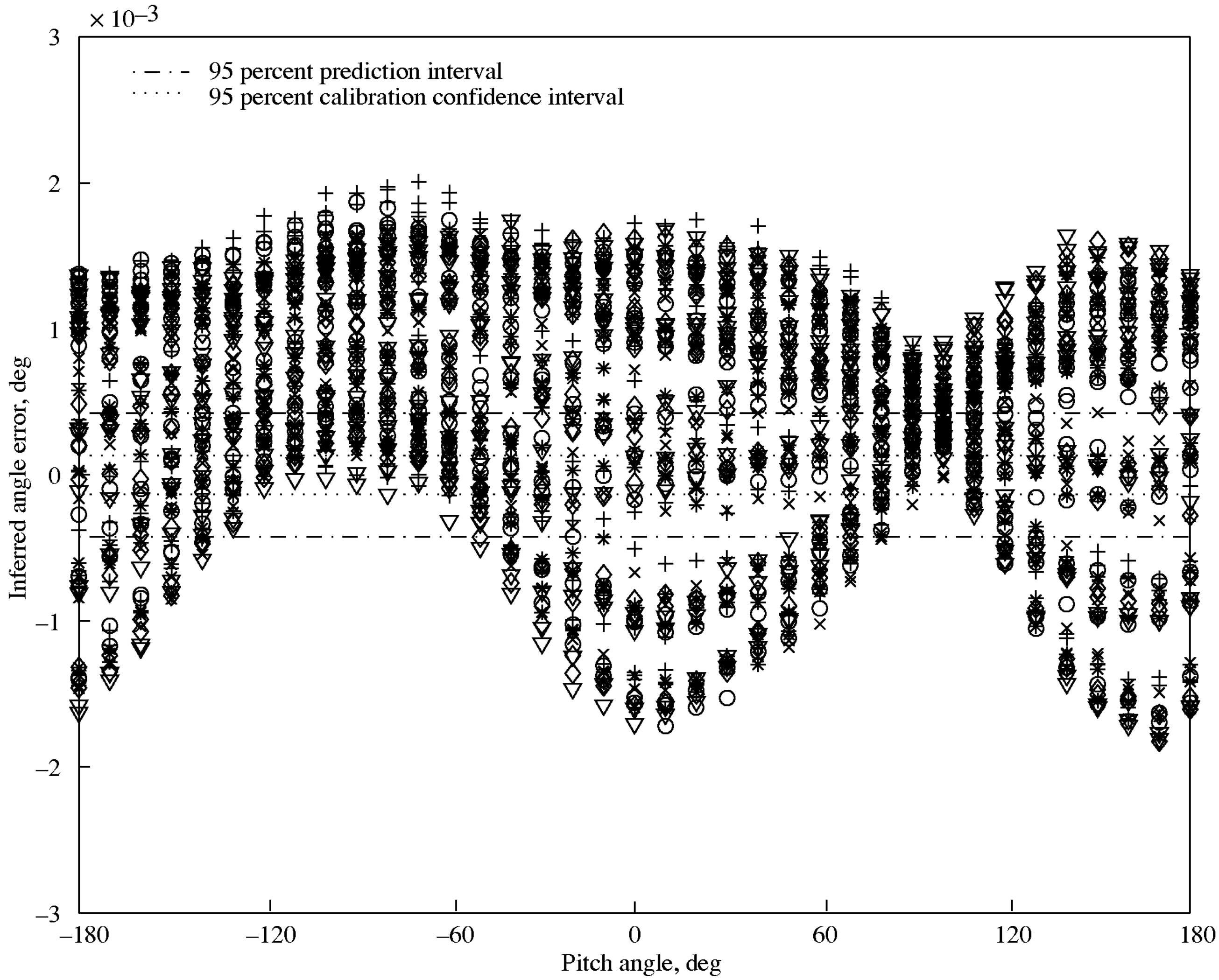

(b) y-axis sensor.

Figure 52. Continued.

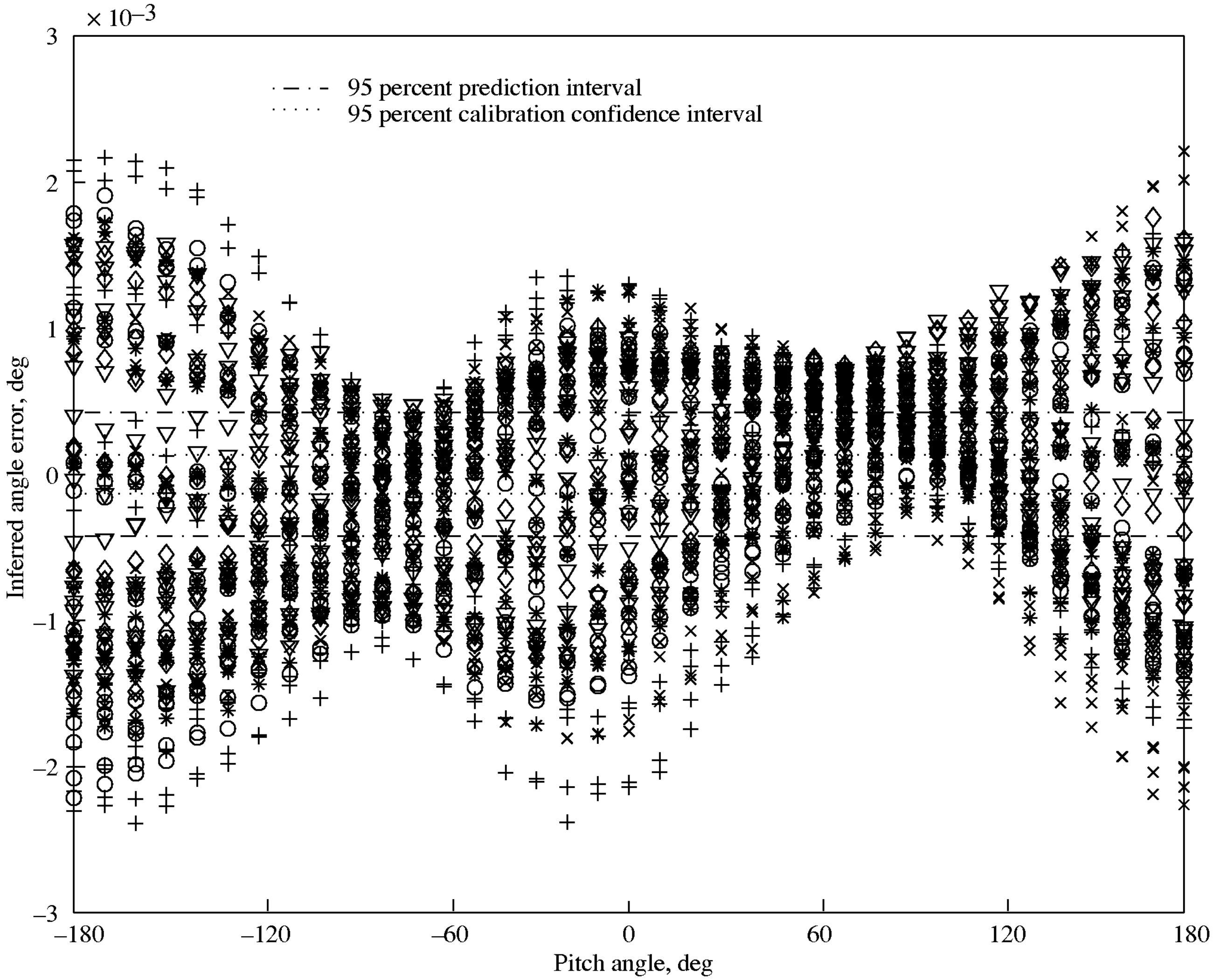

(c) z-axis sensor.

Figure 52. Concluded.

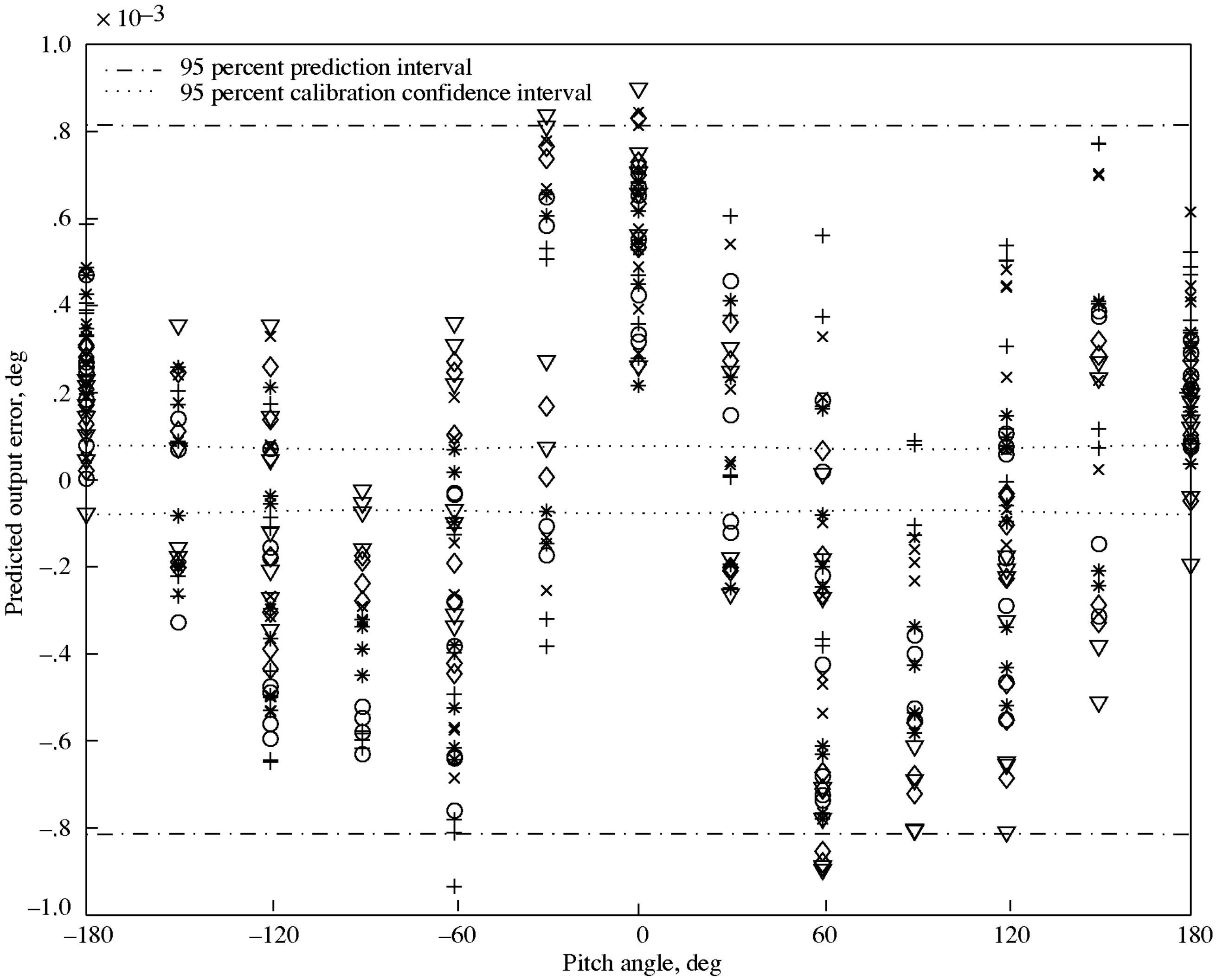

Figure 53. Predicted output residuals of x-axis sensor of three-axis AOA package with roll for fractional design with six replications.

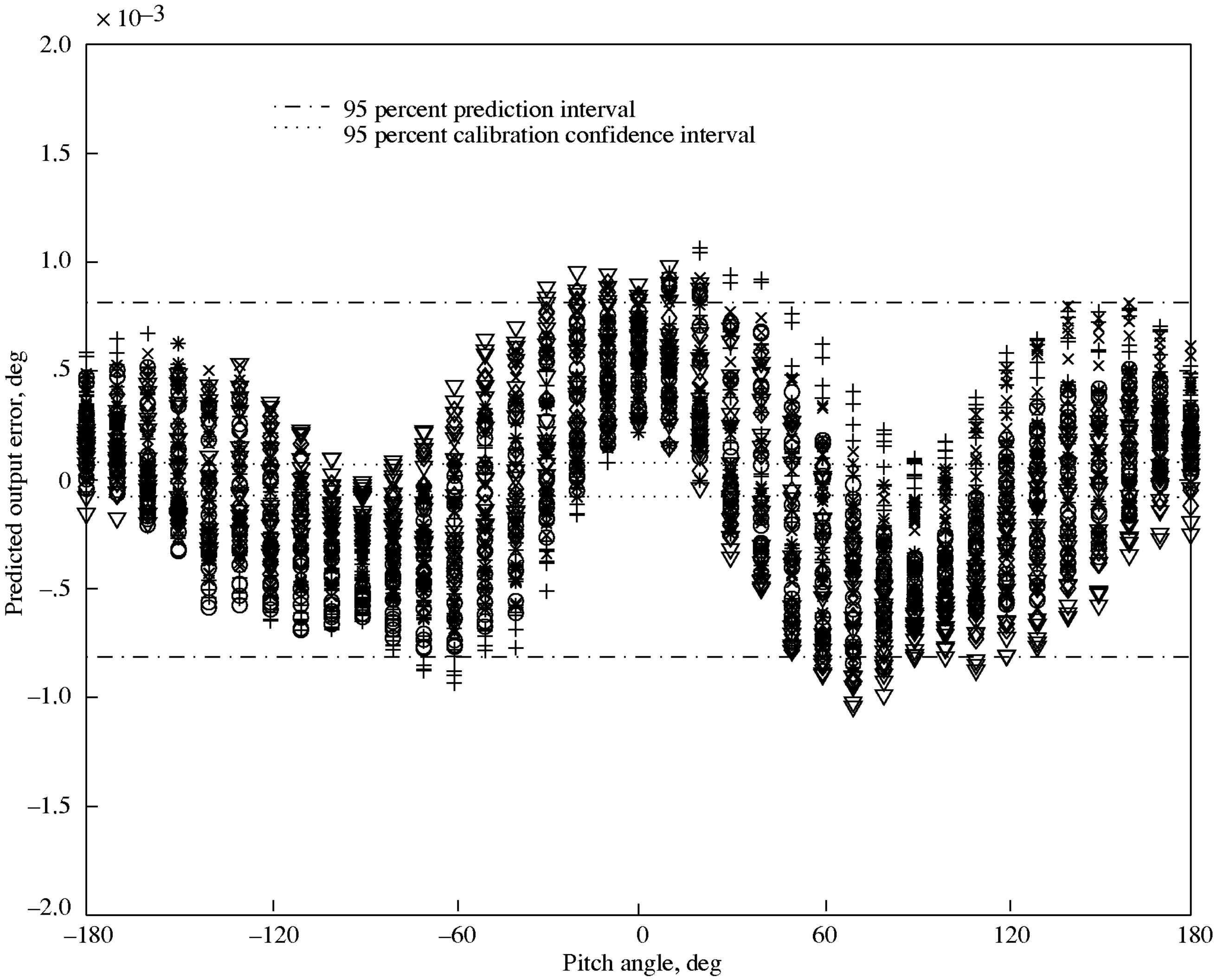

Figure 54. Predicted output residuals of x-axis sensor of three-axis AOA package with roll calculated by using parameters estimated from fractional design.

REPORT DOCUMENTATION PAGE	*Form Approved OMB No. 07704-0188*

1. AGENCY USE ONLY *(Leave blank)*	2. REPORT DATE	3. REPORT TYPE AND DATES COVERED
	December 1999	Technical Publication

4. TITLE AND SUBTITLE Uncertainty Analysis of Inertial Model Attitude Sensor Calibration and Application With a Recommended New Calibration Method	5. FUNDING NUMBERS WU 519-20-21-01
6. AUTHOR(S) John S. Tripp and Ping Tcheng	
7. PERFORMING ORGANIZATION NAME(S) AND ADDRESS(ES) NASA Langley Research Center Hampton, VA 23681-2199	8. PERFORMING ORGANIZATION REPORT NUMBER L-17750
9. SPONSORING/MONITORING AGENCY NAME(S) AND ADDRESS(ES) National Aeronautics and Space Administration Washington, DC 20546-0001	10. SPONSORING/MONITORING AGENCY REPORT NUMBER NASA/TP-1999-209835

11. SUPPLEMENTARY NOTES

12a. DISTRIBUTION/AVAILABILITY STATEMENT Unclassified–Unlimited Subject Category 35 Distribution: Standard Availability: NASA CASI (301) 621-0390	12b. DISTRIBUTION CODE

13. ABSTRACT *(Maximum 200 words)*

Statistical tools, previously developed for nonlinear least-squares estimation of multivariate sensor calibration parameters and the associated calibration uncertainty analysis, have been applied to single- and multiple-axis inertial model attitude sensors used in wind tunnel testing to measure angle of attack and roll angle. The analysis provides confidence and prediction intervals of calibrated sensor measurement uncertainty as functions of applied input pitch and roll angles. A comparative performance study of various experimental designs for inertial sensor calibration is presented along with corroborating experimental data. The importance of replicated calibrations over extended time periods has been emphasized; replication provides independent estimates of calibration precision and bias uncertainties, statistical tests for calibration or modeling bias uncertainty, and statistical tests for sensor parameter drift over time. A set of recommendations for a new standardized model attitude sensor calibration method and usage procedures is included. The statistical information provided by these procedures is necessary for the uncertainty analysis of aerospace test results now required by users of industrial wind tunnel test facilities.

14. SUBJECT TERMS Uncertainty analysis; Model attitude measurement; Calibration procedure; Multiple-axis sensor; Angle of attack; Pitch angle; Roll angle	15. NUMBER OF PAGES 132 16. PRICE CODE A07

17. SECURITY CLASSIFICATION OF REPORT	18. SECURITY CLASSIFICATION OF THIS PAGE	19. SECURITY CLASSIFICATION OF ABSTRACT	20. LIMITATION OF ABSTRACT
Unclassified	Unclassified	Unclassified	UL